
A sensitivity analysis method for evaluating the effect
of input parameter uncertainty on the results of the
PALM model system

Von der Fakultät für Mathematik und Physik
der Gottfried Wilhelm Leibniz Universität Hannover
zur Erlangung des Grades

Doktorin der Naturwissenschaften
Dr. rer. nat.

genehmigte Dissertation von

M.Sc. Simone Pfau

2024

Referent: Prof. Dr. Günter Groß
1. Korreferent: Prof. Dr. Björn Maronga
2. Korreferent: Prof. Dr. Dieter Scherer
Tag der Promotion: 05.04.2024

Kurzzusammenfassung

Im Rahmen dieser Arbeit wird eine Sensitivitätsanalysemethode für Eingangsparameter numerischer Modelle entwickelt und auf das Modellsystem PALM angewendet. PALM ist unter anderem in der Lage, die physikalischen Prozesse im urbanen Raum zu simulieren und kann somit für die Stadtplanung und die Entwicklung von Anpassungsmaßnahmen an den Klimawandel genutzt werden. Im Rahmen des Projekts „Stadtklima im Wandel“ ([UC]²) wurde es weiterentwickelt, evaluiert und angewandt, allerdings wurde die Sensitivität der Modellergebnisse gegenüber den Eingangsparametern noch nicht hinreichend untersucht. Für eine Anwendung von PALM in städtischen Gebieten sind Eingabedaten hinsichtlich Landnutzung, Oberflächen, Bodentyp, Gebäuden und Vegetation erforderlich. Diese können aus verschiedenen Quellen wie kommunalen Daten, Open Street Map, Satellitendaten oder Luftbildern bezogen werden. Die Qualität und Verfügbarkeit der Eingangsdaten ist jedoch sehr heterogen, was zu Unsicherheiten in den Eingangsparametern führt, die sich auf die Modellergebnisse übertragen. In der vorliegenden Arbeit wird die Qualität der Eingangsparameter in Hinblick auf die erforderliche Genauigkeit der Modellergebnisse untersucht. Letztere wird auf der Grundlage einer VDI-Richtlinie, die Anforderungen an numerische Modelle zur Gewährleistung der Qualitätssicherung formuliert, definiert. Darüber hinaus wird eine systematische Sensitivitätsanalyse für die Eingangsparameter durchgeführt, die für PALM-Simulationen der urbanen Umgebung erforderlich sind. Dies ermöglicht die Auswahl der Eingangsparameter, für die eine umfangreiche Datenerfassung lohnend und notwendig ist, um zuverlässige Modellergebnisse mit ausreichender Genauigkeit zu erhalten. Es werden globale Sensitivitätsanalysestudien unter Verwendung der Morris-Methode mit einer OAT-Sensitivitätsstudie für einen städtischen Bereich kombiniert. Die Ergebnisse der Analyse werden hinsichtlich des Einflusses des Gebäudetyps, der Bodenoberflächenparameter und der Baumeigenschaften auf die Modellergebnisse ausgewertet. Zudem erfolgt ein Vergleich der beobachteten Abweichungen mit den geforderten Genauigkeiten der Modellergebnisse und damit eine Aussage bezüglich der Qualität der Eingangsparameter. Die simulierten Abweichungen der Modellergebnisse resultieren aus Veränderungen der Energiebilanz an der Oberfläche und damit der verfügbaren Energie aufgrund der Variationen der Eingangsparameter. Die Untersuchung gibt Empfehlungen, für welche Eingangsparameter, z.B. Bodenparameter und Parameter zur Beschreibung von Kleingewässern, die Verwendung größerer, aber automatisierbarer, flächendeckend verfügbarer Daten ausreicht und für welche Eingangsparameter eine intensivere Datenerfassung erforderlich ist. Für eine zuverlässige Modellierung der Oberflächen-, Innenraum- und Lufttemperatur sollten z.B. die thermischen Eigenschaften eines Gebäudes zur Verfügung stehen. Ein weiterer Parameter, der bei fehlenden Informationen zu Überschreitungen der zulässigen Abweichungen der Modellergebnisse führt, ist die Albedo, die die Strahlungsbilanz über die einfallende kurzwellige Strahlung modifiziert. Baumhöhe und Kronendurchmesser sind weitere Beispiele für Eingangsparameter, die insbesondere durch Modifikation der Verschattungswirkung am Tag zu Überschreitungen der zulässigen Abweichungen der Modellergebnisse führen. Bei der Untersuchung wird festgestellt, dass die gewünschten Genauigkeiten der Modellergebnisse bei der gegebenen Qualität der Eingangsdaten größtenteils erreicht werden können, wobei teilweise intensive Datenerfassung beispielsweise durch Messungen erforderlich ist und eine Erfassung der Modernisierungsmaßnahmen an Gebäuden empfohlen wird, da eine Ungenauigkeit der damit verbundenen Eingangsdaten zu Verletzungen der gewünschten Genauigkeit führen kann. Darüber hinaus werden auf der Grundlage der Ergebnisse der Sensitivitätsanalyse, in der auch Parameter mit großem Einfluss auf die Lufttemperatur und den UTCI diskutiert werden, Schlussfolgerungen zu möglichen Methoden für die An-

passung städtischer Gebiete an den Klimawandel gezogen. Eine Erkenntnis ist, dass eine geeignete Kombination von begrünten Dächern und Fassaden, Grünflächen und Bäumen den größten Kühleffekt in Fußgängerhöhe hat.

Schlagworte: Stadtklima, numerische Simulation, Unsicherheits- und Sensitivitätsanalyse

Abstract

Within the scope of this work, a sensitivity analysis method for input parameters of numerical models is developed and applied to the PALM model system. Inter alia, the PALM model system is capable of simulating the physical processes within urban environments and thus can be used as a tool for urban planning and the development of climate change adaptation measures. Within the framework of the [UC]² project, it has been further developed, evaluated and applied. However, the sensitivity of the model results to the input parameters was not sufficiently addressed yet. For an application of PALM in urban areas, input data concerning land use, surfaces, soil type, buildings and vegetation are required. They can be obtained from various sources like municipal data, Open Street Map, satellite data or aerial imagery. However, quality and availability of input data are very heterogeneous, which results in uncertainties in the input parameters, which are transferred to the model results. In the presented study, the quality of the input parameters is investigated with respect to the required accuracy of the model results. For the latter, required accuracies are defined based on a VDI guideline, that formulates requirements for numerical models to guarantee quality assurance. Furthermore, a systematic sensitivity analysis is carried out for the input parameters required for PALM simulations of the urban environment. This allows for the selection of the input parameters, for which extensive data acquisition is worthwhile and necessary for obtaining reliable model results with a sufficient accuracy. For this, global sensitivity studies using the Morris method are combined with an OAT sensitivity study for an urban domain. The results of the analysis are evaluated concerning the influence of the building type, the land-surface parameters and tree characteristics on the model results. Furthermore, reference is made to the required accuracies of the model results which are compared to the found deviations and associated with the quality of the input parameters. The simulated variations of the model results are due to modifications of the energy balance at the surfaces and thus the available energy due to variations in the input parameters. The investigation gives recommendations for which input parameters, e.g. soil parameters and parameters describing small water bodies, the use of coarser, but more automatable, area-wide available data is sufficient and for which input parameters a more intense data acquisition is required. The thermal properties of a building, for example, should be available for a reliable modeling of surface, indoor and air temperature. Another parameter that leads to exceedings of the permissible deviations of the model results in case of missing information is the albedo which modifies the radiation balance via the incoming short-wave radiation. Tree height and crown diameter are further examples of input parameters that are found to lead to a larger scatter of the model results especially due to the shading effect during day time. In this study it is determined that the desired accuracies of the model results mostly can be achieved with the given quality of the input data, although intensive data acquisition, for example through measurements, is required in some cases, and collection of modernization measures on buildings is recommended, since inaccuracy of the associated input data can lead to violations of the desired accuracy. In addition, conclusions are drawn on possible methods for the adaptation of urban areas to climate change based on the results of the sensitivity analysis discussing quantities with a large impact on the air temperature and the UTCI. One finding is that a proper combination of green roofs and facades, green surfaces and trees has the largest cooling effect in the pedestrian height.

Keywords: urban climate, numerical simulation, uncertainty and sensitivity analysis

Contents

Kurzzusammenfassung	i
Abstract	iii
Contents	v
List of figures	viii
List of tables	xi
List of symbols	xii
List of abbreviations	xiii
I Introduction	1
1 Motivation and goals	1
2 Outline of the work	2
II Existing knowledge and methods	3
3 The PALM model system	3
3.1 Land surface model	4
3.2 Plant canopy model	4
3.3 Urban surface model	5
3.4 Radiation model	6
3.5 Biometeorology module	6
3.6 Nesting	6
3.7 Turbulence-recycling method	7
4 Quality of the input data and required accuracy of the simulation results	7
5 Uncertainty and sensitivity analysis	10
6 The Morris method	11
6.1 The elementary effects	12
6.2 The input parameter space	12
6.2.1 Other distributions than the uniform distribution in $[0, 1]$	12
6.3 The sampling strategy	13
6.4 The sensitivity measures	15
6.5 Dynamic and spatial resolved sensitivity analysis	16
6.6 Identification of relevant parameters	17
6.7 Validation of the implemented Morris method	17
7 Latin hypercube sampling	19
8 Analysis method for computational expensive setups with a large parameter space	20

9	Previous studies and specification of the research questions	21
III	Model setups and simulation results	23
10	Grassland	23
10.1	The PALM model setup for the grassland	23
10.2	PALM model results for the grassland setup	25
11	A paved surface	28
11.1	The PALM model setup for the paved surface	28
11.2	PALM model results for the paved surface setup	28
12	Horizontally homogeneous plant canopy	30
12.1	The PALM model setup for the horizontally homogeneous plant canopy . .	30
12.2	PALM model results for the horizontally homogeneous plant canopy setup	31
13	A domain including a single tree	32
13.1	The PALM model setup for the domain including a single tree	33
13.2	PALM model results for the domain including a single tree	34
14	An urban area	34
14.1	Creation of the PALM model setup	34
14.2	PALM model results for the urban area setup	40
IV	Application of the analysis methods	49
15	Application of the Morris method	49
15.1	Grassland	49
15.2	A paved surface	59
15.2.1	Influence of the albedo on the diurnal cycles of the surface energy fluxes	65
15.3	Horizontally homogeneeous plant canopy	66
15.4	A domain including a single tree	68
15.5	Concluding remarks on the application of the Morris method	72
16	Application of the uncertainty analysis using LHS	73
17	Investigations for an urban area including green and blue elements	74
17.1	Simulation overview and analysis method	75
17.2	Presentation of the analysis results	79
17.2.1	2 m air temperature	79
17.2.2	Surface temperature	82
17.2.3	Wind speed	83
17.2.4	Indoor temperature	86
17.2.5	UTCI	87
17.3	Interpretation of the analysis results	89
17.3.1	Effect of building parameters	89
17.3.2	Effect of land surface parameters	95
17.3.3	Effect of trees	99

17.3.4 Evaluation of the analysis results in terms of ensuring the required accuracy of the model results.	100
V Climate change adaptation recommendations	111
VI Concluding remarks	115
18 Summary	115
19 Outlook	117
VII Appendix	119
20 The Universal Thermal Climate Index (UTCI)	119
21 Figures	120
21.1 Grassland - further results of the Morris method	120
21.2 Paved surface - further results of the Morris method	125
21.3 Urban area - further results of the OAT analysis	131
References	135
Acknowledgements	141
Curriculum Vitae	142
Publications	143

List of Figures

1	Schematic visualization of the soil layers, their thickness (left), and the position of their bottom (middle) and center (right).	4
2	Schematic diagram for the tree parameters.	5
3	A schematic example of a nested configuration with a child domain inside its parent domain. See [33, p. 3188].	7
4	A trajectory in the input parameter quantile space for the Morris method, $k = 2$	14
5	Trajectories in the input parameter quantile space for the Morris method, $k = 3$, $r = 5$	15
6	Validation of the Morris method. a) Result from [57, p. 103], b) Result of the implemented Morris method.	18
7	Visualization of LHS. a) Visualization of the sampling strategy, b) Coverage of the input parameter space for $k = 2$	19
8	Illustration of the analysis method. Left: considered model result, middle: OAT-results, right: Morris method-results. The colors indicate the size of the effect.	21
9	Grid sensitivity study for the grassland setup.	24
10	Grassland: Typical diurnal cycles.	27
11	Paved surface: Typical diurnal cycles.	28
12	Grid sensitivity study for the horizontally homogeneous plant canopy setup.	31
13	Check for stationarity of the model results	31
14	Vertical profiles of the LAD (left) and the u component of the wind (right) for different values of α_{LAD} (top) and LAI (bottom) for the horizontally homogeneous plant canopy.	32
15	Ratio of the u component of the resolved vertical momentum flux to the u component of the total vertical momentum flux for the grid sensitivity study for the single tree setup.	34
16	Horizontal cross-sections of a) LAD and b) BAD at the height of the crown center at 8.75 m.	35
17	Stationary horizontal distribution of the hourly averaged a) u - and b) v -component of the wind at the height of the crown center at 8.75 m.	35
18	Vertical cross-sections of a) LAD and b) BAD at $y=20$ m through the middle of the tree.	35
19	Stationary vertical distribution of the hourly averaged a) u - and b) w -component of the wind at $y=20$ m through the middle of the tree.	36
20	Visualization of the considered urban domain. M_i , $i \in \{1, \dots, 6\}$ mark locations for local vertical profile data extraction. Sub-areas indicated by boxes from top left to bottom right are A1 ‘street canyons’, A2 ‘open place’, A3 ‘court yard’, A4 ‘park’, A5 ‘single houses’.	37
21	Visualization of the total urban domain. For the domain of interest (red) nesting is applied.	38
22	Grid sensitivity study for the urban child domain with neutral stratification.	39
23	Grid sensitivity study for the urban parent domain with neutral stratification.	40
24	Model results for the urban area along a vertical cross section at $y=415$ m.	44
25	Horizontal cross sections for hourly averaged model results for the urban area. The output is terrain following except for g), h).	45

25	Continued: Horizontal cross sections for hourly averaged model results for the urban area. The output is terrain following except for g), h).	46
26	Hourly averaged local vertical profiles extracted at the representative locations M_i , $i \in \{1, \dots, 6\}$	47
27	Diurnal cycles of mean μ , standard deviation σ and extrema within the samples of the considered outputs $y_k(t)$ for the grassland case. The diurnal cycles for the individual samples are indicated by transparent lines.	51
28	Visualization of the Morris sensitivity measures μ , μ^* and σ regarding exemplary diurnal and horizontally averaged quantities for the grassland case.	53
29	Overview of the Morris measures for the grassland case: Colored table for the measures $\mu_{i,j}^*$ and $\sigma_{i,j}$, (p.p.: percentage points).	54
30	Grassland case: Convergence of the sensitivity measures $\mu_{i,2}^*$	54
31	Grassland case: Visualization of the Morris sensitivity measures for the horizontally averaged 2 m air temperature $y_{k=2}(t)$	56
32	Grassland case: Visualization of the Morris sensitivity measures for the horizontally averaged soil moisture $y_{k=7}(t, d)$	57
33	Diurnal cycles of mean μ , standard deviation σ and extrema within the samples of the considered outputs $y_k(t)$ for the paved surface. The diurnal cycles for the individual samples are indicated by transparent lines.	62
34	Overview of the Morris measures for the paved surface case: Colored table for the measures $\mu_{i,j}^*$ and $\sigma_{i,j}$	63
35	Pavement case: Visualization of the Morris sensitivity measures for the horizontally averaged 2 m air temperature $y_{k=2}(t)$	64
36	Diurnal cycle of the a) energy fluxes and b) radiation fluxes at the surface for different pavement albedos.	65
37	Vertical profiles of mean, standard deviation and the extrema within the samples for the horizontally averaged vertical wind profile $y(z)$. The profiles simulated for the individual samples are indicated by transparent lines.	67
38	Horizontally homogeneous plant canopy: Visualization of the Morris sensitivity measures for the horizontally averaged vertical wind profile $y(z)$	68
39	Single tree setup: Standard deviations a) $\sigma_{\text{out},1}(x, y)(z = 10 \text{ m})$, b) $\sigma_{\text{out},3}(x, z)(y = 20 \text{ m})$	70
40	Single tree setup: Colored table for the measures $\mu_{i,j}^*$ and $\sigma_{i,j}$	71
41	Single tree setup: Visualization of the locations for the evaluation.	71
42	Single tree setup: Colored table for the measures $\mu_{i,j}^*$ and $\sigma_{i,j}$ at considered points.	72
43	Paved surface: Dependency of the hourly and horizontally averaged 2 m air temperature at 16 UTC on the albedo and regression.	74
44	Vertical cross sections for LAD distribution in the park at $y = 48 \text{ m}$ for a) S2.2, b) S2.3 and c) S2.4.	77
45	Time series of hourly and spatial averaged 2 m air temperature for the different scenarios and the respective difference to the reference temperature, total domain.	79
46	Local vertical profiles of differences between diurnal averaged scenario and reference air temperature extracted at the representative locations M_i , $i \in \{1, \dots, 6\}$	81
47	Time series of hourly and spatial averaged surface temperature for the different scenarios and the respective difference to the reference surface temperature, total domain.	82

48	Time series of hourly and spatial averaged wind speed for the different scenarios and the respective difference to the reference wind speed. a) 10 m wind, b) 1.5 m wind.	84
49	Local vertical profiles of differences between diurnal averaged scenario and reference wind speed extracted at the representative locations M_i , $i \in \{1, \dots, 6\}$	85
50	Time series of hourly and spatial averaged indoor temperature for the different scenarios and the respective difference to the reference indoor temperature, total domain.	86
51	Time series of hourly and spatial averaged UTCI for the different scenarios and the respective difference to the reference UTCI: a) total domain, b) park.	88
51	Continued: Time series of hourly and spatial averaged UTCI for the different scenarios and the respective difference to the reference UTCI: c) single houses.	89
52	Horizontal distribution of differences between hourly averaged scenario and reference UTCI. a) scenario S3.1, 4 UTC, b) S1.3, 13 UTC, c) S2.3, 13 UTC.	90
53	Bandwidth of local differences between diurnal averaged scenario and reference UTCI at 1.5 m height. a) whole domain, b) park.	91
54	Influence of a facade greening of 29 % at walls on the 2 m air temperature dependent on the distance from the wall for different times and wall orientations: a), b), c): North, d), e), f): East, g), h), i): South, j), k), l): West.	93
55	Influence of a green roof on the diurnal variation of the roof surface temperature.	94
56	Diurnal cycle of the energy fluxes at the surface for different pavement types. a) at the street, b) at the open place	97
57	Scheme: Input parameters with increased influence on the maximal UTCI averaged over the whole urban domain. Left: considered model result $\overline{UTCI}_{max}^{(1h)}$, middle: parameters with increased effect on the model result from the investigations for the urban domain, right: parameters within types with increased effect from preliminary analyses performed with the Morris method.	98
58	Horizontal profiles of UTCI over water surface in the park at $y=134$ m at a) 3 UTC, b) 15 UTC. The location of the water surface is marked blue.	98
59	Grassland case: Visualization of the Morris sensitivity measures for the horizontally averaged 10 m wind speed $y_{k=1}(t)$	120
60	Grassland case: Visualization of the Morris sensitivity measures for the horizontally averaged surface temperature $y_{k=3}(t)$	121
61	Grassland case: Visualization of the Morris sensitivity measures for the horizontally averaged RH $y_{k=4}(t)$	122
62	Grassland case: Visualization of the Morris sensitivity measures for the horizontally averaged UTCI $y_{k=5}(t)$	123
63	Grassland case: Visualization of the Morris sensitivity measures for the horizontally averaged soil temperature $y_{k=6}(t, d)$	124
64	Pavement case: Visualization of the Morris sensitivity measures for the horizontally averaged 10 m wind speed $y_{k=1}(t)$	125
65	Pavement case: Visualization of the Morris sensitivity measures for the horizontally averaged surface temperature $y_{k=3}(t)$	126
66	Pavement case: Visualization of the Morris sensitivity measures for the horizontally averaged RH $y_{k=4}(t)$	127

67	Pavement case: Visualization of the Morris sensitivity measures for the horizontally averaged UTCI $y_{k=5}(t)$	128
68	Pavement case: Visualization of the Morris sensitivity measures for the horizontally averaged soil temperature $y_{k=6}(t, d)$	129
69	Pavement case: Visualization of the Morris sensitivity measures for the horizontally averaged soil moisture $y_{k=7}(t, d)$	130
70	Grid sensitivity study for the urban child domain with stable stratification.	131
71	Further hourly and domain averaged output quantities and differences to the reference run for different averaging domains. a) park, b) open place c) park, d) single houses.	131
71	Continued: Further hourly and domain averaged output quantities and differences to the reference run for different averaging domains. e) street canyons, f) court yard, g) park, 10 m height h) park, 1.5 m height i) single houses j) court yard.	132
72	Bandwidth of local differences between diurnal averaged scenario and reference data in the total domain.	133
73	Local vertical profiles of differences between hourly averaged scenario and reference temperature extracted at the representative locations M_i , $i \in \{1, \dots, 6\}$ at 4 and 17 UTC.	134

List of Tables

1	Data sources for input data required for a PALM-simulation.	8
2	Information on the quality of the data sources regarding urban PALM-simulations.	9
3	Permissible deviations of selected meteorological parameters for urban areas.	10
4	$p_{\geq 0.9}$ and m for the vertical momentum (upper part) and sensible heat (lower part) flux for the grid sensitivity study for the grassland setup.	25
5	Overview of the parameter configuration for the grassland setup.	26
6	Overview of the parameter configuration for the pavement setup.	29
7	Overview of the parameter configuration for the single tree setup.	33
8	Parameter values used in the reference simulation.	41
9	Input parameters and their bandwidths for the grassland setup.	50
10	Input parameters and their bandwidths for the grassland setup including initial atmosphere parameters.	60
11	Input parameters and their bandwidths for the pavement setup.	61
12	Input parameters and their bandwidths for the horizontally homogeneous plant canopy setup.	66
13	Input parameters and their bandwidth for the single tree.	69
14	Single tree setup: List of the model results and the cross-sections considered.	69
15	List of the model results and the points considered.	71
16	Frequency distribution of the tree shapes in the urban area.	76
17	Simulations for the urban area.	78
18	Exceeding of the permissible deviation for the air temperature and corresponding varied input parameters.	101
19	Exceeding of the permissible deviation for the surface temperature and corresponding varied input parameters.	102

19	Continued: Exceeding of the permissible deviation for the surface temperature and corresponding varied input parameters.	103
20	Exceeding of the permissible deviation for the indoor temperature and corresponding varied input parameters.	104
21	Exceeding of the permissible deviation for the wind speed and corresponding varied input parameters.	105
21	Continued: Exceeding of the permissible deviation for the wind speed and corresponding varied input parameters.	106
22	Exceeding of the permissible deviation for the UTCI and corresponding varied input parameters.	107
23	UTCI equivalent temperatures categorised in terms of thermal stress (from [6, p. 489]), [66, p. 30].	119

List of symbols

Symbol	Designation [unit]
BAD	basal area density [m^2m^{-3}]
C_0	heat capacity of the skin layer [$\text{Jm}^{-2}\text{K}^{-1}$]
C_p	heat capacity of the pavement [$\text{Jm}^{-3}\text{K}^{-1}$]
c_{veg}	vegetation coverage []
d_c	crown diameter [m]
d_t	trunk diameter [m]
EE	elementary effect, unit parameter-dependent
h	tree height [m]
h_c	crown height [m]
k	soil depth level numbering []
LAD	leaf area density [m^2m^{-3}]
LAI	leaf area index [m^2m^{-2}]
l_{vG}	coefficient l in the soil hydraulic conductivity parameterization after Van Genuchten []
m_{fc}	volumetric soil moisture at field capacity [m^3m^{-3}]
m_{res}	residual volumetric soil moisture [m^3m^{-3}]
m_{sat}	volumetric soil moisture at saturation (porosity) [m^3m^{-3}]
$m_{\text{soil},k}$	soil moisture at depth level k [m^3m^{-3}]
m_{wilt}	volumetric soil moisture at permanent wilting point [m^3m^{-3}]
n_{vG}	coefficient n in the soil hydraulic conductivity parameterization after Van Genuchten []
P	atmospheric pressure at the surface [hPa]
q	water vapor / total water mixing ratio [kg kg^{-1}]
$r_{\text{c},\text{min}}$	minimum canopy resistance to evaporation [sm^{-1}]
$R_{\text{fr},k}$	root fraction at depth level k []
$r_{\text{soil},\text{min}}$	minimum soil resistance of the uppermost soil layer to evaporation [sm^{-1}]
T	air temperature [K]
T_{deep}	deep soil temperature: bottom boundary condition temperature for the soil model [K]
$T_{\text{soil},k}$	soil temperature at depth level k [K]
T_{surf}	surface temperature [K]
T_{water}	water temperature [K]

Symbol	Designation [unit]
$\mathbf{u} = (u, v, w)$	velocity vector (components) [ms^{-1}]
$\mathbf{u}(t, \mathbf{x}) = \mathbf{u}^*(t, \mathbf{x}) + \mathbf{u}''(t, \mathbf{x})$	unfiltered velocity field [ms^{-1}]
$\mathbf{u}^*(t, \mathbf{x})$	grid resolved velocity field [ms^{-1}]
$\mathbf{u}''(t, \mathbf{x})$	subgrid-scale velocity field [ms^{-1}]
$\mathbf{x} = (x, y, z)$	coordinate vector (components) [m]
x_i	i th input parameter, unit parameter-dependent
y_i	i th model result, unit parameter-dependent
z_0	roughness length for momentum [m]
$z_{0,h}$	roughness length for temperature [m]
α	albedo []
α_{LAD}	shape parameter for vegetation []
α_{vG}	coefficient alpha in the soil hydraulic conductivity parameterization after van Genuchten []
α_{wall}	wall albedo []
α_{window}	window albedo []
β_{LAD}	shape parameter for vegetation []
Δ	difference, unit parameter-dependent
ϵ	surface emissivity []
γ_{sat}	hydraulic conductivity of the soil at saturation [ms^{-1}]
Λ	heat conductivity between atmosphere and soil [$\text{Wm}^{-2}\text{K}^{-1}$]
Λ_{p}	thermal conductivity of the pavement [$\text{Wm}^{-1}\text{K}^{-1}$]
μ_i	Morris measure: estimated mean of the distribution of the elementary effects, unit parameter-dependent
μ^*	Morris measure: estimated mean of the distribution of the absolute elementary effects, unit parameter-dependent
σ_i	Morris measure: standard deviation of the distribution of the elementary effects, unit parameter-dependent
θ	potential temperature [K]
$\langle \bullet \rangle_{x,y,z}$	three dimensional domain average, unit parameter-dependent
$\langle \bullet \rangle_{x,y}$	horizontal average, unit parameter-dependent
$\bar{\bullet}$	temporal average, unit parameter-dependent
$\bar{\bullet}(\bullet)$	temporal average given averaging time in parantheses, unit parameter-dependent
$(\partial \bullet / \partial \bullet)$	partial derivative, unit parameter-dependent
\mathbb{R}	set of real numbers

List of abbreviations

Abbreviation	Meaning
ABL	atmospheric boundary layer
ALKIS	Amtliches Liegenschaftskatasterinformationssystem
ATKIS	Amtliches Topographisch Kartographisches Informationssystem
BAD	basal area density
BMBF	Bundesministerium für Bildung und Forschung
CDF	cumulative distribution function
CLC	CORINE Land Cover

Abbreviation	Meaning
HLRN	Norddeutsche Verbund zur Förderung des Hoch- und Höchstleistungsrechnens
LAD	leaf area density
LAI	leaf area index
LES	large eddy simulation
LHS	latin hypercube sampling
LiDAR	light detection and ranging
LSM	land surface model
NetCDF	Network Common Data Form
OAT	one at a time
OSM	OpenStreetMap
PCM	plant canopy model
PET	physiological equivalent temperature
PT	perceived temperature
RANS	Reynolds-averaged Navier–Stokes
RH	relative humidity
RTM	radiative transfer model
SGS-TKE	subgrid-scale turbulence kinetic energy
[UC] ²	Urban Climate Under Change
UTCI	universal thermal climate index
USM	urban surface model
VDI	Verein Deutscher Ingenieure
1D	one dimensional
3D	three dimensional

Part I

Introduction

1 Motivation and goals

The research programme ‘[UC]² - Urban climate under change’ is funded by the German Federal Ministry of Education and Research (BMBF) within the framework of the Strategy ‘Research for Sustainability’. It includes the development, evaluation and application of an efficient and user-friendly urban climate model for entire cities with a high horizontal resolution based on the large-eddy simulation (LES) code PALM (see [52]; Maronga et al., 2015), with added PALM-4U (PALM for urban applications, read: PALM for you) components [59, p. 97], [43, p. 1336]. The urban climate model PALM-4U developed in the first phase of the research programme is further developed in the second phase for practical application and scientific research. The programme is divided into three modules: Module A is responsible for the further development of PALM-4U, Module B for the evaluation and scientific application of PALM-4U and Module C for the operationalization of PALM-4U [5]. This thesis was written within the module A of the second phase of the research program [UC]².

As the name implies, the aforementioned research programme aims to study urban areas in the context of climate change. The numbers of summer days ($T_{\max} \geq 25 \text{ }^\circ\text{C}$), hot days ($T_{\max} \geq 30 \text{ }^\circ\text{C}$) and tropical nights ($T_{\min} \geq 20 \text{ }^\circ\text{C}$) are predicted to increase in the coming decades due to the anthropogenic climate change. In the urban areas, the consequences of heat episodes are intensified since urbanization influences the local climate through affection of the land use [73, p. 257], [53, p. 22], [68, pp. 4, 6]. Urban surfaces tend to have low albedos and high heat capacities [54, p. 10]. Therefore, they are good at absorbing of short-wave radiation and re-radiating the energy [54, p. 10]. Inter alia, this leads to an increased heat stress in urban areas [68, p. 6]. For urban planning and in order to design actions for climate change mitigation and adaption, reliable information on urban atmospheric processes including quantities influencing health and comfort of the population such as wind speed, temperature and humidity are required with a high spatial resolution [59, p. 95]. These information can be obtained using urban climate models such as the PALM model system. For an application of PALM in urban areas, input data concerning land use, surfaces, soil type, buildings and vegetation are required. Therefore, for the application of PALM, it is usually necessary to specify many detailed input parameters with extremely high spatial resolution. Unfortunately, the study of real urban areas is limited by the effort and costs associated with thorough measurement campaigns [3, p. 2] and data preparation of location data. The values of the input parameters can be obtained from various sources like municipal data, Open Street Map, satellite data or aerial imagery to name a few. However, quality and availability of input data are very heterogeneous, which results in uncertain input parameters [32, p. 5855], which are transferred to the model results.

For an appropriate and successful application of the model, it is necessary to first estimate the size of the influence of the various input parameters on the model output. However, the sensitivity of the model results to the input parameters was not sufficiently addressed so far. Therefore, with the presented study the quality of the input parameters and the required accuracy of the model results are investigated and a systematical sensitivity analysis is carried out for the input parameters required for PALM simulations of the urban environment. The aim of the study is to determine the range of the model results depending on the uncertainty of the input data as well as the necessary accuracy

of the input data to ensure a desired accuracy of the results.

The sensitivity analysis method presented here will be applicable not only to the input parameters of the PALM model system, but also to those of other numerical models. It is especially applicable for models with high computation time and many input parameters. Hence, the new aspect presented in this work is a method for a sensitivity analysis for input parameters of numerical models using the PALM model system as an example. It includes a comprehensive and systematic investigation and the comparison of the influences of various parameter(group)s, which are necessary to describe urban areas, on the model outputs. Through comparison of the effects of the input parameters with desired accuracies of the model results, the analysis provides recommendations for the necessary accuracy in the data acquisition. This allows optimal use of the effort and cost associated with thorough data collection while providing more reliable model results. These analysis results are to be made available to the users of the model. Furthermore, the findings about the effects of the input parameters can be used to make recommendations regarding the adaptation of urban areas to climate change.

2 Outline of the work

Part II describes the existing knowledge. The PALM model system which is used in this work is introduced in Chapter 3, Chapter 4 discusses the quality of the available input data and gives the required accuracy of the model results. Chapter 5 gives general information on uncertainty and sensitivity analysis and Chapters 6 to 8 provide an overview of applied analysis methods. Chapter 9 references to previously performed studies and specifies the aspects to be examined within the framework of the analysis. Part III with Chapters 10 to 14 presents the model setups and shows exemplary results of the model application like typical diurnal cycles. In part IV, the application of the sensitivity analysis methods follows for the previously described model setups: In Chapter 15, the Morris method is applied to the simple setups in order to identify the input parameters within parameter types that are most relevant for the considered model results, in Chapter 16, an exemplary uncertainty analysis based on the use of Latin hypercube sampling as sampling strategy is performed and in Chapter 17, a sensitivity analysis is performed for the more complex urban area, where the previous results are included. In part V, conclusions are drawn on possible methods for the adaptation of urban areas to climate change based on the results of the sensitivity analysis. Part VI summarizes the results of this thesis and gives an outlook.

Part II

Existing knowledge and methods

The following part contains a short description of the PALM model system used in this work as well as information on uncertainty and sensitivity analysis and the applied methods.

3 The PALM model system

The PALM model system, version 6.0, mainly developed by the PALM group at the Institute of Meteorology and Climatology of the Leibniz University Hannover, is used in this work. For a detailed description see [52], [41] and [43].

PALM is a parallelized turbulence-resolving LES model for the atmospheric and oceanic boundary layer. In LES, a separation of scales is used to study complex turbulent processes. The large turbulence elements (eddies) are resolved and only the small-scale turbulence is parameterized within a subgrid-scale model. In contrast, using a turbulence closure based on the Reynolds-averaged Navier–Stokes (RANS) equations, the entire turbulence spectrum is parameterized [43, pp. 1336-1337].

PALM is based on the non-hydrostatic, filtered, incompressible Navier-Stokes equations in Boussinesq-approximated form or alternatively in an anelastic approximation. PALM solves the prognostic equations for the velocity components u , v and w , the potential temperature θ , the water vapor mixing ratio q and optionally a passive scalar s . An equation for the subgrid-scale turbulence kinetic energy (SGS-TKE) (LES mode) or the total turbulence kinetic energy (RANS mode) is also solved [43, p. 1337].

The prognostic equations are solved on a staggered Arakawa-C grid with equidistant horizontal grid spacings. For the parameterization of the subgrid-scale terms, a 1.5-order turbulence closure after Deardorff [13] is used. The spatial discretization is done via finite differences using a fifth-order advection scheme after Wicker-Skamarock [71] and via a third-order Runge-Kutta time stepping scheme [72] the discretization in time is achieved [42, p. 107]. The incompressibility of the flow field is ensured by a predictor corrector method and a pressure solver. In the predictor step, a preliminary velocity is calculated, in the corrector step, a Poisson equation is solved for the modified perturbation pressure whose solution yields a velocity field free of divergence after every time step [41, pp. 2519-2520]. The model is optimized for use on massively parallel computer architectures using the Message Passing Interface and Open Multiprocessing [41, p. 2535].

In order to solve the energy balance equation, a surface classification concerning physical properties such as heat capacity, roughness, albedo and emissivity is required. In PALM, the classification is made via predefined parameter lists for the building, soil and each land surface type, which are vegetation, pavement and water surfaces [32]. Additionally, the user can modify individual parameter values.

Several modules are embedded in PALM. The ones used in this work will be described in the following sub-chapters. The PALM-6.0 model system thus is capable of simulating the physical processes within urban environments and is applicable to various problems with regard to urban planning, air quality, biometeorology and the adaptation to regional consequences of climate change and starts being used for urban planning issues. Furthermore, it is used worldwide by scientists to study atmospheric processes in urban areas [59, p. 97], [53, p. 22]. PALM has already been successfully applied to real urban areas (see e.g. [3], [4] and [26]).

3.1 Land surface model

For the simulation of natural, water and paved surfaces the ‘land surface model’ (LSM) is used [24]. The module contains a solver of the energy balance of the earth’s surface as well as a multi-layer soil model to take into account vertical heat and water transport in the soil [43, pp. 1346-1348]. The surface classification is made via the predefined parameter lists for each land surface type or user modifications of individual parameter values [32]. To take into account the interactions of the surface with the underlying soil, a soil type must be given to PALM for grid cells that are classified as vegetation or pavement surfaces. The classification can again be made via predefined soil types with the corresponding parameter list or modifications of individual parameter values. The soil types are based on the granularity of the soil and properties concerning soil moisture. By default, the soil layers have thicknesses from their respective top to their bottom of 0.01 m, 0.02 m, 0.04 m, 0.06 m, 0.14 m, 0.26 m, 0.54 m and 1.86 m [32, pp. 5837-5839]. The soil layers and their positions are schematically visualized in Figure 1. Prognostic equations for the soil temperature and the volumetric soil moisture are solved in the soil layers. The vertical heat and water transport is modeled using the Fourier law of diffusion and Richards’ equation, respectively. The hydraulic conductivity is calculated after van Genuchten [64]. These aspects are further described in [24, p. 5311]. Furthermore, for vegetated or water surfaces, a skin layer covering the surface that does not have a significant heat capacity is used, while for bare soil and pavements, no skin layer is applied, see [24, p. 5308].

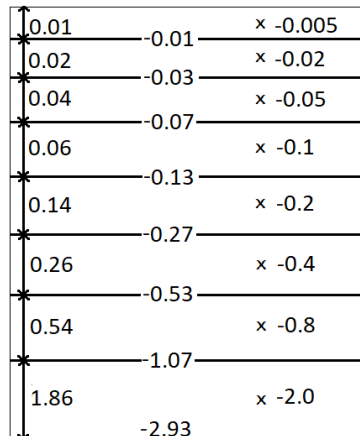


Figure 1: Schematic visualization of the soil layers, their thickness (left), and the position of their bottom (middle) and center (right).

3.2 Plant canopy model

The effect of plants as obstacles can be studied using a ‘plant canopy model’ (PCM) [43, p. 1336]. High vegetation such as trees can be partly resolved depending on the grid size. The resolved vegetation leads to a sink term in the momentum equation and is responsible for shadowing and reflections [32, pp. 5838-5839]. A three dimensional (3D) canopy model is used, which is based on a drag force approach and the leaf area density distribution [42, pp. 111-112]. The high bushes or trees are defined by means of leaf and basal area density (LAD, BAD) fields [32, p. 5851]. For their calculation, the parameters species, tree height h , crown diameter d_c , crown shape, trunk diameter d_t , ratio of crown height h_c and crown diameter d_c are required [32, p. 5845]. A schematic diagram for a spherical shaped tree is given in Figure 2 in order to visualize the tree parameters. To

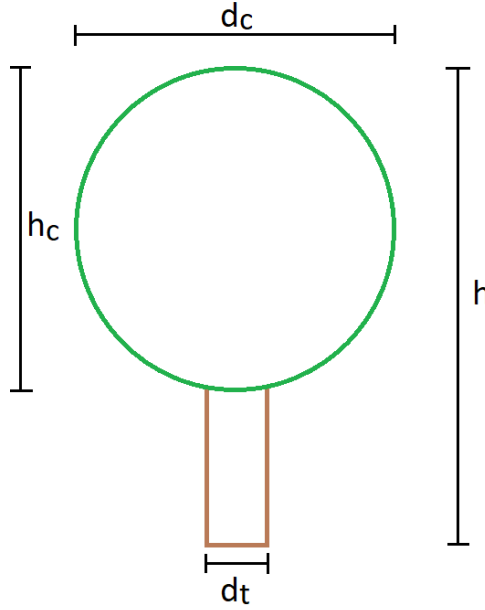


Figure 2: Schematic diagram for the tree parameters.

estimate the LAD of individual trees, the area covered by the crown is determined and it is assumed that the density of the leaf area increases exponentially from the center of the crown towards the outside, while the BAD is increasing towards the center of the crown. Furthermore, the BAD field is determined by means of the trunk diameter, which is assumed to be constant up to the crown center [32, pp. 5851-5852]. If information about individual trees is missing, or if, for example, a forest is to be described, patch data can be used, i.e. an idealized vertical LAD distribution is determined after Markkanen [40] from a leaf area index (LAI) and two parameters α_{LAD} and β_{LAD} and a vegetation height for every location on the horizontal plane. Increasing values for α_{LAD} shift the leaf areas towards the upper limit of the vegetation, increasing values for β_{LAD} shift them downwards [49], [32, p. 5852].

3.3 Urban surface model

The ‘urban surface model’ (USM) corresponds to the LSM for building surfaces. To solve the energy balance for building surfaces, information about the building type with regard to various parameters such as wall thickness, heat capacities and conductivities, window fraction and albedo is required. For building classification, characteristic building types with default values for the building parameters are prescribed [32, p. 5838]. These values are used when no other values are given by the user. The building type is defined by a combination of building use and age [32, p. 5843]. PALM distinguishes between buildings built before 1950, between 1951 and 2000 and after 2000, and between residential and office buildings [31, p. 26]. Each surface element can contain one part of wall or roof, greening, and window area. The energy balance solver calculates the surface temperature of all three parts and a weighted effective surface temperature. For the green fraction on the buildings, the heat conduction through a substrate layer is additionally simulated taking into account the soil water content. The evapotranspiration of the green roof is also included [31, p. 19]. Furthermore, PALM offers an indoor model [51]. The indoor model can be added to model the interaction between the surrounding urban climate and indoor climate. It calculates the indoor temperature and determines the electricity demand, the

heating or cooling demand and the anthropogenic heat emission to the environment [31, pp. 24, 25].

3.4 Radiation model

For the calculation of the radiation budget of the Earth’s surface, a simple fast radiation model for clear sky conditions neglecting the presence of humidity, clouds, and variations in aerosol and trace gas properties in the atmosphere is offered by PALM, see [43, pp. 1348, 1349]. Radiative processes and energy exchanges within the urban or natural canopy layer with geometrically complex structures like shading and reflections are taken into account by the ‘radiative transfer model’ (RTM). Based on the radiation on top of the canopy layer calculated by the radiation model, shortwave and longwave radiative processes inside the canopy layer are modeled. The resulting radiative fluxes are provided to the LSM, USM and the biometeorology module, see [43, pp. 1354-1356].

3.5 Biometeorology module

The biometeorology module consists of a thermal comfort part for the calculation of the thermal indices ‘perceived temperature’ (PT), ‘universal thermal climate index’ (UTCI), see Chapter 20 for a description, and ‘physiologically equivalent temperature’ (PET) approximating human thermal perception, and a UV-exposure part for calculations of biologically weighted human exposure in an urban environment. The indices UTCI, PET and PT are provided for the horizontal level, which is the closest possible to 1.1 m above ground level [43, p. 1362].

3.6 Nesting

For LES of the urban Atmospheric Boundary Layer (ABL) a high grid resolution in the order of typically 1 m is required, in order to satisfactorily resolve most of the complex turbulent structures. At the same time, the vertical extent of the model domain has to be large enough to capture the ABL and the horizontal extent should be several ABL heights in order to capture the dominant turbulent eddies in the ABL. Thus, a large computational domain and a high grid resolution near the considered surface are required. To reduce the need for computational resources, PALM offers a self-nesting scheme allowing for large domain sizes and high spatial resolutions in the domain of interest. Here, two or more domains of different extent and grid spacing are used simultaneously and nested into another. The outermost (root) domain contains one or more inner (child) domains with increasing resolutions. The domains can also be nested recursively into another. Nest domains are surface-bound. A child domain receives boundary conditions for the prognostic quantities from its parent domain via interpolation from the coarser to the finer grid. In case of one-way coupling, the coarse domain is not influenced by the solution of the fine domain, while in the two-way coupling the coarser domain is influenced by its child domains via so-called anterpolation, where the child solution is transferred back to the parent domain and replaces the parent solution within the volume occupied by both domains [43, pp. 1358-1359], [33, p. 3185-3187].

Figure 3 shows a schematic example of a model domain including one nested child domain. The coordinate vector and its components are denoted as $\mathbf{x} = (x, y, z)$.

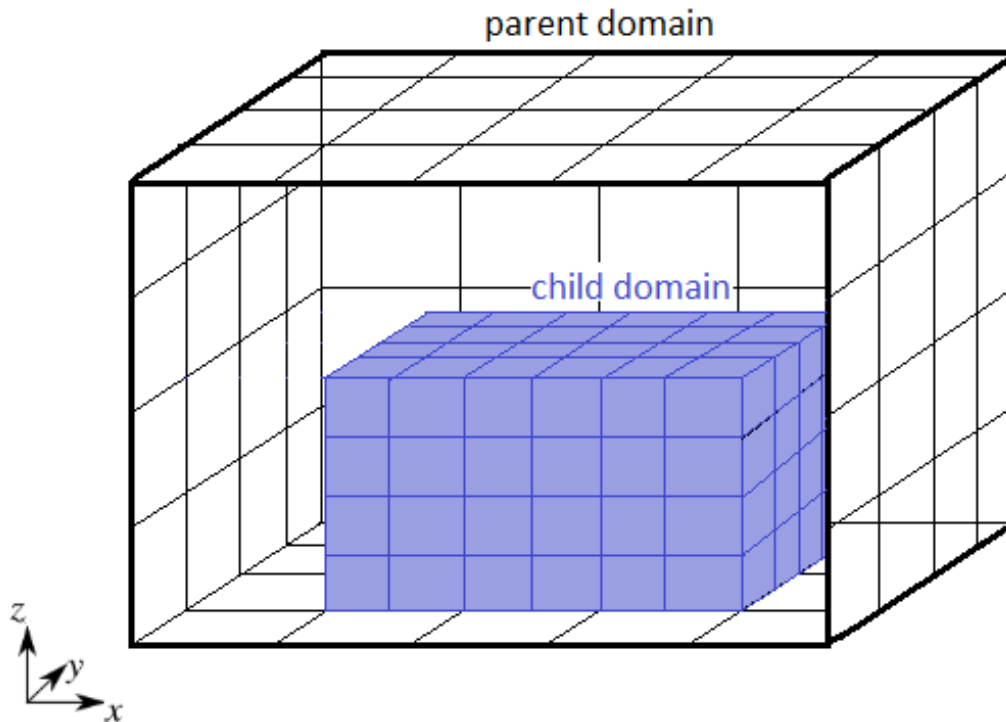


Figure 3: A schematic example of a nested configuration with a child domain inside its parent domain. See [33, p. 3188].

3.7 Turbulence-recycling method

Besides the default option, that cyclic boundary conditions apply at all lateral domain boundaries, PALM offers the turbulence-recycling method, which is used to achieve a fully developed time-dependent turbulence at the inflow boundary. The turbulence-recycling method sets a fixed mean inflow condition at one side of the simulation domain and adds a turbulent signal from a recycling plane within the model domain. An additional recycling area within the model domain is therefore required [43, p. 1343]. A precursor run is used for generating the initial turbulence field. Therefore a domain can be used, that is smaller along the horizontal directions than the main domain. In that case the latter is filled by cyclic repetition of the precursor run data. Topography elements should be placed sufficiently downstream of the recycling plane to prevent effects on the turbulence [41, pp. 2521, 2522].

4 Quality of the input data and required accuracy of the simulation results

For an application of PALM in urban areas, adequate input data concerning land use, road surfaces, soil type, buildings and 3D vegetation need to be available [31, p. 39]. This chapter first discusses the quality of the input data. Their collection is described, as well as their typical quality. For this purpose, it is especially referred to [32], where the input data requirements, data sources and data processing of the geospatial input data for PALM 6.0 are described in detail.

Input data can be obtained from various data sources like municipal data, aerial imagery, satellite data, Corine Land Cover (CLC) and Open Street Map (OSM) [31,

pp. 35, 36]. For small areas of interest, field surveys and manual mapping are also practicable [32, pp. 5839, 5840]. However, the quality and availability of input data are very heterogeneous. A Germany-wide uniform and high-resolution database does not exist at the time the thesis is written [31, p. 5]. Uncertainties in the input data are due to the varying quality of different data sources, insufficient spatial resolution, incorrect assignments [32, p. 5855] and hence due to a lack of information. The use of default or literature values that may not be exactly transferable to the considered situation [29, p. 225] and measurement uncertainties appearing during data collection [34, p. 283] result in input data uncertainties. Table 1 gives the required input data and the corresponding data sources and Table 2 provides information on the quality of the data sources.

Table 1: Data sources for input data required for a PALM-simulation.

Input data	Data sources
terrain height	airborne LiDAR data, satellite-based data [32, p. 5842]
vegetation type	municipal data, ATKIS/ALKIS, OSM, CLC, aerial color and infrared images [32, pp. 5843, 5860].
pavement type	ATKIS/ALKIS, airborne hyperspectral imaging data, OSM [32, pp. 5840-5861].
water	Temperature data are restricted to samples for monitoring the water quality or swimming suitability [30, p. 5]. To map water bodies: OSM, CLC, governmental/ATKIS/ALKIS data, satellite data, aerial images. There are no sufficient and complete data available with a sufficiently high spatial resolution for differentiating between small bodies of water like fountains [32, pp. 5840, 5848, 5868].
soil type	European Soil Database [17], soil map of Germany [8], Soil data are difficult to acquire at high resolutions. Assumptions about horizontal and vertical homogeneity were made in [32, p. 5848]
3D vegetation	Municipal tree register with information about trees on public land: tree species, age, height, and sometimes also crown and stem diameters, information about trees and green spaces on private property has to be derived from additional data sources [32, p. 5840]. Remote sensing data from satellite or airborne imagery: information on the location of the vegetation [32, p. 5843], LiDAR data: tree height and crown diameter [32, p. 5845], field measurements on the ground to sample single trees [32, p. 5847], OSM [32, p. 5843]
building geometry	municipal 3D building data in LOD1 (block model) or LOD2 (more detailed with roof structures) [32, pp. 5840, 5842]
building type	ATKIS/ALKIS data are used to estimate the building age and use [32, p. 5840]. Building properties are difficult to aggregate and often unknown; no cadastral information on restoration, facade changes and heat insulation actions for individual buildings is available in Germany. Overflight data [31, p. 26]/field or drone surveys can be used for small areas [32, pp. 5838, 5843]. Municipal ortho near-infrared (CIR) images: Intensive and extensive green roofs [32, pp. 5844, 5845].

The simulations have to be performed with this limited quality of the input data including mismatches of the surface types and a limited ability of representing trees, which can lead to uncertain model results. Therefore, it is specified with which accuracy the simulation results like air temperature, UTCI or wind speed of a numerical model like the PALM model system should be available in an urban environment, in order to be able to

Table 2: Information on the quality of the data sources regarding urban PALM-simulations.

Data source	Quality
ALKIS/ ATKIS/ municipal data	regularly updated every 1–3 years, not systematically available for vegetation and pavement type [32, pp. 5840-5861], building information from regional studies or municipal planning is often incomplete or inconsistent [31, p. 26], ALKIS provides building data at building block level, thus, they often contain mixed uses [32, p. 5843], municipal 3D building model: LOD2 building data exist for all German states since 2019, accessibility and costs vary [32, pp. 5840, 5842]
OSM	volunteered geographical information [32, p. 5840], basically always available and publicly accessible [31, p. 5], incomplete regarding water bodies [32, p. 5848], no homogeneous data quality, completeness and adherence to a single standard can be guaranteed [32, p. 5840]
CLC	based on satellite data (Sentinel-2 for CLC2018), Minimum Mapping Unit of 25 ha, available for Europe, free access for all users [12]
tree register	tree species, age, height, and sometimes also crown and stem diameters; exclude information about trees and green spaces on private property [32, p. 5840], continuously revised [23]
airborne LiDAR data	1 m spatial resolution, not everywhere available or not all cities in Germany provide access to LiDAR data sets, data sources can cover the variation of the LAI over the phenological cycle [32, pp. 5842-5847]
satellite-based data	area-wide data [32, p. 5843], global coverage, high temporal resolution [37]: depends on orbit, sensor’s characteristics, and swath width, and lies in a range from 1 day to 16 days [47], spatial resolution of Sentinel-2 is 10 m, to reach resolution of 1 m for LAI, a bilinear re-sampling method can be applied [32, p. 5847], provide information on the location of the vegetation and estimates for some vegetation characteristics but not all required by PALM [32, p. 5843]
Aerial im- agery	spatial resolution: up to 1 cm - 5 cm per pixel, smaller field of view compared to satellite images [37], updated in a 2–5-year period to monitor the green volume development, provide information on the location of the vegetation and estimates for some vegetation characteristics but not all required by PALM, the acquisition dates and thus the leave cover differ, usually smaller water bodies like fountains or rivulets are not distinguishable, municipal ortho near-infrared (CIR) images are not always available, even in cities [32, pp. 5840-5848].
Airborne hy- perspectral imaging	spatially and spectrally detailed data that allows for a differentiated classification of urban surface materials, however due to its experimental nature, these data are rarely available for whole cities [32, p. 5847]
European Soil Database	raster data with grid sizes of 1 km x 1 km and 10 km x 10 km [17]
soil map of Germany	available in ratio 1:1.000.000 or 1:200.000, uniform assessment of the soils throughout Germany, 71 soil mapping units [8]

conclude with the help of this work whether this necessary accuracy can be achieved with the quality of the available input data and what the required accuracy of the input data is. Guidelines that apply to numerical models in the field of urban climate provide this kind of information. They can also be applied to PALM and provide information on the

required accuracy of the PALM simulation results. Therefore, with respect to the required accuracy of the simulation results, reference is made to information from VDI guidelines. The VDI guideline [67] formulates requirements for numerical models to guarantee quality assurance. This also includes the specification of permissible absolute and relative deviations between model results and reference values for near-ground temperature and wind. Information regarding the required accuracy of indoor temperature, surface temperature and UTCI were not available in the VDI guidelines. For the indoor temperature and the surface temperature, the same required accuracy as for the air temperature is assumed, since they are measured on the same scale. To define the required accuracy of the UTCI, a different approach is used. Based on the values of the UTCI, a division into stress categories is made. The smallest category covers a 6 K interval, see Chapter 20. In [70], the uncertainties of UTCI due to uncertainties in radiation fluxes are studied. It is referred to the 6 K intervals, since uncertainties being smaller lead to possible errors of the UTCI of only one UTCI scale [70, p. 537]. Since this might be critical, when the thermal comfort is to be evaluated, the maximal allowed uncertainty of the UTCI is assumed to be half of the smallest scale, i.e. 3 K. The permissible deviations or required accuracies are listed in Table 3. The values furthermore coincide with the assumption that differences in the modeled temperature of 0.5 K due to turbulence are reasonable and changes below that value can hence be due to noise.

Table 3: Permissible deviations of selected meteorological parameters for urban areas.

meteorological parameter	permissible deviations		source
	absolute	relative	
u, v, w	0.35 ms ⁻¹	10 %	[67, p. 18]
wind speed	0.5 ms ⁻¹	10 %	[67, p. 18]
air temperature	0.5 K	0.2 %	[67, p. 18]
indoor temperature	0.5 K	0.2 %	assumption
surface temperature	0.5 K	0.2 %	assumption
UTCI	3 K	1.2 %	assumption, [70, p. 537]

5 Uncertainty and sensitivity analysis

A computational model represents a system of interest and maps input data to model results [46, p. 161].

As part of an **uncertainty analysis**, the uncertainty - i.e. bandwidth - of the model result is determined when the input parameters vary within a specified range. The outcome of this study is dependent on this range of the input parameters. Therefore, a representative choice of this range and a suitable probability distribution of the input parameters are crucial for reliable results that are valid for the given accuracy of the input parameters [39, p. 10].

A **sensitivity analysis** can be used to identify the input parameters most responsible for the bandwidth of the output [34, p. 283], i.e. it examines how the uncertainty in the model result can be apportioned to the various uncertain input parameters [58, p. 259]. Sensitivity analysis methods range from local One Factor at A Time (OAT) methods, described e.g. in [34], to global quantitative variance-based methods, see e.g. [58] [11, p. 1509].

In a **local sensitivity analysis**, the change in the considered model output is determined in the event of small changes in the input parameters around a certain point in

the input parameter space. A local sensitivity measure corresponds to the derivative of the output y with respect to the input parameter x_i : $(\partial y / \partial x_i)$ [57, p. 60], [39, p. 40]. Fixed variations of the parameter values are considered instead of the actual uncertainty. Since the parameters are only varied within a small range around the base point, only a fragment of the input parameter space is taken into account [34, p. 284]. That is why the local sensitivity measures are dependent on the base point, at which the derivatives are determined. Furthermore, usually one parameter is varied after the other (OAT sampling), which is why interactions between the input parameters cannot be recognized using the local method [39, p. 40], [34, pp. 283, 384]. Here, the interaction of two input parameters is defined by the fact that the common effect on the model result is not equal to the sum of the individual effects [57, p. 111].

In a **global sensitivity analysis**, the effect of input parameters on output quantities is examined in the entire possible input parameter space [39, p. 42]. A global sensitivity analysis captures the effect of one input parameter while the others are also varied. In addition, they are able to recognize interaction effects, which is important for non-linear and non-additive models [57, p. 49].

In [57, p. 54] the Factors Fixing Setting or Screening is introduced. Input parameters without or with only small effects on the considered model result are to be identified and fixed without any significant loss of information. They can be fixed at any given value within their bandwidth without significantly reducing the output variance, while the remaining input parameters are responsible for most of the output variance. For this setting, the Morris method or variance-based techniques can be used.

Due to the effectiveness and the efficiency of the Morris method [11, pp. 1509, 1510], it will be used in this study and described in more detail in Chapter 6.

6 The Morris method

In 1991, Max D. Morris introduced a method to determine which of the many input parameters have an important effect on the model results [46].

Often, models have a lot of input parameters and model runs can be time-consuming and expensive. The aim of this method was to identify the important input parameters that have a significant influence on the considered model outputs preliminary to performing further computational experiments. The term ‘Factor screening’ is used for this [46, p. 161]. Thus, the Morris method or elementary effect method is called a screening method. Screening methods belong to global sensitivity analysis methods and can be used to identify the important input parameters of a model with a comparatively small number of model runs when the number of input parameters is large and / or the model requires a large amount of computation time [20, p. 374], [46, p. 161].

The Morris method provides qualitative sensitivity measures which can be used to rank the input parameters according to their importance [57, p. 108]. The sensitivity measures provide information about which factors have effects that are negligible, that are linear and additive, or that are non-linear or involved in interactions with other input parameters [46, p. 163], [57, p. 94], [62, p. 331].

Due to the comparatively small number of model runs required, the Morris method is a good compromise between accuracy and efficiency, especially for sensitivity analyzes of large models [11, p. 1509].

6.1 The elementary effects

The Morris method is based on the OAT method, in which elementary effects EE_i are calculated for each input parameter. These describe the ratio of the change in the output to the change in the input Δ_i for the i th input parameter x_i . An elementary effect is a local sensitivity measure for the effect of input x_i in a given area on the output. To obtain a global measure, a set of r elementary effects is sampled from the distribution of the elementary effects F_i for each input parameter. A statistical evaluation is carried out for the elementary effects after their determination: The mean μ and the standard deviation σ of the distribution of the elementary effects F_i and the mean μ^* of the distribution of the absolute values of the elementary effects G_i are estimated as sensitivity measures [20, p. 374], [11, pp. 1509-1511], [62, p. 332] as described in Chapter 6.4.

Assuming that each input parameter takes on values in the interval $[0, 1]$, the elementary effect for the i th input parameter given $\mathbf{x} \in \mathbf{X}$ and the model $y(\mathbf{x})$ is

$$EE_i(\mathbf{x}) = \frac{y(x_1, \dots, x_{i-1}, x_i + \Delta_i, x_{i+1}, \dots, x_k) - y(\mathbf{x})}{\Delta_i} = \frac{y(\mathbf{x} + \mathbf{e}_i \Delta_i) - y(\mathbf{x})}{\Delta_i}, \quad (1)$$

\mathbf{x} is an input parameter sample from \mathbf{X} , $y(\mathbf{x})$ is the corresponding model output, \mathbf{e}_i is the vector, which contains zeros except for one 1 on the i th component, Δ_i is the step size of x_i along the X_i -axis, $\mathbf{x} + \mathbf{e}_i \Delta_i$ is the new sample in the domain of definition, resulting from shifting the i th input from x_i to $x_i + \Delta_i$, $y(\mathbf{x} + \mathbf{e}_i \Delta_i)$ is the corresponding model output [20, p. 375], [46, p. 163].

6.2 The input parameter space

It is initially assumed that each input parameter x_i scales in such a way that it takes on values in the interval $[0, 1]$. The considered region Ω of the input parameter space is thus a k -dimensional unit hypercube [46, p. 163]. The model input can be understood as a k -dimensional vector \mathbf{x} with the components $x_i \in \{0, 1/(p-1), 2/(p-1), \dots, 1\}$. Each dimension of the k -dimensional input parameter space is evenly partitioned into p levels, such that a grid with p^k points $\mathbf{x} \in \mathbb{R}^k$ arises, at which the model can be evaluated. The considered region of the input parameter space Ω is thus a k -dimensional p -level grid. In practical applications, the values that are sampled in Ω are then rescaled in order to generate the values that the input parameters actually take, which will be discussed in section 6.2.1 [57, p. 94], [1, p. 63]. The value of p should be an even number and the step size Δ should satisfy $\Delta = p/(2(p-1))$ [46, p. 163], [57, p. 97].

6.2.1 Other distributions than the uniform distribution in $[0, 1]$

So far, it was assumed that the input parameters satisfy the uniform distribution in the interval $[0, 1]$. This chapter answers the questions how samples are to be created if the input parameters satisfy other distributions than the standard uniform distribution, and how the step size is defined. Sampling is done using the inversion method. In this case, the values of the input parameters are not sampled directly, but samples are generated using the cumulative distribution function (CDF). The CDF of each random variable follows a uniform distribution in the interval $[0, 1]$. At first some random samples q_i can be generated in this interval, which are interpreted as the value of the CDF $F(x)$. Then, the actual input samples x_i can be calculated via the inverse of the CDF $F^{-1}(q)$, i.e. $x_i = F^{-1}(q_i)$ [20, p. 376].

If the actual input values have been calculated using the inversion of the CDF, the value and meaning of Δ_i must also be discussed. There are the options that Δ_i corresponds

to the actual step size Δx_i of the input parameter x_i or to the step size Δq_i of the CDF value.

For this, in [20, p. 376] the following example of the linear input-output relationship $y = g(x) = x_1 + x_2$ is considered, where x_1 and x_2 are uniformly distributed in $[0, 1]$ and $[0, 10]$. It is expected that x_2 will have a greater impact on the output y . Because of the linearity, one group of elementary effects can be considered as the sensitivity measures. Suppose that as CDF values, the points $(0, 1/3)$, $(0, 2/3)$ and $(1/3, 2/3)$ are randomly sampled in $[0, 1]$. Applying the inverse CDF yields the actual samples of the input parameters $(0, 10/3)$, $(0, 20/3)$ and $(1/3, 20/3)$. This results in the following elementary effects:

$$EE_1 = \frac{g(1/3, 20/3) - g(0, 20/3)}{\Delta_1} = \frac{1/3}{\Delta_1}, \quad EE_2 = \frac{g(0, 20/3) - g(0, 10/3)}{\Delta_2} = \frac{10/3}{\Delta_2}.$$

For $\Delta_i = \Delta x_i$, i.e. $\Delta_1 = 1/3$, $\Delta_2 = 10/3$, $EE_1 = 1 = EE_2$ implies that x_1 and x_2 are equally important for the result y . $\Delta_i = \Delta q_i$, i.e. $\Delta_1 = \Delta_2 = 1/3$, yields $EE_1 = 1$, $EE_2 = 10$, which means that x_2 has a greater impact on y than x_1 . The latter corresponds to the expectations given the definition range of the input parameters and the solution of the variance-based analysis. Thus, regardless of the distribution of the input parameters, the step size Δ_i should correspond to the CDF step size in $[0, 1]$. The elementary effects can thus be formulated as follows:

$$EE_i = \frac{y(\mathbf{x} + \mathbf{e}_i \Delta_i) - y(\mathbf{x})}{\Delta_i} = \frac{y(\mathbf{x} + \mathbf{e}_i \Delta x_i) - y(\mathbf{x})}{\Delta q_i} = \frac{\Delta y}{\Delta q_i} = \frac{\Delta y}{\Delta x_i} \frac{\Delta x_i}{\Delta q_i}, \quad (2)$$

with $\Delta q_i = F_{X_i}(\mathbf{x} + \mathbf{e}_i \Delta x_i) - F_{X_i}(\mathbf{x})$ and $F_{X_i}(x_i)$ is the CDF of X_i , $i = 1, 2, \dots, k$. In this way, weighting with the respective definition range of the input parameters is possible.

As an example, the CDF of a random variable X that is uniformly distributed in the interval $[x_{\min}, x_{\max}]$ used in this thesis is given [62, p. 71]:

$$F(x) = \begin{cases} 0 & \text{for } x < x_{\min} \\ \frac{x - x_{\min}}{x_{\max} - x_{\min}} & \text{for } x_{\min} \leq x < x_{\max} \\ 1 & \text{for } x \geq x_{\max} \end{cases} \quad (3)$$

The inverse of the CDF is:

$$F^{-1}(q) = x_{\min} + q \cdot (x_{\max} - x_{\min}). \quad (4)$$

This leads to $\Delta x_i = \Delta q_i \cdot (x_{\max} - x_{\min})$ and thus the elementary effect used in this thesis reads:

$$EE_i = \frac{\Delta y}{\Delta q_i} = \frac{\Delta y}{\Delta x_i} \frac{\Delta x_i}{\Delta q_i} = \frac{\Delta y}{\Delta x_i} \frac{\Delta q_i \cdot (x_{\max} - x_{\min})}{\Delta q_i} = \frac{y(\mathbf{x} + \mathbf{e}_i \Delta x_i) - y(\mathbf{x})}{\Delta x_i} \cdot (x_{\max} - x_{\min}) \quad (5)$$

The value of an elementary effect for the i th input parameter corresponds to the variation of the output when the input is varied from the minimum to the maximum of its parameter range [22, p. 13].

6.3 The sampling strategy

First a base value $\mathbf{q}^* \in \Omega$ is randomly selected, whereby each component q_i^* of \mathbf{q}^* is sampled from the set $\{0, 1/(p-1), 2/(p-1), \dots, 1\}$. \mathbf{q}^* is used to generate other samples

and is not used to evaluate the model at \mathbf{q}^* . The first sample $\mathbf{q}^{(1)}$ is obtained by increasing one or more components of \mathbf{q}^* by Δ , with the condition that $\mathbf{q}^{(1)} \in \Omega$. The second sample is also generated from \mathbf{q}^* , such that it differs from $\mathbf{q}^{(1)}$ in the i th component by $+$ or $- \Delta$: $\mathbf{q}^{(2)} = (q_1^{(1)}, \dots, q_{i-1}^{(1)}, q_i^{(1)} \pm \Delta, q_{i+1}^{(1)}, \dots, q_k^{(1)}) = (\mathbf{q}^{(1)} \pm \mathbf{e}_i \Delta)$. The index i is randomly selected from the set $\{1, 2, \dots, k\}$. Also $\mathbf{q}^{(3)}$ is generated from the basis value \mathbf{q}^* , by increasing one or more of the k components of \mathbf{q}^* by Δ , such that $\mathbf{q}^{(3)}$ differs from $\mathbf{q}^{(2)}$ in only one component j , with $j \neq i$. In this way, a sequence of $(k + 1)$ samples $\mathbf{q}^{(1)}, \mathbf{q}^{(2)}, \dots, \mathbf{q}^{(k+1)}$ is generated, where two consecutive samples differ only in one component. Every component of the basis vector \mathbf{x}^* was varied at least one time by Δ . The sequence of the samples is called a trajectory in the input parameter space, which can be represented via a matrix \mathbf{B}^* of the dimension $(k + 1) \times k$, whose rows correspond to the vectors $\mathbf{q}^{(1)}, \dots, \mathbf{q}^{(k+1)}$ [57, pp. 97,98]. An exemplary trajectory for $p = 4$ in a two-dimensional input parameter quantile space is shown in Figure 4.

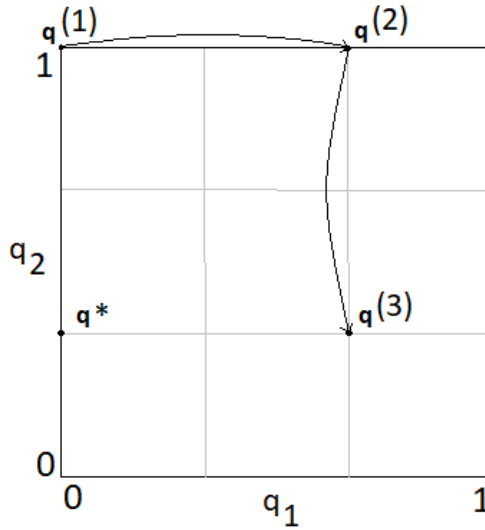


Figure 4: A trajectory in the input parameter quantile space for the Morris method, $k = 2$.

Using two samples, which differ in the i th component, the elementary effect for parameter x_i is obtained via

$$EE_i(\mathbf{x}^{(l)}) = \begin{cases} \frac{y(\mathbf{x}^{(l+1)}) - y(\mathbf{x}^{(l)})}{\Delta q_i}, & \text{if the } i\text{th component of } \mathbf{x}^{(l)} \text{ was increased by } \Delta x_i \\ \frac{y(\mathbf{x}^{(l)}) - y(\mathbf{x}^{(l+1)})}{\Delta q_i}, & \text{if the } i\text{th component of } \mathbf{x}^{(l)} \text{ was decreased by } \Delta x_i. \end{cases} \quad (6)$$

To determine the sensitivity measures, r independent trajectories are required. The trajectories have different randomly generated starting points. Points that belong to a trajectory are not independent, but the r (absolute) elementary effects, that are sampled from the distributions F_i and G_i result from different trajectories and thus are independent. That legitimizes the use of the sample mean μ_i and variance σ_i^2 of the calculated elementary effects for input x_i as estimators for mean and variance of F_i [46, p. 165], [57, S. 99]. The same argument can be used for μ_i^* .

Hence, using the ‘trajectory design’-method as a sampling strategy, i.e. a $(k + 1) \times k$ matrix \mathbf{B}^* , whose $(k + 1)$ rows contain the k -dimensional parameter vectors, k elementary effects can be calculated using $k + 1$ model runs. Since r trajectories are used, $r \cdot (k + 1)$ model runs are required [39, p. 49], [62, p. 334].

The implementation of the construction of r matrices \mathbf{B}^* is done as presented in [46, pp. 163, 164] and [62, p. 334]: A matrix \mathbf{B} of dimension $(k + 1) \times k$ is chosen, the

elements of which have the values 0 and 1. For each column index j with $j = 1, \dots, k$ there are two rows of \mathbf{B} that differ only in the j th entry. The usual choice for \mathbf{B} is a lower triangular matrix filled with ones. Let \mathbf{D}^* be a k -dimensional diagonal matrix with elements taking the values $+1$ or -1 with equal possibility. Let $\mathbf{J}_{k+1,k}$ be a $(k+1) \times k$ matrix, the elements of which take on the value 1. $(1/2)[(2\mathbf{B} - \mathbf{J}_{k+1,k})\mathbf{D}^* + \mathbf{J}_{k+1,k}]$ is a $k+1 \times k$ matrix, in which each column is either equal to the corresponding column in \mathbf{B} , or it is equal to the corresponding column in \mathbf{B} with replacing zeros with ones and ones with zeros. \mathbf{P}^* is a $k \times k$ random permutation matrix in which each column contains an element taking the value 1 while all others take the value 0. Any two columns have the 1 at the same position. Each such matrix has an equal probability of being selected. Let \mathbf{q}^* be the randomly chosen basis vector. This results for the matrix

$$\mathbf{B}^* = (\mathbf{J}_{k+1,1}\mathbf{q}^* + (\Delta/2)[(2\mathbf{B} - \mathbf{J}_{k+1,k})\mathbf{D}^* + \mathbf{J}_{k+1,k}])\mathbf{P}^* \quad (7)$$

\mathbf{B}^* supplies an elementary effect, which is randomly selected from F_i for each input parameter. The matrix for the whole experiment is:

$$\mathbf{Q} = \begin{pmatrix} \mathbf{B}_1^* \\ \mathbf{B}_2^* \\ \dots \\ \mathbf{B}_r^* \end{pmatrix}. \quad (8)$$

For $k = 3$, $r = 5$ and $p = 4$, the trajectories in the input parameter quantile space shown in Figure 5 can be obtained.

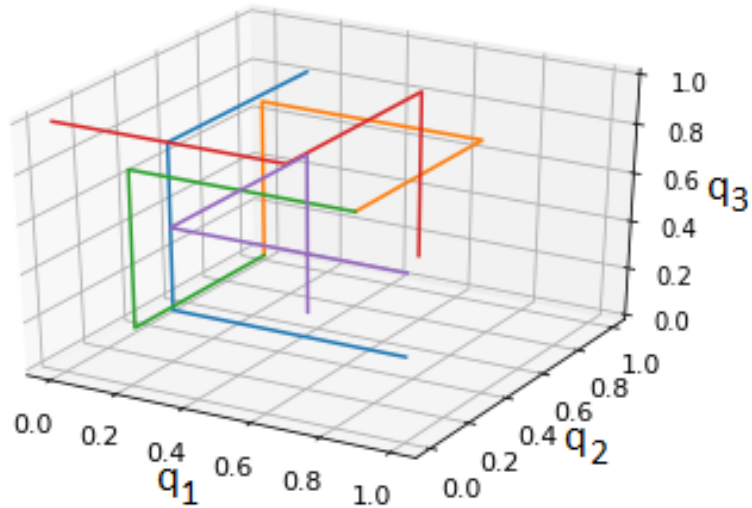


Figure 5: Trajectories in the input parameter quantile space for the Morris method, $k = 3$, $r = 5$.

6.4 The sensitivity measures

As mentioned in Chapters 6.1 and 6.3, a statistical evaluation of the elementary effects is carried out to obtain the sensitivity measures. They will further be explained in the current chapter.

After generating r samples from the distribution of the elementary effects EE_i over the input parameter space, their mean μ_i , their modified mean μ_i^* and their standard

deviation σ_i are calculated for each input parameter x_i [1, p. 63, 64]. The sensitivity measures thus read as follows:

$$\mu_i = \frac{1}{r} \sum_{j=1}^r EE_i^j \quad (9)$$

$$\mu_i^* = \frac{1}{r} \sum_{j=1}^r |EE_i^j| \quad (10)$$

$$\sigma_i = \sqrt{\frac{1}{r-1} \sum_{j=1}^r (EE_i^j - \mu_i)^2} \quad (11)$$

[20, p. 375],[39, p. 48],[22, p. 7].

The estimator of the mean μ_i of the distribution of the elementary effects F_i alone is not suitable to sort the parameters according to their importance, because F_i may contain negative elements, which happens, when the model is non-monotonous. In this case, elementary effects would cancel each other out when calculating the mean. μ_i^* is the estimated mean of the distribution of the absolute values of the elementary effects G_i . The measure μ^* can be used to sort the input parameters according to their importance and thus to identify the input parameters which have an important influence on the considered model result. If μ_i has a large value, the parameter has a large influence on the output. If μ_i^* has the same value, the sign of the effect is the same everywhere. If the value of μ_i is small, but that of μ_i^* is large, the sign of the effect depends on the point in the parameter space at which the effect has been determined. σ_i is the standard deviation of F_i , delivering information about which input parameters are involved in interactions with other input parameters. σ_i thus provides information on the second and higher order effects in which the factor is involved. A high value of σ_i means that the elementary effects with regard to the parameter under consideration are different, i.e. their value depends on the point in the input parameter space and thus on the values of the other input parameters. A small value for σ_i indicates very similar values of the elementary effects, which implies that the effect of x_i is quite independent of the values of the other input parameters [57, pp. 92-96].

This knowledge allows input parameters with small values for μ_i^* to be fixed to a value in their bandwidth without this entailing a significant loss of information [57, p. 107].

6.5 Dynamic and spatial resolved sensitivity analysis

So far, scalar model outputs were considered. However, not only scalar outputs have to be reliable and therefore have to be examined for the input parameters with an effect on the model results, but also their temporal progression or spatial distribution. Therefore it makes sense to carry out the sensitivity analysis for time- and space-dependent output quantities.

If the target quantity is not a scalar value but a time series, a dynamic sensitivity analysis is carried out [39, p. 51]. The definition of the elementary effects can be adjusted as follows:

For $t \in \{t_1, \dots, t_n\}$ let $y(t, x)$ be the result of the model $Y : \{t_1, \dots, t_n\} \times \Omega \rightarrow \mathbb{R}$ at time t with input parameters $x \in \Omega$. The sequential elementary effect $EE_i(t)$ for the parameter x_i is defined as:

$$EE_i(t) = \frac{y(t, \mathbf{x} + \mathbf{e}_i \Delta x_i) - y(t, \mathbf{x})}{\Delta q_i} \quad (12)$$

This also allows the time dependency to be added to the sensitivity measures:

$$\mu_i(t) = \frac{1}{r} \sum_{j=1}^r EE_i^j(t) \quad (13)$$

$$\mu_i^*(t) = \frac{1}{r} \sum_{j=1}^r |EE_i^j(t)| \quad (14)$$

$$\sigma_i(t) = \sqrt{\frac{1}{r-1} \sum_{j=1}^r (EE_i^j(t) - \mu_i(t))^2} \quad (15)$$

Hence, a measure for the influence of each parameter is determined for each time step, showing temporal differences in the influences of parameters [39, p. 143]. An analogous approach can be used for space-dependent sensitivity measures.

6.6 Identification of relevant parameters

In the following, the method used for identification of relevant parameters is described. For this purpose, the aspect mentioned in Chapter 6.2.1 can be used, that the value of an elementary effect for the i th input parameter corresponds to the variation of the output when this input parameter varies from the minimum to the maximum of its parameter range. Thus, as described in Chapter 6.4, the consideration of the Morris measures μ^* and σ is helpful for an evaluation of the relevance of the input parameters. Therefore, for each model result a minimum variation can be defined, from which the causing parameter can be considered to be affecting the model result. This threshold variation can be defined using the standard deviation of the output σ_{out} . A relevance can be assigned to the input parameters x_i according to a by comparing the corresponding measures $\mu_{i,j}^*$ and $\sigma_{i,j}$ to the value $a \cdot \sigma_{\text{out},j}$, $a \in \{0, 1, 2, 3\}$. In case of time dependent model outputs, there are two possibilities to evaluate the influence of the input parameters. In order to evaluate the influence of an input parameter at the individual points in time, the time dependent standard deviation of the model output $\sigma_{\text{out},k}(t)$ can be used, but since the standard deviation varies in time, the assigned relevances for two time steps cannot be directly compared because they arise from two different thresholds. That is why it also makes sense to define the maximum of the time dependent standard deviation of the output $\max_t(\sigma_{\text{out},k}(t))$ in order to define the threshold for the whole day and to compare the time dependent measures to it in order to find the input parameters causing the largest variations during the whole day.

For scalar model outputs y_j , the Morris measures can be visualized via bar or tornado and Morris plots, as well as tables. A colored table can also be used for the visualization of the diurnal variations of the measures in case of time dependent outputs.

6.7 Validation of the implemented Morris method

The implemented Morris method is validated against an example application from [46, pp. 165, 166] and [57, pp. 88, 103] in order to verify whether it is working properly. The test case is a model with 20 input parameters with the following form:

$$y = \beta_0 + \sum_{i=1}^{20} \beta_i w_i + \sum_{i<j}^{20} \beta_{i,j} w_i w_j + \sum_{i<j<l}^{20} \beta_{i,j,l} w_i w_j w_l + \sum_{i<j<l<s}^{20} \beta_{i,j,l,s} w_i w_j w_l w_s \quad (16)$$

with $w_i = 2 \cdot (x_i - \frac{1}{2})$ for $i \in \{1, \dots, 20\} \setminus \{3, 5, 7\}$ and $w_i = 2 \cdot (1.1 \cdot x_i / (x_i + 0.1) - \frac{1}{2})$ for $i \in \{3, 5, 7\}$. For the coefficients yields:

$\beta_i = 20$, $i = 1, \dots, 10$; $\beta_{i,j} = -15$, $i, j = 1, \dots, 6$; $\beta_{i,j,l} = -10$, $i, j, l = 1, \dots, 5$;

$\beta_{i,j,l,s} = 5$, $i, j, l, s = 1, \dots, 4$.

The remaining first- and second-order coefficients are independently generated from a normal distribution with zero mean and unit standard deviation and the remaining third- and fourth-order coefficients are set to zero.

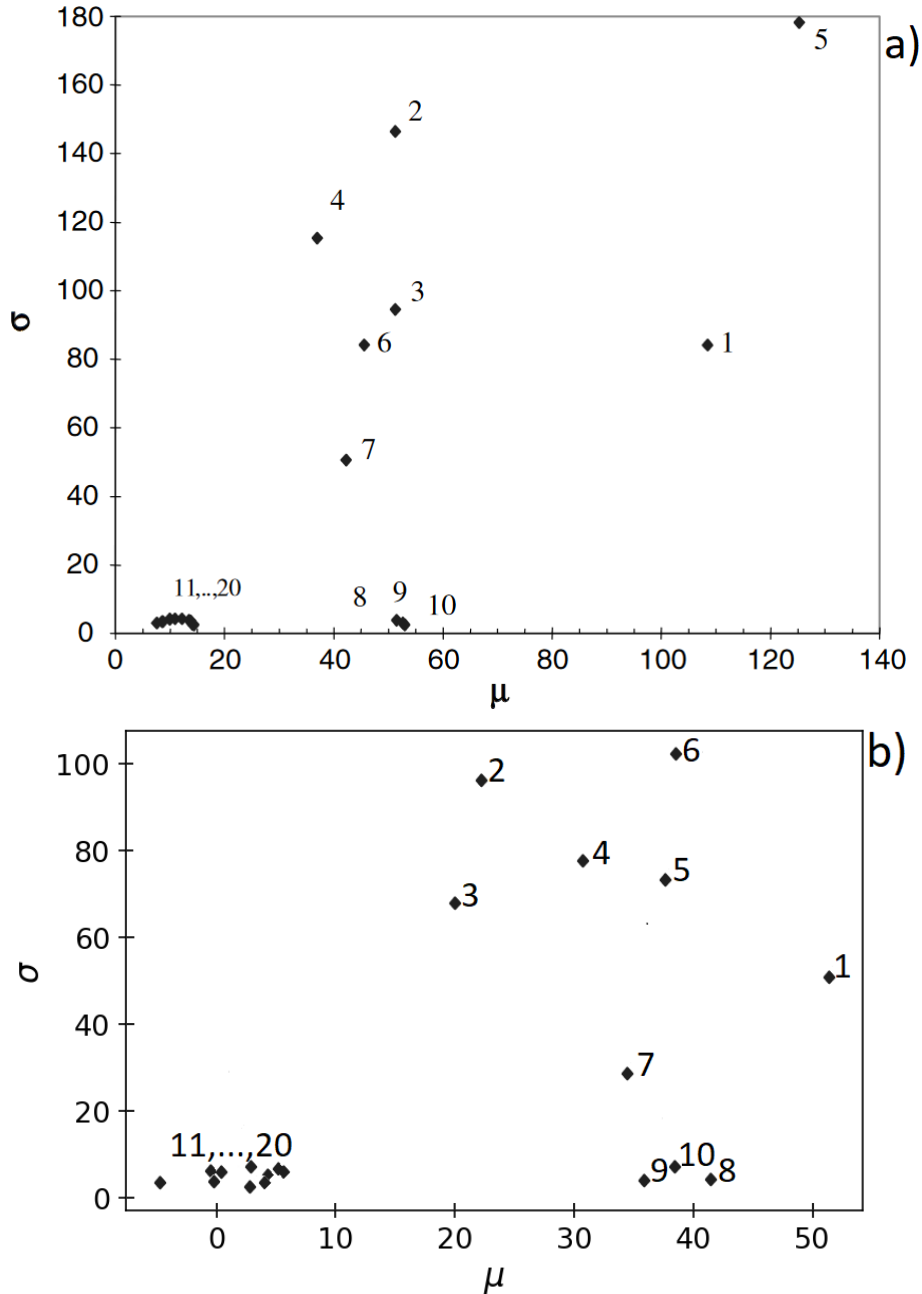


Figure 6: Validation of the Morris method. a) Result from [57, p. 103], b) Result of the implemented Morris method.

The Morris method is applied to this test case and the resulting Morris measures μ and σ are compared to the ones found in [46] and [57]. $r = 4$ trajectories and $p = 4$ are used. Hence, 84 model runs are performed. The calculated sensitivity measures are visualized

in Figure 6. Figure 6 a) is taken from [57, p. 103] and shows the Morris measures the ones obtained by the implemented Morris method 6 b) will be compared to.

Both analysis results imply that the first ten input parameters have an increased importance. Parameters $x_{\{1,\dots,7\}}$ have an increased value of the standard deviation and are thus involved in interactions, while the parameters $x_{\{8,9,10\}}$ have mean elementary effects different from zero, but small standard deviations. The results show slight differences which is reasonable because of the randomly sampled coefficients and the limited number of only four used trajectories, which means that only four samples were taken from the set of the elementary effects. Since the conclusions which can be drawn from the results coincide with the ones from the literature although only four trajectories were used, the validation is successful and the implemented Morris method can be applied to the cases in this work.

7 Latin hypercube sampling

This chapter will introduce the Latin hypercube sampling (LHS) as a sampling strategy for the uncertainty analysis and estimation of required input accuracy applied after evaluation of the results of the Morris method.

LHS is a stratified Monte Carlo sampling method. It is used to improve the coverage of the input parameter space compared to simple random sampling. The method makes use of the CDF $F(\cdot)$ of a random variable. For illustration purposes, an example based on [21] is given in Figure 7. Figure 7 a) shows the graph of the CDF F of a random

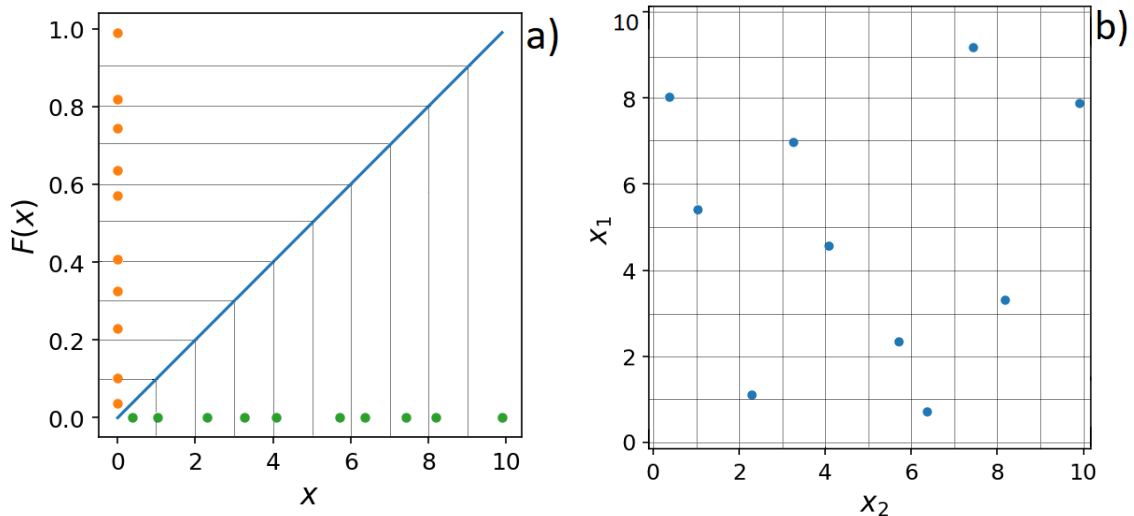


Figure 7: Visualization of LHS. a) Visualization of the sampling strategy, b) Coverage of the input parameter space for $k = 2$.

variable X , evaluated at x . Suppose X is uniformly distributed on the interval $[0,10]$. The vertical axis, i.e. the range of the CDF is divided into n ($n = 10$ in the given example) non-overlapping intervals of equal length. Applying the inverse of the CDF, these n intervals divide the horizontal axis into n equiprobable nonoverlapping intervals. This is shown by the grey lines. Within each of the n CDF-intervals one value is randomly picked (orange dots). Via $F^{-1}(x)$ the actual parameter values are generated (green dots), one per equiprobable interval on the horizontal axis. If k input parameters are to be examined, their Latin hypercube samples are randomly combined for each model run and therefore randomly selected from the samples for each parameter without replacement.

Thus, each value is used once. The coverage of the input parameter space for $k = 2$ is shown in Figure 7b). The number of required model runs is n [35, p. 408], [21]. Thus, in case of LHS the required number of model runs is reduced compared to simple random sampling, while an improvement of the coverage of the input space is warranted [21]. For this reason, [60, p. 1] rates LHS as ‘the most widely used random sampling method for Monte Carlo-based uncertainty quantification’.

8 Analysis method for computational expensive setups with a large parameter space

The Morris method is a global sensitivity analysis method which can also make statements about interactions between parameters and which thus can be applied when non-linear relationships between input parameters and model results are assumed. Furthermore, the Morris method requires a small number of model runs compared to other sensitivity analysis methods which are based on Monte Carlo Sampling. Nevertheless, a high computing time requirement of the model and a large input parameter space, as it is the case for the investigation of an urban area simulated with PALM, lead to the fact that the method would exceed the computational time capacities and is not feasible and a different approach is necessary to determine the input parameters that affect the model results. The method proposed in this work is to divide the investigations into two parts. In a first step, the Morris method is applied to simple setups described by one group of related parameters. The relevant parameters within this group are determined. In a second step, for the complex area to be investigated, a OAT method is applied. Therefore, one parameter group or one parameter is varied, while the rest of the input parameters is kept constant. If the variation of a parameter group has a major influence, the preliminary studies can be used to infer the parameters within the group to be responsible for the relevance. This allows for the investigation and the comparison of the influences of various parameter groups and parameters, which are necessary to describe the complex setup, on the model outputs. The method is illustrated in the scheme shown in Figure 8. The scheme shows input parameters with an increased influence on a considered model output. The latter is given in the left box. The middle box shows the parameter (type)s with increased effects on the model result found by the OAT-investigations and the right box shows the parameters within the types with increased effect found by the analyses performed with the Morris method. The colors indicate the size of the effect. The parameters found to be important with the Morris method are colored as follows: If the Morris measure increases the output standard deviation multiplied with a factor a , the cell is green for $a = 1$, yellow for $a = 2$ and orange for $a = 3$. A similar approach is used for the parameters in the middle box. The difference of the considered model result from the scenario and reference run is compared to the standard variation of the differences resulting from all scenarios. In the given example, the parameter types 1 and 2 as well as the parameters 1, 2 and 3 have an equally sized influence on the output parameter. The parameters a, b and c have an increased influence within the parameter group labeled by parameter type 1, where parameter a has the largest influence. Hence, these are the parameters responsible for the influence of parameter type 1. The parameters a', b' and c' lead to the increased influence of parameter type 2, where parameter b' has the largest influence.

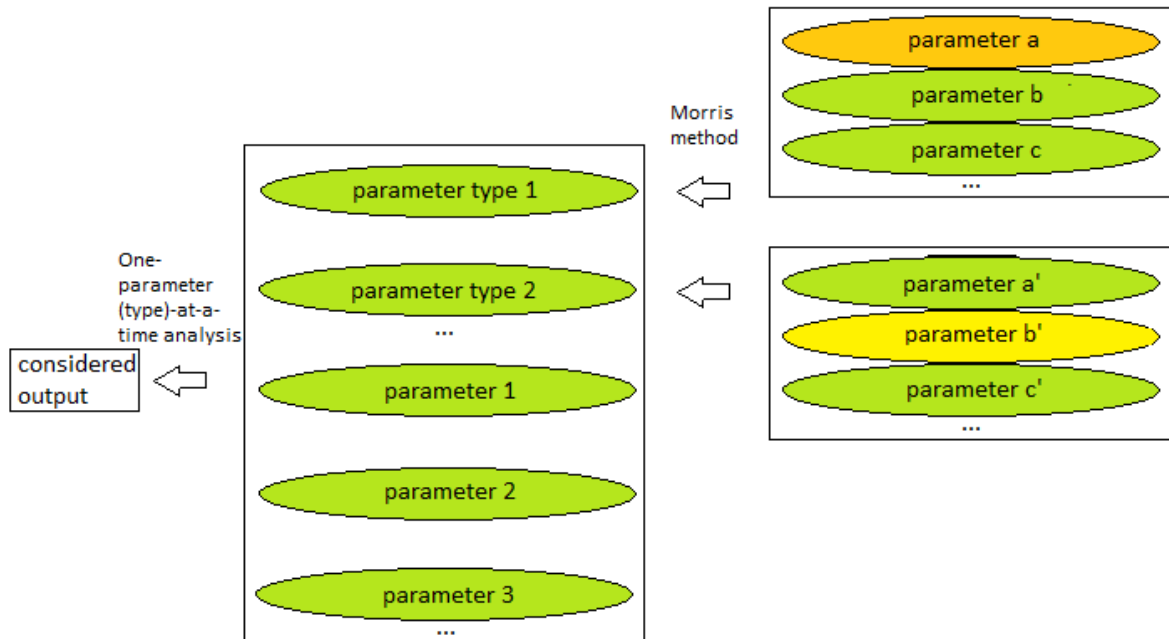


Figure 8: Illustration of the analysis method. Left: considered model result, middle: OAT-results, right: Morris method-results. The colors indicate the size of the effect.

9 Previous studies and specification of the research questions

In the following, reference is made to previously performed studies and the aspects to be examined within the framework of this analysis.

For natural, water and paved surfaces the LSM is used. In order to solve the energy balance equation of the earth's surface, information concerning the physical properties is required that is passed to the model using several parameters whose values should be determined as precisely as necessary in order to predict the meteorological quantities with the required accuracy. In [24] a first sensitivity study was carried out for the land surface parameters of the LSM in PALM by varying them individually in order to estimate the sensitivity of the simulated energy balance components on specific land surface parameters for a horizontally homogeneous setup. Furthermore, initialization parameters like the grid spacing were varied in [24]. It was found that the leaf area index, the albedo, or the initial humidity affect the daytime turbulent sensible and latent heat fluxes and hence temperatures, and that during night, the most dominant parameters are the surface roughness, the grid size used for the setup, and the applied radiation schemes. The parameters of the LSM will be further investigated applying a global sensitivity analysis method. Furthermore, the sensitivity according to the land-surface parameters shall be investigated for an urban environment.

In urban areas, it is also required to provide the model with information about buildings. Various material and surface properties, such as wall thicknesses, heat capacities and conductivities, window fractions and albedos infer the solution of the energy balance on the building surface [32, p. 5838]. Since in Germany, restoration and thermal insulation actions on individual buildings are not recorded and the year of construction is often a poor measure of the thermodynamic properties of buildings [32, p. 5843], the question of the effect of building type and properties on the model results rises.

The set of green elements includes green roofs and facades, trees and green spaces. The one of blue elements contains ponds, lakes, rivers and fountains. Trees are suitable for

producing a cooling effect during day through evapotranspiration and shading [30, p. 1]. For the detailed description of 3D vegetation, the parameters species, tree height, crown diameter, crown shape, trunk diameter and ratio of crown diameter and crown height can be specified in PALM [32, p. 5845]. Since information on public trees are available and else only the parameters tree height and crown diameter can be taken from LiDAR data, while the determination of other parameters requires more intensive measurements [32, p. 5845], the question of whether it is important for the simulation result to precisely define trees in terms of tree type and shape, or whether some basic information like the height of the vegetation is sufficient rises. Blue elements and the temperature difference between water and land result in a thermally induced local air flow system. However, data on the water temperature of the numerous water bodies in urban areas are only available to a limited extent and restricted to samples for monitoring the water quality or swimming suitability [30, p. 5]. Hence, the impact of the temperature of small water surfaces within an urban environment on the simulation results as well as their area of influence are going to be investigated.

In summary, for an accurate prediction of the urban meteorological conditions for a specific setting, information on vegetation, soil properties, and building properties concerning walls, windows and green roofs or facades, etc. are required. For the small grid spacings of around 1 m usually used for urban setups, the information are needed for every surface element and thus in a high spatial resolution and is almost impossible to obtain [42, p. 115]. This is described in Chapter 4. Because of the inadequate or erroneous information about the input parameters, uncertainties in the model results occur. In order to optimally use the effort and costs associated with a thorough data acquisition and data preparation of location data, it is necessary to perform an uncertainty and sensitivity analysis to determine the range of the model results depending on the uncertainty of the input data as well as the necessary accuracy of the input data to ensure a desired accuracy of the results.

A first sensitivity study with respect to land-surface and building parameters in an urban environment was carried out in [4] varying one or more parameters against a reference. The aim of this study is to combine the above mentioned global sensitivity studies with a OAT sensitivity study for various above mentioned input parameters using a more diverse domain, including vegetated and paved areas, 3D-vegetation and variously sized and arranged buildings.

Depending on the studied setup, the relevant model results for comparison will be 2 m air temperature, surface temperature, 2 m and 10 m wind speed and indoor temperature. In order to estimate the thermal comfort, biometeorological quantities like Universal Thermal Climate Index (UTCI) combine the air temperature with further quantities like humidity, wind speed and radiation [7, p. 16], see Chapter 20 in the appendix. The UTCI will be investigated, too, in order to estimate the effect of the input parameters on the thermal comfort. The study is focusing on autochthonous weather conditions which are characterized by a strong daytime insolation, weak winds and a stable nocturnal stratification, since the urban climatic characteristics are particularly pronounced, then, and a strong heat stress is possible [38, pp. 2, 3, 8], [26, p. 2].

Part III

Model setups and simulation results

Idealized areas with horizontally homogeneous properties or single obstacles are considered for preliminary investigations of the surface type parameters with the Morris method. Furthermore, an urban area is considered. The setups to be examined are introduced in this part and basic findings that are typical for the investigated properties are presented in order to find out if they correspond to common knowledge.

10 Grassland

10.1 The PALM model setup for the grassland

For the natural setup with horizontally homogeneous properties concerning grassland, the LSM and the radiation model are used. The domain is assigned a latitude of 55° . The simulated time period starts on a June 21 at 21 UTC and the following 27 hours are simulated. The wind is set to 1.5 ms^{-1} and 0.0 ms^{-1} for the u and v component, respectively. The vertical wind component is $w = 0.0 \text{ ms}^{-1}$ at the beginning. An initial value of the potential temperature θ of 290.0 K is assumed up to a height of 1750 m. A capping inversion is given through a vertical gradient of 0.65 K/100 m from 1750 m to 2716 m. Above the inversion, the potential temperature is initialized with a constant profile. Rayleigh damping was used at the top boundary in order to prevent the reflection of gravity waves. Furthermore, the model soil layers are in depths of -0.005 m, -0.02 m, -0.05 m, -0.1 m, -0.2 m, -0.4 m, -0.8 m and -2.0 m. They are initialized with a soil moisture of $0.4 \text{ m}^3\text{m}^{-3}$ and a temperature of 290.0 K. The deepest level as well as the deep soil temperature, which acts as bottom boundary condition for the heat diffusion in the soil model [48], are set to 286.3 K. Vegetation and soil parameters also need to be specified. Their values are varied as part of the Morris method. The land surface and soil parameters are assumed to be homogeneous over the model domain. The radiation scheme to be used is the clear sky model. Cyclic boundary conditions along the x - and the y -axis are applied and the no-slip condition is used as the bottom boundary condition of the horizontal velocity components. The bottom boundary conditions of the water vapor to total water mixing ratio and the potential temperature are set to Dirichlet, which is required when using the LSM. The time interval for data output and averaging is 3600 s, with the end of the averaging interval coinciding with the output time.

The domain considered in this study has a volume of $2000 \text{ m} \times 2000 \text{ m} \times 4368 \text{ m}$. A horizontal grid size of 50 m and a vertical grid size of 10 m are used, where the latter is stretched above 2000 m, i.e. above the boundary layer top, with a factor of 1.08 until the maximum vertical grid size of 100 m is reached. The aim for this is to reduce the computational time. The given model domain corresponds to the one described in [24, pp. 5314, 5315].

For chosen definition of the grid properties a grid sensitivity study was used. Therefore, the domain size and the horizontal and vertical grid sizes are varied and the results are compared in order to find a setup to satisfy both, resolving the relevant structures as well as requiring an appropriate runtime. Figure 9 exemplarily compares the diurnal cycles of the horizontally and temporally averaged 2 m potential temperature and the 10 m wind speed for different grid spacings. The variations of the mentioned results that arise during the course of the day are described and explained in Chapter 10.2, and the cycles are used here only with respect to the grid sensitivity study.

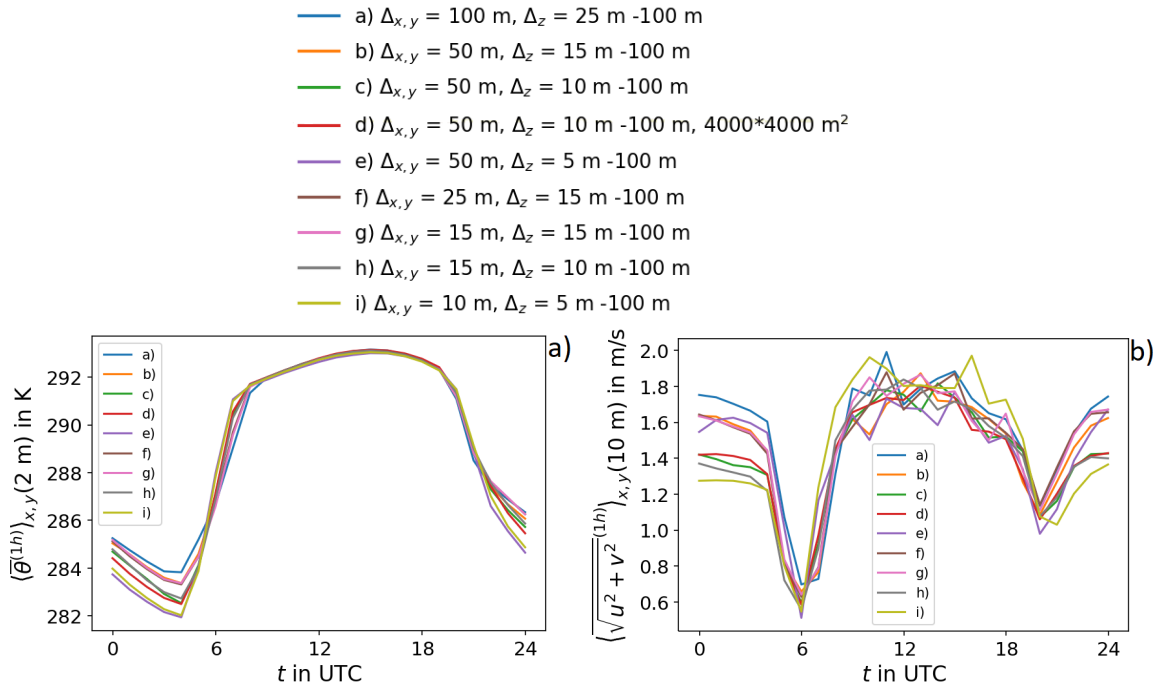


Figure 9: Grid sensitivity study for the grassland setup.

Diurnal cycles of the horizontally and temporally averaged 2 m potential temperature a) and the 10 m wind speed b), respectively, for different grid spacings, see legend above.

Furthermore, the horizontally averaged vertical profiles of the ratios of the absolute values of the u -component of the resolved vertical momentum flux to the sum of the absolute values of the u -component of the subgrid-scale and the resolved vertical momentum flux, $\frac{|\langle w^* u^* \rangle_{x,y}^{(1h)}|}{|\langle w^* u^* \rangle_{x,y}^{(1h)}| + |\langle w'' u'' \rangle_{x,y}^{(1h)}|}$, and the resolved vertical sensible heat flux to the sum of the absolute values of the subgrid-scale and the resolved vertical sensible heat flux, $\frac{|\langle w^* \theta^* \rangle_{x,y}^{(1h)}|}{|\langle w^* \theta^* \rangle_{x,y}^{(1h)}| + |\langle w'' \theta'' \rangle_{x,y}^{(1h)}|}$, at different times are compared for different grid spacings, as these ratios enable an evaluation of the portion of each flow that is resolved and not only parameterized within a subgrid-scale model. The ratios are used to calculate two indices to indicate the fraction of the flow that is resolved at different times. The first index is denoted as $p_{\geq 0.9}$ and describes the percentages of grid levels with $\geq 90\%$ of the vertical momentum and sensible heat flux being resolved. The second index is denoted as m and describes the mean fraction of resolved vertical momentum and sensible heat flux over the grid levels. For every grid configuration given in Figure 9, $p_{\geq 0.9}$ and m are calculated for different times using the grid levels of the lowest quarter of the boundary layer and given. The values are summarized in Table 4. According to Table 4, at night, the fraction of the resolved fluxes is generally lower than during day time due to an enhanced turbulent mixing and the development of larger structures in the unstable case ([26, p. 13]), see Chapter 10.2. A larger grid spacing usually goes along with a lower fraction of resolved structures. The grid spacing of $\Delta_{x,y} = 50$ m and $\Delta_z = 10$ m appropriately reproduces the results of smallest grid spacings $\Delta_{x,y} = 10$ m and $\Delta_z = 5$ m and $\Delta_{x,y} = 15$ m and $\Delta_z = 10$ m (see Figure 9). Furthermore, the comparison of resolved and subgrid-scale fluxes given in Table 4 show that only a small amount of the fluxes is parameterized within a subgrid-scale model for this grid spacing. Except from 0 UTC, the size of the area of the domain does not yield significant differences in the resolution and Figure 9 shows that the grid spacing of $\Delta_{x,y} = 50$ m and $\Delta_z = 10$ m produce very similar results for both domain

Table 4: $p_{\geq 0.9}$ and m for the vertical momentum (upper part) and sensible heat (lower part) flux for the grid sensitivity study for the grassland setup.

Grid	0 UTC		6 UTC		12 UTC		18 UTC	
	$p_{\geq 0.9}$ [%]	m [%]	$p_{\geq 0.9}$ [%]	m [%]	$p_{\geq 0.9}$ [%]	m [%]	$p_{\geq 0.9}$ [%]	m [%]
a)	37.5	84.1	68.8	86.4	18.8	66.4	75.0	87.7
b)	92.3	93.8	69.2	84.5	76.9	90.0	76.9	90.1
c)	57.5	88.1	75.0	86.1	80.0	90.8	85.0	92.3
d)	90.0	94.0	72.5	86.5	82.5	91.6	82.5	91.8
e)	23.8	79.4	42.5	70.6	86.3	93.1	86.3	93.6
f)	88.5	92.3	76.9	90.5	57.7	82.8	88.5	93.1
g)	88.5	93.5	69.2	89.6	88.5	93.8	88.5	94.2
h)	92.5	94.4	77.5	93.1	90.0	95.0	92.5	95.7
i)	73.8	88.8	80.0	94.3	95.0	97.2	95.0	97.2
a)	43.8	74.6	62.5	81.7	75.0	86.7	75.0	86.4
b)	73.1	88.6	69.2	85.6	84.6	91.8	84.6	91.7
c)	82.5	85.2	75.0	87.1	87.5	92.8	87.5	93.0
d)	85.0	87.7	77.5	86.4	87.5	92.9	87.5	92.8
e)	5.0	47.7	13.8	76.1	90.0	94.2	87.5	94.1
f)	84.6	92.1	76.9	89.7	88.5	93.7	88.5	93.6
g)	88.5	92.7	84.6	91.8	92.3	94.3	92.3	94.2
h)	85.0	93.0	82.5	93.4	92.5	95.7	92.5	95.6
i)	7.5	78.7	88.8	94.3	96.3	97.3	95.0	97.2

sizes. Since both the resolution and the amount of required computational resources are acceptable and the considered outputs differ only slightly from the ones with the finest grid spacings, it was decided to use the grid spacing of $\Delta_{x,y} = 50$ m and $\Delta_z = 10$ m and the area of $(2000 \text{ m})^2$ for the simulation domain as it was done in [24].

10.2 PALM model results for the grassland setup

An overview of the parameters for the grassland case is given in Table 5, whereby it is to be noted that some values are given with a greater accuracy than actually measurable. A simulation is performed based on the given parameter configuration and the model setup described in Chapter 10.1 including the optimal choice for the grid spacing given there.

Figure 10 shows typical time-height or -depth cross sections of potential temperature and soil temperature, respectively, as well as the diurnal cycles of the horizontal mean of the 2 m air temperature and the 10 m wind speed with marked extrema. At daytime, the soil is heated by solar radiation and warms up starting at the surface as it is visible in Figure 10 a). In the afternoon the radiation budget becomes negative and the temperature of the surface starts to decrease. Due to the influence of the surface temperature on the air temperature through sensible heat flux, the latter follows the development of the surface temperature, see Figure 10 c). Here is no closed diurnal cycle and no stationarity, and under the given conditions, the temperatures would therefore slightly continue to rise on the following day. In the evening the potential temperature of the lowest levels starts to decrease and an inversion arises, which is most pronounced at sunrise around 4 UTC, see Figure 10 b). This stable stratification is then destroyed again by the solar radiation. The diurnal changes in temperature and atmospheric stratification influence the wind speed. During the day, enhanced turbulent mixing occurs because of the unstable stratification near the surface [29, pp. 228, 229]. The most intense mixing occurs in the early afternoon,

Table 5: Overview of the parameter configuration for the grassland setup.

Parameter	Value	Description
Skin layer parameters		
C_0	$0 \text{ Jm}^{-2}\text{K}^{-1}$	heat capacity of the skin layer
c_{veg}	0.7	vegetation coverage (0.3: bare soil)
LAI	$1.3 \text{ m}^2\text{m}^{-2}$	leaf area index
$r_{c,\text{min}}$	106.67 sm^{-1}	minimum canopy resistance
z_0	0.17667 m (0.005 m for bare soil)	roughness length for momentum
$z_{0,h}$	$0.3 \cdot 10^{-4} \text{ m}$ ($0.5 \cdot 10^{-4} \text{ m}$ for bare soil)	roughness length for temperature
Λ	$11.00 \text{ Wm}^{-2}\text{K}^{-1}$ ($0.0 \text{ Wm}^{-2}\text{K}^{-1}$ for bare soil)	heat conductivity between atmosphere and soil
ϵ	0.97 (0.94 for bare soil)	surface emissivity
α	0.25 (0.08 for bare soil)	albedo
Soil parameters		
m_{res}	$0.01 \text{ m}^3\text{m}^{-3}$	residual volumetric soil moisture
$r_{\text{soil},\text{min}}$	50 sm^{-1}	minimum soil resistance
T_{deep}	286.3 K	deep soil temperature
m_{fc}	$0.347 \text{ m}^3\text{m}^{-3}$	volumetric soil moisture at field capacity
m_{wilt}	$0.18167 \text{ m}^3\text{m}^{-3}$	volumetric soil moisture at permanent wilting point
α_{vG}	3.67	coefficient alpha in the soil hydraulic conductivity parameterization after van Genuchten
l_{vG}	-1.173	coefficient l in the soil hydraulic conductivity parameterization after van Genuchten
n_{vG}	1.28	coefficient n in the soil hydraulic conductivity parameterization after van Genuchten
γ_{sat}	$0.287 \cdot 10^{-5} \text{ ms}^{-1}$	hydraulic conductivity of the soil at saturation
m_{sat}	$0.52 \text{ m}^3\text{m}^{-3}$	volumetric soil moisture at saturation (porosity)
Initial soil profiles		
$T_{\text{soil},k}$	290.0 K, 290.0 K, 290.0 K, 290.0 K, 290.0 K, 290.0 K, 290.0 K, 290.0 K, 286.3 K	soil temperature at depth level k, $k \in \{1, \dots, 8\}$
$m_{\text{soil},k}$	$0.4 \text{ m}^3\text{m}^{-3}$, $0.4 \text{ m}^3\text{m}^{-3}$, $0.4 \text{ m}^3\text{m}^{-3}$, $0.4 \text{ m}^3\text{m}^{-3}$, $0.4 \text{ m}^3\text{m}^{-3}$, $0.4 \text{ m}^3\text{m}^{-3}$, $0.4 \text{ m}^3\text{m}^{-3}$, $0.4 \text{ m}^3\text{m}^{-3}$	soil moisture at depth level k, $k \in \{1, \dots, 8\}$
$R_{\text{fr},k}$	0.12, 0.12, 0.12, 0.19, 0.19, 0.11, 0.11, 0.04	root fraction at depth level k, $k \in \{1, \dots, 8\}$

followed by a decay due to the subsequent decrease of the surface sensible heat flux [16, pp. 79, 80]. Momentum transport from higher layers to near surface layers leads to higher wind speeds in the low layers, see Figure 10 d), and lower wind speeds in higher

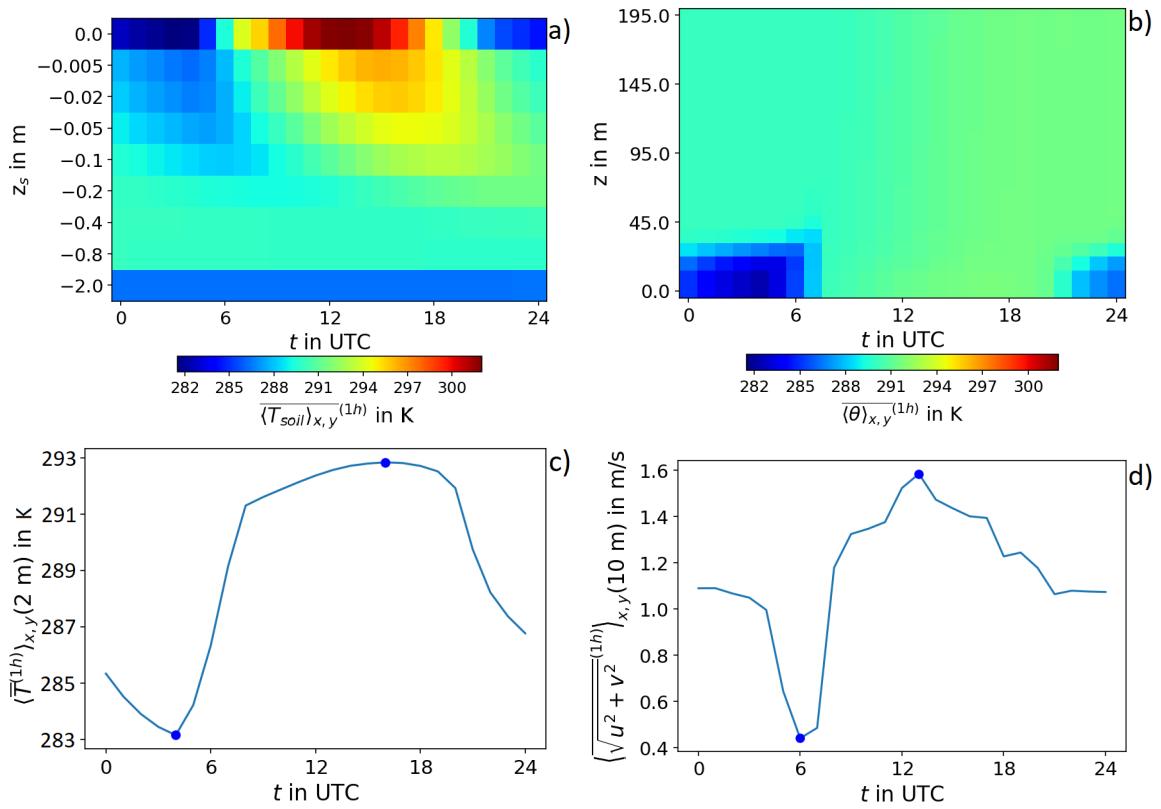


Figure 10: Grassland: Typical diurnal cycles. Time-height cross section of a) the soil temperature, b) the potential temperature in the atmosphere, Diurnal cycles of the horizontal mean of c) the 2 m air temperature and d) the 10 m wind speed with marked extrema.

levels (not shown here) than during night time, when the transport is suppressed by the stable stratification, such that the wind near the surface is decoupled from that at higher altitudes [29, pp. 228, 229].

11 A paved surface

11.1 The PALM model setup for the paved surface

For the horizontally homogeneous properties of a paved surface, the same setup and initialization as for the grassland described in Chapter 10 is used. In contrast to the grassland setup, parameters for the pavement are used instead of vegetation parameters. The depth of the pavement is six grid levels below the surface, i.e. -0.4 m. Below that level, soil parameters take effect.

11.2 PALM model results for the paved surface setup

An exemplary model run is performed for the pavement case. An overview of the parameter configuration is given in Table 6. The setup is characterized by the following differences from the grassland case: The values of the roughness lengths z_0 , $z_{0,h}$ differ and vegetation related parameters as well as the use of a skin layer are omitted. Furthermore, due to the impermeability of the pavement to water, a soil moisture is only assigned to the depth levels in the soil below the pavement, where the soil parameters specify the development of the soil moisture. Typical time-height or -depth cross sections of potential temperature and soil temperature, respectively, as well as the diurnal cycles of the horizontal mean of the 2 m air temperature and the 10 m wind speed obtained by the exemplary model run are shown in Figure 11. As in the grassland case, the ground warms

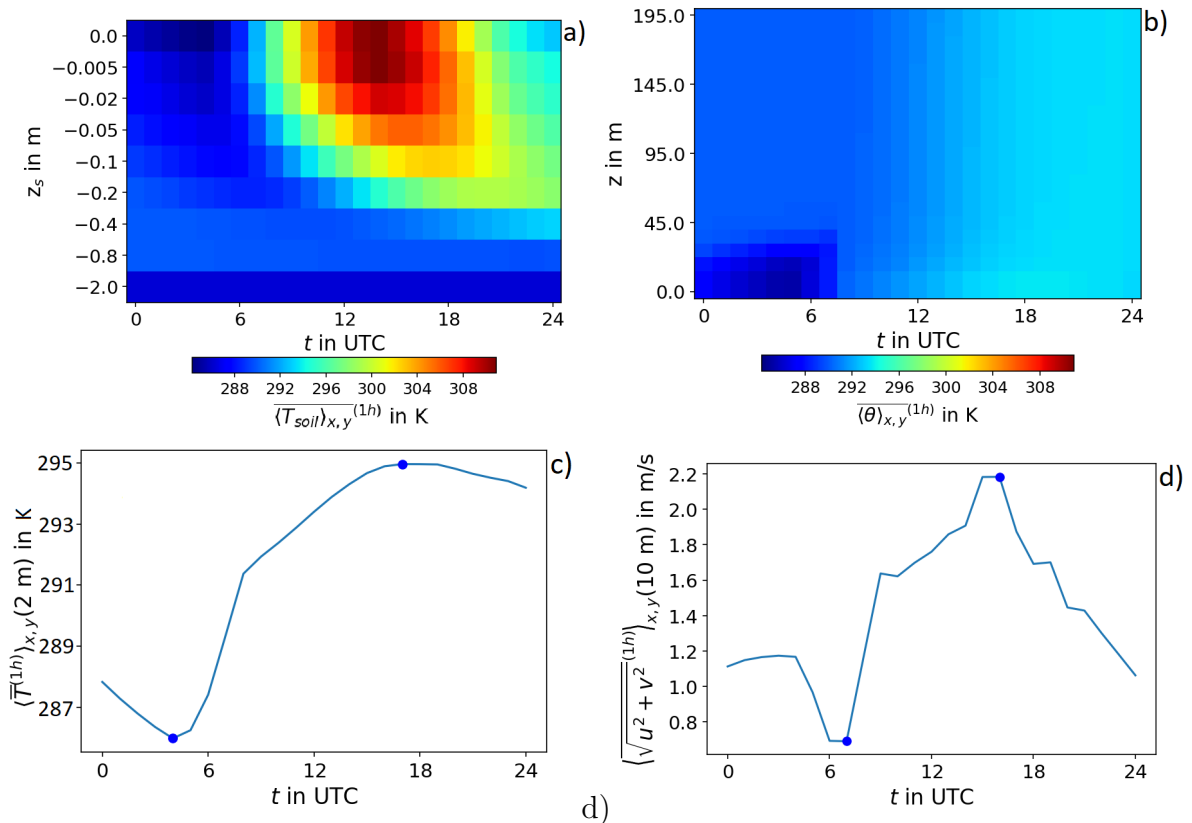


Figure 11: Paved surface: Typical diurnal cycles.

Time-height cross section of a) the soil temperature, b) the potential temperature in the atmosphere, Diurnal cycles of the horizontal mean of c) the 2 m air temperature and d) the 10 m wind speed with marked extrema.

Table 6: Overview of the parameter configuration for the pavement setup.

Parameter	Value	Description
Surface and pavement parameters		
C_p	$0.194 \cdot 10^7 \text{ Jm}^{-3}\text{K}^{-1}$	heat capacity of the pavement
z_0	0.04 m	roughness length for momentum
$z_{0,h}$	$0.4 \cdot 10^{-3}$ m	roughness length for temperature
Λ_p	$0.82 \text{ Wm}^{-1}\text{K}^{-1}$	thermal conductivity of the pavement
ϵ	0.97	surface emissivity
α	0.25	albedo
Soil parameters		
m_{res}	$0.01 \text{ m}^3\text{m}^{-3}$	residual volumetric soil moisture
$r_{\text{soil,min}}$	50 sm^{-1}	minimum soil resistance
T_{deep}	286.3 K	deep soil temperature
m_{fc}	$0.347 \text{ m}^3\text{m}^{-3}$	volumetric soil moisture at field capacity
m_{wilt}	$0.18167 \text{ m}^3\text{m}^{-3}$	volumetric soil moisture at permanent wilting point
α_{vG}	3.67	coefficient alpha in the soil hydraulic conductivity parameterization after van Genuchten
l_{vG}	-1.173	coefficient l in the soil hydraulic conductivity parameterization after van Genuchten
n_{vG}	1.28	coefficient n in the soil hydraulic conductivity parameterization after van Genuchten
γ_{sat}	$0.287 \cdot 10^{-5} \text{ ms}^{-1}$	hydraulic conductivity of the soil at saturation
m_{sat}	$0.52 \text{ m}^3\text{m}^{-3}$	volumetric soil moisture at saturation (porosity)
Initial soil profiles		
$T_{\text{soil,k}}$	290.0 K, 290.0 K, 290.0 K, 290.0 K, 290.0 K, 290.0 K, 290.0 K, 290.0 K, 286.3 K	soil temperature at depth level k, $k \in \{1, \dots, 8\}$
$m_{\text{soil,k}}$	-, -, -, -, -, -, $0.4 \text{ m}^3\text{m}^{-3}$, $0.4 \text{ m}^3\text{m}^{-3}$	soil moisture at depth level k, $k \in \{1, \dots, 8\}$

up due to solar radiation during day time, see Figure 11 a). Between 5 UTC and 7 UTC, the surface and 2 m air temperature increase is stronger for the vegetated case due to the bare soil fraction of 30 % which has a lower albedo and emissivity compared to the grass and the paved surface. However in the paved case, the temperatures reach higher values during day time due to missing evapotranspiration. However, unless they are irrigated, surfaces with grass behave like a sealed space on summer days due to missing shade [68, p. 29]. In the evening the radiation budget becomes negative and the temperature of the ground decreases. In the vegetated surface case, a stronger cooling effect at night occurs due to the thermal characteristics of the upper soil layer and the vegetation [68, p. 29]. As in the grassland case, during night time, an inversion arises, which is most pronounced at sunrise and thereafter destroyed again by the solar radiation, see Figure 11 b). The

paved surface heats up especially in the afternoon hours. An unstable atmospheric stratification develops. As the surface temperature influences the air temperature, diurnal changes occur in the 2 m air temperature visualized in Figure 11 c). A 2 m air temperature of maximal 295 K is simulated, which is low for a summer day over a sealed surface. One reason could be the relatively high albedo of 0.25. In the evening, a comparatively weak cooling occurs as on the ground, whose temperature influences the air temperature. Hence, as in the grassland case, there is no closed diurnal cycle and no stationarity, and under the given conditions, the temperatures would therefore continue to rise on the following day. The diurnal changes in temperature and atmospheric stratification influence the wind speed. During day time, the unstable stratification near the surface leads to an enhanced turbulent mixing. Momentum transport from higher layers to near surface layers leads to higher wind speeds in the low layers and lower wind speeds in higher levels (not shown here) than during night time, when the transport is suppressed by the stable stratification, so that the wind near the surface is decoupled from that at higher altitudes [29, pp. 228, 229]. The diurnal cycle of the 10 m wind is depicted in Figure 11 d). Compared to the grass land case, higher velocities occur both during the day and at night. This is due to the lower roughness length in the paved surface case.

12 Horizontally homogeneous plant canopy

The following two setups described in Chapters 12 and 13 are used to investigate the influence of parameters describing vegetation as obstacles on the stationary wind, which has no trend but a constant mean. No diurnal cycles of radiation and hence temperature and wind speed are assumed. Large scale structures like cellular patterns due to convection can therefore be neglected, allowing for smaller domain sizes.

12.1 The PALM model setup for the horizontally homogeneous plant canopy

For the study of the stationary flow within a model domain being covered by a horizontally homogeneous plant canopy, the PCM is used. The vertical profil of the LAD is calculated using the dimensionless parameters α_{LAD} and β_{LAD} , as well as the leaf area index (LAI). The template for the setup was the `test_canopy` example [49]. The model is initialized with a wind that is constant with height. The wind is set to 2.0 ms^{-1} and 0.0 ms^{-1} for the u and v component, respectively. The Coriolis force is disabled. Thermal stratification is assumed to be neutral. Neumann conditions are adopted for the horizontal wind components at the upper boundary, while the no-slip condition is set at the bottom. For the model domain 95, 47 and 30 grid points in x , y and z direction, respectively, and a grid spacing of 2 m in each direction are used. This choice is based on a grid sensitivity study using $\alpha_{\text{LAD}} = 11.0$, $\beta_{\text{LAD}} = 3.0$, LAI = 3.0 and a height of $h = 20$ m to describe the plant canopy. Some results are given in Figure 12, where vertical profiles are compared for different grid spacings. Figure 12 a) shows the horizontally averaged vertical profiles of the u component of the wind speed. Above the plant canopy, it is a logarithmic wind profile. Within the crown, a decreased wind speed is simulated, where the LAD takes the largest values, because the resolved vegetation leads to a sink term in the momentum equation [32, pp. 5838-5839]. Only small differences occur when the grid spacing is changed from 2 m to 1 m. In Figure 12 b) resolved and subgrid-scale momentum fluxes are compared. Except at the domain top and bottom, only a small amount of the momentum flux is parameterized within a subgrid-scale model. This fraction decreases with decreasing grid

spacing. Since a fraction $> 90\%$ of the momentum flux is resolved for a grid spacing of 2 m (Fig. 12 b) and the differences to the results obtained with 1 m grid spacing are small, 2 m are chosen for the grid spacing. The averaging time is 600.0 s and the simulation time

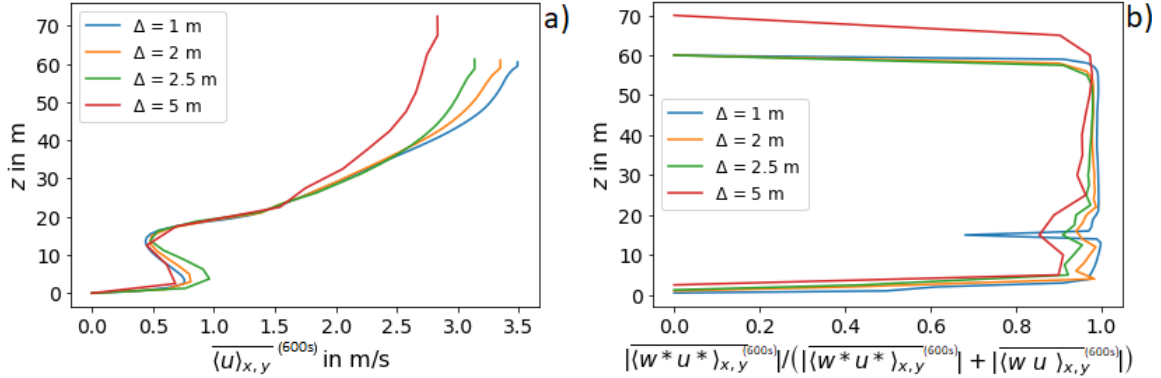


Figure 12: Grid sensitivity study for the horizontally homogeneous plant canopy setup. Vertical profiles of a) the horizontally averaged u component of the wind, b) the horizontally averaged ratios of the absolute values of the u component of the resolved vertical momentum flux to the sum of the absolute values of the u component of the subgrid-scale and the resolved vertical momentum flux.

is 3600.0 s, after which a stationary flow has already developed. Figure 13 shows the time series of the 3D domain averaged total kinetic energy E of the flow and the maximum of the u component of the velocity within the domain as an indication of stationarity, since after a spinup phase, the shown quantities show no trend. The first $t \approx 600$ s are a spinup phase, where artificial random perturbations are added to generate turbulence until it freely develops [50, p. 20] and the logarithmic wind profile develops. The latter results in higher values of u at higher levels. Hence, the time series of the maximum of the u component of the velocity shows an increase within the spinup phase.

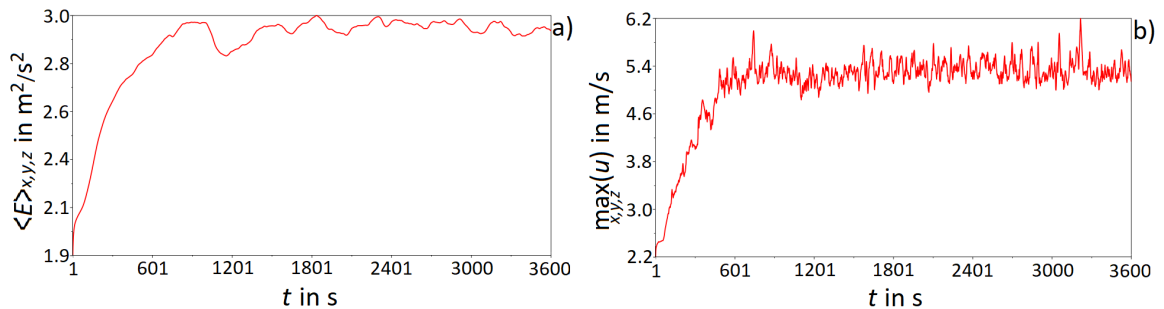


Figure 13: Check for stationarity of the model results

a) Time series of the 3D domain averaged total kinetic energy E of the flow, b) Time series of the maximum of the u component of the velocity.

12.2 PALM model results for the horizontally homogeneous plant canopy setup

Due to the horizontal homogeneity, profile data are considered. To ensure that the model results correspond to common knowledge, and to show the influence of the parameters

used for the calculation of the LAD on the LAD and the corresponding wind profile, mean wind profiles are calculated for various LADs as in [40]. The vertical profiles of the LAD and the corresponding mean wind given in Figure 14 result from different values of α_{LAD} or LAI, respectively, for a canopy height h of 20 m and $\beta_{\text{LAD}} = 3.0$ as it was investigated in [40]. The Figures 14 a) and c) on the left hand side show the LAD used in the simulation. It is modified by the shape parameter α_{LAD} and the LAI, respectively. On the right hand side, Figures 14 b) and d) show the resulting mean wind profiles which depend on the LAD profile. A logarithmic wind profile develops above the plant canopy with a lower wind speed dependent on the magnitude of the LAD value in the corresponding height within the plant canopy, since the resolved vegetation leads to a sink term in the momentum equation [32, pp. 5838-5839]. The results coincide with the findings from [40] and [28], where also a logarithmic wind profile with a wind speed reduction within the crown was simulated.

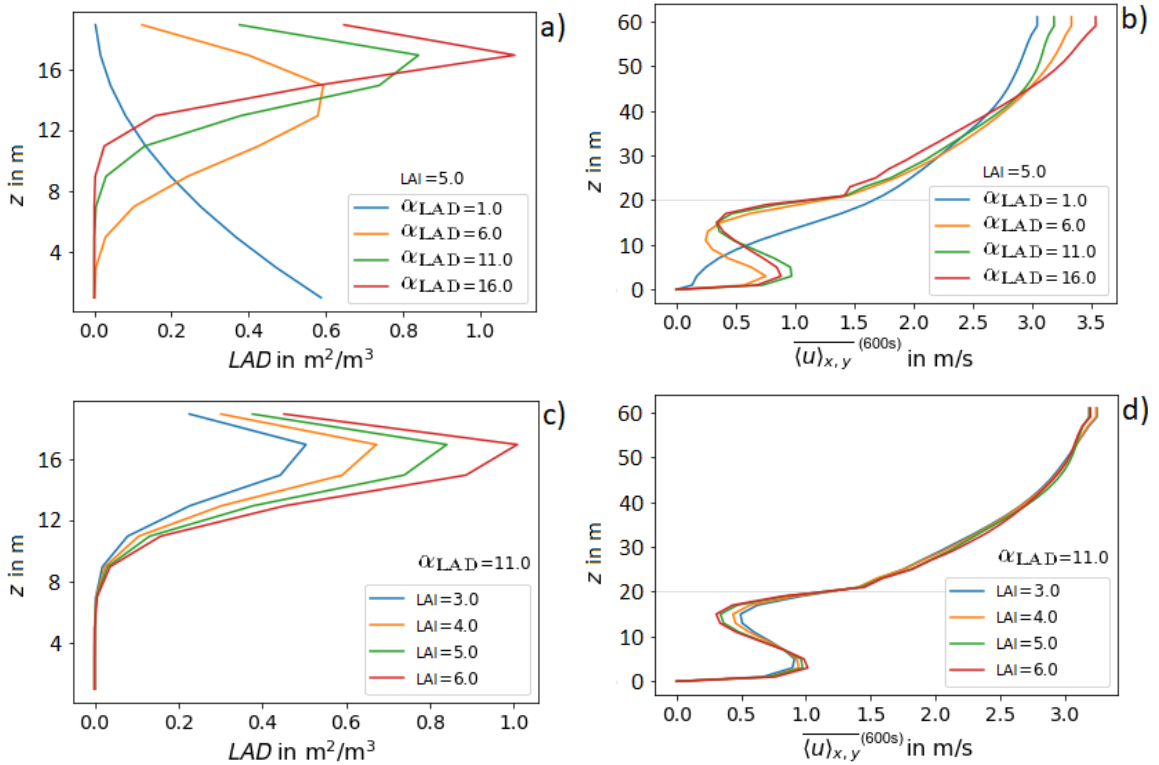


Figure 14: Vertical profiles of the LAD (left) and the u component of the wind (right) for different values of α_{LAD} (top) and LAI (bottom) for the horizontally homogeneous plant canopy.

13 A domain including a single tree

As a further approach for the investigation of the influence of the parameters describing 3D vegetation, the flow around one single tree is considered. This chapter presents the used model setup and typical results for the flow around a individual idealized tree in order to compare them to common knowledge as it is presented in [27] and [28], where among others the flow around single trees was investigated.

13.1 The PALM model setup for the domain including a single tree

The PCM is applied and one tree is placed in the domain with horizontal extent of 140 m \times 40 m. The vertical extent of 32 m is used as it is more than twice the height of the highest tree height of 14.4 m that will be used for the application of the Morris method in Chapter 15.4. Hence, under the condition of a neutral stratification, it is high enough to prevent speed up effects between tree and domain top as can be seen in Figure 19. The results of this chapter are obtained for a tree positioned at ($x=80$ m, $y=20$ m). The creation of the LAD and BAD representing the single tree was based on the script to generate plant canopy that was provided with the PALM revision 21.10-rc.1. In this script, parameters concerning the tree properties as tree height h , crown diameter d_c , crown shape, trunk diameter d_t and ratio of crown height h_c and crown diameter d_c for standard trees of different shapes are given, as well as LAD and BAD calculation methods as mentioned in Chapter 3.2. The values assigned to the tree parameters in this chapter are roughly oriented to those for the default tree defined in the script. They are listed in Table 7. Cyclic boundary conditions are used in y direction, but non-cyclic boundary

Table 7: Overview of the parameter configuration for the single tree setup.

Parameter	Value	Description
h	11 m	tree height
h_c/d_c	1.2	ratio of crown height and crown diameter
LAI	3.6 m ² m ⁻²	leaf area index
d_c	4.5 m	crown diameter
d_t	0.5 m	trunk diameter
c_d	0.57	canopy drag coefficient

conditions along the x axis are used in order to prevent the disturbances generated by the obstacle to enter the domain again. Instead, the turbulence-recycling method (see Chapter 3.7) is used to realize a turbulent inflow. With the cyclic-fill method, 3D data from a precursor run, i.e. an initial turbulence field, are read by the main run. The wind is initialized with a component of 2 ms⁻¹ in x direction and a component of 0.1 ms⁻¹ in y -direction. A neutrally stratified atmosphere and a roughness length of 0.1 m are assumed. A simulation time of 10800 s is used after which stationarity has been reached. The averaging interval is chosen to be 1 h which is longer than for the horizontally homogeneous plant canopy, because the investigation of stationarity showed a larger variation around the mean which should be captured by a longer averaging time. The numbers of grid points in x , y and z direction are 140, 40 and 32, respectively, using a grid spacing of 1 m in each direction. This choice is based on a grid sensitivity study, where the results for the different grid spacings of 0.5 m, 1 m and 2 m are compared in order to find the best compromise between computational effort and resolution. Figure 15 shows the horizontally averaged vertical profiles of the ratios of the absolute values of the u component of the resolved vertical momentum flux to the sum of the absolute values of the u component of the subgrid-scale and the resolved vertical momentum flux, which enables a comparison of the portion of the vertical momentum flux that is directly resolved and the portion that is parameterized within a subgrid-scale model. The portion of the resolved vertical momentum flux increases with decreasing grid spacing. The figure indicates a good resolution beginning at a grid spacing of 1 m, with a minimal improvement for $\Delta = 0.5$ m. Hence, the grid spacing of $\Delta = 1$ m was chosen in order to obtain a good resolution and meanwhile to reduce the computational resources.

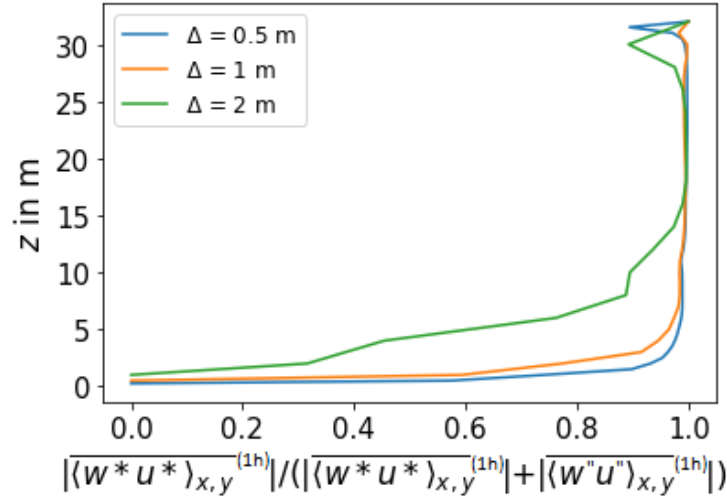


Figure 15: Ratio of the u component of the resolved vertical momentum flux to the u component of the total vertical momentum flux for the grid sensitivity study for the single tree setup.

13.2 PALM model results for the domain including a single tree

The Figures 16 to 19 show the LAD and BAD used for the exemplary model run and the resulting flow around the individual idealized tree. Horizontal cross-sections at the height of the center of the tree crown (Figures 16 and 17) as well as vertical cross-sections along the middle of the tree at $y = 20$ m (Figures 18 and 19) are shown. Figures 17 a) and 19 a) show that the wind speed is reduced in front of the tree, however, the flow enters the crown, since it is permeable. The mentioned figures furthermore show a wake region with reduced wind speed behind the tree. Also visible in Figures 17 b) and 19 b) is that the wind must avoid the tree crown inducing a flow around the tree sideways and an over- and an underflow. Therefore, on the sides and near the top of the tree an increased wind speed occurs. These results match the current knowledge presented in [27] and [28], except for the absence of a recirculation zone behind the tree. However concerning the wake structure, a dependency on the superimposed wind and the permeability of the tree is given [27, p. 4]. Figure 17 shows that the flow is not completely symmetrical which is due to the initial wind.

14 An urban area

In order to perform the sensitivity analysis for the input parameters for an urban area, an adequate model setup is required and the model results need to be checked for reasonableness. This chapter presents the used model setup and model results for an idealized urban area.

14.1 Creation of the PALM model setup

In the following, the considered urban area setup which is used in order to study is described. A building resolving simulation is going to be performed. Therefore, self nesting and hence a coarser-gridded parent and finer-gridded child domain are used. An energy-balance model applied to natural and building surfaces. Therefore, the USM, the LSM and the indoor model are used. The RTM is applied to account for shading

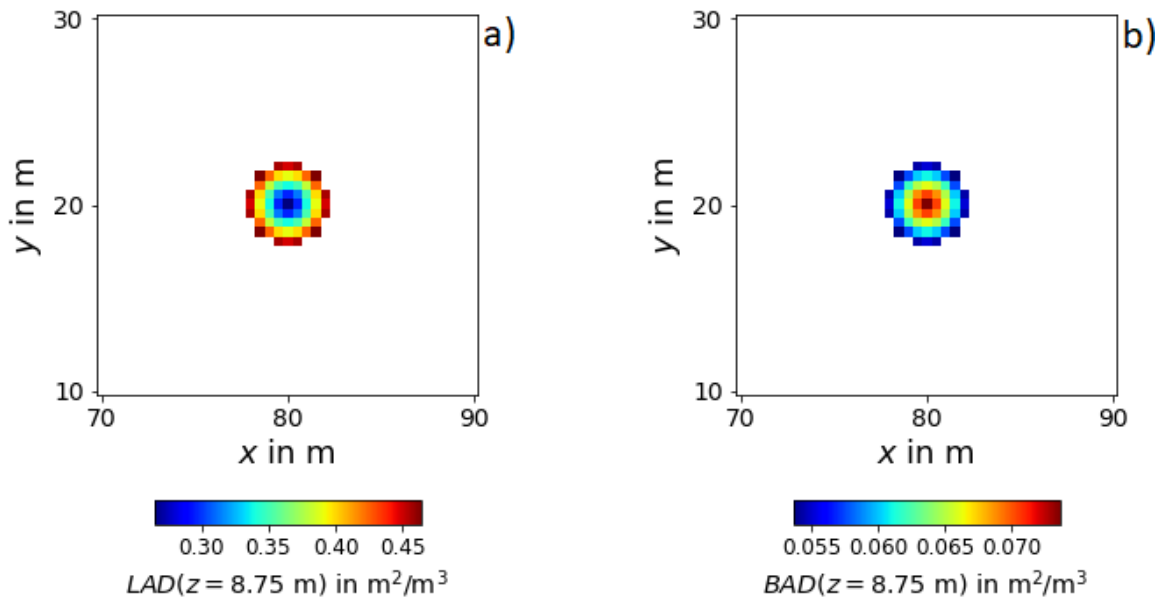


Figure 16: Horizontal cross-sections of a) LAD and b) BAD at the height of the crown center at 8.75 m.

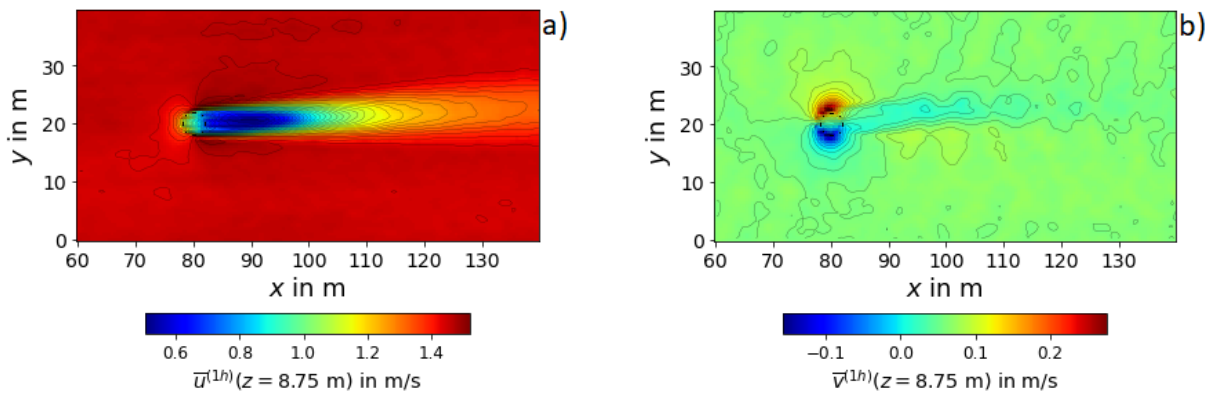


Figure 17: Stationary horizontal distribution of the hourly averaged a) u- and b) v-component of the wind at the height of the crown center at 8.75 m.

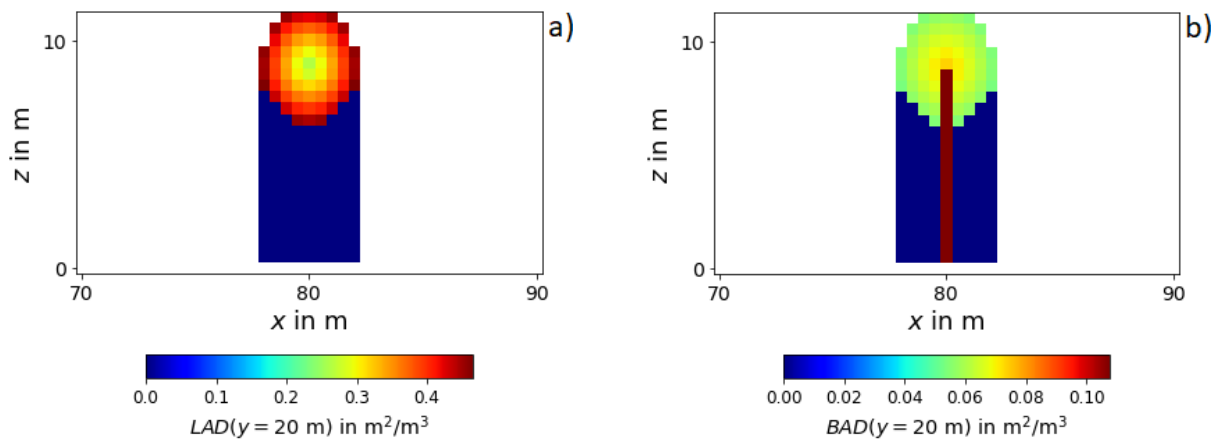


Figure 18: Vertical cross-sections of a) LAD and b) BAD at $y=20$ m through the middle of the tree.

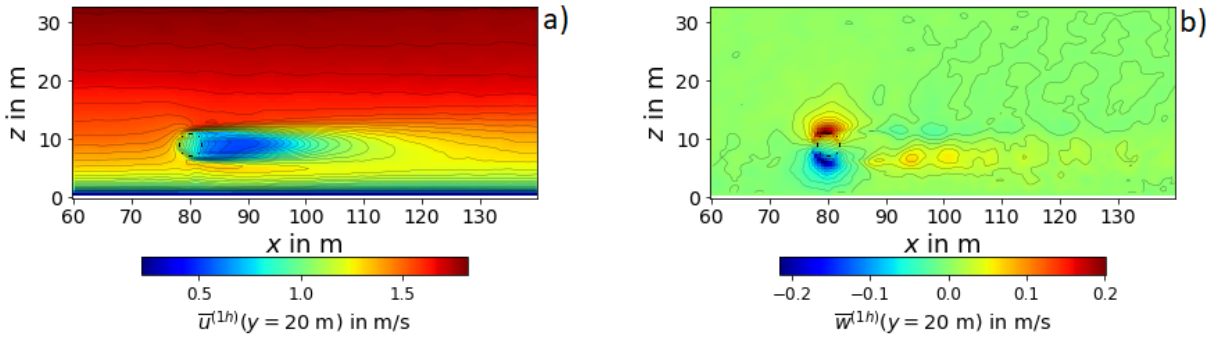


Figure 19: Stationary vertical distribution of the hourly averaged a) u - and b) w -component of the wind at $y=20$ m through the middle of the tree.

and reflections and the PCM is used to account for evapotranspiration and tree shading. The meteorological quantities are simulated for a summer day. The study is focusing on autochthonous weather conditions which are characterized by a strong daytime insolation, weak winds and a stable nocturnal stratification, since the urban climatic characteristics are particularly pronounced, then, and a strong heat stress is possible in the following daytime hours [38, pp. 2, 3, 8], [26, p. 2]. The simulated time period starts on June 21 at 21 UTC and the following 27 hours are simulated. The simulated day of interest will hence be June 22nd. The domain of interest has dimensions of $480 \text{ m} \times 480 \text{ m} \times 120 \text{ m}$. It is visualized in Figure 20 and contains 41.9 % paved surface, 36.6 % vegetated surface, 21.4 % building covered surface, 0.1 % water covered surface ($8 \text{ m} \cdot 8 \text{ m}$ for each water surfaces) and 348 trees. A specification of the vegetation, pavement and water types can be found in Table 8. These surfaces are distributed on a park, an open place, street canyons with different aspect ratios, i.e. building height to canyon width ratios, and tree arrangements, a court yard and areas with single houses with gardens. The buildings are assumed to be flat-roofed. Figure 20 furthermore shows the locations of sub-areas with uniform properties as well as specific extraction sites M_i , $i \in \{1, \dots, 6\}$ for local vertical profile data, which will be used for the evaluation of the sensitivity study. The sub-areas are referred to as ‘street canyons’, ‘open place’, ‘court yard’, ‘park’ and ‘single houses’. The domain is assigned a latitude of 55° . In order to resolve the most important turbulent structures between the buildings of the urban area, a grid spacing in the order of 1 m is typically required [33, pp. 3185, 3186]. Since the largest turbulent eddies are of size of the boundary layer height, which in Europe can reach up to 2.5 km in summertime, and the horizontal model domain size must be at least 2–3 times the boundary layer height in order to resolve the turbulent transport of these eddies [4, p. 4447], the total model domain is of the size $5760 \text{ m} \times 5760 \text{ m} \times 3494 \text{ m}$. Due to the limited computational resources, for the total domain, a larger grid spacing is applied than for the domain of interest. The corresponding setup is created by repeating the domain of interest in the horizontal plane with an y -offset of 300 m in order to prevent infinite street canyons and applying nesting for one main domain as it was done in [4]. The described setup is visualized in Figure 21. The nesting is applied for the red domain. This way, the small turbulent structures on the street scale and the large ones on the ABL scale can be captured simultaneously with an adequate need of computational resources [33, p. 3186]. The whole setup is shown in Figure 21. Grid sensitivity studies are required for the definition of the grid spacings for the coarser-gridded parent and finer-gridded child domain. In a first process, the grid size of the child domain is studied for a neutrally stratified atmosphere. Input data describing buildings and trees is created for the domain under consideration and provided to PALM. The steady-state wind profile from a one-dimensional (1D) version of PALM, where the

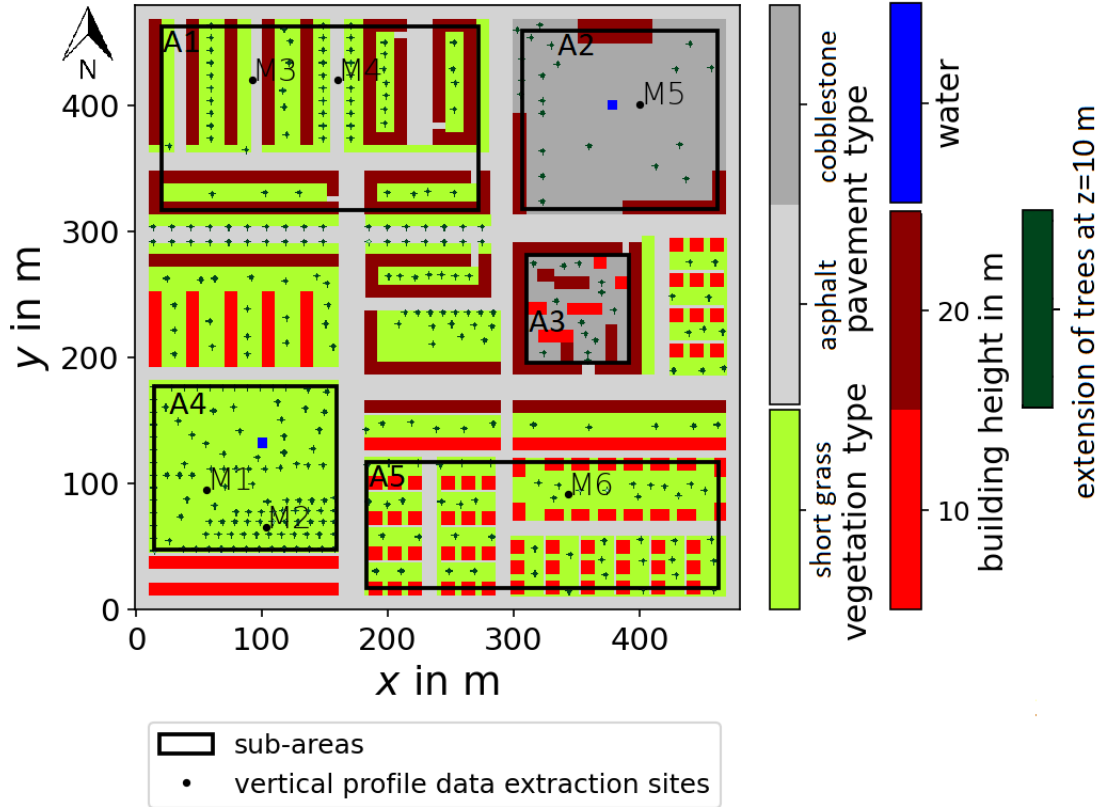


Figure 20: Visualization of the considered urban domain. M_i , $i \in \{1, \dots, 6\}$ mark locations for local vertical profile data extraction. Sub-areas indicated by boxes from top left to bottom right are A1 ‘street canyons’, A2 ‘open place’, A3 ‘court yard’, A4 ‘park’, A5 ‘single houses’.

wind is initialized with 2 ms^{-1} and 0 ms^{-1} for the u and v component, respectively, is used as initialization of the 3D model. This is a useful approach in case of neutral stratification, where inertial oscillations can persist for several days. The application of the 1D model is computationally less expensive and a stationary state of the wind profiles can be provided much faster in the 3D model [41, pp. 2525, 2534, 2535]. Along the x - and the y -direction, cyclic boundary conditions are used and the left/right boundary is shifted by 300 m along y . This method is chosen in order to prevent from infinite street canyons and to alleviate the persistence of streak-like structures due to the cyclic boundary conditions. For the bottom and the top boundary condition of the horizontal velocity components, Dirichlet and Neumann conditions are assumed, respectively. The model is run until stationarity is reached and the results for different grid spacings are compared. Figure 22 visualizes model results after 2 hours of the grid sensitivity analysis runs for the child domain. For different grid spacings, in Figure 22 a) the horizontally averaged vertical profiles of the u component of the velocity is shown and Figure 22 b) shows vertical profiles of the fraction of the turbulent momentum flux that is directly resolved. The building heights in the area are 10 m and 20 m, respectively, which is reflected in velocity increases above these heights in the vertical profile and in a decrease of the resolved vertical turbulent momentum flux in these heights. Only slight differences between the results obtained with a grid spacing of 0.5 m and 1 m and a high amount of turbulent momentum flux that is directly resolved, i.e. a good resolution, for these grid spacings are noticed. Additionally, Figure 22 c) shows the CDFs of the 10 m horizontal wind speed for the different grid

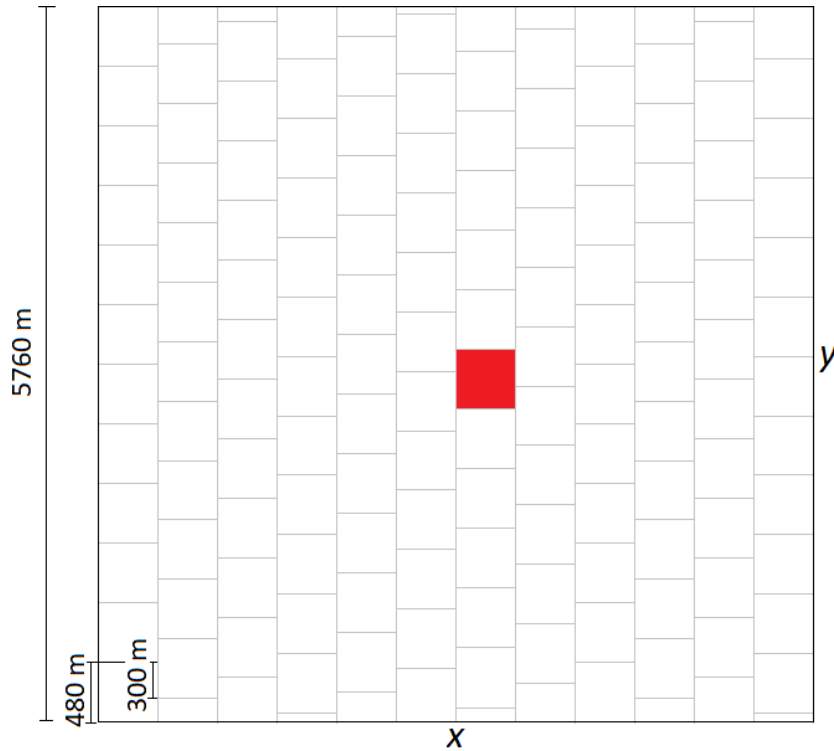


Figure 21: Visualization of the total urban domain. For the domain of interest (red) nesting is applied.

spacings in order to investigate the distribution of the 10 m wind speed in the considered urban area. This approach is based on [26] where it was used to find an appropriate setup for a ventilation study of Hong Kong using PALM. A Kolmogorov–Smirnov test is applied in order to compare two distribution functions. Therefore, a maximum distance between the two considered distribution functions is calculated. The smaller this value is, the smaller is the difference between the distribution of the considered quantities. For a bin width of 0.01 ms^{-1} , the maximum distance between the CDFs for grid spacings of 0.5 m and 1 m is 0.0143, the one for grid spacings of 1 m and 2 m is 0.0653 and the one for grid spacings of 2 m and 3 m is 0.0569. The difference between the distribution of the wind speeds resulting from grid spacings of 0.5 m and 1 m are smallest. Hence, the results for the grid spacings of 0.5 m and 1 m differ only slightly from each other. A grid spacing of 0.5 m does not yield significantly different results compared to a grid spacing of 1 m but would significantly increase the computational demands, which is why a grid spacing of 1 m in all directions is selected for the child domain.

The smallest turbulent structures are expected in a stably stratified atmosphere. It is known that a grid spacing of 0.5 m - 2 m is required for LES of the urban boundary layer with narrow streets or for simulations of the stable boundary layer [41, p. 2515]. Hence, the grid sensitivity study for the child domain is repeated, initializing an inversion up to a height of 50 m. The wind is set to 1.0 ms^{-1} and 0.0 ms^{-1} for the u and v component, respectively, and the simulation time is 10800 s. Also in the stable case, the results for the grid spacings of 0.5 m and 1 m differ only slightly from each other, which can be seen in the Appendix in Figure 70. This confirms the choice of the grid spacing of 1 m in all directions for the child domain and the further use of a neutrally stratified atmosphere for the following grid sensitivity study for the parent domain.

Additionally, the grid size of the parent domain is studied and therefore varied for the neutral stratified case while the grid spacing of the child domain is fixed at 1 m.

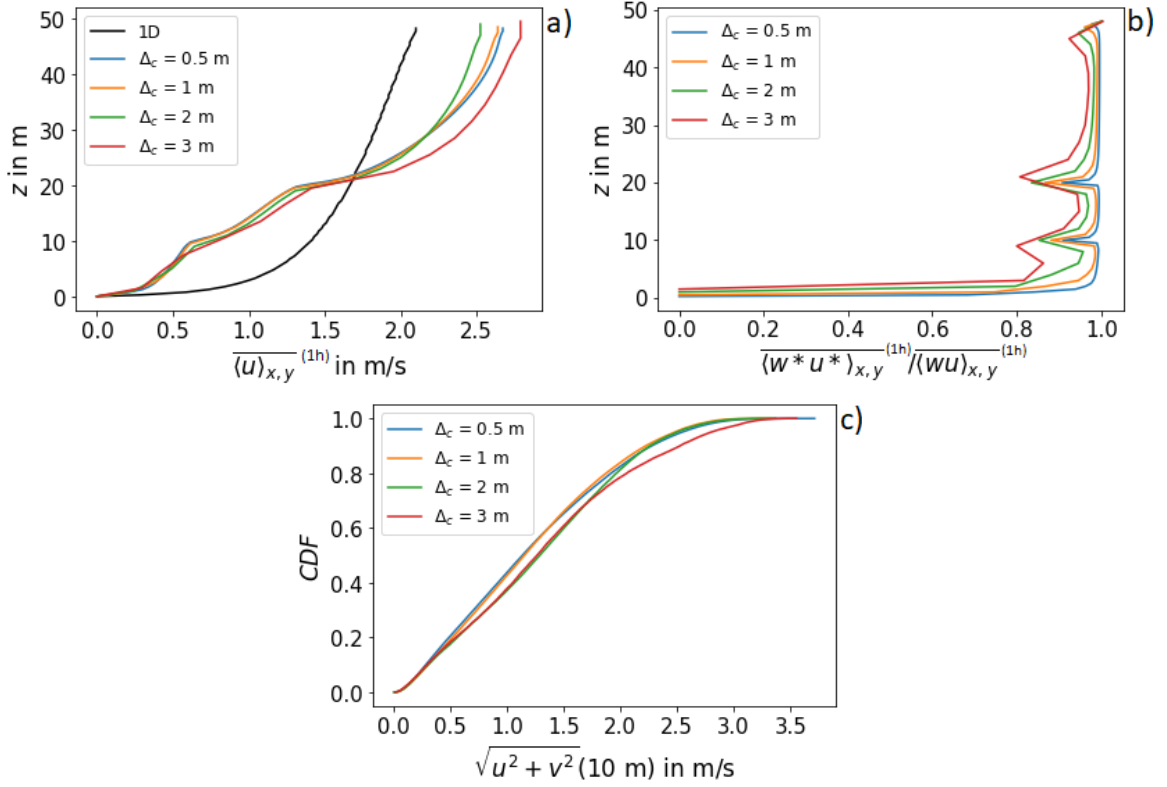


Figure 22: Grid sensitivity study for the urban child domain with neutral stratification. Horizontally averaged vertical profiles of a) the u component of the wind and b) the ratio of the u component of the resolved and the total vertical turbulent momentum flux, c) CDF of the horizontal 10 m wind speed.

For the parent model, x and y direction, cyclic boundary conditions are used. For the bottom and the top boundary condition of the horizontal velocity components, Dirichlet and Neumann conditions are assumed, respectively. One-way nesting is used. The results of the grid sensitivity analysis for the parent domain are presented in Figure 23. Figure 23 a) shows the horizontally averaged vertical profiles of the u component of the velocity within the child domain for the different grid spacings of the parent domain. In Figure 23 b), vertical profiles of the fraction of the turbulent momentum flux that is directly resolved, are visible. As in the grid sensitivity analysis for the child domain, the building heights of 10 m and 20 m influence the profiles. The resolution is better using a grid spacing of 5 m for the parent domain than using a grid spacing of 10 m, however, the vertical wind profiles obtained using these grid spacings do not show large differences. The same can be seen in Figure 23 c), where the CDFs of the horizontal 10 m wind in the child domain are shown for the different grid spacings for the parent domain. A Kolmogorov–Smirnov test is applied in order to compare the distribution functions. For a bin width of 0.01 ms^{-1} , the maximum distance between the CDFs for grid spacings of 5 m and 10 m is 0.0268 and thus only 30.6 % of the one for grid spacings of 10 m and 20 m which is 0.0875. The results for the grid spacings of 5 m and 10 m differ only slightly from each other and a grid spacing of 5 m would significantly increase the computational demands, which is why a grid size of 10 m is chosen for the parent domain even though the resolution is not as good as in the 5 m grid spacing case.

In order to simulate diurnal cycles, in addition to the PCM, the clear-sky radiation scheme of the radiation model, the LSM and the USM are also used. Date and time at model start are set to June 21, 21 UTC and the following 27 hours are simulated. The

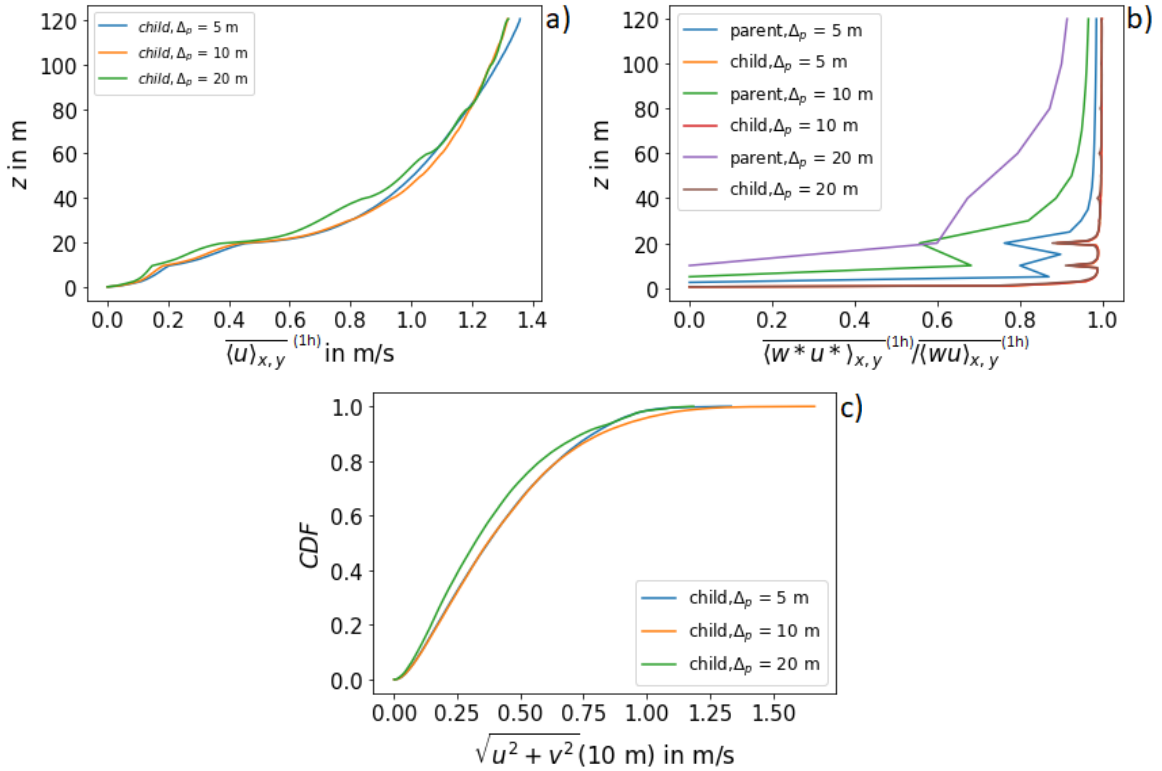


Figure 23: Grid sensitivity study for the urban parent domain with neutral stratification. Horizontally averaged vertical profiles of a) the u component of the wind and b) the ratio of the u component of the resolved and the total vertical turbulent momentum flux, c) CDF of the horizontal 10 m wind speed.

stratification is not assumed to be neutral and therefore the prognostic equation for the has to be solved. According to the grid sensitivity analysis, the grid spacing of the child domain is 1 m, the one of the parent domain is 10 m, where the vertical grid spacing is stretched by a factor of 1.08 in a height of 800 m until a maximum of 50 m is reached to reduce the computational time. As in the grid sensitivity analysis, one-way nesting is used. For the parent model, cyclic boundary conditions are used. For the bottom and the top boundary condition of the horizontal velocity components and the water vapor to total water mixing ratio, Dirichlet and Neumann conditions are assumed, respectively. At the bottom, the Dirichlet boundary condition is used for the potential temperature and the value of the potential temperature gradient at the top is calculated from the initial temperature profile. The initialization is done with a u component of the wind of 1.5 ms^{-1} and a potential temperature of 290.0 K with a vertical gradient of $0.65 \text{ K}/100 \text{ m}$ and thus a capping inversion from 1750 m to 2716 m heights, and constant vales above the inversion. Rayleigh damping was used at the top boundary in order to prevent the reflection of gravity waves.

14.2 PALM model results for the urban area setup

This chapter presents the model results of an exemplary model run using the setup for the idealizes urban area presented in Chapter 14.1. This model run will be used as the reference run for the sensitivity analysis presented in Chapter 17. Hence, for this reference simulation, the default values prescribed to the surface types and trees in PALM are used. The parameter values are listed in Table 8. The data from each simulation that is used for

Table 8: Parameter values used in the reference simulation.

parameter	value
vegetation type:	short grass:
$r_{c,\min}$	110.0 sm^{-1}
LAI	2 m^2m^{-2}
c_{veg}	1.0
z_0	0.03 m
$z_{0,h}$	$0.3 \cdot 10^{-4}$ m
Λ	10.0 $\text{Wm}^{-2}\text{K}^{-1}$
C_0	0 $\text{Jm}^{-2}\text{K}^{-1}$
ϵ	0.95
α	0.25
pavement type:	asphalt; inner courtyard, open place: cobblestone:
z_0	0.05 m (asphalt), 0.01 m (cobblestone)
$z_{0,h}$	$0.5 \cdot 10^{-3}$ m (asphalt), $0.1 \cdot 10^{-3}$ m (cobblestone)
α	0.08 (asphalt), 0.3 (cobblestone)
ϵ	0.95 (asphalt), 0.94 (cobblestone)
Λ_p	0.82 $\text{Wm}^{-1}\text{K}^{-1}$ (asphalt), 2.19 $\text{Wm}^{-1}\text{K}^{-1}$ (cobblestone)
C_p	$0.194 \cdot 10^7$ $\text{Jm}^{-3}\text{K}^{-1}$ (asphalt), $0.225 \cdot 10^7$ $\text{Jm}^{-3}\text{K}^{-1}$ (cobblestone)
T_{water}	283 K (default)
soil type:	medium-fine (default):
α_{vG}	0.83
l_{vG}	-0.588
n_{vG}	1.25
γ_{sat}	$0.26 \cdot 10^{-6}$ ms^{-1}
m_{sat}	0.43 m^3m^{-3}
m_{fc}	0.383 m^3m^{-3}
m_{wilt}	0.133 m^3m^{-3}
m_{res}	0.01 m^3m^{-3}
$r_{\text{soil},\min}$	50 sm^{-1}
T_{deep}	287 K
trees:	default-type:
shape	spherical/elliptical
h	12 m
h_c/d_c	1.0
d_c	4.0 m
LAI	3.0
d_t	0.35 m
c_d	0.47
building type:	Residential, built before 1950 (default):
α_{wall}	0.07
ϵ_{wall}	0.93
Λ_{wall}	23.0 $\text{Wm}^{-2}\text{K}^{-1}$
C_{wall}	20000.0 $\text{Jm}^{-2}\text{K}^{-1}$
window fraction	0.18
α_{window}	0.12
ϵ_{window}	0.91
Λ_{window}	23.0 $\text{Wm}^{-2}\text{K}^{-1}$
C_{window}	20000.0 $\text{Jm}^{-2}\text{K}^{-1}$
green fraction	0.0

the analysis includes horizontal cross sections of the model results as well as vertical cross sections along street canyons. They are shown for the reference run in Figures 24 and 25 which highlight the heterogeneity of meteorological properties in urban environments including a network of street canyons of different widths and orientations, buildings of varying dimensions, openings and parks. Figure 24 visualizes vertical cross sections at $y=415$ m and $x \in [10 \text{ m}, 190 \text{ m}]$ of the air temperature, as well as the u component and

the w component of the wind at 3 UTC and 15 UTC. The cross section is oriented in east-west direction. At 3 UTC, the air temperature is lower between the buildings, see Figure 24 a). The lowest temperatures occur directly above the ground, especially over vegetated surfaces, as the ground cools down at night with a stronger cooling effect at vegetated surfaces, see Chapter 11. The building walls have a higher thermal conductivity than the soil surface and the minimal indoor temperature is about 20°C as can be seen in Figure 50, which might lead to a smaller decrease of the surface temperature and hence the air temperature around the buildings than at the ground surface. Slightly increased temperatures appear at the west-oriented walls of the buildings, correlating with the downward flow, that transports warmer air from higher layers. At 15 UTC (24 b)), the temperature is higher than at 3 UTC due to incoming short-wave radiation and a better mixing is present, corresponding to the higher u and w components of the wind than at night, see Figures 24 d) and f). Figure 24 b) shows that the temperature within the street canyons is higher than above the buildings due to the warm surfaces, which were heated by solar radiation. The highest temperatures occur at west walls above paved surfaces, as it is the case at the second and fourth building counted from the left. For the third and sixth building this effect is reduced by shading from a tree. Due to the combined effect of wall and soil surface the temperature increase occurs especially at lower levels. Furthermore, subfigures c) and e) show that there is only a weak rotor in the canyon at night, and a stronger one during the day (d) and f)). This may be due to the low wind speed, so that at night there is almost no wind between the buildings and no pronounced rotor forms. Figure 25 visualizes horizontal cross sections at specific heights. The air temperature is shown at a terrain-following height of 2 m, i.e. at 2 m over ground, which can be either ground surface (also in case of trees) or roof surface. The horizontal wind speed is given at a terrain following height of 10 m. The surface temperature also follows the terrain. UTCI is provided for the horizontal level, which is the closest possible to the 1.1 m level. With the used grid, this is 1.5 m. The Figures 25 a) and c) again show the stronger night-time cooling of and above vegetated surfaces compared to paved surfaces and a corresponding temperature distribution. Below trees, the cooling of the air is less pronounced and the temperatures are higher than at open spaces due to the modified radiation fluxes compared to open places. This is particularly visible in Figure 25 a) in the park, which has its highest tree density in the south-east part. Trees emit an amount of longwave radiation that increases the small amount of incoming longwave radiation from the clear sky the trees obscure [19, p. 123]. At 3 UTC, the roof surfaces are cold compared to other surfaces, however, the air temperature in a height of 2 m above the roof warm compared to the air temperature 2 m above the ground surface, which might be due to the inversion visible in Figure 24 a). During day (subfigure b)), the surfaces heat up according to the surface properties. Trees lead to shadowing and reduced surface temperatures below them. The surface warms the air during the day to 294 K to 296 K at 15 UTC dependent on the surface temperature. The highest air temperatures of 296 K to 299 K appear at south and west walls directly at the building, and thus, where the air is additionally heated by warm building wall surfaces. Furthermore, as mentioned in Chapter 10.2, during the day, enhanced turbulent mixing because of the unstable stratification near the surface leads to a momentum transport from higher layers to near surface layers and thus to higher wind speeds in the low layers than during night (see Figures 24 e) and f)). Roughness elements like trees and buildings decrease the wind speed. It takes its lowest values within courtyards, higher values where the flow is mostly undisturbed like at the open place, and its highest values above the buildings. Due to the small wind speed at night, spatial differences in the 10 m wind speed above the ground surface due to roughness elements are barely visible. Beside the

described meteorological quantities, also UTCI as a measure of heat stress is calculated at 1.5 m height. Table 23 in the appendix gives the categorization of the UTCI ranges in terms of thermal stress. Figure 25 h) shows that at 15 UTC, moderate heat stress occurs in the non shadowed areas.

In addition to the cross sections, vertical mean profiles at representative locations shown in Figure 20 are extracted. A set of temperature and wind profiles for the reference run is given in Figure 26. At 3 UTC, the air temperature increases with height and takes its lowest value at the lowest height level at every location, see subfigure a). At the vegetated surface with a low tree density (M1), the strongest cooling appears, which was already described above. The highest temperatures appear at M3 within a street canyon without trees, where the air is additionally heated by the wall surfaces. The horizontal wind speed within the urban canopy layer at 3 UTC given in Figure 26 b) is low due to the stable stratification. At 9 UTC, surfaces are heated by solar radiation and in turn heat the air. Due to the lack of shading, the surface and near surface air temperature at the paved open place take the largest values. At locations M3 and M4, the warming effects of the 20 m height east walls on the air temperature up to building height are visible, while at low levels, shading within the street canyons results in a smaller temperature increase. At M4, the temperatures are lower due to shading from trees and a larger distance from the building walls. The deconstruction of the stable stratification leads to higher wind speeds than at 3 UTC. These aspects are visible in subfigures c) and d). Figure 26 e) shows that at 15 UTC, the heating process due to solar radiation has continued. Up to the corresponding building height of 20 m, location M3 has the highest temperatures, again, while in the park at M1 and M2, the lowest temperatures occur. The increased tree density at M2 leads to lower temperatures than at M1 near the surface due to shading and to higher temperatures at the crown. The wind speed given in subfigure f) is further increased. The profiles at the locations M1, M2, M5 and M6 illustrate the influence of obstacles on the wind: At M6, buildings and trees of a height of 10 m reduce the wind speed up to this height, while at M5, the wind speed in the lower levels is comparably high because less obstacles influence the wind. Within the street canyons at M3 and M4, the vortex structure is again visible, indicated by higher wind speeds at the bottom and the top of the street canyon and a lower one at the vortex center. At 21 UTC, the surfaces are not heated by solar radiation anymore. An inversion arises in the lower levels except at location M5 at the paved place, where the surface had reached the highest temperatures during day and cools down slower. Hence, also the wind speed decreases again. These aspects are visible in subfigures g) and h).

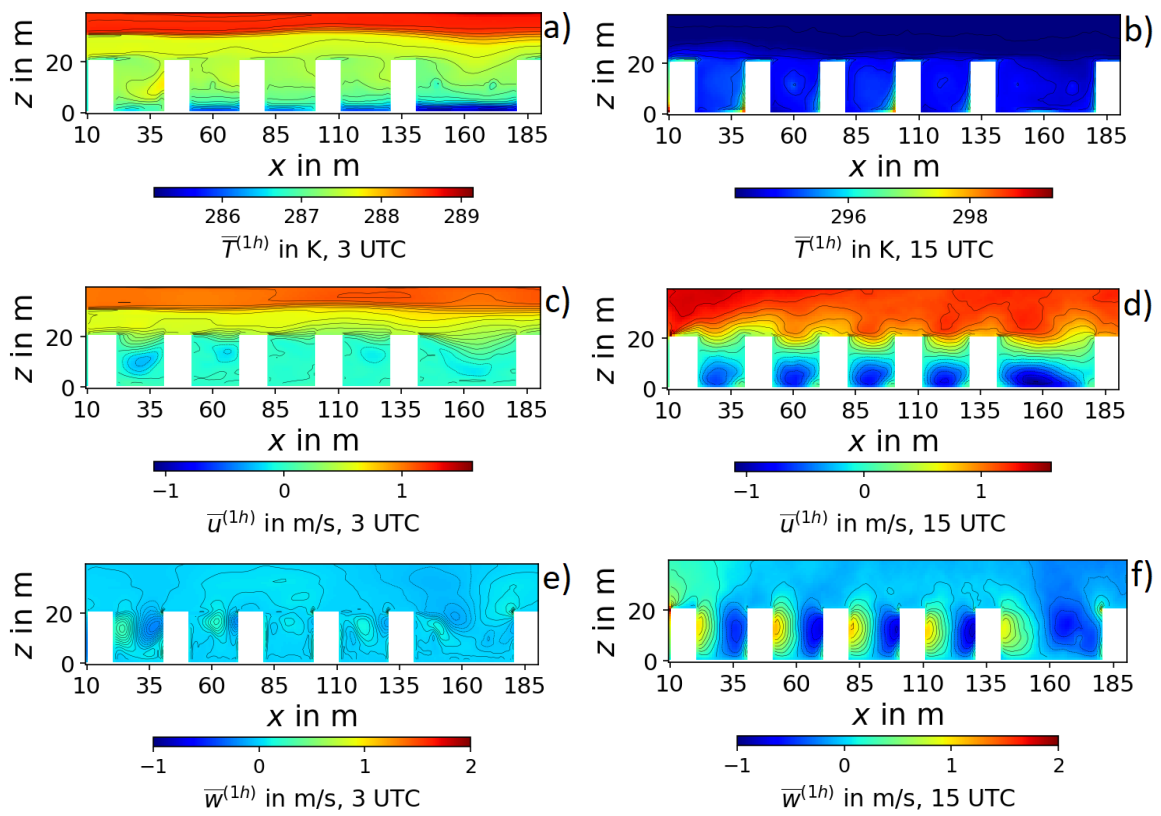


Figure 24: Model results for the urban area along a vertical cross section at $y=415$ m.

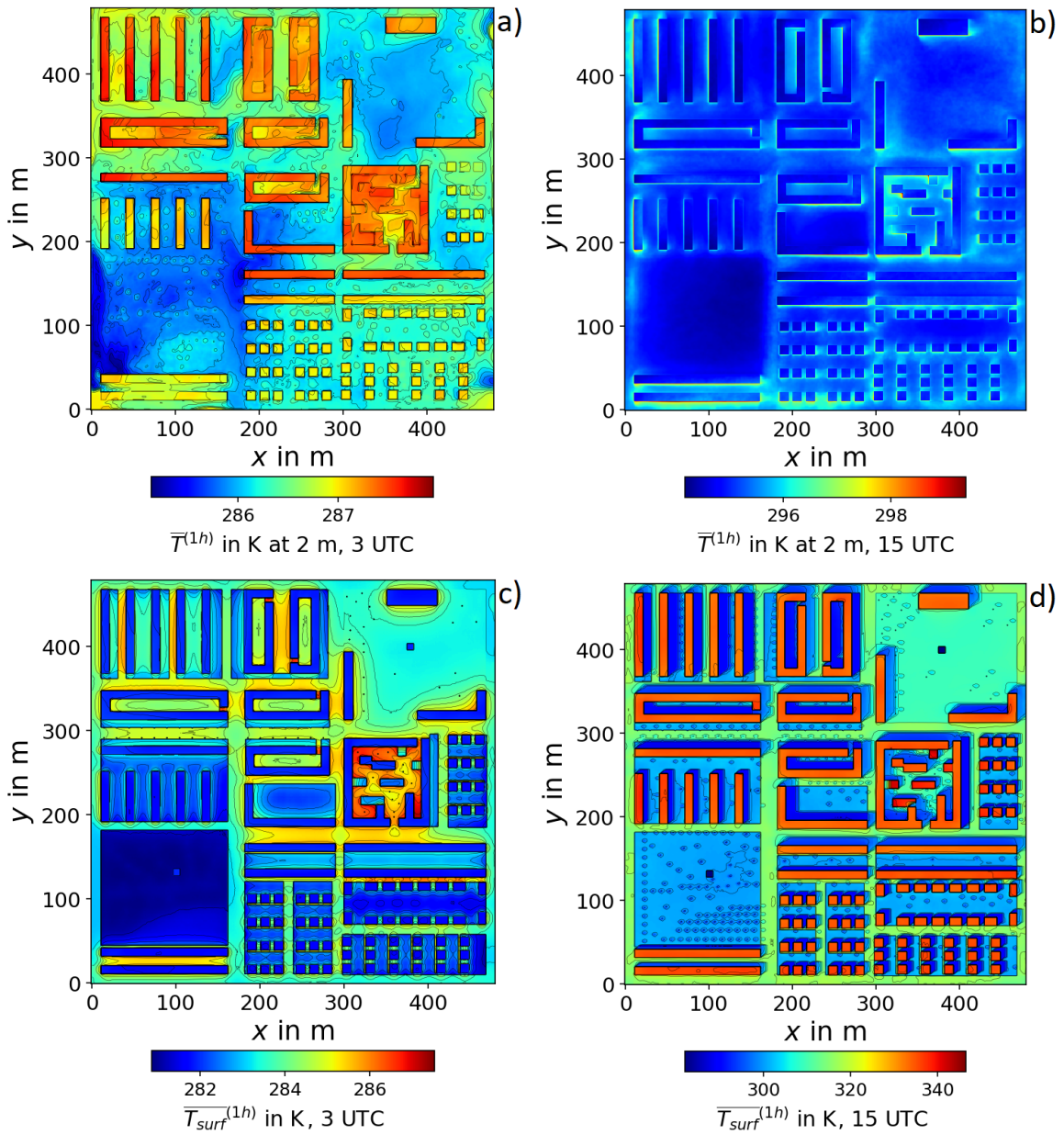


Figure 25: Horizontal cross sections for hourly averaged model results for the urban area. The output is terrain following except for g), h).

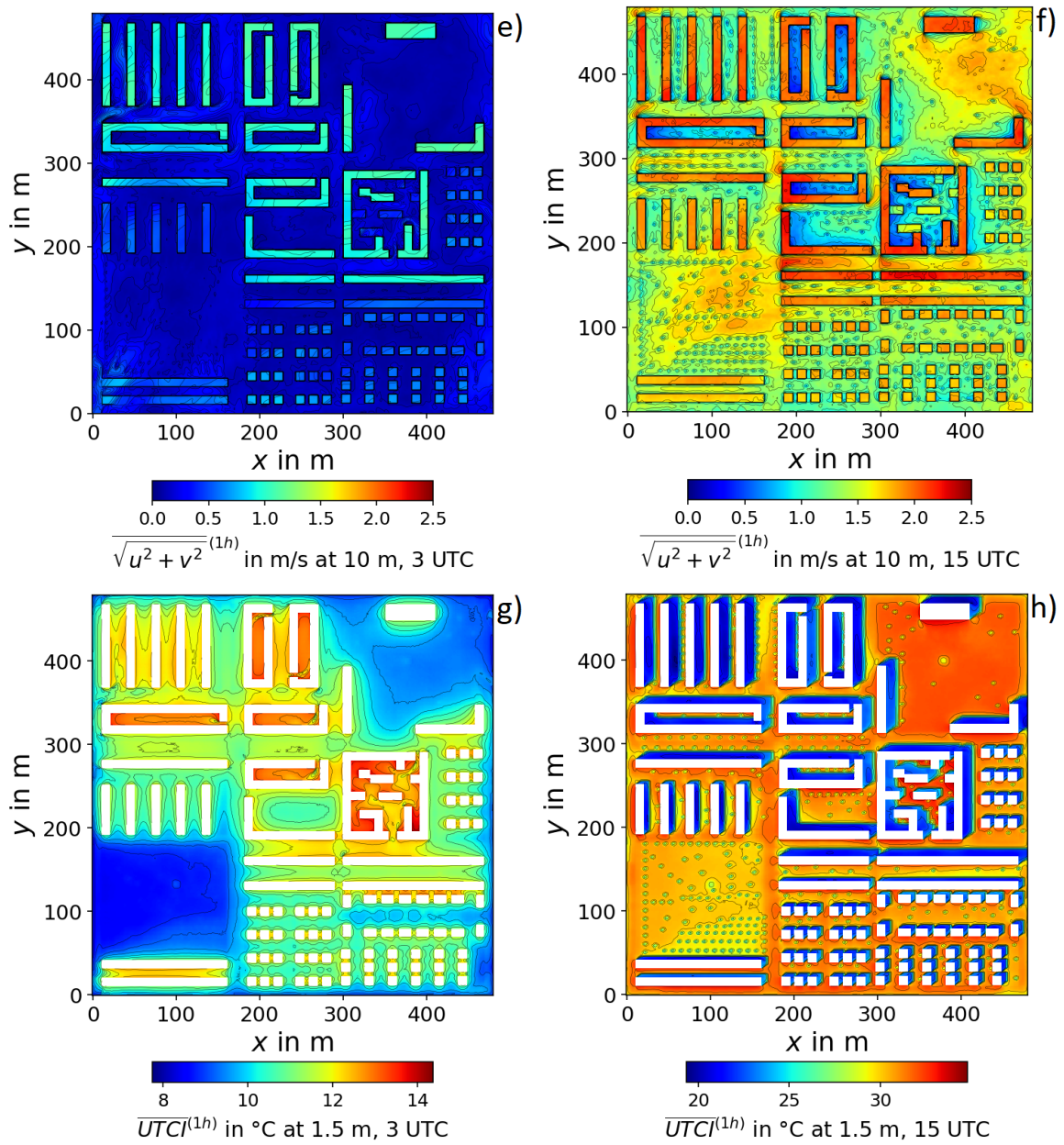


Figure 25: Continued: Horizontal cross sections for hourly averaged model results for the urban area. The output is terrain following except for g), h).

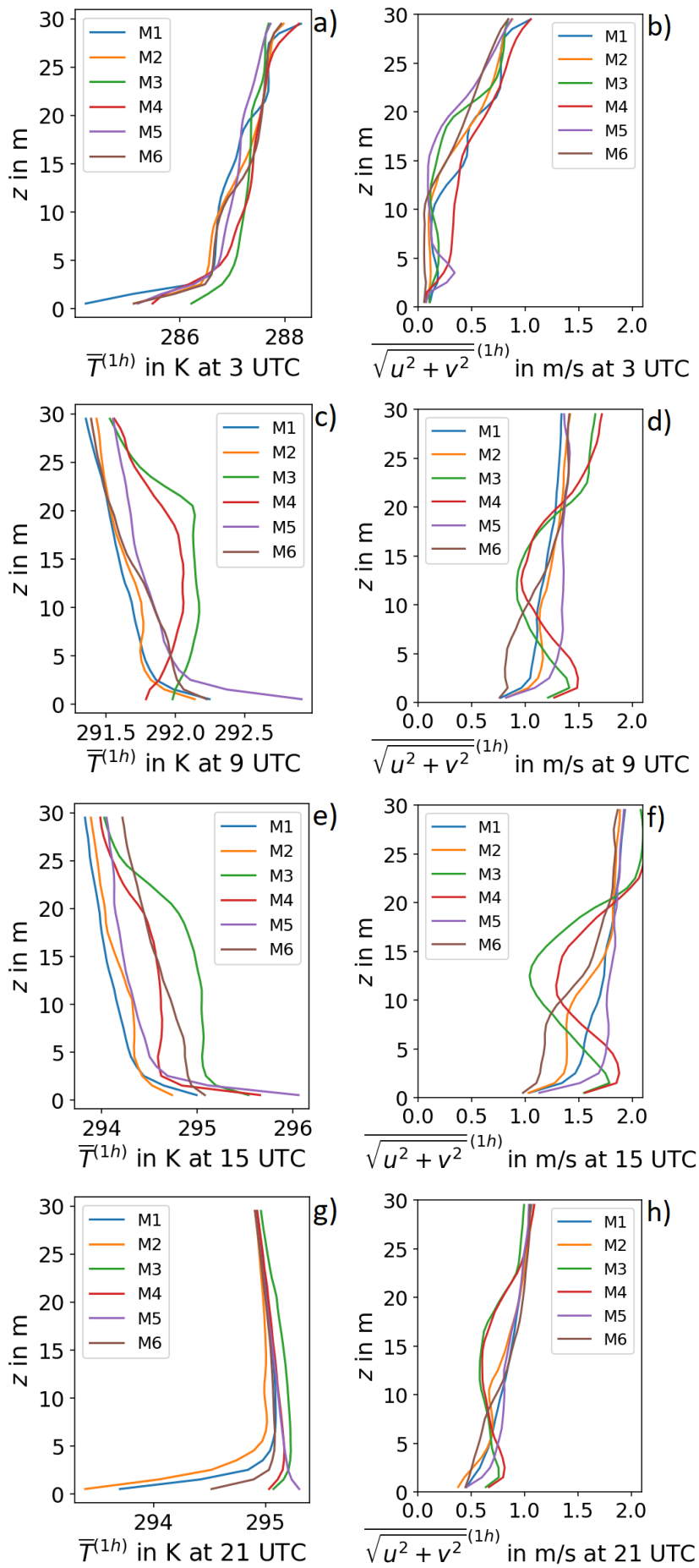


Figure 26: Hourly averaged local vertical profiles extracted at the representative locations M_i , $i \in \{1, \dots, 6\}$.

Part IV

Application of the analysis methods

In the following chapters, the sensitivity analysis method introduced in Chapter 8 is performed. First, the Morris method will be applied to the results of the PALM simulations presented in the Chapters 10-13 in order to identify the input parameters that are most relevant for the considered model results. An uncertainty analysis based on Latin hypercube samples can then be carried out with a reduced number of parameters. For the already computationally intensive urban setup treated in Chapter 14, the investigation of a large parameter space would be necessary, which is why the application of the Morris method would exceed the computing time capacity and is thus not feasible. For this reason, a parameter or a parameter group represented by a type is varied, while the other parameter (groups) are kept constant. If the variation of a type has a major influence on the output, the studies performed with the Morris method can be used to infer the parameters responsible for the relevance, since the parameters determined within a type are examined via Morris method.

15 Application of the Morris method

In this chapter, the Morris method will be applied to the results of the various PALM simulations presented in Chapters 10-13. The aim is to identify the input parameters that are most relevant for the considered model outputs by performing a statistical evaluation of elementary effects whose values correspond to the variation of the output when the input varies from the minimum to the maximum of its parameter range. In PALM, a classification is made via predefined parameter lists for the building and each land surface type [32]. Imprecise classifications of the parameter types defining the input parameters within PALM are considered for the determination of the input parameter bandwidths. Since the parameters determined within a parameter type are examined via Morris method, this chapter presents the basics of a method for conducting a study of the importance of individual parameters without covering the entire spectrum of possible ranges and parameters. This chapter is thus to be seen as preliminary work for the determination of important parameters in the urban setup.

The following methods have been implemented for the application of the Morris method:

- a method to construct r trajectories in the input parameter space according to Chapter 6.3,
- a program to generate the respective PALM input file given a parameter sample,
- a shell script with a loop over all samples to generate the PALM input file and to start PALM model run and
- programs for determining and visualizing the Morris sensitivity measures.

15.1 Grassland

The simulation setup presented in section 10 is used in this chapter. In order to determine the most influential input parameters among the ones given in Table 9 for the grassland setup, the Morris method is performed. The bandwidths of the parameters are also

given in Table 9. As described above, they are defined using the parameters defined within the scope of two parameter types in each case, for the vegetation type and the soil type. Sixteen parameters are varied and ten trajectories are used. According to Chapter 6.3, $10 \cdot (16 + 1) = 170$ samples are required. The considered outputs of a model

Table 9: Input parameters and their bandwidths for the grassland setup.

Parameter	Name	Bandwidth	Description
LAI	x_1	$(1 - 2) \text{ m}^2\text{m}^{-2}$	leaf area index
c_{veg}	x_2	$0.7 - 1.0$ *	vegetation coverage
z_0	x_3	$(0.03 - 0.47) \text{ m}$ *	roughness length for momentum
$z_{0,h}$	x_4	$(0.30 \cdot 10^{-4} - 0.47 \cdot 10^{-2}) \text{ m}$ *	roughness length for temperature
λ_s	x_5	$(9 - 11) \text{ Wm}^{-2}\text{K}^{-1}$	heat conductivity between atmosphere and soil in case of stable stratification
λ_u	x_6	$(9 - 11) \text{ Wm}^{-2}\text{K}^{-1}$	heat conductivity between atmosphere and soil in case of unstable stratification
$r_{c,\text{min}}$	x_7	$(100 - 110) \text{ sm}^{-1}$ *	minimum canopy resistance
α	x_8	$0.18 - 0.25$ *	albedo
ϵ	x_9	$0.95 - 0.97$ *	surface emissivity
α_{vG}	x_{10}	$0.83 - 3.67$ **	coefficient alpha in the soil hydraulic conductivity parameterization after van Genuchten
l_{vG}	x_{11}	$-2.342 - -0.588$ **	coefficient l in the soil hydraulic conductivity parameterization after van Genuchten
n_{vG}	x_{12}	$1.10 - 1.28$ **	coefficient n in the soil hydraulic conductivity parameterization after van Genuchten
γ_{sat}	x_{13}	$(0.26 \cdot 10^{-6} - 2.87 \cdot 10^{-6}) \text{ ms}^{-1}$ **	hydraulic conductivity of the soil at saturation
m_{sat}	x_{14}	$(0.430 - 0.520) \text{ m}^3\text{m}^{-3}$ **	volumetric soil moisture at saturation (porosity)
m_{fc}	x_{15}	$(0.347 - 0.448) \text{ m}^3\text{m}^{-3}$ **	volumetric soil moisture at field capacity
m_{wilt}	x_{16}	$(0.133 - 0.279) \text{ m}^3\text{m}^{-3}$ **	volumetric soil moisture at permanent wilting point

*: The bandwidths meet the values set in PALM for short and tall grass.

** : The bandwidths meet the values set in PALM for medium to fine soil granularity.

run are time series for the horizontally averaged 10 m wind speed ($y_{k=1}(t)$), 2 m air temperature ($y_{k=2}(t)$), surface temperature ($y_{k=3}(t)$), relative humidity (RH) ($y_{k=4}(t)$), UTCI ($y_{k=5}(t)$) and depth d dependent soil temperature ($y_{k=6}(t, d)$) and soil moisture ($y_{k=7}(t, d)$), evaluated in every depth level. Additionally, the daily means are considered for the following horizontally averaged quantities: the 10 m wind speed ($y_{j=1}$), the 2 m air temperature ($y_{j=2}$), the surface temperature ($y_{j=3}$), the RH ($y_{j=4}$) and the UTCI ($y_{j=5}$). UTCI is provided for the horizontal level, which is the closest possible to the 1.1 m level. With the used grid, this is 5 m. The same height level is used for the RH.

As mentioned in Chapter 6.6, the relevance of the input parameters on these model results can be assessed using the standard deviation of the output σ_{out} . For the outputs

$y_k(t)$, Figure 27 shows the diurnal cycles of the mean μ , the standard deviation σ and the extrema within the samples for each time step, taking into account the results of all samples which are indicated by transparent lines. Figure 27 a) shows the described quantities

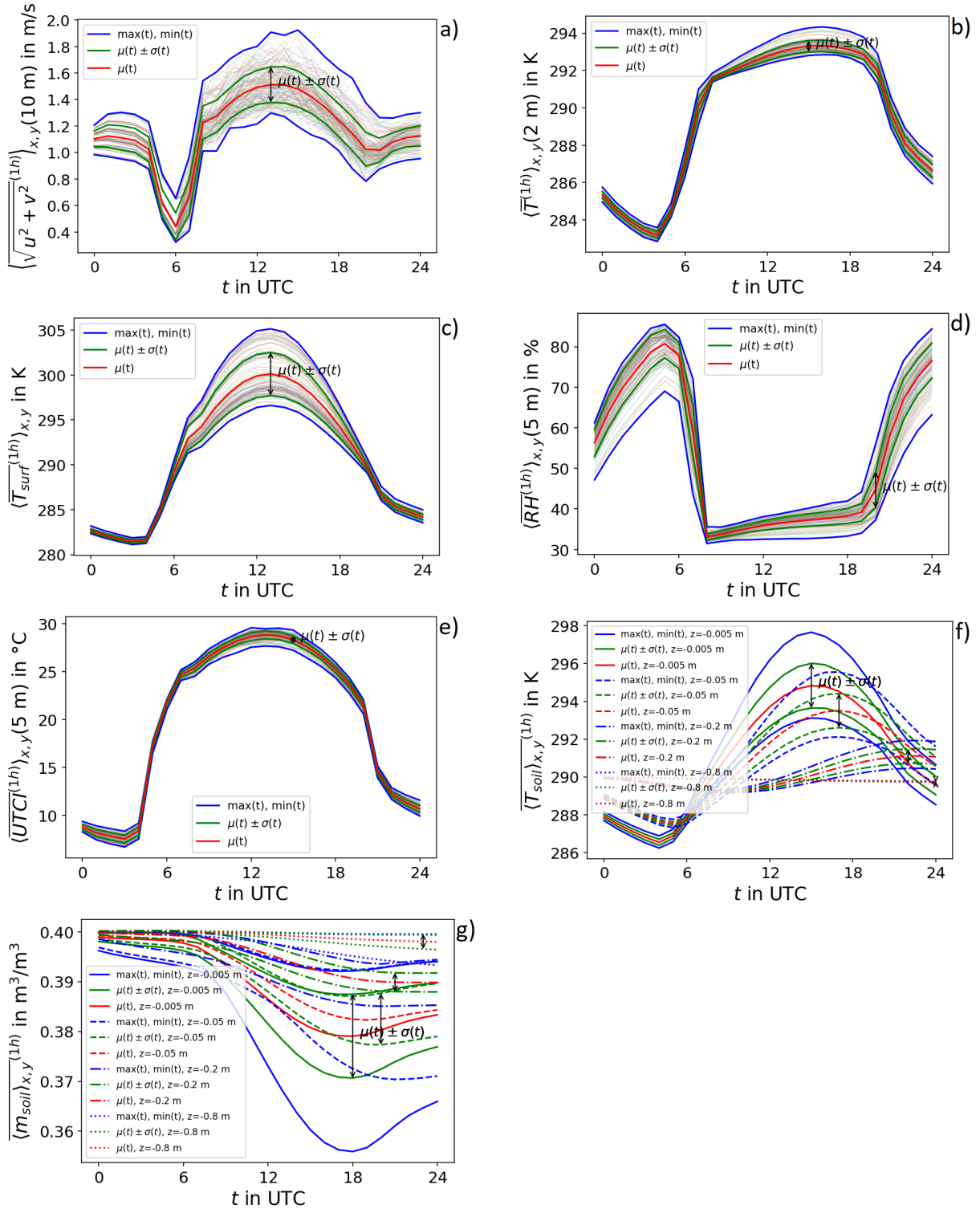


Figure 27: Diurnal cycles of mean μ , standard deviation σ and extrema within the samples of the considered outputs $y_k(t)$ for the grassland case. The diurnal cycles for the individual samples are indicated by transparent lines.

for the horizontal wind in a height of 10 m. The diurnal cycle including the minimum in the early morning and the maximum in the afternoon has already been discussed in Chapter 10.2. Variations throughout the day can be seen within the samples. Figure 27

b) shows the quantities for the 2 m air temperature, the diurnal variation of which is also explained in more detail in Chapter 10.2. The standard variation takes its largest values in the late afternoon. Subfigure c) shows the diurnal cycle of the mean μ , standard deviation σ and extrema within the samples of the surface temperature. The surface temperature depends on the amount of solar radiation that warms up the ground. Hence, during day, especially around noon, the largest values occur, accompanied by the largest standard deviations. The RH, see subfigure d), strongly correlates with the air temperature. In the early morning, when the air temperature is low, a high RH is simulated. A low RH, on the other hand, occurs during the day. Variations throughout the day occur within the samples, with larger values during the night. Subfigure e) shows the quantities for the UTCI. It also shows a diurnal variation with maximum at noon. Increased standard variations occur during night and around noon. Subfigures f) and g) show the depth dependent soil quantities. The properties of the soil temperature are strongly correlated with those of the surface temperature. With increasing depth, the maximum of the soil temperature and the standard deviation occur later. The soil moisture takes its minimum in the evening after the evaporation that occurred during daytime. The variations of the soil moisture are also largest in the evening in the uppermost layer. Figures 27 f) and g) furthermore show no closed diurnal cycle and no stationarity. Dependent on the parameter combination (see the large spread at the end of the day), the temperature will increase and the soil moisture will decrease on the following day in case of same conditions.

The Morris sensitivity measures μ , μ^* and σ are determined for the considered outputs in order to investigate which input parameters are responsible for the described variations. As mentioned in Chapter 6.6, for scalar outputs, the measures can be visualized via bar and Morris plots. In the Morris plots, the importance of the input parameters is indicated by different colors. The colors along the μ^* and the σ axes represent the factor a in the expression $a \cdot \sigma_{\text{out},j}$. Areas with $\mu^*, \sigma \geq a \cdot \sigma_{\text{out},j}$ are blue for $a = 0$, green for $a = 1$ and yellow for $a = 2$. Exemplary results are visualized in Figure 28. Furthermore, the sensitivity measures for the considered scalar output quantities are summarized in Figure 29 which shows a table for the measures $\mu_{i,j}^*$ and $\sigma_{i,j}$. The color of each cell is also chosen according to $\mu_{i,j}^*$ or $\sigma_{i,j} \geq a \cdot \sigma_{\text{out},j}$ and is blue for $a = 0$, green for $a = 1$, yellow for $a = 2$ and orange for $a = 3$. As described in Chapter 6.4, the measure μ^* can be used to sort the input parameters according to their influence on the considered model results. Taking the measures for the diurnal and horizontally averaged UTCI shown in Figure 28 e) and f) as an example, increased values occur for the roughness length for momentum (x_3) indicating an increased influence of this parameter on the output. This effect can be further specified using the fact that the value of an elementary effect for the i -th input parameter corresponds to the variation of the output when the input varies from the minimum to the maximum of its parameter range. Figure 29 gives the mean of the absolutes of these output variations, i.e. the value of the sensitivity measure $\mu_{3,5}^* = 0.76$ K, when the surface roughness length z_0 (x_3) is varied between 0.03 m and 0.47 m (see Table 9). Thus, if one cannot distinguish between short and tall grass due to a lack of information, the uncertainty in the diurnal and horizontally averaged UTCI due to the surface roughness length z_0 (x_3) is 0.76 K. The positive value of $\mu_{3,5}$ shown in Figure 28 e) means that an increased roughness length for momentum leads to an increased UTCI in contrast to the wind speed, where an increased roughness length leads to a decrease (28 a). A decrease of the wind speed thus coincides with an increase of the UTCI, i.e. the effect of wind chill is visible: Wind speed has a direct influence on the heat balance of the human body. Increased wind speed leads to increased cooling in the skin area when the skin temperature is higher than the air temperature [14].

Additionally, the sensitivity measures were checked for convergence indicating that

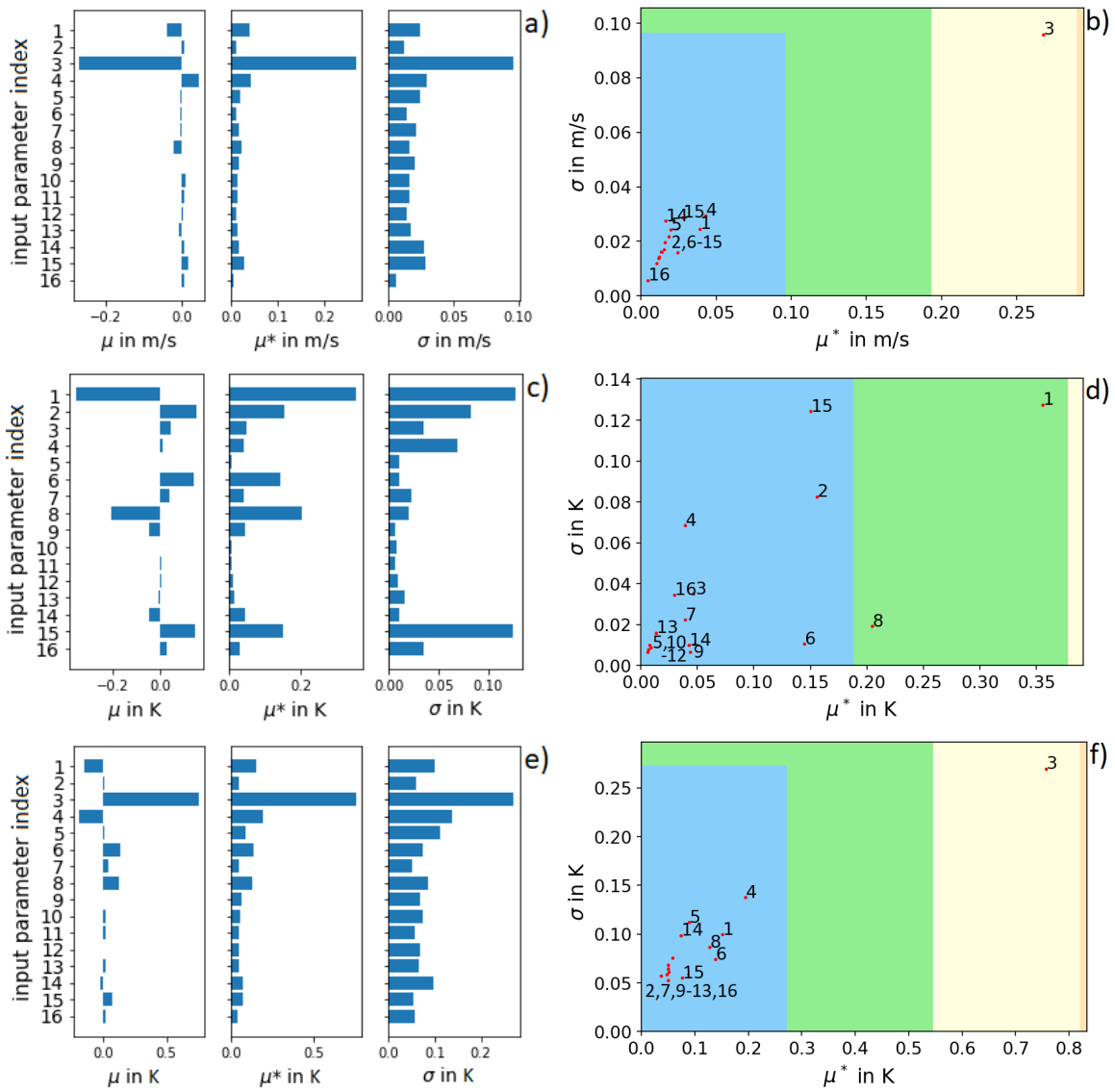


Figure 28: Visualization of the Morris sensitivity measures μ , μ^* and σ regarding exemplary diurnal and horizontally averaged quantities for the grassland case.

a) 10 m wind speed $y_{j=1}$, bar plot, b) Morris plot, c) 2 m air temperature $y_{j=2}$, bar plot, d) Morris plot, e) UTCI $y_{j=5}$, bar plot, f) Morris plot.

the chosen number of trajectories is sufficient. For this purpose, the measures are plotted as a function of the number of trajectories used and it is checked whether they tend to a limit value and the variations are sufficiently reduced. Figure 30 exemplary shows that convergence is given for the sensitivity measures $\mu_{i,2}^*$. The same yields for the other output quantities, which is not shown here.

In order to determine the diurnal cycles of the sensitivity measures for the time dependent outputs $y_k(t)$, single measures are calculated for each time step as described in Chapter 6.5. Exemplary visualizations of the results are given in Figures 31 and 32. Further visualizations of Morris measures treating other model results can be found in the appendix in Figures 59-68. The figures show the time and depth dependent output standard deviation, as well as the diurnal cycles of the sensitivity measures represented via colors and $\max_{t,(d)}(\mu_{i,k}^*(t, d))$ and $\max_{t,(d)}(\sigma_{i,k}(t, d))$ with the corresponding time (and soil layer). The latter can be used to show the largest variation of the result when the

	X_1	X_2	X_3	X_4	X_5	X_6	X_7	X_8	$\sigma_{out,j}$
$\mu^*_{i,1}$ [m/s]	0.0393	0.0107	0.2679	0.0429	0.0196	0.0118	0.0183	0.0242	0.0968
$\sigma_{i,1}$ [m/s]	0.0246	0.012	0.0959	0.0295	0.0242	0.0137	0.0214	0.0158	
$\mu^*_{i,2}$ [K]	0.3557	0.1556	0.0464	0.0392	0.008	0.1444	0.039	0.2045	0.1891
$\sigma_{i,2}$ [K]	0.1276	0.0826	0.0351	0.0685	0.0099	0.0105	0.0224	0.0192	
$\mu^*_{i,3}$ [K]	0.8759	0.312	0.6862	1.5718	0.0366	0.1551	0.1272	0.5554	1.039
$\sigma_{i,3}$ [K]	0.2544	0.1872	0.4032	0.9248	0.04	0.0221	0.0329	0.0685	
$\mu^*_{i,4}$ [p.p.]	4.9248	4.6574	0.9206	0.8396	0.2818	0.2752	0.5654	0.3865	2.3709
$\sigma_{i,4}$ [p.p.]	1.6381	1.4664	0.585	0.5906	0.3635	0.3346	0.2673	0.2647	
$\mu^*_{i,5}$ [K]	0.1511	0.0512	0.7571	0.1947	0.0895	0.1385	0.0504	0.1279	0.2736
$\sigma_{i,5}$ [K]	0.0998	0.061	0.2697	0.1378	0.1122	0.0742	0.0525	0.0864	

	X_9	X_{10}	X_{11}	X_{12}	X_{13}	X_{14}	X_{15}	X_{16}	$\sigma_{out,j}$
$\mu^*_{i,1}$ [m/s]	0.0162	0.0135	0.0139	0.0122	0.0156	0.0164	0.0276	0.0044	0.0968
$\sigma_{i,1}$ [m/s]	0.0199	0.0161	0.0161	0.0142	0.017	0.0275	0.0288	0.0058	
$\mu^*_{i,2}$ [K]	0.0438	0.0067	0.0058	0.0089	0.0134	0.0426	0.1505	0.0299	0.1891
$\sigma_{i,2}$ [K]	0.0066	0.0079	0.0067	0.0087	0.016	0.01	0.1242	0.0345	
$\mu^*_{i,3}$ [K]	0.0622	0.0196	0.0168	0.0228	0.0178	0.0385	0.3936	0.078	1.039
$\sigma_{i,3}$ [K]	0.027	0.0219	0.0234	0.025	0.0232	0.0414	0.2689	0.0933	
$\mu^*_{i,4}$ [p.p.]	0.163	0.2658	0.1825	0.2848	0.2042	0.1781	2.1737	0.3795	2.3709
$\sigma_{i,4}$ [p.p.]	0.1981	0.3404	0.2177	0.3393	0.2325	0.2251	1.802	0.5223	
$\mu^*_{i,5}$ [K]	0.0613	0.0582	0.0475	0.0495	0.0503	0.0737	0.0768	0.0374	0.2736
$\sigma_{i,5}$ [K]	0.0684	0.0757	0.0584	0.0681	0.0645	0.0988	0.055	0.0572	

Figure 29: Overview of the Morris measures for the grassland case: Colored table for the measures $\mu^*_{i,j}$ and $\sigma_{i,j}$, (p.p.: percentage points).

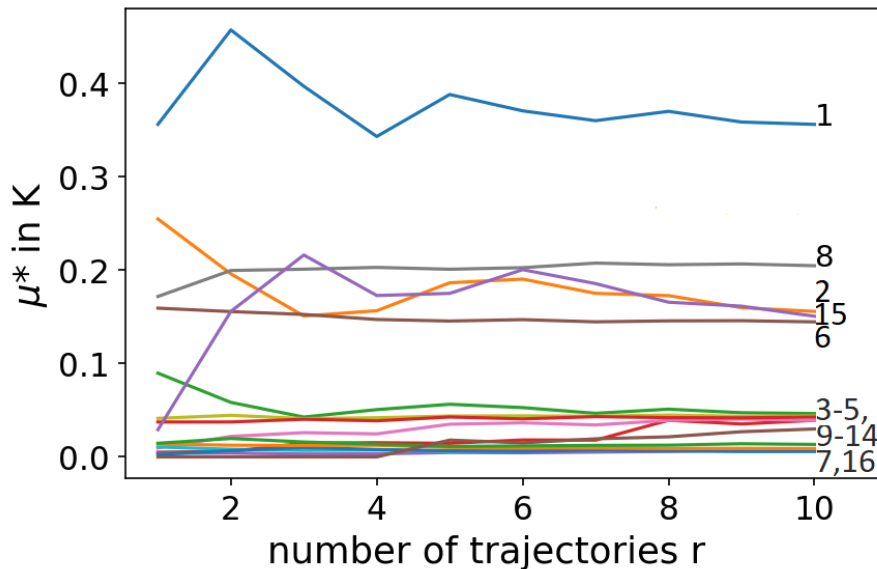


Figure 30: Grassland case: Convergence of the sensitivity measures $\mu^*_{i,2}$.

input parameter varies from the minimum to the maximum of its parameter range and the corresponding time and soil layer, while the visualization via colors can be used to qualitatively infer the important input parameters. Figure 31 b) uses the time dependent

standard deviation $\sigma_{\text{out},k}(t, d)$) and thus time dependent thresholds in order to give information on the current influences of the input parameters on the current variation of the output. The left part of Figure 31 c), as well as Figure 32 b) use $\max_{t(d)}(\sigma_{\text{out},k}(t, d))$ and thus fixed thresholds for the whole day in order to give information on the current influences of the input parameters on the output variation compared to the largest output variations. The upper part of each box represents $\mu_{i,k}^*(t)$, the lower part represents $\sigma_{i,k}(t)$. Hence, a box can contain two different colors. Furthermore, the sign of $\mu_{i,k}(t, d)$ and thus the sign of the effect of the i th input parameter on the considered model result is displayed via + and – within the tables.

In the following, the most important input parameters with the bandwidths given in Table 9 are discussed for the different outputs considered for the grassland surface. Figure 31 a) shows that the standard deviation of the horizontally averaged 2 m air temperature has a minimum at 08:00 UTC and two maxima at 07:00 UTC and 21:00 UTC at the times of the strongest temperature increase and decrease. Hence, especially the heating and cooling process is influenced by the parameter variation. Figures 31 b) and c) refer to the input parameters responsible for the standard deviation. At 7 UTC, the roughness length for heat (x_4) and the albedo (x_8) show an increased effect on the 2 m temperature with $\mu_{i \in \{4,8\}, k=2}^*(t) \geq 1 \cdot \sigma_{\text{out}, k=2}(t)$ and $\mu_{i \in \{4,8\}, k=2}^*(t) \geq 1 \cdot \max_t(\sigma_{\text{out}, k=2}(t))$, with $\{4, 8\}$ indicating the set of the input parameter indices. Furthermore, the right part of Figure 31 c) shows that the sensitivity measures for these input parameters $\mu_{i \in \{4,8\}, k=2}^*(t)$ take their largest values at 7 UTC. The albedo (x_8) also shows a slightly increased influence at 19 and 20 UTC compared to other input parameters. An increased albedo leads to a decrease in temperature from sunrise and also affects the temperature in the evening. The latter is due to the fact that the energy input during the day is lower because of the higher reflected shortwave radiation. The lower available amount of energy at the surface results in smaller sensible and latent heat fluxes [24, p. 5318]. From the second maximum of the standard deviation at 21 UTC, the roughness length for temperature (x_4) and the LAI (x_1) show an increased effect on the horizontally averaged 2 m air temperature. During day time, with a maximum at 20 UTC, the leaf area index (x_1) has the largest impact, leading to a temperature decrease for increasing values. The leaf area index determines the distribution of the available energy into surface sensible and latent heat fluxes by influencing the available moisture through evapotranspiration. A higher value for LAI increases the latent heat flux, and decreases the sensible heat flux, which leads to lower surface temperatures during the day. Lower surface temperatures result in a lower outgoing longwave radiation [24, pp. 5318, 5325]. In the early morning, the vegetation coverage (x_2) and the heat conductivity (x_6) have an increased effect, both leading to temperature increases for increasing values. (x_6) has its strongest influence in the morning. The increased influence also occurs the following night, but this is not evident from this figure. The reason for the temperature increasing effect of the vegetation coverage might be a reduced amount bare soil and thus of available soil moisture and thus a reduced latent and increased sensible heat flux. The results coincide with the ones from [24], where it was found that the leaf area index and the albedo influence the daytime turbulent sensible and latent heat fluxes.

Figure 32 a) shows the time and soil layer dependent standard deviation of the horizontally averaged soil moisture. It takes larger values in the afternoon and in the evening. With increasing depth the values decrease and the maximum occurs at later time. Figures 32 b) and c) show that the largest variations of the soil temperature in combination with interactions between input parameters are induced by the hydraulic conductivity of the soil at saturation (x_{13}), followed by the vegetation coverage (x_2), both leading to increases

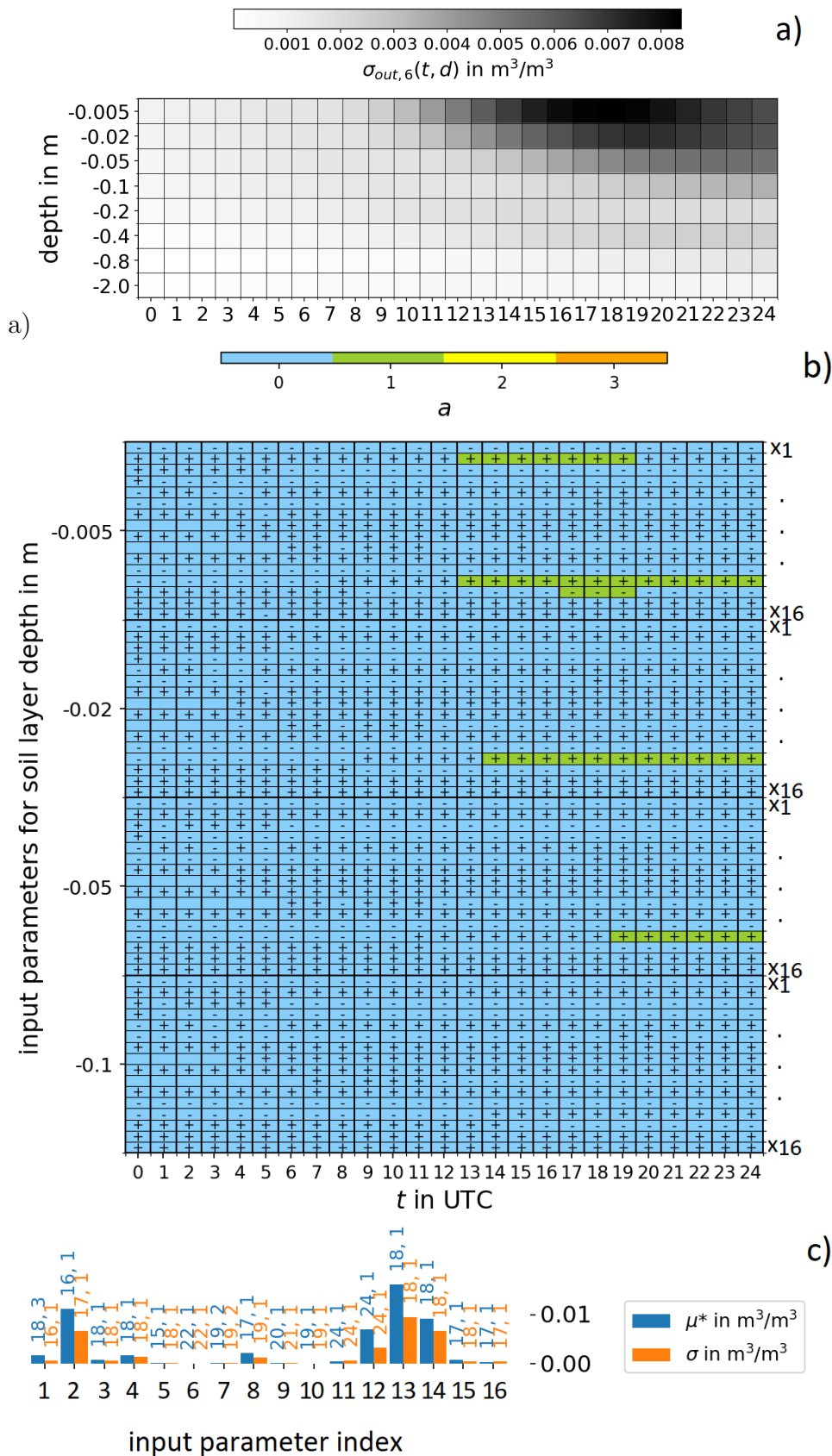


Figure 32: Grassland case: Visualization of the Morris sensitivity measures for the horizontally averaged soil moisture $y_{k=7}(t, d)$.

a) $\sigma_{out,k=7}(t, d)$, b) Sensitivity measures colored according to $\mu_{i,k=7}^*(t, d)$ or $\sigma_{i,k=7}(t, d) \geq a \cdot \max_{t,d}(\sigma_{out,k=7}(t, d))$, c) $\max_{t,d}(\mu_{i,k=7}^*(t, d))$, $\max_{t,d}(\sigma_{i,k=7}(t, d))$ and t [UTC], soil layer.

for increasing values, and the saturation moisture (x_{14}) and the value of the coefficient n_{vG} for the calculation of the hydraulic conductivity of soil in the parameterization after Van Genuchten (x_{12}), both leading to decreases for increasing values. The notable influence of the hydraulic conductivity (x_{13}) reaches down to the third soil layer.

The evaluation is also performed for the other meteorological variables and the related results are shown in the Figures 59-68 in the appendix. The horizontally averaged 10 m wind speed is mainly influenced by the roughness length for momentum (x_3) during the whole day, which leads to larger variations during day time when higher wind speeds occur. An increased roughness length leads to a decrease of the wind speed. The standard deviation of the horizontally averaged surface temperature takes a maximum at 12 UTC. The roughness length for heat (x_4) leads to the largest variations in the surface temperature during day time. An increased roughness length for heat leads to a temperature decrease. It is followed by the leaf area index (x_1), as higher values for LAI increase the latent heat flux, and decrease the sensible heat flux and lower the surface temperatures during the day, and the roughness length for momentum (x_3), also leading to decreases due to higher wind speeds. The variations of the night time minimum of the surface temperature are comparatively small. They are induced by the leaf area index (x_1), the vegetation coverage (x_2), the heat conductivity (x_6) and the saturation moisture (x_{14}) during night and the albedo (x_8) in the morning and the evening hours. The standard deviation of the horizontally averaged RH is smaller during day than during night. The input parameters inducing the largest variations are the vegetation coverage (x_2) leading to decreases especially in the early morning and the night, the leaf area index (x_1), which also has an increased influence during day and the roughness length for heat (x_4) and the albedo (x_8) in the morning. The RH is strongly dependent on temperature and hence dependent on similar input parameters. Since the air temperature only shows a small variation, especially at night, the RH, however, a large one, see Figure 27 d), the question of an additional moisture source arises. Larger values for the vegetation coverage have a lowering influence of up to more than 10 percentage points at 3 UTC on the RH, especially at night, while they have an increasing influence on the soil moisture as described above, see Figures 32 and 61. This indicates that the soil should be considered as a source of moisture depending on the degree of coverage. The biometeorological quantity UTCI shows the largest influence from the roughness length for momentum (x_3). An increase of the roughness length leads to a decrease of the diurnal averaged 10 m wind speed, but to an increase of UTCI as a lower wind speed leads to higher values of UTCI due to wind chill. Additionally, UTCI depends on the air temperature, radiation and humidity. Higher temperatures lead to higher UTCI. On the UTCI maximum during day, the albedo, the leaf area index and the heat conductivity, which also affect the above mentioned quantities, have an increased influence. The increase of the albedo leads to decreases of the air and surface temperature and to an increase of UTCI during day. The latter was also found by [4] and attributed to increased reflections at the surface. During night, roughness length for momentum and heat and heat conductivity have an increased influence on UTCI. In addition, there are many interactions between parameters, as UTCI is influenced by several meteorological quantities. The standard deviation of the horizontally averaged soil temperature has the same properties as that of the soil moisture. The largest variations of the soil temperature and interactions between input parameters are induced by the roughness length for heat (x_4) in the first soil layer, followed by the leaf area index (x_1), which leads to a decreased ground heat flux for higher values [24, p. 5319], and the roughness length for momentum (x_3), all leading to decreases for larger values. The notable influence of the roughness length for heat (x_4) reaches down to the third soil layer.

The described sensitivities are valid for the used atmospheric conditions. In order to account for the effect of the initialization of the atmospheric conditions and potential interactions with the sensitivities described in the above section, in an additional application of the Morris method on the grassland surface, parameters which are responsible for the initialization of the atmospheric conditions were also varied according to the bandwidths given in Table 10. The atmosphere is initialized as before, but with varied u component of the wind, potential temperature and water vapor to total water mixing ratio above the surface. For 23 input parameters, 10 trajectories were used and thus, simulations for $10 \cdot (23 + 1) = 240$ samples were performed. The results are evaluated as in the above section and the findings are described, but not visualized in the following. The investigation showed that the initial value of the u component of the wind (x_1) has the largest impact on the horizontally averaged 10 m wind speed, followed by the initial value for the roughness length for momentum (x_8). On the horizontally averaged 2 m temperature, the initial value of the potential temperature (x_2) has the largest impact during the whole day. The soil temperature (x_4) and roughness length for heat (x_9) have a slightly increased influence on the minimum, too. The horizontally averaged surface temperature is mostly influenced by the roughness length for heat (x_9), the soil moisture (x_{15}) and the potential temperature (x_2). The minimum shows less variation which is induced by the initial value for the potential temperature (x_2), the soil temperature (x_4) and the emissivity (x_{14}). Therefore, an adequate choice of initial values for the parameters to controlling the atmospheric conditions is essential. Since these parameters are not involved in interactions (except from a slightly increased interaction of the soil moisture for the output of the surface temperature), one can assume that their values will not significantly affect the results of the previous study for the vegetation and soil parameters.

15.2 A paved surface

The Morris method is applied to the pavement setup presented in section 11 in order to determine the input parameters among the ones given in Table 11 with the corresponding bandwidths that have the largest effect on the model results. Parameters related to soil moisture are included in this study, as there are soil layers placed under the six pavement layers, however, pavement prohibits the vertical transport of soil moisture up to the surface [24, p. 5313]. Hence, these parameters are assumed not to have a large effect on the model results, but are also varied for completeness. Thirteen parameters, ten trajectories and thus, according to Chapter 6.3, $10 \cdot (13 + 1) = 140$ samples are used. As in the grassland setup, the considered results of a model run are time series of the horizontally averaged 10 m wind speed ($y_{k=1}(t)$), the 2 m air temperature ($y_{k=2}(t)$), the surface temperature ($y_{k=3}(t)$), the RH ($y_{k=4}(t)$), UTCI ($y_{k=5}(t)$) and the depth dependent soil temperature ($y_{k=6}(t, d)$) and soil moisture ($y_{k=7}(t, d)$). The latter is not expected to show large (any) variations below (within) the pavement layers due to the impermeability of the pavement to water. For completeness, this model result is also investigated. Additionally, the diurnal averages of the following horizontally averaged quantities are considered: the 10 m wind speed ($y_{j=1}$), the 2 m air temperature ($y_{j=2}$), the surface temperature ($y_{j=3}$), the RH ($y_{j=4}$) and the UTCI ($y_{j=5}$). UTCI is provided for the horizontal level, which is the closest possible to the 1.1 m level. With the used grid, this is 5 m. The same height level is used for the RH.

The relevance of the input parameters on the selected model results can be assessed using the standard deviation of the output σ_{out} as it was introduced in Chapter 6.6. Therefore, for the outputs $y_k(t)$, Figure 33 shows the diurnal cycles of the mean, the standard deviation and the extrema within the samples for each time step, taking into

Table 10: Input parameters and their bandwidths for the grassland setup including initial atmosphere parameters.

Parameter	Name	Bandwidth	Description
u	x_1	(2 - 5) ms^{-1}	u component of the wind
θ	x_2	(290 - 294) K	potential temperature
P	x_3	(1008 - 1018) hPa	atmospheric pressure at the surface
$T_{\text{soil},k}$	x_4	(290 - 294) K (lowest level ($k = 8$): T_{deep})	soil temperature at depth level k , $k \in \{1, \dots, 7\}$
T_{deep}	x_5	(285 - 289) K	deep soil temperature
LAI	x_6	(1 - 2) m^2m^{-2}	leaf area index
c_{veg}	x_7	0.7 - 1.0 *	vegetation coverage
z_0	x_8	(0.03 - 0.47) m *	roughness length for momentum
$z_{0,h}$	x_9	($0.30 \cdot 10^{-4}$ - $0.47 \cdot 10^{-2}$) m *	roughness length for temperature
λ_s	x_{10}	(9 - 11) $\text{Wm}^{-2}\text{K}^{-1}$	heat conductivity between atmosphere and soil in case of stable stratification
λ_u	x_{11}	(9 - 11) $\text{Wm}^{-2}\text{K}^{-1}$	heat conductivity between atmosphere and soil in case of unstable stratification
$r_{c,\text{min}}$	x_{12}	(100 - 110) sm^{-1} *	minimum canopy resistance
α	x_{13}	0.18 - 0.25 *	albedo
ϵ	x_{14}	0.95 - 0.97*	surface emissivity
$m_{\text{soil},k}$	x_{15}	(0.3 - 0.4) m^3m^{-3}	soil moisture at depth level k , $k \in \{1, \dots, 8\}$
α_{vG}	x_{16}	0.83-3.67 **	coefficient alpha in the soil hydraulic conductivity parameterization after van Genuchten
l_{vG}	x_{17}	-2.342 - -0.588 **	coefficient l in the soil hydraulic conductivity parameterization after van Genuchten
n_{vG}	x_{18}	1.10 - 1.28 **	coefficient n in the soil hydraulic conductivity parameterization after van Genuchten
γ_{sat}	x_{19}	($0.26 \cdot 10^{-6}$ - $2.87 \cdot 10^{-6}$) ms^{-1} **	hydraulic conductivity of the soil at saturation
m_{sat}	x_{20}	(0.430 - 0.520) m^3m^{-3} **	volumetric soil moisture at saturation (porosity)
m_{fc}	x_{21}	(0.347 - 0.448) m^3m^{-3} **	volumetric soil moisture at field capacity
m_{wilt}	x_{22}	(0.133 - 0.279) m^3m^{-3} **	volumetric soil moisture at permanent wilting point
q	x_{23}	(0.0036-0.0047) kg kg^{-1}	water vapor / total water mixing ratio

*: The bandwidths meet the values set in PALM for short and tall grass.

** : The bandwidths meet the values set in PALM for medium to fine soil granularity.

account the results of all samples. Figure 33 a) shows the described quantities for the horizontal wind in a height of 10 m. The diurnal cycle including the minimum in the early morning and the maximum in the afternoon has already been discussed in Chapter 11.

Table 11: Input parameters and their bandwidths for the pavement setup.

Parameter	Name	Bandwidth	Description
z_0	x_1	$(3.0 \cdot 10^{-2} - 6.0 \cdot 10^{-2})$ m	roughness length for momentum
$z_{0,h}$	x_2	$(3.0 \cdot 10^{-4} - 6.0 \cdot 10^{-4})$ m	roughness length for temperature
C_p	x_3	$(1.94 \cdot 10^6 - 2.11 \cdot 10^6)$ Jm ⁻³ K ⁻¹ *	heat capacity of the pavement
Λ_p	x_4	$(0.82 - 1.51)$ Wm ⁻¹ K ⁻¹ *	thermal conductivity of the pavement
α	x_5	0.08 - 0.35 *	albedo
ϵ	x_6	0.90 - 0.95 *	surface emissivity
α_{vG}	x_7	0.83 - 3.67 **	coefficient alpha in the soil hydraulic conductivity parameterization after van Genuchten
l_{vG}	x_8	-2.342 - -0.588 **	coefficient l in the soil hydraulic conductivity parameterization after van Genuchten
n_{vG}	x_9	1.10 - 1.28 **	coefficient n in the soil hydraulic conductivity parameterization after van Genuchten
γ_{sat}	x_{10}	$0.26 \cdot 10^{-6} - 2.87 \cdot 10^{-6}$ ms ⁻¹ **	hydraulic conductivity of the soil at saturation
m_{sat}	x_{11}	$(0.430 - 0.520)$ m ³ m ⁻³ **	volumetric soil moisture at saturation (porosity)
m_{fc}	x_{12}	$(0.347 - 0.448)$ m ³ m ⁻³ **	volumetric soil moisture at field capacity
m_{wilt}	x_{13}	$(0.133 - 0.279)$ m ³ m ⁻³ **	volumetric soil moisture at permanent wilting point

*: The bandwidths meet the values set in PALM for the pavement types asphalt and concrete.

** : The bandwidths meet the values set in PALM for medium to fine soil granularity.

Variations within the samples are induced especially during day time. Here and in the following subfigures, the variation of the input parameters leads to a spread in the course of the day including the end of the day. No closed diurnal circles and no stationarity are present. Figure 33 b) shows the quantities for the 2 m air temperature. The diurnal cycle of the 2 m air temperature is also explained in more detail in Chapter 11. The standard deviation takes its largest values in the late afternoon and evening. Subfigure c) shows the diurnal cycle of the mean μ , standard deviation σ and extrema within the samples of the surface temperature. During day, especially around noon, the largest values occur due to the largest amount of solar radiation warming up the ground at noon, accompanied by the largest standard deviations. The RH treated in subfigure d) strongly correlates with the air temperature. In the early morning, when the air temperature is low, a higher RH is simulated. A low RH, on the other hand, occurs during the day. In contrast to the grassland case, variations mainly occur on the second half of the day beginning at noon as it is also the case for the air temperature. Subfigure e) shows the quantities for the UTCI. It also shows a diurnal variation with maximum at noon. Increased standard deviations occur during night and around noon. Subfigure f) shows the depth dependent quantities for the surface temperature. As in the grassland case, the properties of the

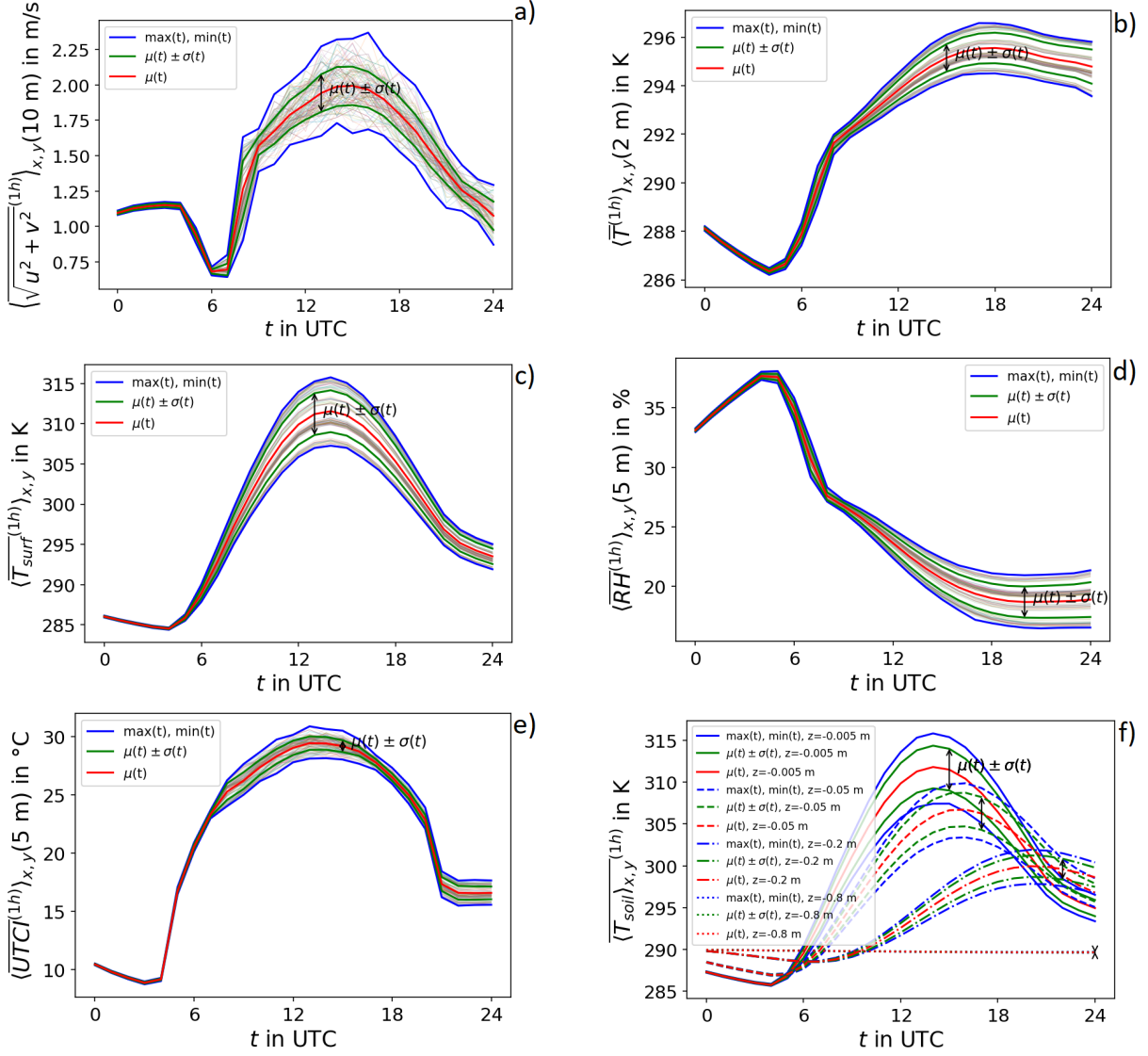


Figure 33: Diurnal cycles of mean μ , standard deviation σ and extrema within the samples of the considered outputs $y_k(t)$ for the paved surface. The diurnal cycles for the individual samples are indicated by transparent lines.

soil temperature are strongly correlated with those of the surface temperature. With increasing depth, the maximum of the soil temperature and the standard deviation is reached later. The Morris method will help identifying the input parameters responsible for these standard deviations.

The values of the standard deviations $\sigma_{out,j}$ of the diurnal averages y_j , $j = 1, \dots, 5$ are included in Figure 34, where the Morris measures for the diurnal averages y_j , $j = 1, \dots, 5$ are presented and each cell is colored according to the values of $\mu_{i,j}^*$ or $\sigma_{i,j} \geq a \cdot \sigma_{out,j}$ and is blue for $a = 0$, green for $a = 1$ and yellow for $a = 2$. The largest value in Figure 34 is $\mu_{5,3}^* = 3.74$ K. That means that the estimated mean of the absolute variation of the diurnal and horizontally averaged surface temperature when the albedo (x_5) is varied between 0.08 and 0.35 is 3.74 K. Columns that only include zeros are omitted. The van Genuchten coefficient α_{vG} (x_7), the volumetric soil moisture at field capacity m_{fc} (x_{12}) and the volumetric soil moisture at permanent wilting point m_{wilt} (x_{13}), and thus the parameters determining the soil moisture below the pavement, have no effect on the considered model results.

As described in Chapter 6.5, single Morris measures are calculated for each time step

	x_1	x_2	x_3	x_4	x_5	x_6	x_8	x_9	x_{10}	x_{11}	$\sigma_{out,j}$
$\mu^*_{i,1}$ [m/s]	0.0251	0.0127	0.0258	0.021	0.1586	0.0216	0.0183	0.0225	0.0264	0.0208	0.0598
$\sigma_{i,1}$ [m/s]	0.0251	0.0135	0.0322	0.0272	0.0191	0.0247	0.0277	0.0249	0.0295	0.0236	
$\mu^*_{i,2}$ [K]	0.0435	0.0704	0.0105	0.0136	1.0891	0.1194	0.0081	0.0125	0.0152	0.0071	0.3772
$\sigma_{i,2}$ [K]	0.0141	0.0087	0.0121	0.0165	0.0354	0.016	0.0086	0.0149	0.0186	0.0085	
$\mu^*_{i,3}$ [K]	0.1851	0.2261	0.0398	0.0386	3.7384	0.2628	0.0375	0.0391	0.0479	0.0359	1.3444
$\sigma_{i,3}$ [K]	0.0403	0.0548	0.0539	0.0387	0.0889	0.0549	0.0524	0.0432	0.0528	0.0441	
$\mu^*_{i,4}$ [p.p.]	0.0768	0.1747	0.0539	0.0989	2.1183	0.2477	0.0604	0.0707	0.0757	0.0509	0.7356
$\sigma_{i,4}$ [p.p.]	0.0921	0.0484	0.0773	0.1163	0.0875	0.1109	0.0717	0.0828	0.1089	0.0672	
$\mu^*_{i,5}$ [K]	0.1236	0.0769	0.0778	0.0691	0.2451	0.1349	0.0689	0.0747	0.0386	0.102	0.1112
$\sigma_{i,5}$ [K]	0.0554	0.0738	0.0846	0.0882	0.1007	0.1226	0.0887	0.0727	0.0544	0.1244	

Figure 34: Overview of the Morris measures for the paved surface case: Colored table for the measures $\mu^*_{i,j}$ and $\sigma_{i,j}$.

in order to determine the diurnal cycles of the sensitivity measures for the time dependent outputs $y_k(t)$. They are exemplary visualized for the 2 m air temperature in Figure 35. Visualizations for the other output quantities can be found in the appendix in Figures 64-69. As in the grassland case, the figures show the time dependent standard deviation (a)), which is used for coloration of the tables given in subfigures b) and c). Figure 35 b) uses the time dependent standard deviation $\sigma_{out,k}(t)$ and thus time dependent thresholds in order to give information on the current influences of the input parameters on the current variation of the output. The left part of Figure 35 c) uses $\max_t(\sigma_{out,k}(t))$ and thus a fixed threshold for the whole day in order to give information on the current influences of the input parameters on the output variation compared to the largest output variations. The upper part of each box represents $\mu^*_{i,k}(t)$, the lower part represents $\sigma_{i,k}(t)$. Furthermore, the sign of $\mu_{i,k}$ is shown as sign of the effect of the i th input parameter. $\max_{t(d)}(\mu^*_{i,k}(t(d)))$ and $\max_{t(d)}(\sigma_{i,k}(t(d)))$ are given in the right part of Figure 35 c) with the corresponding time. In the following, the results are summarized. Figure 35 a) shows that the standard deviation of the horizontally averaged 2 m air temperature takes its largest values in the evening and the following night. It is mostly induced by the albedo (x_5), which leads to a temperature reduction for increased values due to a increased amount of outgoing short-wave radiation. The emissivity (x_6) has an increased influence in the early morning leading to a temperature reduction. At 6 UTC, its maximal sensitivity measure $\mu^*_{6,2} = 0.22$ K occurs. In the early morning, the heat conductivity of the pavement (x_4) follows the emissivity in order of importance. Note, that the variations in the morning are much smaller than during day and in the following night. Thus, compared to the maximum standard deviation, only the albedo shows an increased influence, see subfigure c). The albedo (x_5) also influences the wind speed, leading to a decreased wind speed for increased albedo values, beginning at 7 UTC. The roughness length for momentum (x_1) has an increased influence on the horizontally averaged 10 m wind speed in the morning and is thus most important for the minimum wind speed. Increased values lead to a decreased wind speed. The values of the standard deviation of the horizontally averaged surface temperature are largest during day time. The largest variation is caused due to changes in the albedo (x_5), leading to a temperature decrease for larger values, especially at 13 UTC. The emissivity (x_6) has an increased influence in the early morning. It is thus most important for the minimal surface temperature, where only small variations occur. Also on the RH, the albedo has the largest impact. An increased albedo leads to an increased RH, which might be due to the decreased air temperature resulting from the increased albedo. Again, the emissivity (x_6) has an increased influence in the early morning, when the standard deviation of the RH is small. The same yields for the heat conductivity of the pavement (x_4). In the grassland case it was concluded that the soil

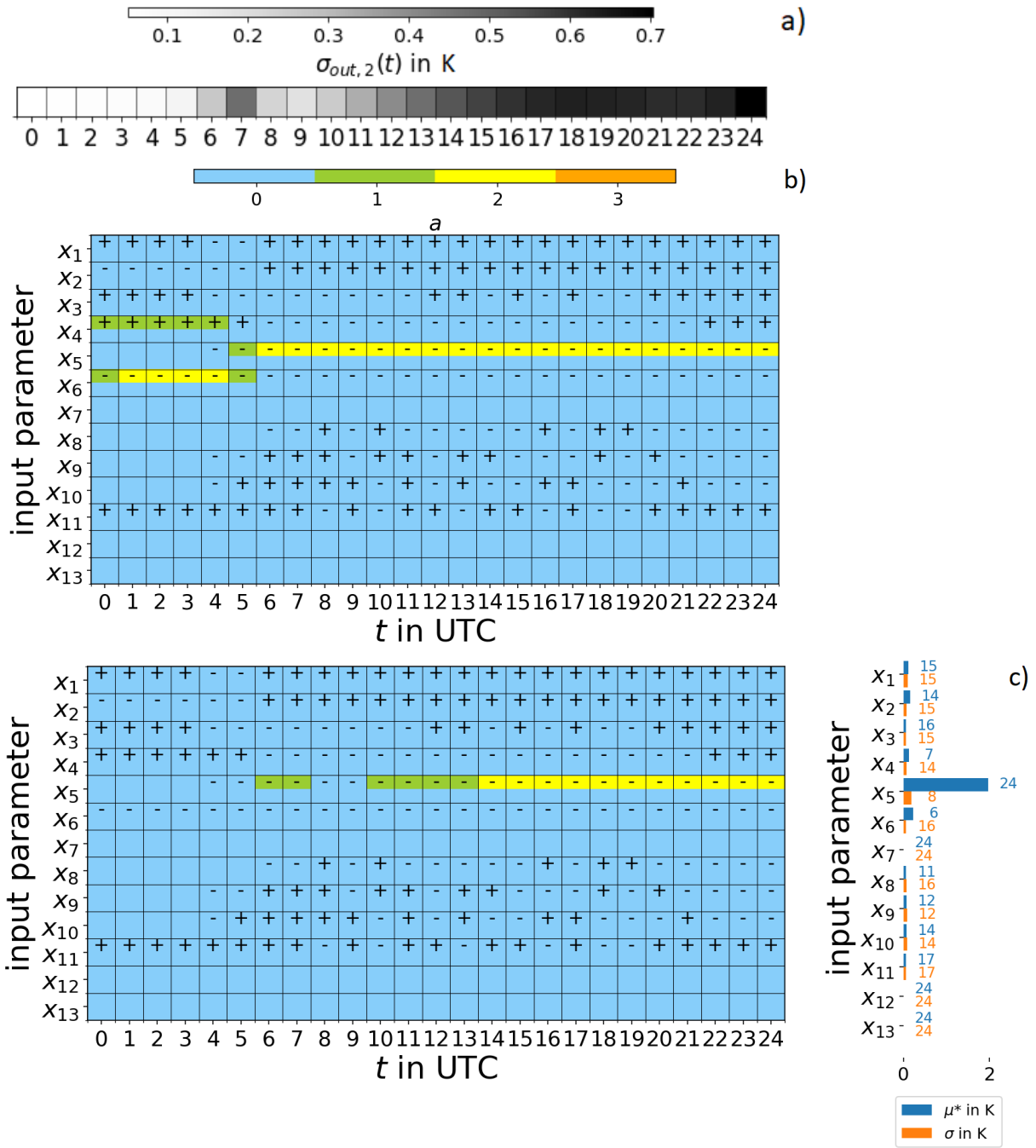


Figure 35: Pavement case: Visualization of the Morris sensitivity measures for the horizontally averaged 2 m air temperature $y_{k=2}(t)$.
 a) $\sigma_{out,k=2}(t)$, b) Sensitivity measures colored according to $\mu_{i,k=2}^*(t)$ or $\sigma_{i,k=2}(t) \geq a \cdot \sigma_{out,k=2}(t)$, c) Sensitivity measures colored according to $\mu_{i,k=2}^*(t)$ or $\sigma_{i,k=2}(t) \geq a \cdot \max_t(\sigma_{out,k=2}(t))$ (left), $\max_t(\mu_{i,k=2}^*(t))$, $\max_t(\sigma_{i,k=2}(t))$ and corresponding t [UTC] (right).

should be considered as a source of moisture. This study also provides evidence for this conclusion, since the additional scatter is not present and the influence of soil moisture on RH is suppressed by the paved surface. The albedo (x_5) has the largest impact on UTCI beginning at sunrise. During the time of incoming shortwave radiation, an increased albedo leads to an increased value for the biometeorological quantity. In the following night, an increased albedo results in a lower UTCI. This is due to the air temperature decrease resulting from an increased albedo, which persists until night. The increased

reflection leading to an increase of the UTCI during day time is missing and the UTCI therefore is lowered by an increased albedo in the night. The other parameters except the van Genuchten coefficient α_{vG} (x_7), the volumetric soil moisture at field capacity (x_{12}) and the volumetric soil moisture at the permanent wilting point (x_{13}) are also involved in interactions and have a slightly increased effect during day time. The standard deviation of the horizontally averaged soil temperature takes on larger values during day, especially in the noon and afternoon. The values decrease with depth while the maximum is also reached later. The largest variations of the soil temperature and interactions between input parameters are induced by the albedo (x_5) leading to temperature decreases for larger values. The notable influence of the albedo (x_5) reaches down to the fifth soil layer at -0.2 m depth, where it reaches a maximum in the evening.

15.2.1 Influence of the albedo on the diurnal cycles of the surface energy fluxes

The previous results lead to the conclusion, that the important input parameters are those affecting the energy balance at the surface. Due to the large effect of the albedo α , its influence on the energy balance at the surface is studied in more detail. Figure 36 shows the components of the energy balance for two different albedos which were exemplary chosen from the interval $[0.08, 0.35]$ given in Table 11 using the middle of the interval $\pm 20\%$, i.e. $\alpha \in \{0.17, 0.25\}$. In the following, E is the surface latent heatflux, H the surface sensible heatflux, G the ground heat flux and R_n is the net radiation flux at the surface. L_\downarrow represents the incoming longwave radiation flux, L_\uparrow the outgoing longwave radiation flux, S_\downarrow the incoming shortwave radiation flux and S_\uparrow is the outgoing shortwave radiation flux. Concerning the signs, $R_n = G + H + E$ yields in the figure. The signs of the fluxes directed towards the surface are positive, those of the fluxes that are directed into the atmosphere are negative. The energy balance for a surface without storage of energy in

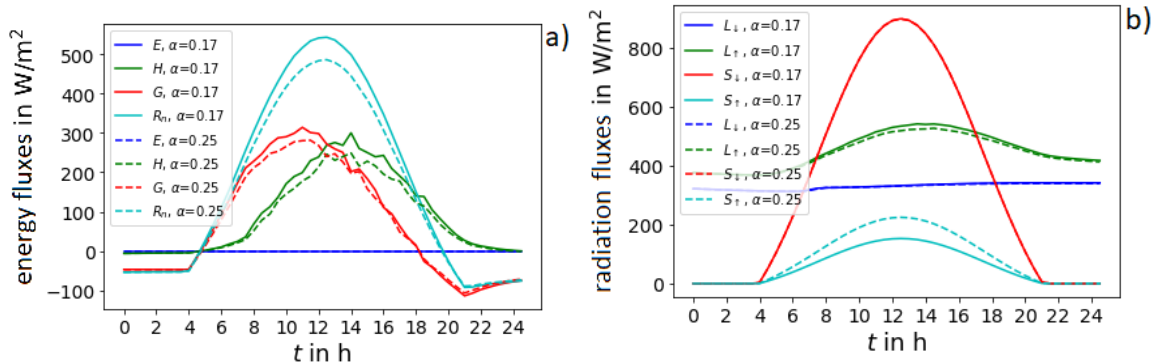


Figure 36: Diurnal cycle of the a) energy fluxes and b) radiation fluxes at the surface for different pavement albedos.

form of heat is given here for the case of no rain, wind and anthropogenic heat flux density: $R_n = G + H + E$. R_n is the simplified radiation balance at the surface without storage capacity and unaffected by advection. It yields $R_n = (S_\downarrow + L_\downarrow) - (S_\uparrow + L_\uparrow)$, all in Wm^{-2} [38, pp. 8, 9]. The components show a diurnal cycle driven by the diurnal changes in the energy input via the incoming solar short wave radiation. The diurnal changes of the radiation balance lead to changes of the temperature and thus to a vertical temperature gradient in the soil. This leads to a ground heat flux which is proportional to the thermal conductivity of the soil and the vertical temperature gradient. Furthermore a temperature gradient in the atmosphere close to the ground arises, resulting in a sensible heat flux. In

general, a humid soil leads to evaporation resulting in a water vapor transport into the atmosphere above the soil. This latent heatflux E is proportional to the vertical humidity gradient [15, pp. 338, 339]. However, the pavement is dry and impermeable to water and no phase transition occurs. Consequently the surface latent heatflux E is zero. As it is visible from Figure 36 b), the incoming shortwave radiation flux is the same in both simulation runs. Figure 36 b) shows that a higher albedo leads to an increased outgoing shortwave radiation flux and a slightly decreased outgoing longwave radiation flux, since this follows the Stefan-Boltzmann law and is proportional to T_{surf}^4 [15, p. 339]. This leads to a decreased net radiation flux at the surface. In conclusion, the ground heat flux and the surface sensible heat flux take smaller values, see Figure 36 a). Due to its influence on the energy input during day, the albedo affects the night time temperature, too.

15.3 Horizontally homogeneous plant canopy

In the following two chapters, the influence of varying obstacle parameters for a plant canopy and a single tree on the stationary wind is investigated. No diurnal cycles of radiation and hence temperature and wind speed are assumed, hence, no effects on temperature are considered. Here, the Morris method is applied to the horizontally homogeneous plant canopy setup presented in section 12 in order to study the influence of the drag coefficient $c_d(x_1)$, the shape coefficient for calculating the LAD profile after Markkanen [40] $\alpha_{\text{LAD}}(x_2)$, the LAI (x_3) and the plant canopy height $h(x_4)$ on the horizontally averaged vertical wind profile $y(z)$. The bandwidth of the drag coefficient (x_1) is chosen according to [29, p. 227]. As in [40, p. 440], α_{LAD} is varied while a fixed value for β_{LAD} of 3.0 is assumed. α_{LAD} is chosen to cover a wide range of canopy shapes. The bandwidths used are given in Table 12. Ten trajectories, four input parameters and thus $10 \cdot (4 + 1) = 50$ samples are used. Figure 37 shows the horizontally averaged vertical

Table 12: Input parameters and their bandwidths for the horizontally homogeneous plant canopy setup.

Parameter	Name	Bandwidth	Description
c_d	x_1	0.1 - 0.4	drag coefficient
α_{LAD}	x_2	1.0 - 18.0	coefficient for calculating the LAD profile after Markkanen [40]
LAI	x_3	(5.0 - 6.0) m^2m^{-2}	leaf area index
h	x_4	16 m - 22 m	plant canopy height

profiles of the mean, the standard deviation and the extrema within the samples for the u component of the wind for each height taking into account the results of all samples. As described in Chapter 12, a logarithmic wind profile has developed above the plant canopy with a decreased wind speed within the crown region, where the LAD takes the largest values. The resolved vegetation leads to a sink term in the momentum equation [32, pp. 5838-5839]. The variations near the top boundary are traced back to the model setup in which the volume flow through the vertical $x - z$ and $y - z$ cross-sections of the model domain remains constant throughout the run. Therefore, the modifications of the wind speed within the canopy layer affect the wind speed at the top boundary. Analogous to the determination of the sensitivity measures for time dependent outputs, single sensitivity measures for the height dependent output $y(z)$ are calculated for each height level in the atmosphere. Vertical profiles of the Morris measures are therefore determined. They are visualized in Figure 38. In Figure 38 b), the table is colored according to the height dependent standard deviation $\sigma_{\text{out}}(z)$ in order to compare the effect of the parameters on

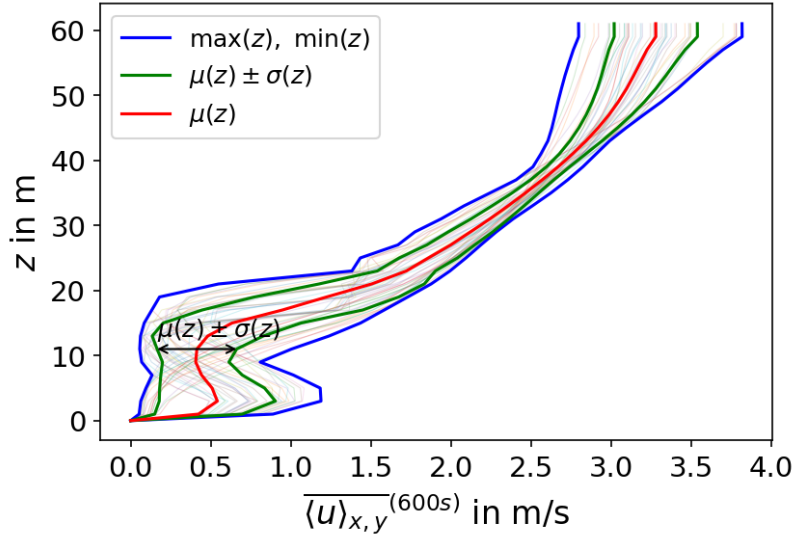


Figure 37: Vertical profiles of mean, standard deviation and the extrema within the samples for the horizontally averaged vertical wind profile $y(z)$. The profiles simulated for the individual samples are indicated by transparent lines.

the variation of the output at individual heights, while Figure 38 c) uses $\max_z(\sigma_{\text{out}}(z))$ and thus a fixed threshold for every height to get information on the influences of the input parameters on the output variation compared to the largest output variations. The upper part of each box represents $\mu_{i,k}^*(t)$, the lower part represents $\sigma_{i,k}(t)$. The vertical profile of the standard deviation as well as $\max_z(\mu_i^*(z))$ and $\max_z(\sigma_i(z))$ with the corresponding height are visualized in Figure 38 a) and in subfigure d), respectively. Figure 38 a) shows that the maximum value of the standard deviation of the horizontally averaged vertical wind profile $\sigma_{\text{out}}(z)$ occurs at 17 m and hence in a height that is above or within the tree canopy depending on the canopy height (x_4) that varies between 16 m to 22 m. The largest variation due to the given input parameter ranges is induced by the plant canopy height (x_4) at 19 m, and thus at or above crown height. An increasing plant canopy height shifts the LAD upwards if the other input parameters are constant. An increasing height therefore leads to a decrease in the wind speed at the corresponding height levels that become covered by leaves as they lead to a sink term in the momentum equation and furthermore, an increased height results in an increase below these levels where the LAD decreases. This interaction between the plant canopy height and the LAD is also visible in the increased values for $\sigma_2(z)$ and $\sigma_4(z)$. In order of importance, the height is followed by α_{LAD} (x_2), and thus the tree shape, especially at higher tree parts with a maximum at 15 m. As described in Chapter 3.2, increasing (decreasing) values for α_{LAD} shift the leaf areas from the lower (higher) levels within the tree canopy towards the top (bottom) of the tree canopy as it is visible in Figure 14. In the levels with increasing leaf area density, the wind speed decreases and it increases in the levels, where the leaf areas are shifted away from. The variation of these two input parameters mainly lead to the maximal standard deviation at 17 m. It should be noted that the range of α_{LAD} was chosen to be quite large in order to investigate the influence of the widest possible range of canopy shapes. It can further be stated that the variation of the LAI (x_3) results in the slightest variations in the resulting wind speed at all heights using the parameter range under consideration. The also small influence of the canopy drag coefficient (x_1) reaches its maximum at a height of 13 m.

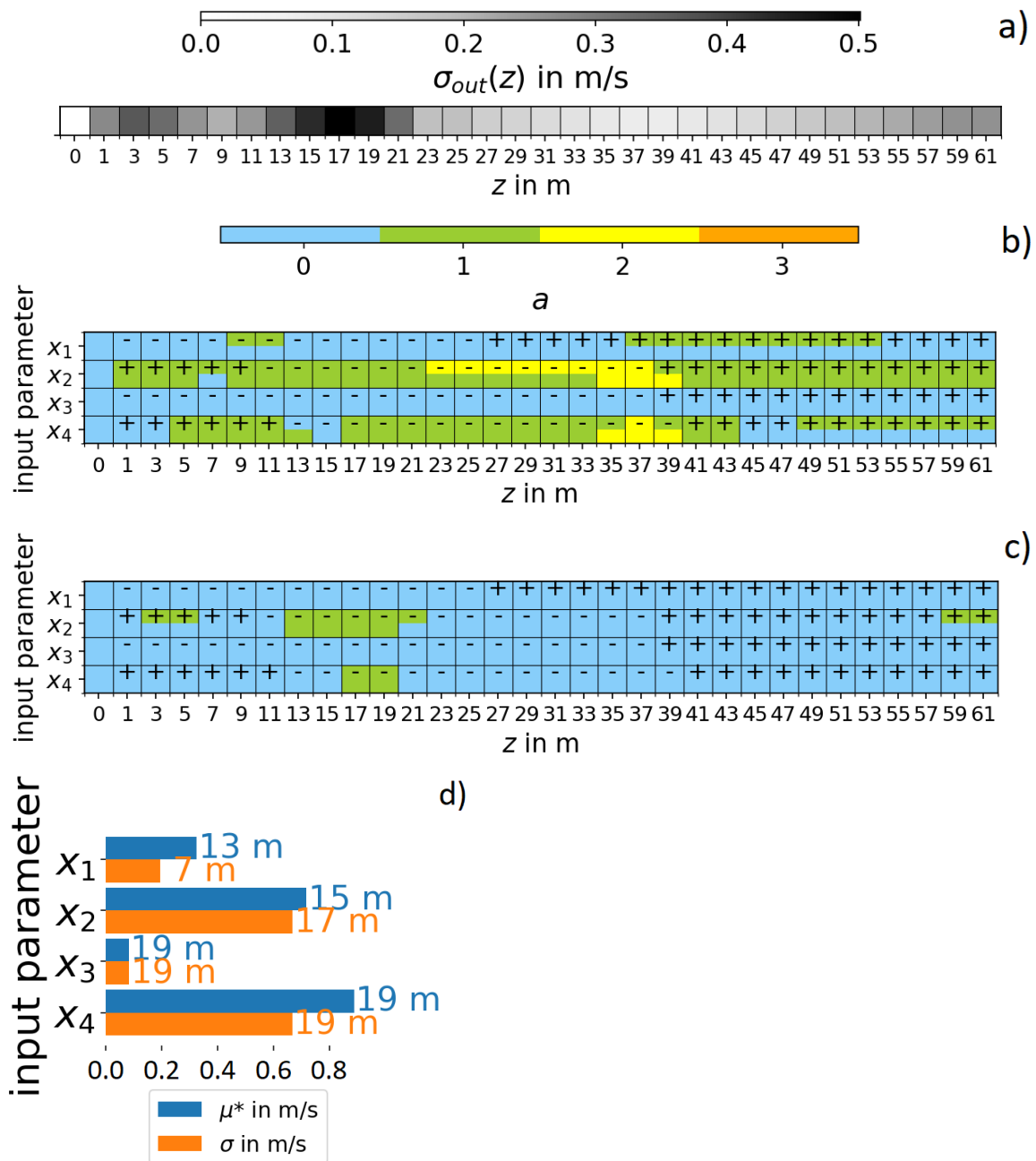


Figure 38: Horizontally homogeneous plant canopy: Visualization of the Morris sensitivity measures for the horizontally averaged vertical wind profile $y(z)$. a) $\sigma_{out}(z)$, b) Sensitivity measures for $y(z)$ colored according to $\mu_i^*(z)$ or $\sigma_i(z) \geq a \cdot \sigma_{out}(z)$, c) Sensitivity measures for $y(z)$ colored according to $\mu_i^*(z)$ or $\sigma_i(z) \geq a \cdot \max_z(\sigma_{out}(z))$, d) $\max_z(\mu_i^*(z))$, $\max_z(\sigma_i(z))$ and corresponding height.

15.4 A domain including a single tree

The influence of varying tree parameters on the stationary wind is investigated. For this, the results of numerical simulations for the domain with a single tree are used to apply the Morris method. The simulation setup presented in section 13 is used. The parameters concerning the tree properties are varied for the Morris method in a parameter range of $\pm 20\%$. The mean value of 0.59 for the approximation for the canopy drag coefficient for unsheltered tree arrays is taken from [3, p. 10]. The parameters which are modified and the corresponding bandwidths are shown in Table 13. The BAD inside the trunk takes the

value $1 \text{ m}^2\text{m}^{-3}$. If the trunk diameter is smaller than the grid size, the PALM program for the creation of trees weights the BAD in the corresponding grid cell by the circular area occupied by the trunk. Also, when calculating the LAD, the vegetation percentage is considered based on the extent of the crown in the grid cell under consideration. Ten trajectories, six parameters and thus $10 \cdot (6 + 1) = 70$ samples are used. The effect of the

Table 13: Input parameters and their bandwidth for the single tree.

Parameter	Name	Bandwidth	Description
h	x_1	(9.6 - 14.4) m	tree height
h_c/d_c	x_2	0.8 - 1.2	ratio of crown height and crown diameter
LAI	x_3	2.4 - 3.6	leaf area index
d_c	x_4	(3.2 - 4.8) m	crown diameter
d_t	x_5	(0.28 - 0.42) m	trunk diameter
c_d	x_6	0.47 - 0.71	canopy drag coefficient

input parameters on the wind conditions around the position of the tree is studied using the Morris method. The horizontal distributions of the Morris measures $\mu_{i,j}^*(x, y)$ are determined for the horizontal wind speed $\sqrt{u^2 + v^2}^{(1h)}$ in the height of 10 m ($y_{j=1}(x, y)$), which is within or slightly above the tree crown, and in the pedestrian area in a height of 1.5 m ($y_{j=2}(x, y)$). Furthermore, the vertical distributions of the Morris measures $\mu_{i,j}^*(x, z)$ are determined for $\sqrt{u^2 + v^2}^{(1h)}$ ($y_{j=3}(x, z)$) and the w component of the wind ($y_{j=4}(x, z)$) at $y=20$ m through the middle of the tree. The w component is used for the investigation of variations in the over- and underflow of the tree crown. The considered outputs are summarized in Table 14. The standard deviations of the outputs under consideration

Table 14: Single tree setup: List of the model results and the cross-sections considered.

j	model result	cross-section
1	$\sqrt{u^2 + v^2}^{(1h)}$	horizontal, $z=10$ m
2	$\sqrt{u^2 + v^2}^{(1h)}$	horizontal, $z=1.5$ m
3	$\sqrt{u^2 + v^2}^{(1h)}$	vertical, $y=20.5$ m
4	$\bar{w}^{(1h)}$	vertical, $y=20.5$ m

$\sigma_{\text{out},j}(x, y)$ and $\sigma_{\text{out},j}(x, z)$ are calculated at each point of the considered cross-sections. Visualizations can be found in Figure 39 for $j \in \{1, 3\}$ as the standard deviations for the other considered model results are comparably small. Remember that the tree center is positioned at $x=80$ m, $y=20$ m, which is visualized through a green cross. The standard deviation of the 10 m wind speed given in Figure 39 a) takes increased values around and behind the tree position. The values of the standard deviation of the 1.5 m wind speed are comparably small and hence not shown here. This is probably due to the distance from the tree crown and the generally smaller wind speed at this height. The vertical cross section of the standard deviation of the horizontal wind speed given in Figure 39 b) shows two regions of larger values. They are located at the height of the upper and lower crown region at positions that are covered by the crown for only some samples. The coverage of the position by the crown results in a reduced wind speed. For other samples, the positions are not covered by the tree crown, which leads to an over- or underflow of the crown in these regions. This leads to a comparably large standard deviation at these positions. The standard deviation of the w component of the wind is

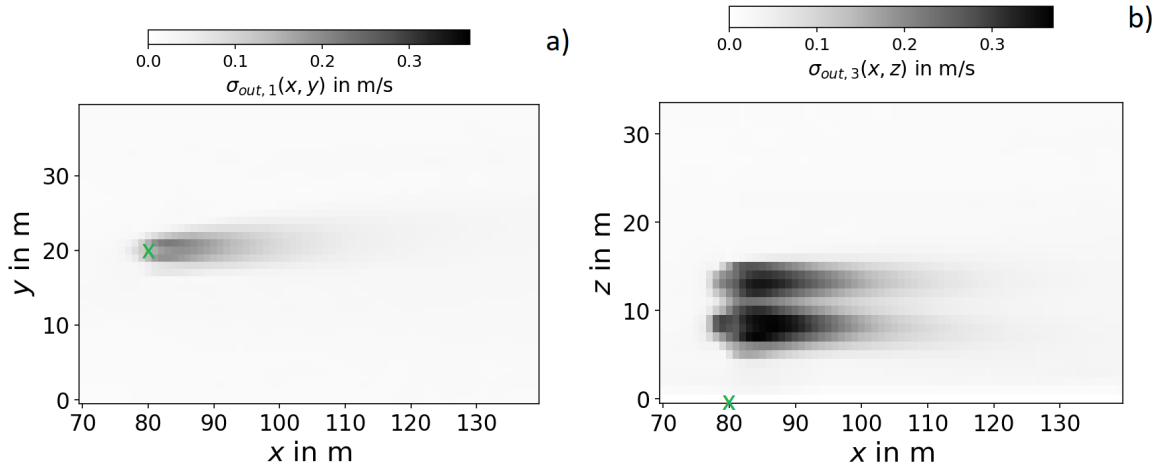


Figure 39: Single tree setup: Standard deviations a) $\sigma_{out,1}(x, y)(z = 10 \text{ m})$, b) $\sigma_{out,3}(x, z)(y = 20 \text{ m})$.

also comparably small and hence not shown here. In a further step it will be checked which parameters are responsible for the output variations using the Morris sensitivity measures. In order to be able to evaluate the resulting measures, the standard deviation of the model output is used as it was described in Chapter 6.6. Based on the standard deviation, a threshold is required to compare the sensitivity measures to. It is decided to use a fixed threshold for the whole domain, which allows for giving information on the local influences of the input parameters on the output variation compared to the largest output variations within the domain. Therefore, the largest standard deviation $\sigma_{out,max}$ in the domain is determined according to $\sigma_{out,max} = \max(\max_{x,y,z}(\sigma_{out}(x, y, z)), \max_{x,z}(\sigma_{out,4}(x, z)))$.

$\sigma_{out}(x, y, z)$ is the standard deviation of the horizontal wind speed $\sqrt{u^2 + v^2}^{(1h)}$ calculated at each grid point. For the variation of the input parameters in the considered range of $\pm 20\%$ the largest variations in the output occur in the vertical cross-section $j = 3$ (Figure 39 b)) at the point $(x=87 \text{ m}, y=20 \text{ m}, z=7.5 \text{ m})$, i.e. behind the tree, with $\sigma_{out,max} = 0.36 \text{ ms}^{-1}$.

For each input and output quantity the maximal sensitivity measures

$$\mu_{i,j}^* = \begin{cases} \max_{x,y} \mu_{i,j}^*(x, y) & , \text{ x, y-cross-section} \\ \max_{x,z} \mu_{i,j}^*(x, z) & , \text{ x, z-cross-section} \end{cases}$$

and

$$\sigma_{i,j} = \begin{cases} \max_{x,y} \sigma_{i,j}(x, y) & , \text{ x, y-cross-section} \\ \max_{x,z} \sigma_{i,j}(x, z) & , \text{ x, z-cross-section} \end{cases}$$

are determined. They are given in Figure 40. The color of each cell is chosen according to $\mu_{i,j}^*$ or $\sigma_{i,j} \geq a \cdot \sigma_{out,max}$ and is blue for $a = 0$ and green for $a = 1$. Since the point at which the largest output variation occurs is included in the vertical cross-section $j = 3$, the largest Morris measure can be found there caused mainly by the tree height (x_1). The tree height (x_1), the ratio of maximum crown height to the maximum crown diameter (x_2), the crown diameter (x_4) and the drag coefficient (x_6) are involved in interactions. The variations of the horizontal wind speed at the reference heights of 10 m and 1.5 m and the variations of the vertical component of the wind at $y=20.5 \text{ m}$ are smaller, but

also mainly induced by the variation of the drag coefficient (x_6) and the tree height (x_1), respectively.

	x_1	x_2	x_3	x_4	x_5	x_6	x_7
$\mu^*_{i,1}$ [m/s]	0.2934	0.1376	0.0359	0.0418	0.1173	0.0312	0.2299
$\sigma_{i,1}$ [m/s]	0.493	0.282	0.0604	0.066	0.2101	0.0521	0.1727
$\mu^*_{i,2}$ [m/s]	0.0355	0.0433	0.035	0.0383	0.0379	0.0342	0.0707
$\sigma_{i,2}$ [m/s]	0.052	0.0726	0.06	0.0659	0.0637	0.0608	0.0683
$\mu^*_{i,3}$ [m/s]	0.5951	0.2142	0.0403	0.0464	0.2093	0.0466	0.2646
$\sigma_{i,3}$ [m/s]	0.6408	0.4349	0.0674	0.079	0.4352	0.0635	0.4801
$\mu^*_{i,4}$ [m/s]	0.1288	0.0469	0.0112	0.0168	0.0521	0.0065	0.0793
$\sigma_{i,4}$ [m/s]	0.1725	0.1034	0.0205	0.0296	0.1041	0.0125	0.1403

Figure 40: Single tree setup: Colored table for the measures $\mu^*_{i,j}$ and $\sigma_{i,j}$.

Since the point with maximal output standard deviation is located directly behind the tree, specific points around 5 m, 10 m and 30 m behind the tree crowns largest horizontal extent at the reference heights of 10 m and 1.5 m given in Table 15 are additionally considered and the impact of the input parameters on the local standard deviation are studied. The locations are visualized in Figure 41.

Table 15: List of the model results and the points considered.

j	model result	point
5	$\sqrt{u^2 + v^2}$	$x=88$ m, $y=20$ m, $z=10$ m
6	$\sqrt{u^2 + v^2}$	$x=88$ m, $y=20$ m, $z=1.5$ m
7	$\sqrt{u^2 + v^2}$	$x=93$ m, $y=20$ m, $z=10$ m
8	$\sqrt{u^2 + v^2}$	$x=93$ m, $y=20$ m, $z=1.5$ m
9	$\sqrt{u^2 + v^2}$	$x=113$ m, $y=20$ m, $z=10$ m
10	$\sqrt{u^2 + v^2}$	$x=113$ m, $y=20$ m, $z=1.5$ m

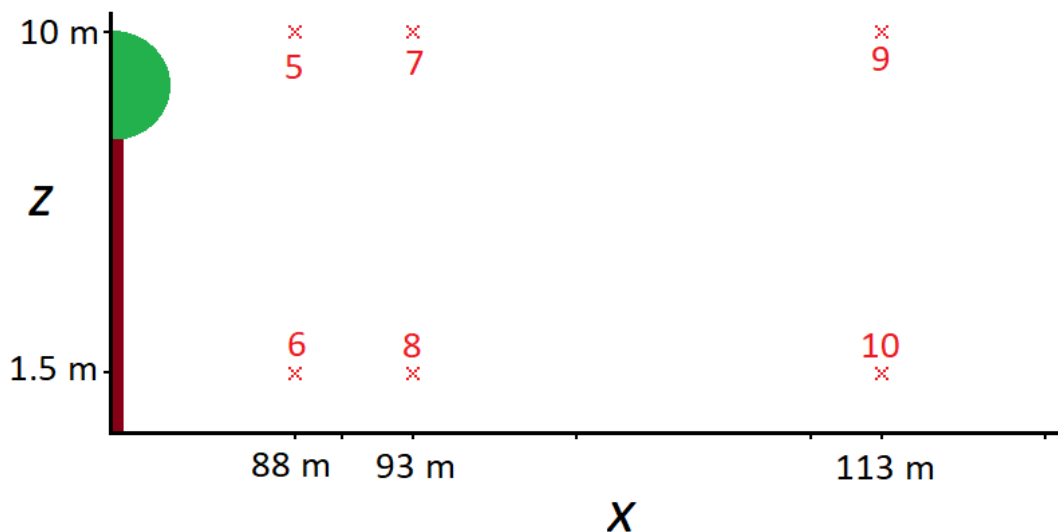


Figure 41: Single tree setup: Visualization of the locations for the evaluation.

	x_1	x_2	x_3	x_4	x_5	x_6	$\sigma_{out,j}$
$\mu^*_{i,5}$ [m/s]	0.1873	0.114	0.0196	0.1069	0.02	0.2015	0.1761
$\sigma_{i,5}$ [m/s]	0.3138	0.2223	0.0411	0.1654	0.0335	0.1696	
$\mu^*_{i,6}$ [m/s]	0.0257	0.0322	0.0147	0.0292	0.0121	0.0418	0.0366
$\sigma_{i,6}$ [m/s]	0.0366	0.0544	0.0271	0.0487	0.0213	0.0561	
$\mu^*_{i,7}$ [m/s]	0.1705	0.0847	0.0116	0.1116	0.0227	0.1397	0.1387
$\sigma_{i,7}$ [m/s]	0.2775	0.1593	0.0222	0.16	0.0334	0.1616	
$\mu^*_{i,8}$ [m/s]	0.0211	0.034	0.0174	0.0172	0.0083	0.0383	0.0264
$\sigma_{i,8}$ [m/s]	0.0305	0.0548	0.0307	0.0289	0.0237	0.049	
$\mu^*_{i,9}$ [m/s]	0.0419	0.0317	0.0111	0.0644	0.0272	0.0548	0.0476
$\sigma_{i,9}$ [m/s]	0.0715	0.0558	0.0188	0.0991	0.0407	0.076	
$\mu^*_{i,10}$ [m/s]	0.0091	0.0251	0.0163	0.0343	0.0126	0.0338	0.0279
$\sigma_{i,10}$ [m/s]	0.0142	0.0435	0.0299	0.0632	0.028	0.038	

Figure 42: Single tree setup: Colored table for the measures $\mu^*_{i,j}$ and $\sigma_{i,j}$ at considered points.

The resulting Morris measures are given in Figure 42. The color of each cell is chosen according to $\mu^*_{i,j}$ or $\sigma_{i,j} \geq a \cdot \sigma_{out,j}$, $j \in \{5, 6, 7, 8\}$ and is blue for $a = 0$, green for $a = 1$ and yellow for $a = 2$. The output standard deviation decreases with the distance from the tree, except for 10 m and 30 m behind the tree in a height of 1.5 m, which do not differ much. At every considered point behind the tree, the variation of the drag coefficient (x_6) leads to increased Morris measures. It has an effect at each of the considered points and it is involved in interactions. With $\mu^*_{6,5} = 0.2015 \text{ ms}^{-1}$ the largest impact on the wind speed is reached at 10 m height 5 m behind the tree. The tree height (x_1) has an increased impact on the wind speed at 10 m height in the distances of 5 m and 10 m and is furthermore involved in interactions down to the lower height at larger differences. The ratio of maximum crown height to the maximum crown diameter (x_2) is involved in interactions in both heights at the considered points. Furthermore, it has an increased effect on the wind speed at 1.5 m height and 10 m distance. The diameter (x_4) is involved in increased interactions and shows an increased importance in a distance of 30 m behind the tree.

15.5 Concluding remarks on the application of the Morris method

In Section 15, the Morris method was applied. Values adopted by the elementary effects are determined. They correspond to the variation of the considered model result when the input parameter varies from the minimum to the maximum of its parameter range. Using the mean of the absolute values of the elementary effects, the input parameters can be ranked in order of their influence on the considered output. The values of input parameters concerning surfaces, soil type, and vegetation were varied within different simulation setups describing idealized areas. The simulated variations of the model results resulted from modifications of the energy balance on the surfaces and thus the available energy due to variations in the input parameters. As it was found applying the Morris method to the parameters describing the vegetated surface, the 2 m air temperature is mostly lowered by the leaf area index beginning in the morning. Furthermore, the albedo and the roughness length for heat have an effect, especially in morning and evening hours. When there is no incoming shortwave radiation available, a higher vegetation coverage and heat conductivity between atmosphere and soil were found to result in a higher

air temperature, while an increased roughness length for temperature results in a lower air temperature. The daytime surface temperature is mostly affected by the roughness length for heat. An increase of the values of the leaf area index and the roughness length for momentum also lead to decreases of the surface temperature. An increase of the roughness length for momentum leads to a decrease of the 10 m wind speed, but to an increase of UTCI. In case of paved surfaces, the roughness length for momentum, the heat conductivity of the pavement, the albedo and the emissivity were found to have the largest impacts on the considered model results. In the investigations for the 3D vegetation described in Chapters 15.3 and 15.4, the tree shape was found to have an increased effect on the wind. Furthermore, the tree height, the drag coefficient (especially for the single tree), the crown diameter and the ratio of the height and width of the tree crown have a major influence.

16 Application of the uncertainty analysis using LHS

The input parameters of a model can be ranked in order of their influence on the considered model results applying the Morris method. This ranking allows for further studies with a reduced number of input parameters to be investigated. With the input parameters found to have an increased influence on the considered model results an uncertainty analysis can be performed in order to further study their effects and estimate the required accuracy of the input parameters for the considered PALM model setup using the LHS sampling strategy presented in Chapter 7. An exemplary application of this approach is presented in this chapter.

The setup for the horizontally homogeneous paved surface presented in section 11 is used. The roughness length for momentum (x_1), the heat conductivity of the pavement (x_4), the albedo (x_5) and the emissivity (x_6) were found to have the largest impacts on the considered model results in Chapter 15.2. Therefore, they are used in this investigation and LHS samples are created from their bandwidths given in Table 11. As described in Chapter 7, the LHS is based on the division of the range of the CFD of the considered input parameter into n intervals and within each of these intervals one value is randomly picked. The number n corresponds to the number of the required model runs. In the given example, $n = 300$ is chosen to achieve a good coverage of the input parameter space. The mean values are assumed for the remaining parameters, which were not found to have strong effects on the model results. Since the application of the Morris method indicated a strong effect of the albedo on maximum temperature, this input parameter and model result are in the focus of the following exemplary study. Figure 43 shows the dependency of the hourly and horizontally averaged 2 m air temperature at 16 UTC on the albedo, which is nearly linear. 16 UTC was chosen because most of the time series obtained from the Morris samples take their diurnal maximum at this time, see Figure 33 b). A regression with a correlation coefficient $R=-0.9707$ was performed. Furthermore, the values of the albedo leading to a ± 0.25 K-variation of the air temperature were determined, since this variation results in a temperature interval of 0.5 K which corresponds to the permissible absolute deviation for the air temperature given in Table 3. The dotted lines in Figure 43 mark the values of the albedo for an increase/decrease of 0.25 K. Thus, in the given case, the uncertainty of the albedo should not increase $0.25-0.18=0.07$ in order to predict 2 m air temperature with an accuracy of 0.5 K. Ryan et al. [56] presents a method to obtain the albedo with centimeter resolution and accuracies of $\pm 5\%$, which would be in the magnitude of 0.01, from digital cameras and unmanned aerial vehicles. Furthermore, the results visualized in Figure 43 can be used to estimate the expected uncertainty of the output when the input parameter, in the given case the albedo, is only known with a given

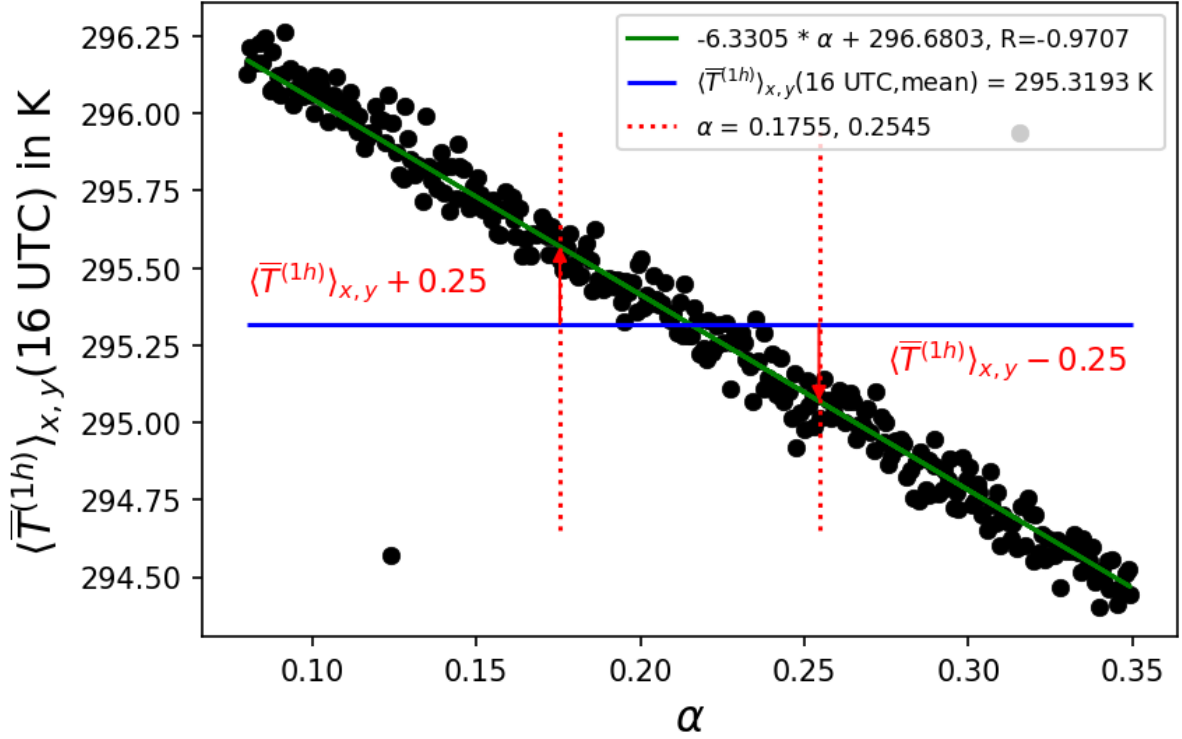


Figure 43: Paved surface: Dependency of the hourly and horizontally averaged 2 m air temperature at 16 UTC on the albedo and regression.

uncertainty. Let the uncertain albedo be $0.25 \pm 20\%$, i.e. it is known to be within the interval $[0.2, 0.3]$. Thus, using the regression function, the 2 m air temperature modeled with the given setup will lie within the interval $[294.78 \text{ K}, 295.41 \text{ K}]$.

17 Investigations for an urban area including green and blue elements

The aim of this chapter is an uncertainty and sensitivity analysis for a complex urban area. Using the urban surface model, the indoor model, the land surface model and the radiation model, the influence of various input parameters on the considered model results in the urban area or uniformly characterized sub-areas shown in Figure 20 is studied and compared in order to find out for which parameters a particularly precise data collection is required. The considered model results are the diurnal cycles of the wind speed at 1.5 m and 10 m height, the 2 m air temperature, the surface temperature, the biometeorological quantity UTCI and the indoor temperature. Among the input parameters studied are those related to green and blue surfaces, as these are suitable for climate change adaptation measures and their effects should therefore be reliably modeled, which requires an appropriate accuracy of the input parameters.

The study of the input parameters for the urban domain is also focusing on autochthonous weather conditions which are characterized by a strong daytime insolation, weak winds and a stable nocturnal stratification, since the urban climatic characteristics are particularly pronounced, then, and a strong heat stress is possible [38, pp. 2, 3, 8], [26, p. 2].

17.1 Simulation overview and analysis method

As the relationships between input parameters and model results are mostly non-linear, the Morris method was used in the preliminary investigations in order to be able to make statements about interactions between the parameters. A large parameter space is necessary for the already computationally intensive urban setup, which is why the application of the Morris method cannot be carried out, since it would exceed the computational time capacities. For this reason, a parameter or a parameter group represented by a type is varied only once, while the other parameter (groups) are kept constant and are fixed on meaningful values that occur typically in reality. This allows for the investigation of uncertain type classifications. If the variation of a type has a major influence on the output under consideration, the studies described in section 15 can be used to infer the parameters responsible for the relevance. It is worth mentioning here that in PALM there is a classification of many parameters into different types, e.g. vegetation types, for which default values are specified for the associated parameters.

A total of 23 simulations are carried out. Table 17 gives an overview of the varied parameters of the simulations carried out. The parameter values used in a reference simulation are listed in Table 8.

In addition to the **reference** simulation, the analysis can be divided into three scenario packages. In scenario package **S1** the land-surface parameters, in **S2** parameters regarding the 3D vegetation and in **S3** building parameters are varied. The **reference** simulation was described in Chapter 14. The default type and the associated default parameters are used for all trees, buildings and the soil. Furthermore, asphalt is used for streets, cobblestones are used in squares and in inner courtyards and short grass as vegetation type on the unpaved surfaces.

In **S1** the water temperature, as well as the pavement type, the vegetation type and the soil type are varied. The variation of the parameters within the types has already been investigated in Chapters 15.1 and 15.2 and is now compared to the one of other urban parameters. The water temperature is set to the default value given by PALM, 283 K. This might be quite cold for the simulated summer day, which is why the water temperature is set to 293 K in S1.1 in order to investigate whether the use of the default value is sufficient. In **S2** there is a basic run without trees to determine their general influence on atmospheric quantities. In a further setup, different tree types predefined in PALM are used and the results are compared with the setup with the default types. Here a spherical shape is used for all trees. A changed spherical tree type can lead to different trunk diameter at breast height, tree height and crown diameter. In a further run (S2.3, see Table 17), the influence of the tree shape is to be examined by changing it and comparing the result to the one from the previous run from S2.2 with the spherical shaped tree types. In S2.3, the shape of the trees is therefore changed from the one used in S2.2. Frequencies of the different tree shapes in an urban area are assumed to create samples. The inverted shapes are assumed to be less probable with 10 % each, the remaining shapes are assumed to have a frequency of 20 % each. The tree shape distribution in the considered area is given in Table 16.

To represent the trees, the leaf area density and the basal area density are specified on the basis of various parameters. If this information about individual trees is missing, as mentioned in Chapter 3.2, an idealized vertical LAD distribution can be determined from a leaf area index and two parameters α_{LAD} and β_{LAD} and a vegetation height for every location on the horizontal plane. Hence, a tree can be constructed only knowing the vegetation height at every location and calculating a vertical LAD at this position from a LAI and the shape parameters α_{LAD} and β_{LAD} . This method to create patch data is to be used in a subsequent simulation based on the vegetation height field and LAI used in

Table 16: Frequency distribution of the tree shapes in the urban area.

shape	number of trees	frequency of the total number of trees
spheres and ellipsoids	57	16 %
cylinder shapes	78	22 %
cone shapes	75	22 %
inverted cone shapes	27	8 %
paraboloid shapes	72	21 %
inverted paraboloid shapes	39	11 %
sum	348	100 %

S2.2 in order to examine the necessity of the other parameters for characterizing trees by comparing the results to those from S2.2. To clarify the modification of the representation of the trees, exemplary resulting LADs are visualized in Figure 44. The figure shows exemplary vertical cross-sections in the park at $x = 0 \text{ m} - 175 \text{ m}$, $y = 48 \text{ m}$, $z = 0 \text{ m} - 26 \text{ m}$ of LAD for S2.2 (a)), where different spherically shaped tree types are used, S2.3 (b)), where additionally the different shapes are used, and S2.4 (c)), where idealized vertical LAD distributions are determined from the LAI, the two shape parameters α_{LAD} and β_{LAD} and a two-dimensional vegetation height field based on S2.2. In S2.2, the trees differ in tree height and crown diameter. It is also visible that the leaf area increases towards the outside as mentioned in Chapter 3.2. In S2.3, tree height and crown diameter of the individual trees are taken from S2.2 and they additionally differ in tree shape. Hence, compared to S2.2, different air volumes are covered with the tree crown. Figure 44 c) visualizes that at every location - in this case on the x -axis - up to a height taken from S2.2, a vertical LAD is specified. Compared to the trees from S2.2, where the leaf area increases exponentially towards the outside, using the patch data, a maximum appears at higher levels of the tree crown and a soft demarcation from the surrounding area occurs. These properties are transferable to the remaining trees in the simulation domain. In the preliminary investigations described in Chapters 15.3 and 15.4, the tree shape was found to have an increased effect on the wind. Furthermore, the preliminary investigations allow conclusions to be drawn about a major influence of the tree height, the drag coefficient (especially for the single tree), the crown diameter and the ratio of the height and width of the tree crown, which is why these are varied separately in the following simulations and their influence in urban areas is investigated on the wind, but also on the other considered simulation results. In **S3**, the influence of the variation of building parameters on the considered model results mentioned at the beginning of this chapter is investigated. The building type and thus the associated default building parameters are varied in S3.1 and take the values of a newer building type built after 2000. In two further simulations, S3.2 and S3.4, the facade color is varied via the albedo and the window fraction is varied, respectively. Facade and extensive roof greening¹ is added to the wall and roof surfaces of the buildings, respectively, and its influence on the considered model results mentioned at the beginning of this chapter is determined. In the literature, green roofs were found to provide greater cooling potential than light roofs, since the latter reflect the radiation to other surfaces and may lose up to one-third of their reflectivity in a few years [54, pp. 10, 11]. In order to be able to estimate possible interactions of the effect of albedo, window fraction and facade greening with the effect of building type on the model results, the corresponding simulations are also carried out with the more modern building type

¹There are extensive and intensive green roofs. Extensive green roofs generally use shallow growing medium and vegetation. Furthermore, they are only entered for maintenance and care [7, pp.6,7].

used in S3.1. Following remark has to be made concerning the window fraction: In S3.4, the window fraction is set to 0.29. Since this is the value that is assigned to the window fraction by default in case of the newer building type, it is changed to the default value for this parameter in case of the reference building type such that the size of the variation is comparable.

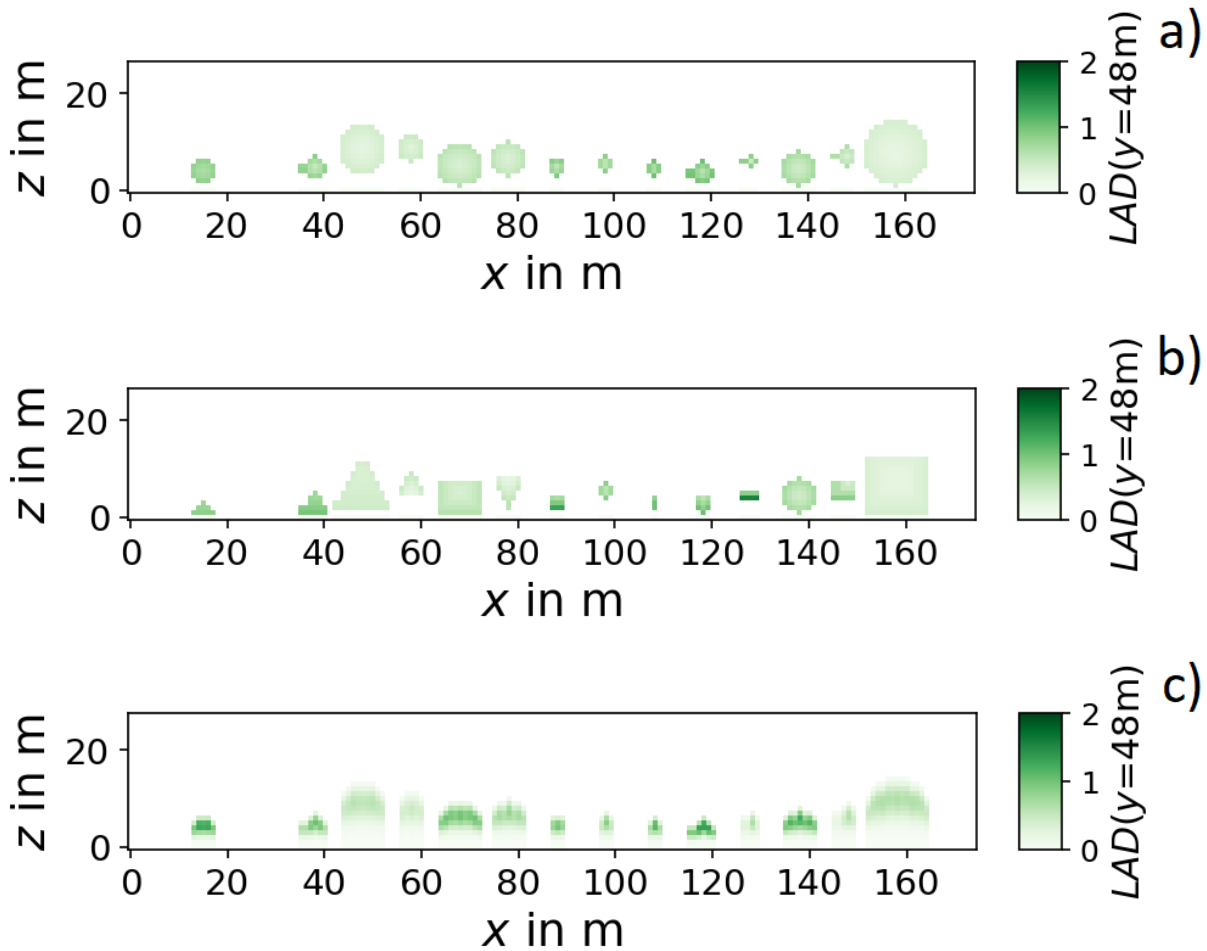


Figure 44: Vertical cross sections for LAD distribution in the park at $y = 48$ m for a) S2.2, b) S2.3 and c) S2.4.

The analysis methods is applied in the post-processing. Therefore, time series of hourly and spatial averaged data for the different scenarios and the respective difference to the reference data are calculated and visualized for different averaging areas in order to be able to make separate statements for selected land uses. These different sub-domains are visualized in Figure 20 and contain the park, the open place, street canyons, single houses with gardens and the court yard, respectively, each including pedestrian area. Furthermore, local differences between diurnal or hourly averaged scenario and reference data are taken at the grid points of the model domain and investigated. Their bandwidths are given using box plots and their horizontal distributions are visualized. In addition, local vertical profiles of differences between diurnal averaged scenario and reference data and between the hourly averaged ones at the diurnal extrema extracted at the representative locations M_i , $i \in \{1, \dots, 6\}$ are given. In Chapter 14, it was mentioned that the 2 m air temperature and the 10 m wind speed are terrain following, i.e. PALM delivers them in 2 m or 10 m above the ground which can be either soil or roof surface. Trees do not affect the height at which the output takes place. Also, the given surface temperature includes

Table 17: Simulations for the urban area.

The scenarios, the parameter (type)s to be varied, their values or properties and the number of simulations n in the scenario package are given.

scenario	parameter (type)	value/properties	n
reference			1
S1: land-surface parameters			4
1	water temperature	293 K	
2	pavement type:	concrete:	
	z_0	0.05 m	
	$z_{0,h}$	$0.5 \cdot 10^{-3}$ m	
	α	0.35	
	ϵ	0.9	
	Λ_p	$1.51 \text{ Wm}^{-1}\text{K}^{-1}$	
	C_p	$2.11 \cdot 10^7 \text{ JK}^{-1}\text{m}^{-3}$	
3	vegetation type:	tall grass:	
	$r_{c,\min}$	100.0 sm^{-1}	
	LAI	$2 \text{ m}^2\text{m}^{-2}$	
	c_{veg}	0.7	
	z_0	0.47 m	
	$z_{0,h}$	$0.47 \cdot 10^{-2}$ m	
	Λ	$10.0 \text{ Wm}^{-2}\text{K}^{-1}$	
	C_0	$0 \text{ Jm}^{-2}\text{K}^{-1}$	
	ϵ	0.97	
	α	0.18	
4	soil type:	medium granularity:	
	α_{vG}	3.14	
	l_{vG}	-2.342	
	n_{vG}	1.28	
	γ_{sat}	$1.16 \cdot 10^{-6} \text{ ms}^{-1}$	
	m_{sat}	$0.439 \text{ m}^3\text{m}^{-3}$	
	m_{fc}	$0.347 \text{ m}^3\text{m}^{-3}$	
	m_{wilt}	$0.151 \text{ m}^3\text{m}^{-3}$	
	m_{res}	$0.010 \text{ m}^3\text{m}^{-3}$	
	$r_{\text{soil},\min}$	50 sm^{-1}	
	T_{deep}	287 K	
S2: 3D-vegetation			8
1	no trees		
2	different spherical tree types		
3	different tree types of different shapes		
4	only height according to different tree types: patch data		
5	h	14 m	
6	h_c/d_c	1.2	
7	d_c	4.8 m	
8	c_d	0.376	
S3: building parameters			10
1	building type	residential, built after 2000	
2	α_{wall}	0.3	
3	α_{wall} , building type	0.3, residential, built after 2000	
4	window fraction	0.29	
5	window fraction, building type	0.18, residential, built after 2000	
6	green fraction	0.18	
7	green fraction	0.29	
8	green fraction, building type	0.18, residential, built after 2000	
9	green fraction, building type	0.29, residential, built after 2000	
10	green roof	extensive roof greening	
sum			23

roof surfaces. In case of terrain following model outputs, their values at building positions were not considered for consistency to exclude above roof values.

17.2 Presentation of the analysis results

In the following, the analysis results for every considered model result are described using exemplary figures. The next chapter comes up with explanations for the simulated results. Since the UTCI is an important measure for the human comfort, the effects on this quantity will be investigated in more detail in Chapter 17.2.5. Representative figures which were created for every model result and sub-area are given for the UTCI. Additionally, one figure showing the diurnal cycle is given for each output. Further figures can be found in the appendix in Chapter 21.3.

17.2.1 2 m air temperature

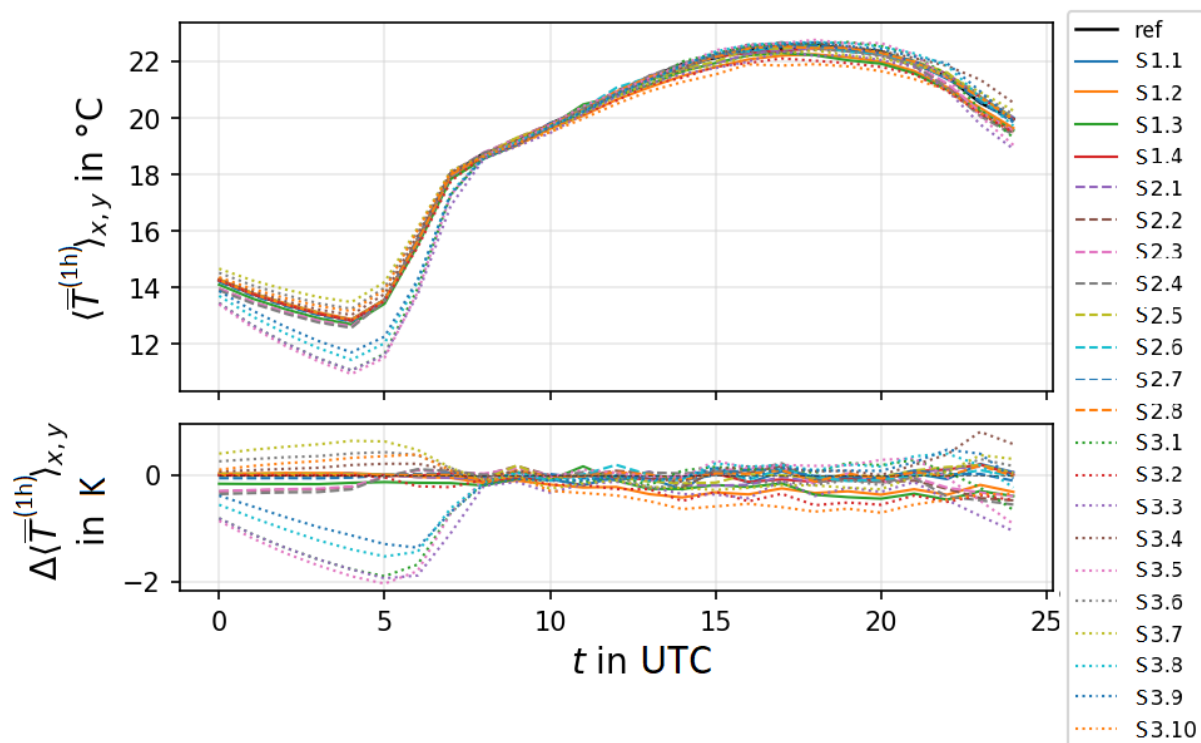


Figure 45: Time series of hourly and spatial averaged 2 m air temperature for the different scenarios and the respective difference to the reference temperature, total domain.

This chapter describes the influence of the changes in the input parameters on the 2 m air temperature. Figure 45 shows the time series of hourly and spatial averaged 2 m air temperature for the different scenarios and the respective difference to the reference temperature. The averaging domain is the total urban domain. The minimum is taken in the early morning and the temperature maximum occurs in the late afternoon for all scenarios. The largest variations of the hourly averaged 2 m air temperature occur around the diurnal temperature minimum in the morning, where the largest decreases of nearly -2 K in domain average are also induced by scenarios with the building type changed to a newer type that indicates that the building was built after 2000 (S3.1, S3.3, S3.5). The largest decreases occur in court yards, as these areas are surrounded by building walls, which is not shown here. Temperature variations concerning the total domain are smaller

during day time and at the temperature maximum than during night and early morning, since the reduction of heat emission due to a newer building type seems to overweight the effects of the other parameters. The largest variation concerning the whole area is a temperature decrease of -0.5 K due to green roofs and an increased wall albedo. The diurnal averaged local differences (Figure 72 a) in the appendix) show similar behavior for every considered sub-area. They also show the largest median response of -0.7 K (-0.6 K for the open place, not shown here) in scenario S3.3 when the wall albedo is increased and the building type is changed to the one for buildings built after 2000, what both - especially the change of the building type - lead to reductions of the diurnal averaged temperature themselves. Increasing the buildings green fraction (S3.8, S3.9) weakens this decrease. In case of the buildings being built before 1950, the green walls lead to a morning temperature increase compared to the reference situation without green walls, which is reflected in the diurnal average. A larger (smaller) window fraction also leads to an 2m air temperature increase (decrease) at night (S3.4 (S3.5)). An influence on the considered sub-domain is also visible in case of the temperature. In the park and in the area of single houses, the vegetation type also has an increased influence in the afternoon in shadowed areas concerning the temperature maximum, which is reached earlier, followed by a temperature decrease of around -0.5 K until the end of the simulation in the night. The resulting time series for the park are given in the appendix in Figure 71 a). At locations, that are exposed to the sun light, temperature increases are simulated (not shown here). Furthermore, the diurnal averaged local differences (Figure 72 a) in the appendix) show an increased median response of -0.2 K for S1.2 and S1.3 with decreases of -0.5 K and -0.7 K locally, respectively, concerning the whole area. The strongest dependency of the effect of a variation in the input parameters on the locations is visible in the scenarios S2.2, S2.3, S2.4 and S2.7. At some locations larger variations occur. This is the case around tree positions and the variation depends on the way of the tree type and shape change and the corresponding differences in irradiation and radiance. Using the park as the evaluation domain, the time series of the hourly and domain averaged differences shows a slightly increased influence of the tree parameters (S2.2, S2.3, S2.4) during night compared to the average over the whole domain, see Figure 71 a). Averaging over the open place (see Figure 71 b) in the appendix) shows smaller effects in the morning due to buildings. Furthermore, the change of the pavement type does not show a large effect at the open place since the used different pavement types have nearly the same albedo. The magnitude of the results is consistent with the one found in [4].

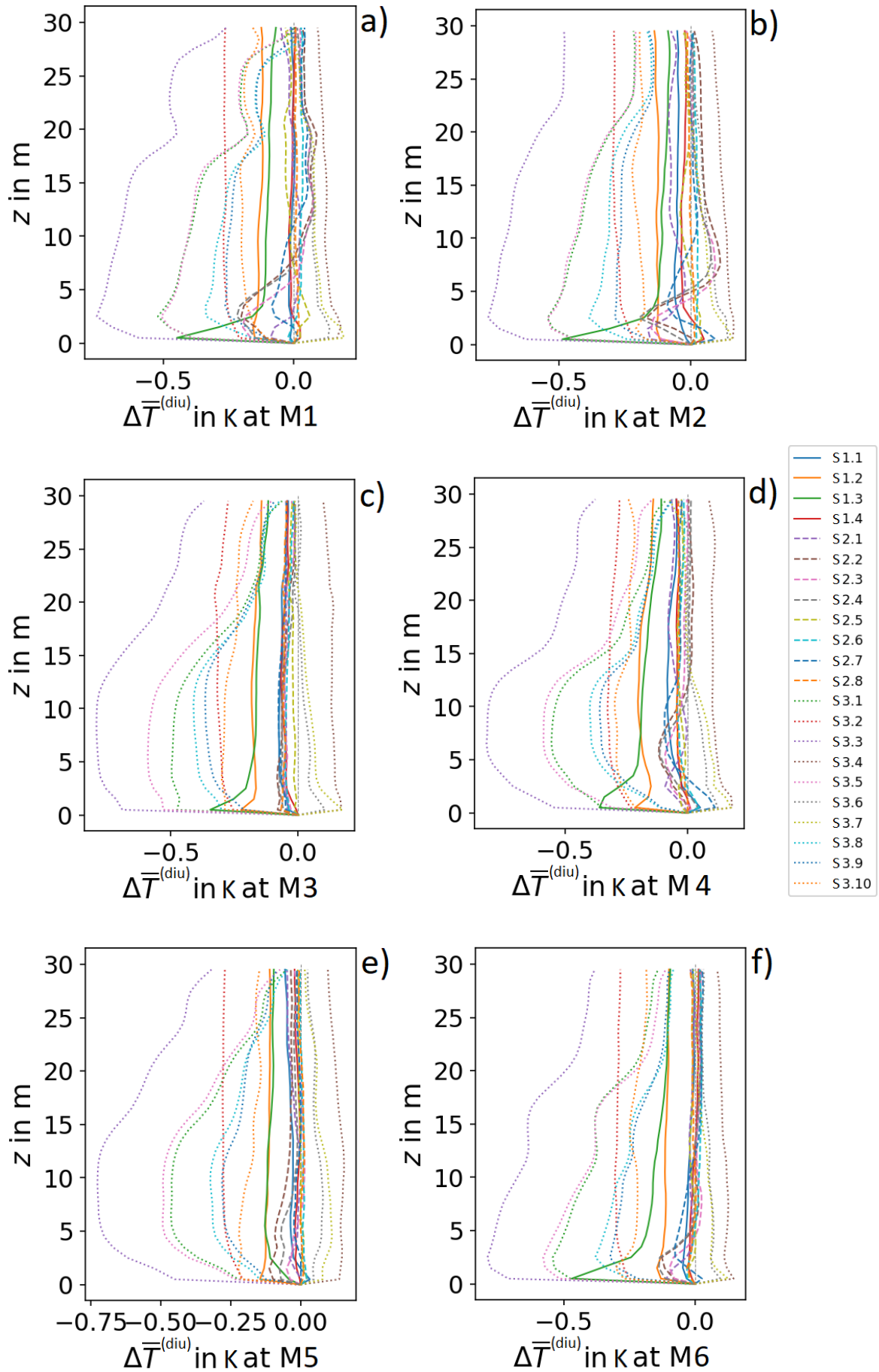


Figure 46: Local vertical profiles of differences between diurnal averaged scenario and reference air temperature extracted at the representative locations M_i , $i \in \{1, \dots, 6\}$.

The local vertical profiles of the differences between the diurnal averaged scenario and reference air temperature visualized in Figure 46 show the largest decrease for S3.3 at every considered position. Changing the building type to a newer one - especially up to building height at 10 m or 20 m, respectively - and increasing the wall albedo thus lead to the prominent decrease of air temperature. Furthermore, a decrease of the window fraction and a change of the pavement type lead to a temperature decrease. Except at M5, the change of the vegetation type to higher grass leads to a temperature decrease as well, especially at the lowest levels. This can also be seen for S2.1, S2.2, S2.3 and S2.4. An increased window fraction and an increased green fraction lead to a temperature increase. Figure 73 in the appendix shows the local vertical profile differences for 4 UTC and 17 UTC. For the temperature minimum at 4 UTC, the largest overall effect can be found when the building type is changed to the newer one with a change of -2 K up to building height. An additional small temperature decrease can be seen for additionally decreasing the window fraction (S3.5). Scenarios S3.7 and S3.10 at higher levels lead to the largest temperature increases of nearly 1 K. The effect of tree parameters on the temperature minimum is comparably small at the considered locations. In the densely vegetated part of the park at position M2, the effect is up to -1 K. At this location, the variation includes a decreased height and an increased crown diameter of the surrounding trees (not shown here). In the lower height levels, that do not contain leaf area in the reference, but do in the scenario runs, the temperature decrease occurs due longwave emittance from the tree crown. At the temperature maximum at 17 UTC, the largest over all effect of about -0.6 K is induced by S3.10. An albedo increase follows with up to -0.5 K. Especially in the park, temperature variations due to tree properties occur.

17.2.2 Surface temperature

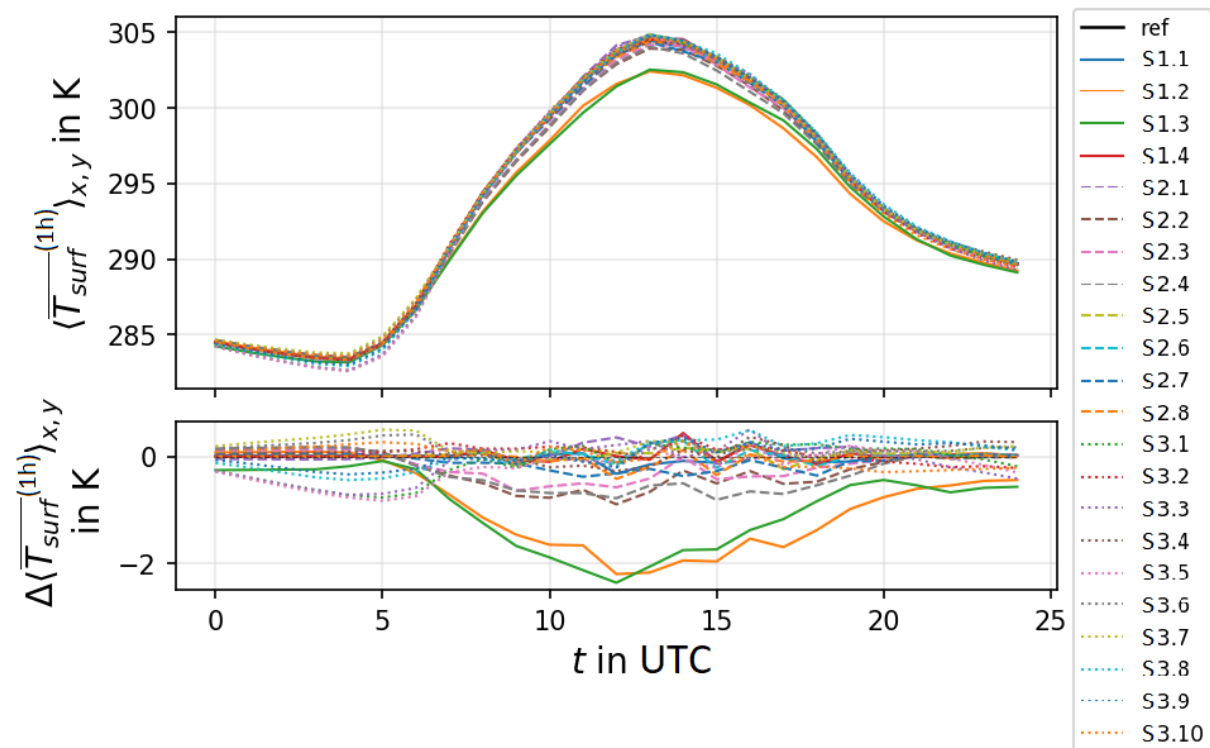


Figure 47: Time series of hourly and spatial averaged surface temperature for the different scenarios and the respective difference to the reference surface temperature, total domain.

Figure 47 shows the time series of hourly and spatial averaged surface temperature for the different scenarios and the respective difference to the reference surface temperature. The averaging domain is the total urban domain. The largest variation of the hourly and domain averaged surface temperature of about -2 K at noon is caused by to a change of the vegetation type (S1.3) and the pavement type (S1.2). In S1.2, the hourly averaged surface temperature is decreased at streets and slightly decreased at the open place and in S1.3, it is decreased at vegetated surfaces, with slighter decreases below trees, not shown here. The dependence on the fraction of the considered varied quantity is again visible, when the values are spatially averaged for the different sub-areas. In the park (Figure 71 c) in the appendix), a strong effect of the vegetation type (-5 K at noon) is visible during day time until night. Furthermore, especially during day time, the effect of tree parameters is increased. There is no effect of the pavement type. Regarding the domains including the single buildings (Figure 71 d)) and the canyons (Figure 71 e)), vegetation type and pavement type show increased influences depending on their fraction. Between the canyons, there is less vegetated surface, hence, the influence of the vegetation type is smaller. At the open place, the pavement type has the largest influence during day time, while the vegetation type has no effect. In the court yard (Figure 71 f)), the magnitude of the effect of the building parameters in the morning equals the one of the tree parameters, the pavement type and the wall albedo during day time. With a mean of -1 K, S1.2 and S1.3 also show the largest deviations in diurnal averaged local differences concerning the whole area, which is visible in Figure 72 b). An increased effect of tree properties varied in S2.2, S2.3 and S2.4 during day time is visible, too. Depending on the location, the effect can be up to -20 K (-6 K) hourly (diurnal) averaged local difference at tree positions corresponding to tree type and shape change and shadowing. The lack of trees realized in scenario S2.1 leads to hourly averaged local differences of up to +10 K at 14:00 UTC (not shown here). During night time, the variations of the hourly and domain averaged surface temperature are smaller than during day time and dominated by scenarios with varied building properties as for the air temperature.

17.2.3 Wind speed

Figure 48 shows the time series of the hourly and spatial averaged wind speed for the different scenarios and the respective difference to the reference wind speed for the 10 m wind (subfigure a)) and the 1.5 m wind (subfigure b)) for the total urban area. Concerning the whole area, the hourly and domain averaged horizontal 10 m wind speed's largest variations occur in the afternoon around the wind speed maximum induced by scenarios of all three packages, eg. for S2.1 in most times an increased wind speed is calculated, while the modifications made in scenario S1.2 lead to a decreased wind speed in most times. In the park (see Figure 71 g)), the largest 10 m wind speed increase due to missing trees appearing during day time is up to $+0.5 \text{ ms}^{-1}$ in the afternoon. This corresponds to an increase of 30 %. Furthermore, the influence of the tree properties is increased. In the sub-domain containing street canyons (not shown here), generally smaller variations occur. During night, those building parameters influencing the temperature and the thermal stratification also have an increased effect on the wind speed. In the morning, a decrease due to the increased wall albedo in combination with the building type for buildings built after 2000 in S3.3, also affecting the thermal stratification, is simulated in every subdomain. Concerning the diurnal averaged local differences shown in Figure 72 c) in the appendix, the largest responses occur for S2.1 with up to 0.5 ms^{-1} at tree positions, and S2.2, S2.3 and S2.4 with up to -0.5 ms^{-1} dependent on the location and the way of tree type and shape change.

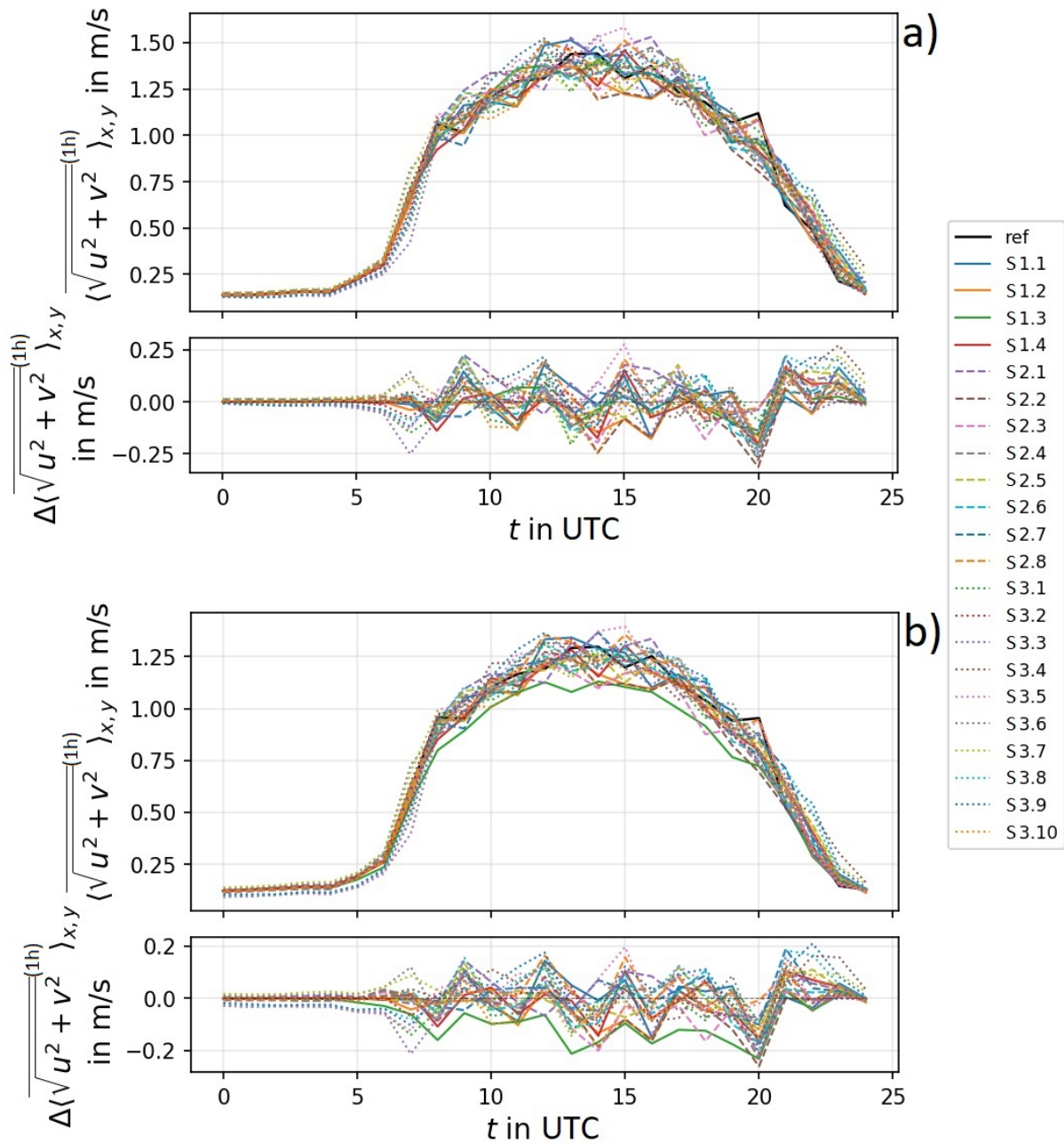


Figure 48: Time series of hourly and spatial averaged wind speed for the different scenarios and the respective difference to the reference wind speed. a) 10 m wind, b) 1.5 m wind.

Furthermore, the effects on the wind speed in the pedestrian area were investigated. Concerning the whole domain, for the hourly and domain averaged horizontal 1.5 m wind speed, the largest variations occur during daytime induced by scenarios of all three packages. The largest decrease is due to the change of the vegetation type to tall grass in S1.3, which can also be seen in diurnal averaged local differences in Figure 72 d). The increase of the hourly and domain averaged wind speed due to missing trees in S2.1 is much smaller in a height of 1.5 m, S1.2 still leads to a decreased wind speed. This can also be found for the park (see Figure 71 h)), where trees are still important, and the largest decrease of up to nearly -0.5 ms^{-1} is due to the vegetation type. Like for the 10 m wind speed, the decrease due to the changes made in scenario S3.3 in the morning occurs in the whole domain. Concerning the diurnal averaged local differences, the largest responses occur for S2.2, S2.3 and S2.4 with up to -0.5 ms^{-1} dependent on the location and the way

of tree type and shape change. The local vertical profiles of the differences between the

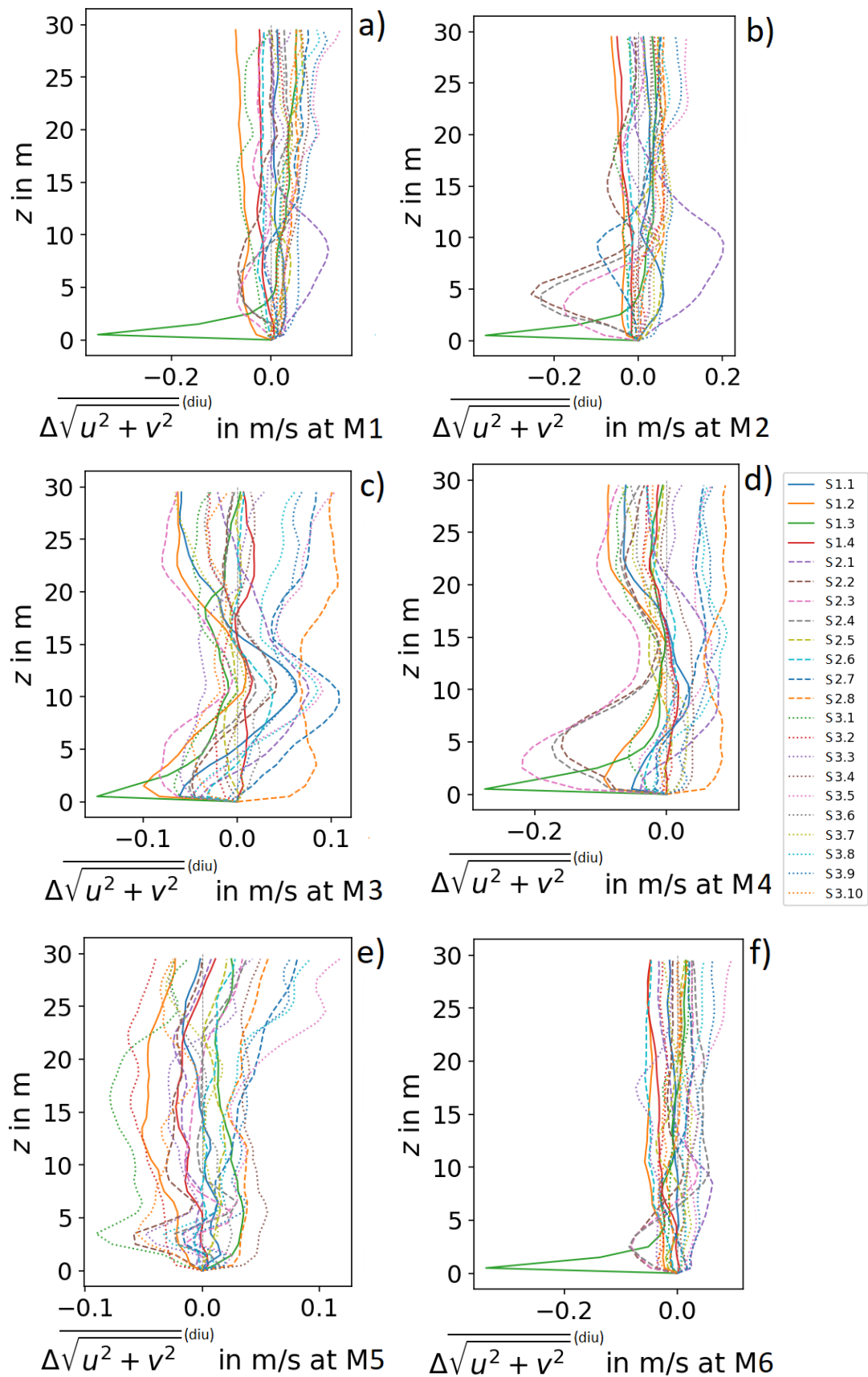


Figure 49: Local vertical profiles of differences between diurnal averaged scenario and reference wind speed extracted at the representative locations M_i , $i \in \{1, \dots, 6\}$.

diurnal averaged scenario and reference horizontal wind speed are visualized in Figure 49 and show a decrease of the wind speed at lower levels for the modified vegetation type in scenario S1.3 except at M5, since M5 is at the open place where the surface is not vegetated. Especially at M2, a place with high tree density, the lack of trees in scenario S2.1 leads to an increased wind speed. S2.2, S2.3 and S2.4 come along with a wind speed decrease, especially at locations M2 and M4. At M3 and M4, a stronger reduction occurs for scenario S1.2. At location M3, smaller absolute differences occur due to the smaller wind speed and at M5, the influence of obstacles and thus roughness can be neglected. Building parameters, which also lead to temperature and thermal stratification differences at this location, are more important. Note, that the variations have small absolute values, however, they make up a non-negligible proportion of the wind speed given in the profiles in Figure 26.

17.2.4 Indoor temperature

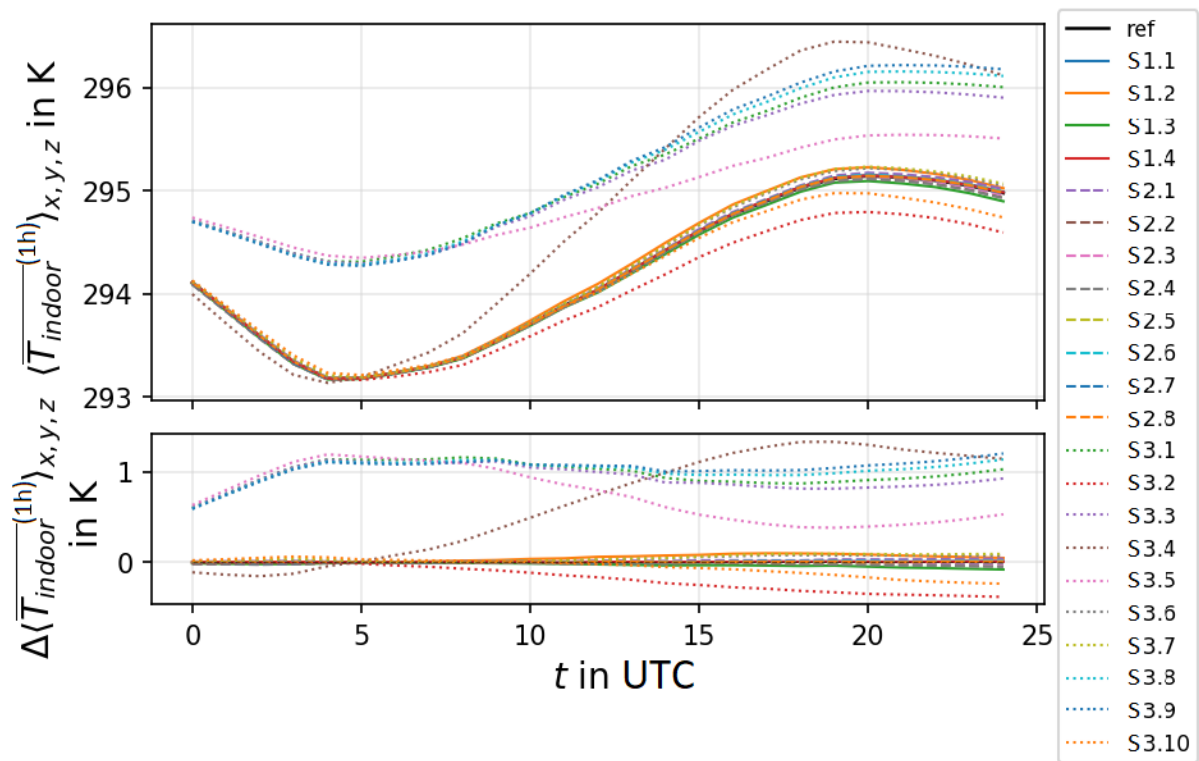


Figure 50: Time series of hourly and spatial averaged indoor temperature for the different scenarios and the respective difference to the reference indoor temperature, total domain.

Figure 50 shows the time series of hourly and spatial averaged indoor temperature for the different scenarios and the respective difference to the reference indoor temperature. The averaging domain is the total urban domain, where every grid point inside a building is considered. The largest variations of the hourly and domain averaged, as well as of the diurnal averaged (see Figure 72 e)) indoor temperature are due to building parameters. Setting the building type to the newer one results in a higher temperature minimum in the morning and to a higher indoor temperature maximum in the evening, but with a slightly lower increase during day. The larger window fraction used in scenario S3.4 leads to the largest increase of the indoor temperature maximum after a stronger temperature increase during day. The hourly averaged local differences can reach up to +9 K at single locations at 18 UTC, which is shown in Figure Figure 72 e) in the appendix. The analog behavior

is visible in S3.5, where the reduction of the window fraction for the newer building type leads to a smaller indoor temperature increase during day. The increased wall albedo for the older building type used in scenario S3.2 leads to a smaller indoor temperature increase during day and thus a smaller maximum of the hourly and domain averaged indoor temperature of -0.5 K. This effect is also visible for the newer building type, but much smaller. In case of the modification of the green fraction at buildings nearly no effect is visible. S3.10 comes along with an indoor temperature reduction beginning at noon. It reaches up to a hourly averaged value of -3 K at some locations in the following night. Looking at the different sub-domains leads to similar results. The hourly and domain averaged data for the small single houses (Figure 71 i)) show a stronger effect of windows. In the court yard (Figure 71 j)), the window fraction and the albedo have a smaller effect.

17.2.5 UTCI

This chapter describes the influence of the changes in the input parameters on the UTCI. Figure 51 shows the time series of the hourly and spatial averaged UTCI for the different scenarios and visualizes the time series of the differences to the UTCI modeled with the reference run. The vertical axis is colored according to the stress categories given in Table 23. Since Figure 51 shows spatial averaged data, the results shown there depend on the fraction of the changed input quantity in the considered averaging domain. Figure 52 presents three horizontal distributions of differences between hourly averaged UTCI modeled with three different scenario runs and the reference run. Figure 53 shows the bandwidths of local differences between diurnal averaged scenario and reference UTCI at 1.5 m. The local differences are taken from the whole urban domain in subfigure a) and from the sub-domain that includes the park in subfigure b) and serve as an addition to the spatial averaged data. Figure 51 shows that the UTCI reaches its minimum in the early morning and its maximum in the early afternoon. Concerning the whole area (subfigure a)), the largest overall variations of the hourly and domain averaged UTCI occur around the minimum, where the largest decreases of more than -1 K - which however does not change the stress category - are induced by scenarios with the building type changed to the newer type indicating that the building was built after 2000 (S3.1, S3.3, S3.5). The strongest decreases occur around and between buildings, which is shown in Figure 52 a). Furthermore, Figure 51 a) shows that an increase of 1 K at the minimum occurs for scenario S3.7, where a green fraction of 29 % is added to the building walls. The effect occurs especially near houses, which is indicated by Figure 51 c) but not further shown. During day time, including the UTCI maximum around 13 UTC, the influence of trees is increased. The scenarios S2.2, S2.3 and S2.4 lead to a UTCI reduction, S2.1 slightly increases the hourly and domain averaged UTCI at noon. The variations mostly occur locally at the tree positions corresponding to tree type and shape change and shadowing. Large local deviations are possible, which can be seen in the horizontal differences distribution at noon presented in Figure 52 c) and which can also be seen in the diurnal averaged local differences presented in Figure 53. Variations at locations that do not directly correspond to tree positions are smaller and might be due to flow changes and thus wind speed changes caused by changes in obstacle shapes. The differences between S2.3 and S2.2 and between S2.4 and S2.2 were additionally calculated and visualized in Figure 53 in order to investigate the influence of the tree shape and the use of patch data. It was found that local differences appear which are in diurnal averages up to -4.5 K in case of the shape change and up to 1.5 K in case of the use of patch data. The change of the vegetation type in scenario S1.3 (see Figures 51 and 52 b)) leads to a decrease of

hourly and domain averaged UTCI starting from the early morning, while the change of the pavement types in S1.2 leads to an increase of UTCI until the evening, when a decrease follows, see Figure 51. A dependence on the considered sub-area is furthermore found. In the park, strongly increased variations due to tree parameters during day time of nearly -2 K occur, which is visible in Figure 51 b). Furthermore, the vegetation type leads to a change of -1 K during day time. In case of buildings (subfigures a) and c)), variations due to building parameters in the morning as described dominate, i.e. the building type has

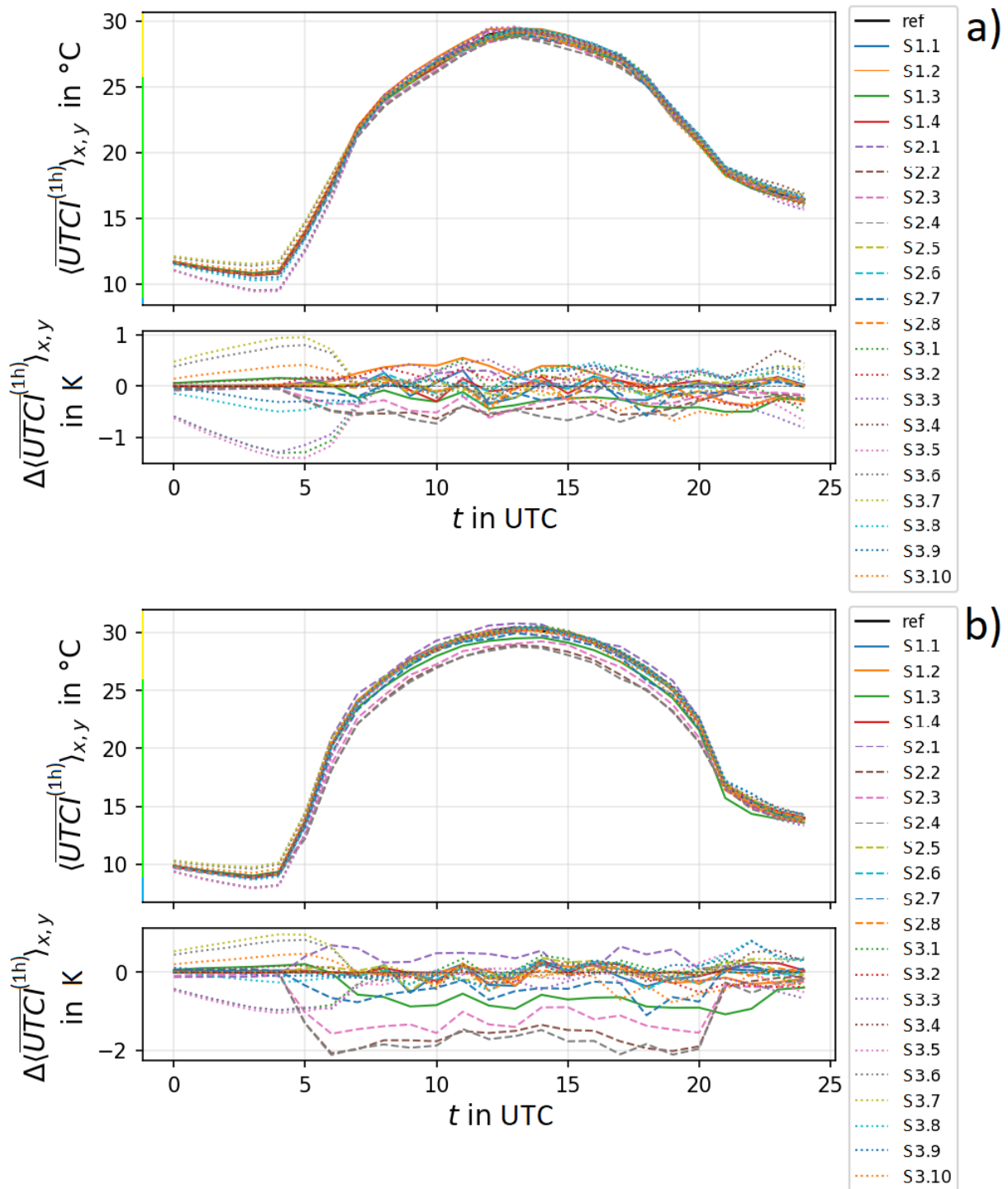


Figure 51: Time series of hourly and spatial averaged UTCI for the different scenarios and the respective difference to the reference UTCI: a) total domain, b) park.

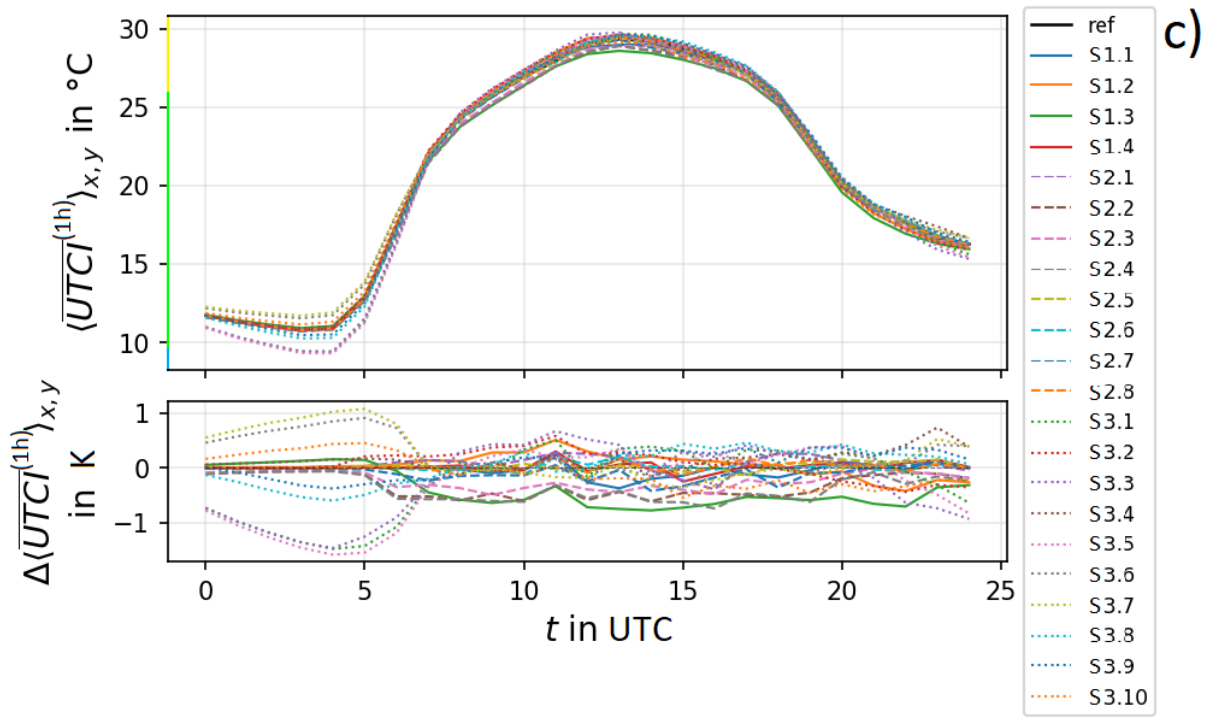


Figure 51: Continued: Time series of hourly and spatial averaged UTCI for the different scenarios and the respective difference to the reference UTCI: c) single houses.

an increased influence at night and in the morning. During day time and at the maximum at noon, the wall albedo has a small influence resulting in an increase of UTCI. In case of single houses with gardens, especially the vegetation type leads to a decrease beginning in the early morning, see Figure 51 c). Concerning the diurnal averaged local differences shown in Figure 53, the dependence on the considered sub-area and thus e.g. on number of trees and the surface fraction of the considered quantity is also visible. I.e. in the park, the tree properties and the vegetation type have an increased median response, meaning that the median of the variations differs from zero.

17.3 Interpretation of the analysis results

The simulation results shown in the previous chapter are explained and evaluated in the following chapter. For this purpose, the influence of the building type, the LSM parameters and the tree characteristics on the model results is first discussed separately. Furthermore, reference is made to the required accuracy of the model results which are compared to the simulated deviations and associated with the quality of the input parameters. It has to be noted, that the findings presented in this work are valid for the selected area with a fraction of 41.9 % of the surface being paved, 36.6 % being vegetated, 21.4 % being covered with buildings and 0.1 % of the surface being covered with water. Furthermore, the domain includes 348 trees and is positioned at a latitude of 55°. The simulations were performed under autochthonous weather conditions on June 22nd.

17.3.1 Effect of building parameters

The results show a sensitivity of the considered model results to the building type. The change from the older to the newer building type leads to a decrease of the 2 m air temperature and the UTCI in the morning especially near the buildings. The amount

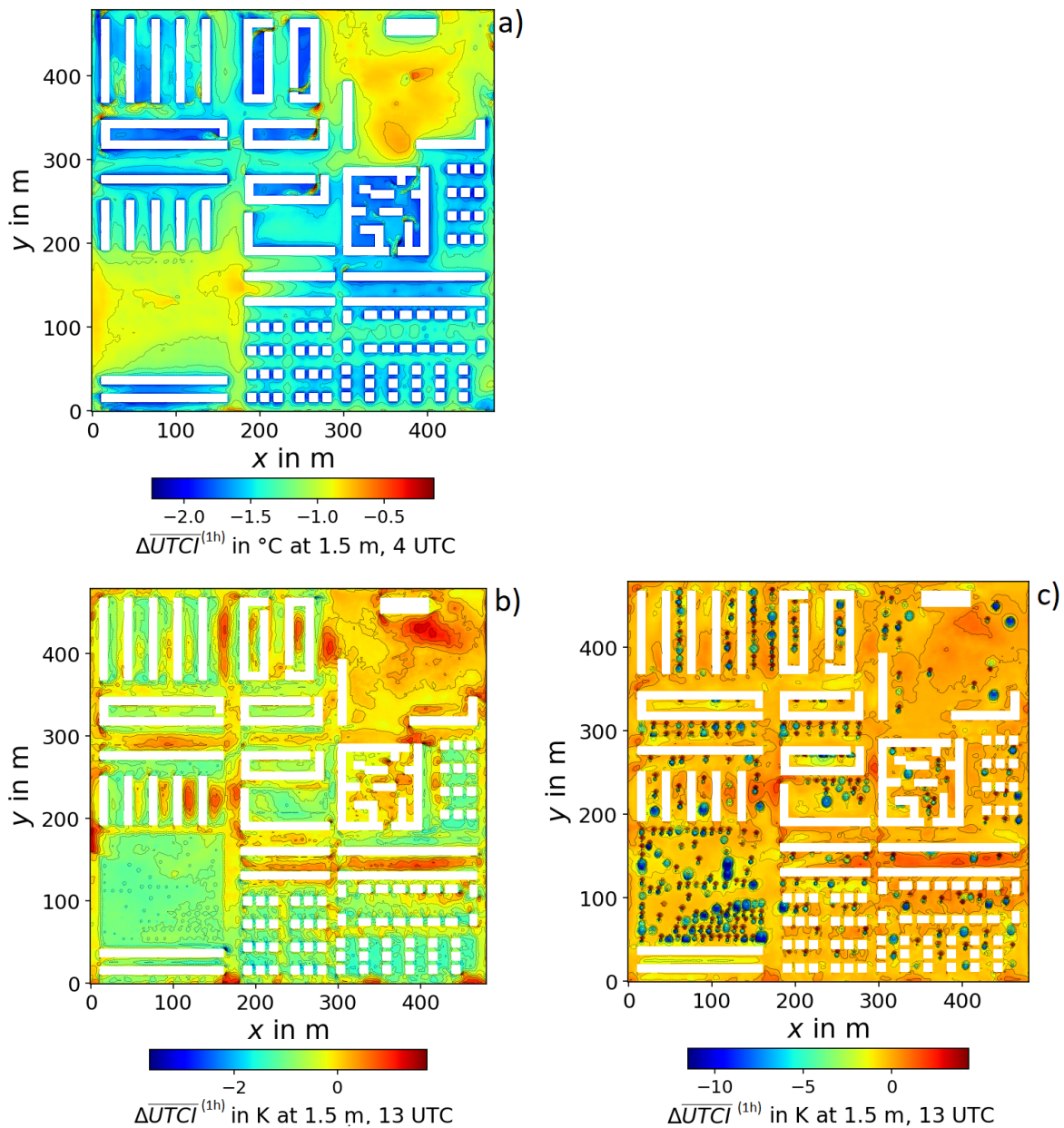


Figure 52: Horizontal distribution of differences between hourly averaged scenario and reference UTCI. a) scenario S3.1, 4 UTC, b) S1.3, 13 UTC, c) S2.3, 13 UTC.

of this decrease is increased with the fraction of buildings in the considered sub-area. In order to be able to further understand this sensitivity, it should be mentioned that PALM uses 150 building parameters. For each building type, default values are assigned to them when no other values are explicitly specified. The following parameters differ for the older to the newer building type: A building with the newer building type has a larger (smaller) window (wall) fraction, a smaller ground floor level and storey height, thicker walls, except the ground plate, a smaller heat capacity and thermal conductivity of the wall layers, except the first wall layer at the ground plate, a slightly increased wall emissivity, a smaller window emissivity, transmissivity and thermal conductivity, triple layer glazing (instead of double layer glazing) and thus thicker windows with a higher albedo. Furthermore, a building with newer building type has a smaller shading factor, g-value and u-value for

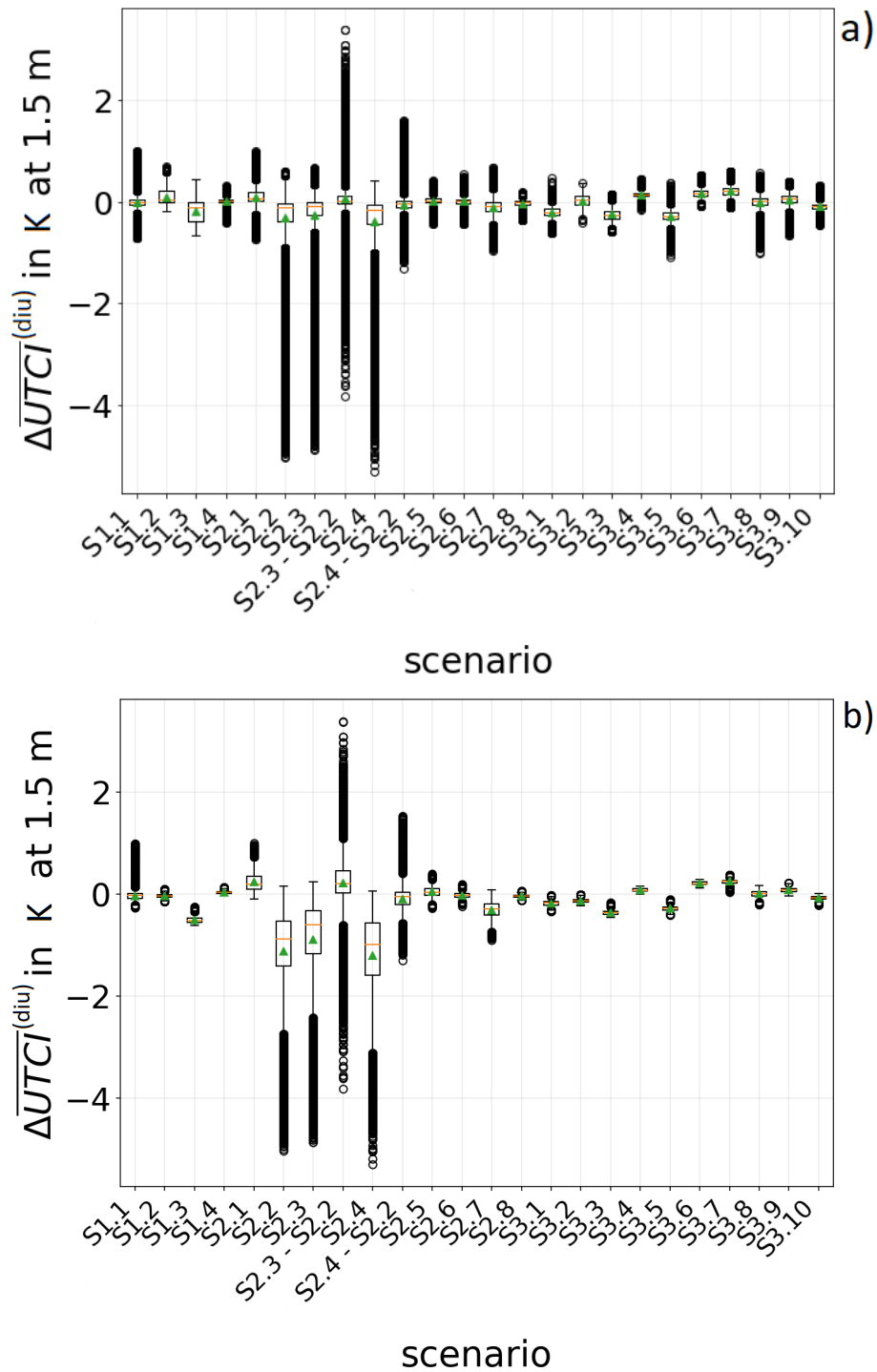


Figure 53: Bandwidth of local differences between diurnal averaged scenario and reference UTCI at 1.5 m height. a) whole domain, b) park.

windows², an increased heat recovery efficiency, a smaller dynamic parameter inner heat storage, a smaller maximal heating capacity, and a smaller anthropogenic heat output for heating and cooling. In [4], where the sensitivity of PALM with respect to land-surface

²The u-value (heat transmission coefficient) is a parameter of thermal insulation quality for the window. It describes the amount of heat flow that is transported through one square meter of the window at a temperature difference of 1 K. The g-value (solar heat gain coefficient) is a parameter of total energy transmittance of the windows. The shading factor is the ratio of the g-value of the window to the g-value of a glazing without shading elements [44, p. 1].

and building properties is tested in a densely built-up urban environment in Prague, Czech Republic, it was found that of these parameters, the thermal conductivity of the walls, the emissivity, and the volumetric heat capacity of walls, roofs and surfaces show a high sensitivity for the air and surface temperature, while the lowest sensitivity could be assigned to the wall thickness and the transmissivity of windows. Insulated walls of the new building type result in lower heat emission at night, lowering the temperature especially in the surrounding area compared to the simulation using the older building type as it was found in Chapter 17.2.1. The lower anthropogenic heat output affects the whole domain and has an effect in the park, too, which might result from the infinity of the considered domain. Hence, the westwind transports air into the park, that is influenced by many further buildings. For the 2 m air temperature and the UTCI an increase of the green fraction at buildings leads to an increase in the morning around buildings, which is also visible in the diurnal averaged data, especially for the temperature. This might be due to the higher value for the longwave albedo assigned to green walls (0.34) than for the default wall (0.07). However, the magnitude of these variations is smaller than the desired accuracy of 3 K for the UTCI given in Chapter 4. Although the effect of facade greening on temperature and UTCI was found to be small in this study, especially during day time, the magnitude of the effect to be expected and the distance from the wall to which these effects extend into the surrounding area will shortly be further investigated here dependent on the wall orientation, since the use of green facades is discussed as a method to adapt urban areas to climate change [7, p. 3]. Figure 54 shows the differences between the 2 m air temperature modeled with the reference run and the simulation for scenario S3.7, where a facade greening of 29 % distributed over all walls of different orientation is added compared to the reference run. Different times and wall orientations are considered for the investigation of the influence of a facade greening at walls dependent on the distance from the wall. The boxplots include the 2 m air temperature difference at every position in the considered distance from a building wall with the respective orientation considering each building of 10 m and 20 m height. The reduction of the ambient 2 m air temperature due to the green facade is caused by evaporative cooling [7, p. 12]. Figure 54 indicates that directly at walls exposed to the sun light, which heat up most, the strongest air temperature decreases occur. During day, a general temperature decrease arises due to the green walls. The outliers may be due to different building constellations and thus interactions with the effects of other walls. This is for example the case for the north oriented wall in Figure 54. Some outliers indicating a comparably large temperature decrease are shown. The corresponding locations are probably affected by heated south and west oriented walls. The dependence of the effect on the wall orientation thus coincides with the findings from [7, p. 22], where it is stated that the orientation of the facade plays a role for the magnitude of the effect. An analogous but less clear behavior occurs for UTCI (not shown here), which could be due to an increased albedo associated with a change from a default building wall to a green wall. For a more detailed study of the effect of green walls and roofs on indoor and outdoor climate it is referred to [69]. In [69, p. 52] a mean effect of complete green walls on the 2 m air temperature of -1.79 K is given. This magnitude of the effect is larger than for the green fraction of only 29 % used in this study. Since a dependency of the effect on the fraction was also simulated in this study, it is here investigated for the day time cooling effect in the court yard and the area with small houses as averaging domains. The maximal hourly averaged decrease of the 2 m air temperature is about -0.29 K. Assuming a linear dependency between green fraction and temperature decrease leads to a decrease of -1.86 K which is comparable to the result of [69]. Furthermore, an increase in the window fraction leads to a slight increase in air temperature at night, which is due to the fact that walls have a higher heat storage

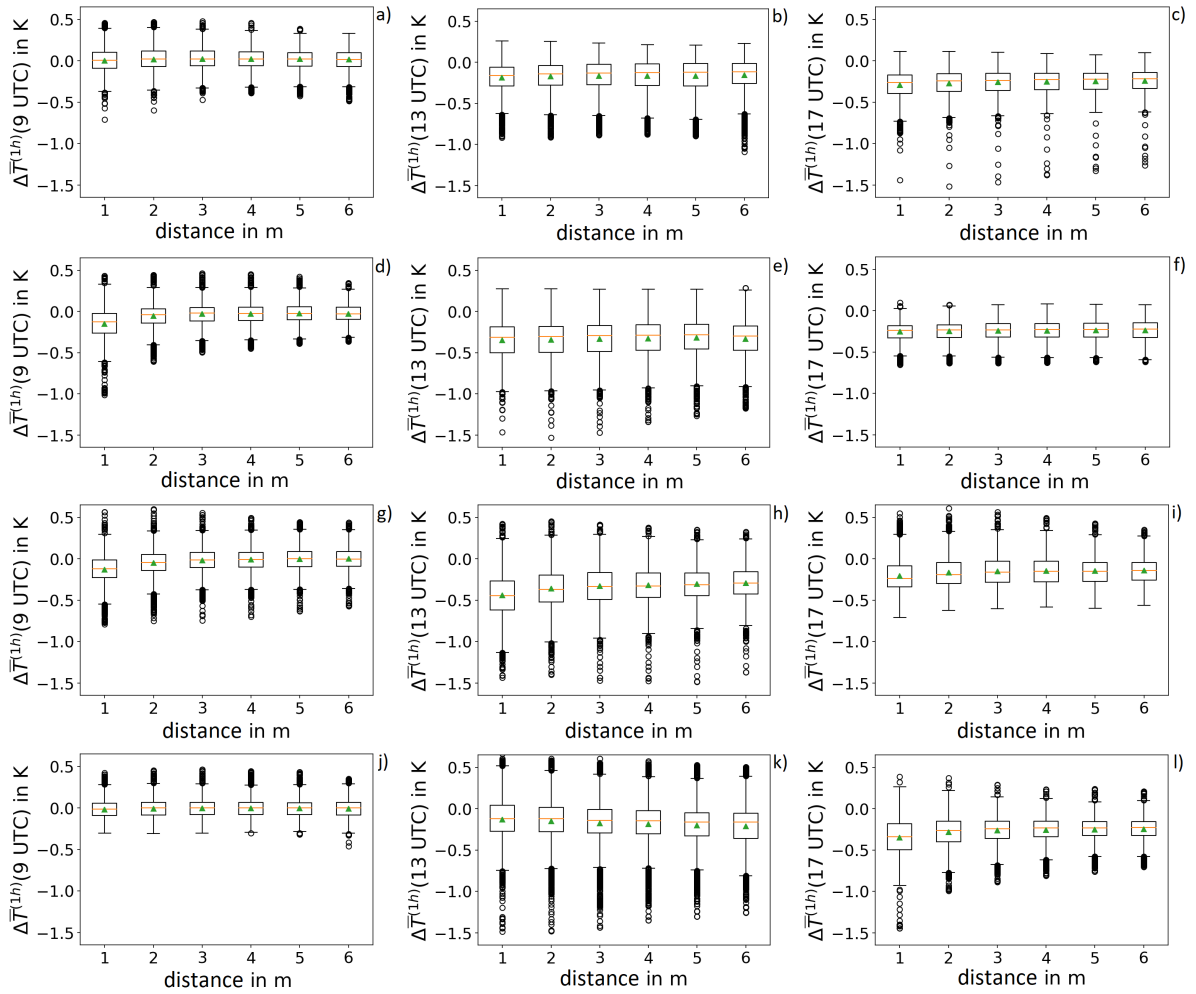


Figure 54: Influence of a facade greening of 29 % at walls on the 2 m air temperature dependent on the distance from the wall for different times and wall orientations: a), b), c): North, d), e), f): East, g), h), i): South, j), k), l): West.

than windows, and therefore the indoor temperature receives a greater impact on the air temperature, since the heat can leave the interior through a larger window area. During night time, the surface temperature also shows variations due to the building properties as for the air temperature depending on the fraction of buildings in the considered sub-area due to a modification of the energy balance. Furthermore, a decrease of the 2 m temperature due to an increased wall albedo starting in the morning is simulated which was described in Chapter 17.2.1. In case of scenario S3.3, the effects of the change to the newer building type and the the additional decrease of the albedo overlapp and lead to the strongest decrease of the temperature. An increase of the UTCI occurs in case of the presence of buildings in the considered area when the albedo is increased, as it was described in Chapter 17.2.5. This influence of the albedo also agrees with the findings from [4], where a high sensitivity for the temperature to the albedo is found. As stated in [4], the increased albedo leads to more reflections at the surfaces, which again increase the biometeorological quantity. Furthermore, the temperature in the canopy layer is influenced by roof greening. Compared to the reference case, as green walls, green roofs lead to temperature increases at height levels above the roof at the temperature minimum which was seen in Figure 73. At the maximum they result in an overall air temperature decrease compared to the reference run starting at noon and remaining for the night. This

can be explained with the increased value for the albedo, which is associated with the change from default (0.07) to green (0.25) roofs in PALM, and evapotranspiration [61, p. 507], [7, pp. 12, 21, 22]. This leads to a cooling of roof surface during day time, see Figure 55, which reduces the air temperatures above the roof. This cooler air then mixes locally into the surrounding [54, p. 9]. These findings coincide with those from [7, pp. 21, 22], where it is stated that a change from dark bitumen roofs to green roofs reduces the maximal temperature and the temperature amplitude in the diurnal cycle. Furthermore,

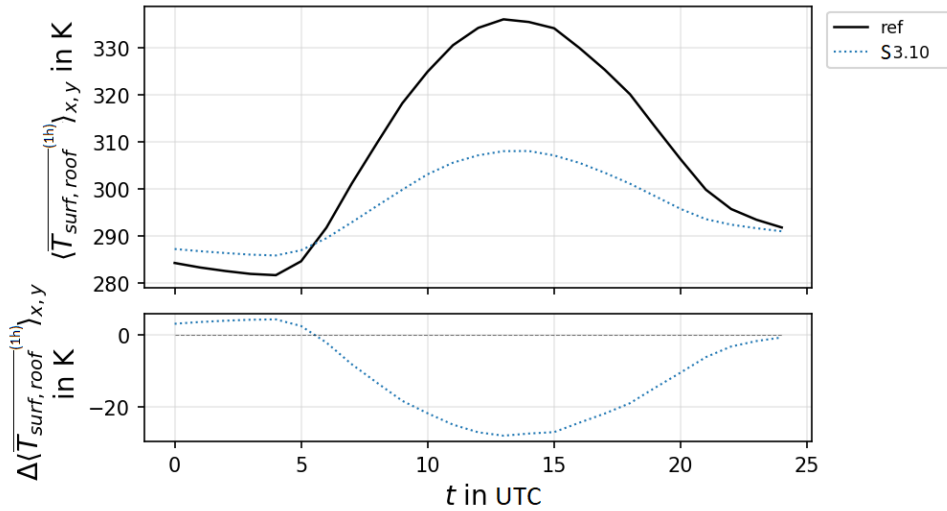


Figure 55: Influence of a green roof on the diurnal variation of the roof surface temperature.

[7, p. 12] mentions measurements in Braunschweig, Germany on a summer day, with in average 11 K lower surface temperature on a roof with extensive greening compared to a conventional roof and a maximal reduction of 17.4 K. The simulated values are of the same size, even though a stronger reduction is simulated which might be due to the simplified radiation conditions using the clear sky scheme. [7, pp. 15, 16] mentions a dependence of the temperature effect in urban areas on the ratio of roof surface to other surfaces and building density, which was also found in this study, however is not shown here. In the court yard sub-domain with a high percentage of roofs, the strongest effect on the 2 m air temperature occurs, while in the park, the difference between the results of the reference run and scenario S3.10 is smaller, but effects from the surrounding environment are visible due to mixing. In [7, p. 15], it is referred to further simulations for the effect of extensive green roofs. A simulation for New York, USA showed a decrease of the maximum 2 m air temperature of 0.37 K - 0.76 K and a mean decrease of 0.1 K - 0.8 K in case of 50 % of the roofs in New York City being green. Further simulations for Tokio, Japan and Hong Kong, China [7, p. 15] refers to showed a negligible influence in the street level due to large heights of the green roofs. Hence, the simulated values presented in this study seem to be reasonable, since the results have a similar order of magnitude as in other studies and the height of the houses included in the considered area is comparatively low, with 10 m and 20 m respectively. Another aspect to be mentioned concerning the effects of building properties is the dependency on the building height, which is visible especially for surface temperature and the UTCI and can be seen in Figure 25. During night time, higher values occur between the higher buildings which might be due to a larger heat input from the buildings. During day time, a higher degree of shadowing and hence a lower amount of available energy between the higher buildings lead to lower values of the

considered model results near the buildings.

Concerning the indoor temperature, the change to the newer building type leads to a slighter decrease in the night and thus a higher indoor temperature minimum. The temperature increase during day time is also slightly decreased, however, the maximum temperature is higher than in the reference case. This behavior results from the improved insulation through thicker walls, a smaller thermal conductivity, the triple layer glazing and the smaller g-value and u-value that goes along with the newer building type. The default values that are assigned to these parameters via the building type in PALM change with the change to the newer building type. The insulated walls lead to lower heat emission at night, hence, the indoor temperature increases compared to the reference run, since in both simulations, the initial value for the indoor temperature is the same. The indoor temperature at the following days would show a further increasing trend in both simulations, with a higher difference between the results from the two model runs because of the higher indoor temperature at night in case of insulated wall compared to the initial value and the value for the reference run. The temperature in the pedestrian area decreases compared to the reference run due to a lower surface temperature at the walls and thus a lower heat input from the buildings. A larger window fraction leads to a stronger indoor temperature increase during day, i.e. a larger amplitude, and a larger indoor temperature maximum. This effect is smaller for the newer building type, which might be due to the triple layer glazing and the smaller g-value and u-value for windows assigned to the newer building type. An albedo increase leads to a smaller indoor temperature increase and thus a smaller maximum due to reflection at the outer wall and hence a lower energy input through the wall. This effect is smaller for the newer building type, which might be due to the above mentioned changes in the building properties. A green roof leads to an indoor temperature reduction beginning at noon. It reaches up to a hourly averaged value of -3 K at some locations within the building in the following night, especially in the near roof building parts. This agrees with [7, p. 9] and [69, p. 80] where the thermal advantages of green roofs, especially for the attic as an adjacent room, are mentioned. The roof surface temperatures are lowered by green roofs and thus, the heat conduction into the building is reduced [54, p. 11]. These results were seen to be valid in Chapter 17.2.4 for every considered building containing sub-area with slight differences: In the area containing single houses, the effect of the window fraction is increased, i.e. the difference of the indoor temperature maximum in the scenario and the reference run is larger than for the other sub domains. This might be due to the larger building surface interacting with the environment, leading to a stronger warming due to solar radiation. Furthermore, in the court yard, window fraction and wall albedo have a smaller effect which is due to shading.

Furthermore, the wind speed is primarily dominated by the roughness elements. At position M5, where the influence of modified obstacles and thus roughness can be neglected, building parameters, which also lead to temperature differences and modified thermal stratification at this location, are more important as it was found in Chapter 17.2.3.

17.3.2 Effect of land surface parameters

The change of the pavement type from asphalt and cobblestone to concrete and also the change of the vegetation type from short to tall grass lead to a decreased diurnal averaged 2 m air temperature, as it was described in Chapter 17.2.1. The vegetation type has an effect in the afternoon in shadowed areas concerning the temperature maximum, which is reached earlier, followed by a temperature decrease of around -0.5 K until the

end of the simulation in the night. At locations, that are exposed to the sun light, temperature increases can be seen. An effect of pavement and vegetation type on the surface temperature with the largest effect around noon was also found, see Chapter 17.2.2. Smaller effects occur at the open place and at tree positions.

As it was found applying the Morris method to the horizontally homogeneous grass land, the 2 m air temperature is mostly lowered by the leaf area index beginning in the morning. Furthermore, the albedo and the roughness length for heat have an effect, especially in morning and evening hours. An increased albedo leads to a 2 m air temperature decrease compared to the reference run beginning at sunrise, also slightly effecting the night time temperature on the following day. When there is no incoming shortwave radiation available, a higher vegetation coverage and heat conductivity between atmosphere and soil were found to result in a higher air temperature due to the lower bare soil fraction and thus reduced latent and increased sensible heat flux, and heating from the ground, respectively, while an increased roughness length for temperature results in a lower air temperature. The daytime surface temperature is mostly affected by the roughness length for heat as it affects the heat flux at the surface. An increased roughness length for heat leads to a surface temperature decrease, since the heat exchange between surface and atmosphere is higher. An increase of the values of the leaf area index and the roughness length for momentum also lead to decreases of the surface temperature. The increased air temperature at sunny positions therefore results from the lower albedo assigned to the tall grass in PALM. The temperature decrease in shadowed areas results from the smaller value of the vegetation coverage assigned to tall grass, as well as the higher roughness length for heat. Furthermore, the change from short to tall grass goes along with a higher roughness length for heat and momentum lowering the surface temperature. In sub-areas with a high fraction of vegetated surfaces but also a high fraction of obstacles, i.e. the park and the area with single houses and gardens, the change of vegetation type to higher grass leads to an earlier occurrence of the temperature maximum, followed by a temperature decrease compared to the reference, due to shading and the temperature reduction in shadowed areas for taller grass. In case of the changed pavement type, the 2 m air and surface temperature are mostly affected by the albedo during day, when the incoming short-wave radiation dominates the radiative balance [4, p. 4450]. In case of variations in the albedo, at shadowed areas smaller variations occur, which can be seen in case of the surface temperature in a street canyon. The largest variations in the north-south oriented canyons appear around noon. Otherwise the ground is shadowed.

Furthermore, in Chapter 17.2.1, the change of the pavement type in scenario S1.2 was not found to show a large effect at the open place since the used different pavement types have nearly the same albedo. As in Chapter 15.2.1 the energy balance will be investigated in dependence of the pavement type. Figure 56 shows the resulting diurnal cycles of the energy fluxes at the surfaces for two stations at the street and the open place, respectively. Concerning the signs, $R_n = G + H + E$ yields. The diurnal development was explained in Chapter 15.2.1. In the reference run, cobblestone with an albedo of 0.3 was used instead of asphalt with an albedo of 0.08 which is used for the remaining paved surfaces, except the court yard. The change of pavement type to concrete includes a change to an albedo of 0.35. The change of the pavement type from asphalt and cobblestone, which are used in the reference run, to concrete leads to a decreased net radiation flux at the surface. Furthermore, the ground heat flux and the surface sensible heat flux take smaller values. Evapotranspiration does not occur, here. As changes from pavement type asphalt and cobblestone to concrete means an increase of the albedo from 0.08 to 0.35 and 0.3 to 0.35, respectively, this leads to an increased outgoing shortwave radiation flux. Due to the larger albedo increase in case of the change from pavement type asphalt to concrete,

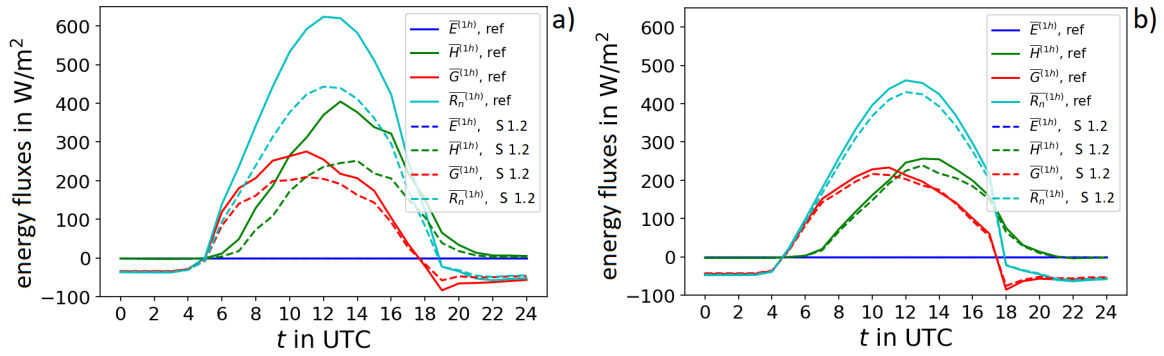


Figure 56: Diurnal cycle of the energy fluxes at the surface for different pavement types. a) at the street, b) at the open place

larger variations occur. The small effect of the pavement type change on the temperature at the place shows the importance of the parameter ranges. The given changes of the pavement type hence lead to a smaller energy input during day and a lower temperature. Thus, an influence of the changed pavement type is visible through lower temperatures during night, too, due to the smaller amount of available energy to be re-emitted.

The UTCI is decreased by the given change of the vegetation type starting from the early morning, while the change of the pavement type leads to an increase of UTCI until the evening, when a decrease follows. This increase during the period with incoming shortwave radiation is again due to the increased reflections due to the albedo increase included in the change of pavement type, since using the results of the Morris method, the increase of UTCI in case of the changed pavement type can be assigned to the increased albedo which leads to increased reflections. A change from short grass to tall grass leads to an albedo decrease from 0.25 to 0.18, hence a UTCI decrease is expected due to this parameter, when the vegetation type is changed. According to the Morris method, the roughness length for momentum had the strongest influence, when the vegetation type is changed. An increase of the roughness length leads to a decrease of the diurnal averaged 10 m wind speed, but to an increase of UTCI. However, the effect of the albedo on the UTCI seems to prevail, which might be to the low wind speed in the urban area. To illustrate the relationship between the results of the Morris Method for the parameters included in the parameter types and the results for the scenario-based analysis of the urban area based on the vegetation and pavement type, the scheme presented in Figure 57 is used. It shows a composition of the input parameters which have an increased influence on the maximal UTCI averaged over the whole considered urban area. In the middle the parameters resulting from the investigations for the urban domain are listed. These are the pavement and vegetation type as described above, the green roof, see previous chapter, and the drag coefficient and the tree type, which will be discussed in the next chapter on the effect of trees. On the right, the parameters found to be relevant in the preliminary analyses performed with the Morris method are listed. The latter are colored as in the analysis with the Morris method: If the Morris measure increases the output standard deviation multiplied with a factor a , the cell is green for $a = 1$, yellow for $a = 2$ and orange for $a = 3$. A similar approach is used for the parameters in the middle box. The difference of the considered model result from the scenario and reference run is compared to the standard variation of the differences resulting from all scenarios.

Furthermore, the change of the pavement type, which leads to a temperature decrease, is responsible for a decrease of the wind speed. This can also be found when the Morris method is applied to the paved surface. There, the albedo, which also mainly affects the

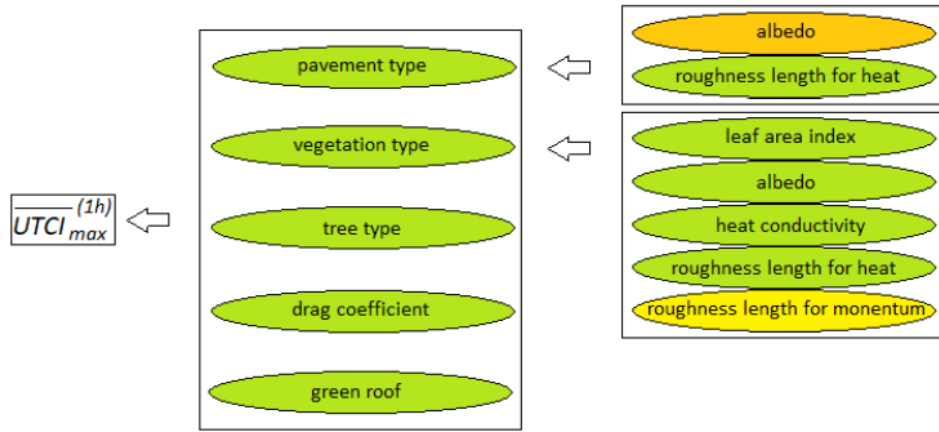


Figure 57: Scheme: Input parameters with increased influence on the maximal UTCI averaged over the whole urban domain. Left: considered model result $\overline{UTCI}_{max}^{(1h)}$, middle: parameters with increased effect on the model result from the investigations for the urban domain, right: parameters within types with increased effect from preliminary analyses performed with the Morris method.

temperature, has an influence on the wind. A reduced urban canopy temperature leads to a reduced vertical turbulent transport [4, p. 4458].

The change of the water temperature from 283 K to 293 K (scenario S1.1) shows only a local effect on the model results due to the small size of the water surfaces. The surface temperature is affected only directly at the water position and the UTCI in a height of 1.5 m is mainly affected directly at the water position and slightly effected up to a distance of maximal 10 m (not shown here). The effect of the water temperature on the UTCI will be further investigated. Figure 58 shows horizontal profiles of the UTCI over the water surface in the park located at $y=134$ m at 3 UTC (subfigure a)) and 15 UTC (subfigure b)). The location of the water surface is marked blue. The largest differences

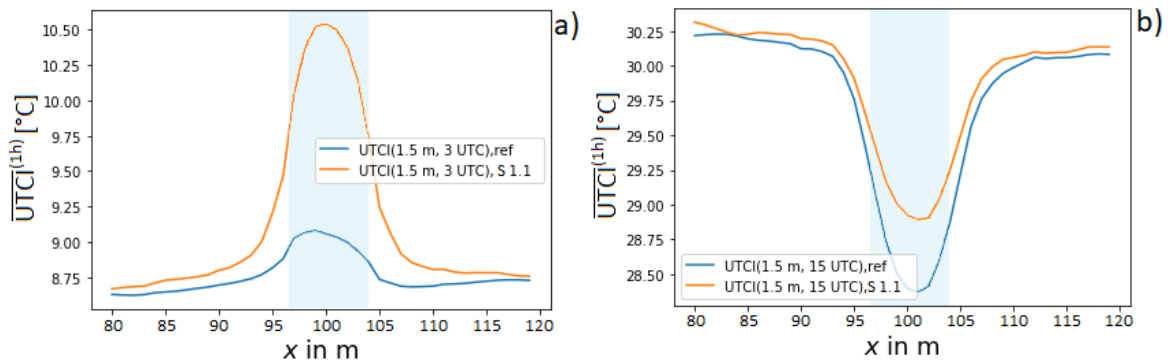


Figure 58: Horizontal profiles of UTCI over water surface in the park at $y=134$ m at a) 3 UTC, b) 15 UTC. The location of the water surface is marked blue.

of UTCI due to the variation of the water temperature occur over the water surface and thus not in the pedestrian area. For the water surface in the park, they are up to 1.5 K at 3 UTC and 0.5 K at 15 UTC. The different magnitude of the effects at 3 UTC and 15 UTC might result from a higher wind speed during day time than during night time resulting in an enhanced mixing. In the pedestrian area next to the water surface the differences are about 0.5 K at 3 UTC and 0.25 K at 15 UTC and they strongly decrease with distance. Similar results are obtained for the open place but not shown

here. Since the water temperature of small water surfaces included in the urban area does not seem to have a large impact on the model results compared to the desired accuracy, especially in the pedestrian area, the exact water temperature or its diurnal variation are not essential and of minor importance. Furthermore, the effect of the small water surfaces on the surrounding area decreases exponential with increasing distance from the surface. An effect of at least 0.1 K UTCI-difference is simulated up to a distance of 3 m to 5 m from the water surface. However, in this study, only small water surfaces of 8 m · 8 m are investigated and the findings are not transferable to large water surfaces. In [30] it is given that the latter can lead to cooling effects between 0.5 K and 5 K of during daytime in the summer, that can have a range between some meters and 400 m. Due to the greater effect of larger water surfaces on the ambient temperature, a greater effect of varying water temperature can also be expected.

17.3.3 Effect of trees

The tree type, and thus tree height and crown diameter, and the tree shape were found to have a local effect on the diurnal and hourly averaged surface temperature, UTCI, but also on the 2 m air temperature. This effect is most pronounced during the day at tree positions and is then caused by a modification of the shaded area and thus a change in the radiation balance at the respective location. The lack of trees leads to an increased surface temperature, UTCI and 2 m air temperature compared to the reference run during day, especially at noon, This agrees with the common knowledge that trees lower the air temperature and thus the heat stress level through shade and an increased evapotranspiration [27, p. 1]. Shading results in a reduction of incoming shortwave radiation and thus in a reduction of surface and radiation temperature compared to locations that are exposed to the sun. In addition, evapotranspiration results in a higher amount of latent heat to the disadvantage of sensible heat [38, p. 28]. Furthermore, in the park, during night, the tree parameters have a slightly increased influence on the air temperature compared to averaging over the whole domain. The lack of trees leads to a decreased surface temperature, UTCI and 2 m air temperature during night at tree positions. During night time, below trees, the cooling is less pronounced than at open spaces due to the modified radiation fluxes. Trees emit an amount of longwave radiation that increases the small amount of incoming longwave radiation from the clear sky the trees obscure [19, p. 123]. There are local differences between the results from the scenarios S2.2 and S2.4, where patch data (idealized vertical LAD distributions at every location) is created for the trees used in S2.2, see Chapter 17.1. Hence, it is recommended to carefully use the patch data, especially at near ground levels, where the largest differences between the LADs used in the scenarios S2.2 and S2.4 occur. The latter was described in Chapter 17.1, where it was visible in Figure 44 c) that the leaf areas in the scenario using patch data differ from the other ones (see subfigure a)) in a softer demarcation from the surrounding area, especially at the lower levels of the tree. The local differences between the results from the scenarios S2.2 and S2.3 lead to the conclusion that the tree shape has an increased influence at the tree positions which coincides with [9, p. 927], where it is stated that the effectiveness of shading concerning a reduction of ground and wall surface temperatures depends on plant geometry. The local differences are again explainable with the changes in the shadowing and hence modifications of the radiation budget. The local wind changes are due to modified obstacle shapes and hence a different flow around the obstacles. The increased horizontal wind speed, especially at crown height, in case of missing trees coincides with the fact that resolved vegetation leads to a sink term in the momentum equation. Furthermore, the wind speed is dependent on roughness elements.

This behavior also explains in the decreased wind speed at lower levels due to a change of the vegetation type to tall grass. With the Morris method applied to the grassland setup a strong dependency of the wind speed on the roughness length was found when changing the vegetation type. An increased roughness length leads to a decrease of the wind speed.

17.3.4 Evaluation of the analysis results in terms of ensuring the required accuracy of the model results.

The performance of PALM depends on the quality of the available input data. The simulated variations of the model output resulted from modifications of the energy balance on the different surfaces and thus the available energy due to variations in the input parameters. Summarized, the available energy at the surface determines the surface temperature. The air temperature is then determined by the transfer of heat between the surfaces and the air [4, pp. 4451, 4452] as it was described in Chapter 15.2.1. The wind is affected by the thermal stratification and the UTCI is affected by the air temperature, the air humidity, the wind speed and the mean radiation temperature as described in Chapter 20.

In Chapter 4 the required accuracies of the model results of air temperature, surface temperature, indoor temperature, UTCI and wind speed in an urban environment were specified. Up to here, the effect of the input parameters on the model results was investigated. Now, the required accuracy of the input parameters in order to achieve the required accuracies of the model results given in Table 3 will be discussed and it has to be concluded with the help of this work if this desired accuracy of the results can be achieved with the given quality of the input data (see Tables 1 and 2).

It can be seen from the Tables 18 to 22, which input parameters result in an exceeding of the permissible deviation (see Table 3) for the considered model results when they are varied as given in Table 17 and hence in case of a lack of knowledge of the actual value. Apart from the domain averaged deviations, information concerning local deviations are also included for the diurnal averaged output quantities. If a model result is to be studied, the corresponding listed input parameters should be more accurate than they are in the study in order to achieve compliance with the required accuracy given in Table 3.

Due to the comparably small wind speeds used in this study, the allowed relative deviations also given in Table 3 are used. Concerning the wind, it should be noted, that large fluctuations occurred, especially during day time, and a clear signal often was missing.

The variation of the building type results in an exceeding of the permissible deviation for the model results given in Table 3 in case of $\overline{T}_{min}^{(1h)}$ in every considered sub-domain, $\overline{T}_{max}^{(1h)}$ in the court yard, $\overline{T}^{(diu)}$ in the sub-domains containing street canyons, single houses and a court yard, $\overline{T}_{surf\ min}^{(1h)}$ especially in sub-domains with buildings, $\overline{T}_{indoor\ min}^{(1h)}$, $\overline{T}_{indoor\ max}^{(1h)}$, $\overline{T}_{indoor}^{(diu)}$ in every domain with buildings, $\sqrt{u^2 + v^2}_{min}^{(1h)}$ and $\sqrt{u^2 + v^2}_{max}^{(1h)}$. As described in Chapter 3.3, PALM building types combine information on building use and building age. As mentioned in Chapter 4, this does not necessarily represent the energetic properties of a building, since information on renovation and modernization of the building are not included. Since the use of a wrong predefined building type leads to an exceeding of the permissible deviations for surface, indoor and air temperature and wind, a classification via age and use is not sufficient due to the lack of information on renovation and the energetic properties should be available more precisely. Building age and use are delivered by ATKIS/ALKIS data. Further field studies are required for the building properties to capture the thermodynamic properties of the single buildings. Especially the thermal

Table 18: Exceeding of the permissible deviation for the air temperature and corresponding varied input parameters.

model result	varied input	averaging domain	domain with local deviations	deviation from reference result [K]
$\overline{T}_{min}^{(1h)}$	building type	single houses	-	-2.0
	building type	court yard	-	-1.9
	building type	park	-	-1.9
	building type	street canyons	-	-1.8
	building type	open place	-	-1.3
	green fraction (29 %)	street canyons	-	0.8
	green fraction (29 %)	court yard	-	0.7
	green fraction (29 %)	park	-	0.7
	green fraction (29 %)	single houses	-	0.6
	green fraction (29 %)	open place	-	0.5
$\overline{T}_{max}^{(1h)}$	green roof	court yard	-	-0.6
	building type	court yard	-	-0.5
	wall albedo	open place	-	-0.5
	green roof	street canyons	-	-0.7
	green roof	open place	-	-0.7
	green roof	park	-	-0.6
	green roof	single houses	-	-0.5
$\overline{T}^{(diu)}$	tree shape	-	park	0.6
	vegetation type	-	street canyons	-0.7
	vegetation type	-	single houses	-0.6
	building type	-	street canyons	-0.6
	building type	-	single houses	-0.6
	building type	-	court yard	-0.6

conductivity of the walls, the volumetric heat capacity of walls, roofs and surfaces and window properties (see below) should be investigated in order to prevent exceedings in the allowed uncertainties. They should be known more precise than the variation used in this investigation that lead to the exceedings. For the thermal conductivity of the walls this is averaged $0.1 \text{ Wm}^{-1}\text{K}^{-1}$ and a value of $270000 \text{ Jm}^{-3}\text{K}^{-1}$ for the volumetric heat capacity of walls and roofs. However, the determination of the heat capacity and the thermal conductivity is difficult because individual products in a product group of building materials may have varying material properties and generically assigned values might not match the specific case [55, p. 135]. Furthermore, different materials are used for walls and roofs. Hence, a recording of information on renovation and modernization and thus the thermodynamic properties of the single buildings would be desirable to achieve the desired accuracy of the model results. Due to the lack of these information, exceedings of the permissible deviations can not be excluded. The variation of the green fraction at the building walls from 0 % to 29 % results in an exceeding of the allowed

Table 19: Exceeding of the permissible deviation for the surface temperature and corresponding varied input parameters.

model result	varied input	averaging domain	domain with local deviations	deviation from reference result [K]
$\overline{T}_{surf_{min}}^{(1h)}$	building type	street canyons	-	-0.9
	building type	court yard	-	-0.8
	building type	single houses	-	-0.8
	building type	park	-	-0.5
	green fraction (29 %)	park	-	0.5
	green fraction (29 %)	single houses	-	0.5
	green fraction (29 %)	street canyons	-	0.5
$\overline{T}_{surf_{max}}^{(1h)}$	tree type	park	-	0.5
	pavement type	single houses	-	-1.5 K
	pavement type	street canyons	-	-1.5 K
	pavement type	court yard	-	-0.8 K
	pavement type	open place	-	-0.8 K
	vegetation type	park	-	-5.1 K
	vegetation type	single houses	-	-3.6 K
	vegetation type	street canyons	-	-2.4 K
	tree type	park	-	-1.8 K
	tree type	court yard	-	-0.9 K
	tree type	single houses	-	-0.5 K
	tree type	street canyons	-	-0.5 K
	tree shape	park	-	0.8 K
	crown diameter	park	-	-0.5 K
	no trees	open place	-	0.5 K
	wall albedo	park	-	-0.8 K
	$\overline{T}_{surf}^{(diu)}$	vegetation type	park	-
vegetation type		single houses	-	-1.6
vegetation type		street canyons	-	-0.9
pavement type		single houses	-	-0.6
pavement type		street canyons	-	-0.6
tree type		park	-	-0.7

deviation for $\overline{T}_{min}^{(1h)}$ and $\overline{T}_{surf_{min}}^{(1h)}$ in various sub-areas. This leads to the recommendation that the green fraction of a building wall should be more accurate than the used variation of 29 % for these model results, which can be obtained from field studies. Furthermore, exceedings of the permissible deviations were found for $\sqrt{u^2 + v^2}_{min}^{(1h)}$ especially in the street canyons and the court yard, but already for the variation of the green fraction from 0 % to 18 % with a smaller effect in case of a newer building type. The wind speed is dominated here, by the temperature emission from the buildings. It is assumed to obtain this accuracy of the green fraction from field surveys. The specification of extensive green roofs results in an exceeding of the allowed deviation for $\overline{T}_{max}^{(1h)}$ in the court yard and for $\sqrt{u^2 + v^2}_{min}^{(1h)}$ in the court yard in a height of 10 m. This leads to the

Table 19: Continued: Exceeding of the permissible deviation for the surface temperature and corresponding varied input parameters.

model result	varied input	averaging domain	domain with local deviations	deviation from reference result [K]
$\overline{T}_{surf}^{(diu)}$	tree type	-	single houses	-4.6
	tree type	-	open place	-4.5
	tree type	-	park	-4.0
	tree type	-	street canyons	-3.4
	tree type	-	court yard	-3.0
	tree shape	-	open place	-4.5
	tree shape	-	street canyons	3.4
	tree shape	-	single houses	3.2
	tree shape	-	park	3.0
	tree shape	-	court yard	2.5
	patch data	-	open place	-1.8
	patch data	-	park	-1.5
	patch data	-	court yard	-1.5
	patch data	-	single houses	-1.4
	patch data	-	street canyons	-1.3
	crown diameter	-	park	-1.0
	crown diameter	-	single houses	-0.9
	crown diameter	-	court yard	-0.7
	no trees	-	court yard	1.1
	no trees	-	park	1.0
	no trees	-	single houses	1.0
	no trees	-	street canyons	0.9
	no trees	-	open place	0.9
	pavement type	-	single houses	-3.3
	pavement type	-	street canyons	-2.9
	pavement type	-	court yard	-0.6
	vegetation type	-	street canyons	-3.9
	vegetation type	-	single houses	-3.9
	vegetation type	-	open place	-3.6
	vegetation type	-	court yard	-3.0

recommendation that for dense development and low building heights, information on green roofs is required for an accurate determination of the 2 m maximum temperature. Furthermore, it is required for an accurate determination of the wind speed at building height in case of dense development. These information can be obtained from municipal ortho near-infrared images, which however are not always available, even in cities. Further field surveys would be required. The considered variation of the albedo of the building walls from 0.07 to 0.3 leads to an exceeding of the permissible deviation for $\overline{T}_{max}^{(1h)}$ at the open place and for $\overline{T}_{surf,max}^{(1h)}$ at the park and hence, at building walls that are not shaded by other buildings. Hence, the albedo of walls that are strongly exposed to sunlight should be known more precisely than the bandwidth of the variation using remote sensing to accurately model the maximum air and surface temperature. The variation of the window fraction between 18 % and 29 % leads to an exceeding of the permissible deviation for $\overline{T}_{indoor,max}^{(1h)}$ in every sub-domain with buildings in case of the old building type, and at the

Table 20: Exceeding of the permissible deviation for the indoor temperature and corresponding varied input parameters.

model result	varied input	averaging domain	domain with local deviations	deviation from reference result [K]	
$\overline{T_{indoor\ min}}^{(1h)}$	building type	open place	-	1.2	
	building type	court yard	-	1.1	
	building type	single houses	-	1.1	
	building type	street canyons	-	1.1	
$\overline{T_{indoor\ max}}^{(1h)}$	building type	open place	-	1.0	
	building type	court yard	-	0.9	
	building type	single houses	-	0.8	
	building type	street canyons	-	0.8	
	window fraction	single houses	-	1.7 (old building)	
	window fraction	open place	-	1.3 (old building)	
	window fraction	court yard	-	1.2 (old building)	
	window fraction	street canyons	-	1.2 (old building)	
	window fraction	open place	-	0.6 (new building)	
	window fraction	single houses	-	0.5 (new building)	
	$\overline{T_{indoor}}^{(diu)}$	building type	open place	-	1.0
		building type	court yard	-	0.9
building type		single houses	-	0.9	
building type		street canyons	-	0.9	
window fraction		single houses	-	0.8 (old building)	
window fraction		court yard	-	0.6 (old building)	
window fraction		open place	-	0.6 (old building)	
window fraction		street canyons	-	0.6 (old building)	

place and the domain with single houses also in case of the newer building type, and for $\overline{T_{indoor}}^{(diu)}$ in every sub-domain with buildings in case of the old building type. For the accurate modeling of the indoor temperature, the window fraction should be available more accurately than the given bandwidth, which can be obtained from field surveys. However, for large areas, the data acquisition would be expensive. This requirement is especially true for the older building type, which in turn underscores the need for more detailed knowledge of the building type.

The considered variation of the vegetation type results in an exceeding of the permissible deviation for $\overline{T}^{(diu)}$ in the sub-areas with the street canyons and the single houses, for $\overline{T_{surf\ max}}^{(1h)}$ in the sub-areas with the street canyons, the single houses and the park, for

Table 21: Exceeding of the permissible deviation for the wind speed and corresponding varied input parameters.

model result	varied input	averaging domain	domain with local deviations	deviation from reference result	
$\sqrt{u^2 + v^2}_{min}^{(1h)}$	building type	court yard	-	-47.0% (10 m)	
	building type	street canyons	-	-37.6% (10 m)	
	building type	single houses	-	17.8% (10 m (roof top))	
	building type	court yard	-	-50.5% (1.5 m)	
	building type	street canyons	-	-45.3% (1.5 m)	
	building type	open place	-	-21.1% (1.5 m)	
	green roof	court yard	-	-33.8% (10 m)	
	tree type	court yard	-	-10.6% (10 m)	
	tree type	park	-	26.2% (10 m)	
	tree type	open place	-	-16.0% (1.5 m)	
	tree type	street canyons	-	-11.5% (1.5 m)	
	tree type	single houses	-	13.6% (1.5 m)	
	crown diameter	court yard	-	-10.0% (10 m)	
	green fraction (18%/29%)	street canyons	-	21.0%/29.2% (1.5 m, old building)	
	green fraction (18%/29%)	street canyons	-	17.4%/24.4% (10 m, old building)	
	green fraction (18%/29%)	street canyons	-	11.1%/14.1% (10 m, new building)	
	green fraction	court yard	-	40.0% (1.5 m, old building)	
	green fraction	open place	-	16.0% (1.5 m, old building)	
	$\sqrt{u^2 + v^2}_{max}^{(1h)}$	no trees	open place	-	10.0% (1.5 m)
		crown diameter	open place	-	-18.2% (1.5 m)
crown diameter		park	-	13.4% (1.5 m)	
no trees		park	-	15.6% (10 m)	
no trees		street canyons	-	14.7% (10 m)	
no trees		park	-	21.3% (1.5 m)	
no trees		single houses	-	20.3% (1.5 m)	
patch data		park	-	13.5% (10 m)	
tree height		single houses	-	11.0% (10 m)	
vegetation type		street canyons	-	-12.8% (1.5 m)	
tree type		single houses	-	12.9% (10 m)	
tree type		court yard	-	10.2% (10 m)	
tree type		street canyons	-	10.3% (1.5 m)	
crown height/width		open place	-	14.2% (10 m)	
crown height/width		single houses	-	11.6% (10 m)	

Table 21: Continued: Exceeding of the permissible deviation for the wind speed and corresponding varied input parameters.

model result	varied input	averaging domain	domain with local deviations	deviation from reference result	
$\overline{\sqrt{u^2 + v^2}}_{max}^{(1h)}$	crown height/width	open place	-	12.8% (1.5 m)	
	drag coefficient	park	-	20.6% (10 m)	
	crown height/width	court yard	-	12.3% (10 m)	
	drag coefficient	single houses	-	18.1% (10 m)	
	drag coefficient	open place	-	17.8% (10 m)	
	drag coefficient	single houses	-	16.5% (10 m)	
	drag coefficient	court yard	-	11.3% (10 m)	
	drag coefficient	street canyons	-	23.9% (1.5 m)	
	drag coefficient	park	-	11.0% (1.5 m)	
	drag coefficient	court yard	-	10.7% (1.5 m)	
	drag coefficient	open place	-	10.5% (1.5 m)	
	drag coefficient	single houses	-	10.2% (1.5 m)	
	building type	single houses	-	15.3% (10 m)	
	building type	court yard	-	11.4% (1.5 m)	
	building type	street canyons	-	18.6% (1.5 m)	
	building type	court yard	-	10.5% (10 m)	
	patch data	single houses	-	15.4% (10 m)	
	patch data	open place	-	23.1% (10 m)	
	patch data	open place	-	16.7% (1.5 m)	
	no trees	street canyons	-	16.1% (10 m)	
	no trees	park	-	29.6% (10 m)	
	no trees	single houses	-	22.9% (10 m)	
	no trees	park	-	15.3% (1.5 m)	
	no trees	single houses	-	15.8% (1.5 m)	
	crown diameter	street canyons	-	16.2% (10 m)	
	crown diameter	street canyons	-	10.6% (1.5 m)	
	tree height	single houses	-	28.6% (10 m)	
	vegetation type	park	-	-23.3% (1.5 m)	
	vegetation type	single houses	-	-12.8% (1.5 m)	
	$\overline{\sqrt{u^2 + v^2}}^{(diu)}$	no trees	park	-	16.5% (10 m)
		vegetation type	park	-	-21.3% (1.5 m)
		vegetation type	single houses	-	-15.5% (1.5 m)
		vegetation type	street canyons	-	-17.4% (1.5 m)

$\overline{T}_{surf}^{(diu)}$ in the sub-areas with the street canyons, the single houses and the park and locally at the open place and in the court yard, for $\overline{\sqrt{u^2 + v^2}}_{min}^{(1h)}$ in the street canyon at a height of 1.5 m, for $\overline{\sqrt{u^2 + v^2}}_{max}^{(1h)}$ in the park and the sub-area with single houses at a height of 1.5 m and for $\overline{\sqrt{u^2 + v^2}}^{(diu)}$ in the sub-areas with the park, single houses and street canyons at a height of 1.5 m. Hence, to guarantee the desired accuracy of the above mentioned model results, the input parameters concerning the vegetation type must be more accurate than in the bandwidth used for the variation at hand. This applies in

Table 22: Exceeding of the permissible deviation for the UTCI and corresponding varied input parameters.

model result	varied input	averaging domain	domain with local deviations	deviation from reference result [K]
$\overline{UTCI}^{(diu)}$	tree type	-	park	-5.0
	tree type	-	open place	-4.9
	tree type	-	single houses	-4.3
	tree shape	-	park	-3.8

particular to the parameters within the vegetation type that have been found to have an effect on the considered model result by applying the Morris method, which would be LAI, albedo and roughness lengths. Information concerning the vegetation type can be obtained from ATKIS/ALKIS data as it was mentioned in Chapter 4, however it is not systematically available and only updated every one to three years. Hence, for the above mentioned model results, further information from OSM or current aerial images are required. Ryan et al. [56] present a method to obtain the albedo with centimeter resolution and accuracies of $\pm 5\%$ from digital cameras and unmanned aerial vehicles. In this study, the albedo was varied between 0.18 and 0.25, and 5% would be in the magnitude of 0.01. A variation of the LAI also led to slight exceedances of the permissible deviations, especially for the surface temperature with a variation of up to 2 K (see Fig. 60), when using the Morris method and a bandwidth of $1 \text{ m}^2\text{m}^{-2} - 2 \text{ m}^2\text{m}^{-2}$. According to Campbell [10] and Fang et al. [18, p. 763] a determination of the LAI with a magnitude of the error of $\pm 5\%$ or an absolute error < 0.1 is possible. In this study, the roughness length was varied between 0.03 m and 0.47 m. For the uncertainty analysis of the input parameters for a flat terrain with low vegetation, [29, p. 227] uses a deviation around a characteristic mean found in the literature of 0.03 m which is assumed to be possible to obtain from measurements.

The considered variation of the pavement type results in an exceeding of the allowed deviation for $\overline{T}_{surf_{max}}^{(1h)}$ and $\overline{T}_{surf}^{(diu)}$ in every sub-domain, except the park since this domain does not contain paved surfaces. To guarantee the desired accuracy of the surface temperature, the input parameters concerning the pavement type must be more accurate than in the bandwidth used for the given variation. This applies in particular to the parameters within the pavement type that have been found by the Morris method to have an effect on the surface temperature. Information concerning the pavement type can also be obtained from ATKIS/ALKIS data. Since it is not systematically available and only updated every one to three years, further data from OSM or measurement campaigns are required especially for the albedo, which should be more precise than $0.35-0.08=0.27$, which is the given variation bandwidth leading to the exceedings. Achieving this accuracy is assumed to be possible, see above.

Furthermore, the effect of the water temperature on the considered model results was investigated as the water temperature measurements are restricted to samples, no sufficient and complete data to map water bodies with a high spatial resolution are available, and OSM data are incomplete regarding water bodies, as it was mentioned in Chapter 4. It was found that small water bodies and the variation of their temperature have only local effects and even temperature uncertainties of the used 10 K do not lead to exceedings of the permissible deviations in the pedestrian area. No additional measures are required to define the small urban water bodies.

Changes of the soil type also do not lead to exceedings of the permissible deviations for

the model results. The assumptions about horizontal and vertical homogeneity mentioned in Chapter 4 are acceptable and no further measures are required and more automatable, area-wide available data can be used.

In addition, the effect of the 3D vegetation data was investigated. The variation of the tree type and thus a combination of a variation of tree height and crown diameter leads to an exceeding of the permissible deviation for $\overline{T_{surf_{min}}^{(1h)}}$ in the park, for $\overline{T_{surf_{max}}^{(1h)}}$ in every sub-domain, except the open place, for $\overline{T_{surf}^{(diu)}}$ in the park and locally at every tree position, for $\overline{\sqrt{u^2 + v^2}_{min}^{(1h)}}$ in every sub-domain, for $\overline{\sqrt{u^2 + v^2}_{max}^{(1h)}}$ in the domains with the single houses, the court yard and the street canyons and locally for $\overline{UTCI}^{(diu)}$ in the sub-domains with the park, the open place and the single houses. The variation of the tree shape leads to exceedings for $\overline{T}^{(diu)}$ locally in the park, for $\overline{T_{surf_{max}}^{(1h)}}$ in the park, for $\overline{T_{surf}^{(diu)}}$ locally in every sub-area and for $\overline{UTCI}^{(diu)}$ locally in the park. The variations of the crown diameter lead to exceedings for $\overline{T_{surf_{max}}^{(1h)}}$ in the park, for $\overline{T_{surf}^{(diu)}}$ locally in the domains with the park, the single houses and the court yard, for $\overline{\sqrt{u^2 + v^2}_{min}^{(1h)}}$ in the domains with the park, the open place and the court yard and for $\overline{\sqrt{u^2 + v^2}_{max}^{(1h)}}$ at the street canyons. The lack of trees results in an exceeding of the permissible deviations for $\overline{T_{surf_{max}}^{(1h)}}$ at the open place, for $\overline{T_{surf}^{(diu)}}$ locally at every tree position, for $\overline{\sqrt{u^2 + v^2}_{min}^{(1h)}}$ in every sub-domain, for $\overline{\sqrt{u^2 + v^2}_{max}^{(1h)}}$ in every sub-domain and for $\overline{\sqrt{u^2 + v^2}^{(diu)}}$ in the park. The use of patch data for the representation of the 3D vegetation results in an exceeding for $\overline{T_{surf}^{(diu)}}$ locally at every tree position, for $\overline{\sqrt{u^2 + v^2}_{min}^{(1h)}}$ in the park and for $\overline{\sqrt{u^2 + v^2}_{max}^{(1h)}}$ at the open place and at single houses. The variation of the tree height results in exceedings for $\overline{\sqrt{u^2 + v^2}_{min}^{(1h)}}$ and $\overline{\sqrt{u^2 + v^2}_{max}^{(1h)}}$ at single houses. The variation of the crown height to width ratio leads do an exceeding for $\overline{\sqrt{u^2 + v^2}_{max}^{(1h)}}$ in the sub-domains with the open place, the single houses and the court yard. The variation of the drag coefficient leads do an exceeding of the permissible deviations for $\overline{\sqrt{u^2 + v^2}_{max}^{(1h)}}$ at every sub-domain in the heights above ground of 1.5 m and 10 m. Concerning the 3D vegetation, tree registers only deliver information on tree parameters on public land. LiDAR measurements can give information on crown diameters and tree height. Therefore, the question arose whether crown diameters and tree height or patch data are sufficient for the description of the 3D vegetation or extensive field surveys are required, when data from tree registers is not available or has to be checked. The effects of the tree parameters are especially focused on the tree positions. Uncertainties in tree height and crown diameter result in the largest amount of exceedings of the permissible deviations for the surface temperature, wind speed and UTCI. It is recommended to focus on these parameters and know their values more accurate than the used bandwidth of 2 m for the tree height and 0.8 m for the crown diameter. In [2] LiDAR measurements of the tree height were performed with an error up to about half a meter. Individual tree height measurements can be performed with an error <2 cm using a total station survey [2, p. 355], however, for large areas with a lot of trees, this data acquisition would be expensive. If the simulation results have to be accurate at tree positions or if an area with a lot of trees is investigated, the tree shape should be acquired from OSM, tree registers or field studies and patch data should be used carefully for the surface temperature and especially near the ground levels concerning the wind speed. Concerning an accurate modeling of the wind speed, the drag coefficient is required with a higher accuracy than 0.094 used in this investigation, which might be difficult to obtain, since the drag coefficient of a tree depends on wind speed,

crown morphology, and tree species [45, p. 2]. Furthermore, wake interactions affect the drag coefficient. In [3, p. 10], this effect is considered through lowering the considered value by 20 %, which corresponds to an absolute value of about 0.1. Hence, exceeding of the permissible deviations for $\sqrt{u^2 + v_{max}^2}^{(1h)}$ cannot be excluded. The uncertainties in the crown height-width ratio should not be more than the used 0.2 since this resulted in an exceeding of the allowed uncertainty in the wind speed in the sub-domains with the open place, the single houses and the court yard.

This investigation was able to give recommendations for which input parameters a more intense data acquisition is required, e.g. for the thermal quantities of buildings. Furthermore, it was found that for some parameters like soil parameters and parameters describing small water bodies, the use of coarser, but more automatable, area-wide available data is sufficient as it was suggested by [31, p. 35].

Part V

Climate change adaptation recommendations

Figure 25 h) shows that under the given initial conditions moderate heat stress occurs in the non shadowed areas of the considered urban domain during day. This underlines the need for methods to adapt urban areas to the climate change, since the number of summer days, hot days and tropical nights will increase [73, p. 257], also leading to increased values of the biometeorological quantities, especially in the urban areas as the generally low albedos of urban surfaces result in a good absorption and re-radiation of the solar energy [54, p. 10]. In this chapter, the quantities which were found to have a large impact on the air temperature are discussed concerning utilization in climate change adaptation. The biometeorological quantity UTCI is also used as target quantity since it is a measure for the human thermal comfort and also captures effects of investigated mitigation strategies like reflections that reduce the thermal comfort although the air temperature might decrease. The previous findings about the effects of the input parameters on the air temperature and the UTCI can be used to make recommendations regarding the adaptation of urban areas to climate change. Furthermore, it should be noted that the large effect of the input parameters considered below on the 2 m air temperature and the UTCI can lead to the fact that the effect of a climate change adaptation method was incorrectly estimated if the implementation of the measure does not correspond to the input data for the model, which can lead to deviations between the actually obtained and the simulated 2 m air temperature and UTCI. Green and blue elements are often discussed in order to adapt urban areas to the climate change. Hence, the effectiveness of these methods will be discussed in the following. The reduction of heat absorption through solar radiation and thus a lower surface temperature can be achieved by the shading effect of trees [9, p. 927]. Shading through trees is also mentioned in [73, p. 260] to improve the thermal comfort. Trees also increase the surface roughness and reduce the wind speed and thus the cooling through wind [9, p. 927], but the UTCI shows that the cooling through the shading effect prevails. As the UTCI, the air temperature is also decreased by trees. During night, trees lead to an increase of the temperature due to a reduced outgoing radiation as the trees emit longwave radiation. Also the night time UTCI is increased by adding trees. Hence, a comparison between an area covered with trees and one covered with grass yields a lower temperature and UTCI for the scenario with trees during day and for the grass scenario during night. Thus, one can also conclude that a larger outgoing radiation reduces the night time temperature, while during daytime shadowed areas lead to a reduction. Hence, in order to either lower the day time temperature and UTCI, trees are recommended or to lower the night time temperature and UTCI, free grass covered areas are recommendable, with the remark that the night time or day time temperature and UTCI are increased, respectively. To reduce the heat stress which especially develops during day time, it should be focused on the shading effect of trees. When planning the measure, care should be taken to estimate tree height, crown diameter and tree shape as accurately as possible, as their uncertainty causes the greatest uncertainties in 2 m air temperature and UTCI. Compared to paved surfaces, parks with grass, shrubs and small groups of trees provide shade from trees and cooling due to evaporation and transpiration during the day and during cloudless nights with low winds, these parks cool down [68, p. 29]. Furthermore, Figures 25 b), d) and h) show lower temperatures and an improved thermal comfort in case of surface covered with grass compared to paved surfaces. Hence,

unsealing is recommended. When planning the measure, care should be taken to estimate the LAI, the albedo and the roughness length for temperature as accurately as possible, as their uncertainty causes the greatest uncertainties in 2 m air temperature. A combination of different forms of urban greening achieve the greatest cooling effect in urban areas. This includes parks, open green spaces, street greening and greening at building level [68, p. 28].

Since the cooling of the skin through wind increases with the wind speed, which results in a decrease of UTCI, a good ventilation of the urban area is recommendable. A good ventilation is also mentioned in [25, p. 9] as a method for the mitigation of heat stress by mixing cooler air from rural areas into the urban area.

The effect of small water surfaces on UTCI was found to be restricted to the very local environment of the surface and the placing of small water bodies, unlike large water surfaces, is not very effective for lowering the UTCI.

It was furthermore found that insulated walls lead to a lower heat emission from the buildings at night resulting in a temperature decrease as well as a UTCI decrease at pedestrian level. When planning insulation measures, the thermal properties of the building walls should be estimated as accurately as possible since a lack of information led to an exceedance of the permissible deviation for the 2 m air temperature in this study, hence a wrong estimation of the effect of the method could be the result. Effects that could only be seen very weakly in the results of this work but are stated in [53] are on the one hand the temperature and UTCI increase at pedestrian level during the day due to lower heat storage in the building walls and a higher surface temperature of the walls. On the other hand, this temperature increase could be countered by an albedo increase or green walls. The effect of the albedo of walls exposed to the sunlight, on the other hand, was visible in the results of the current thesis during day time but the method has to be used carefully due to the increase of the UTCI. Concerning the green walls, [7, p. 16] stated that the cooling effect is larger in narrow streets than in wider streets, where the air temperature is increasingly influenced by the horizontal surface. In the current investigation, analogous results were obtained with a 2 m air temperature decrease of maximal 0.5 K hourly averaged at 15 UTC as the cooling effect of green walls averaged for the sub-domains of the court yard and the small houses. In [69, p. 52], it was found that the effect of green walls in the pedestrian area is larger than the one of the green roof since they are closer to the pedestrian area. This was not seen in this work for a green wall fraction of maximal 29%. Due to the dependency of the effect on the green fraction, an increase to 100 % is assumed to be able to reproduce this result, see Chapter 17.3.1. Analogous, a maximum hourly averaged decrease of 0.4 K was discovered for UTCI for the court yard and single houses averaging domains for 0.29 % green fraction. Even under the assumption of 100 % green fraction, this variation would not increase the desired accuracy for UTCI. In addition, the orientation of the facade plays a major role. In the case of walls, which are exposed to the sun, greater temperature reductions can be achieved. Concludingly, the use of green facades with a high green fraction at illuminated walls can be recommended. The thermal advantages for all storeys of the building with green facades stated in [7, p. 9] could not be reproduced in this work which might be due to the fact that the resulting mean indoor temperature is the horizontal building average at each storey and furthermore, the green fraction of 29% was too small. Furthermore, with PALM a room orientation which also has an influence on the diurnal cycle of the indoor temperature cannot be considered since the indoor temperature is horizontally averaged over the whole building [69, p. 54]. Further investigations would be required and it is referred to [69]. The thermal advantages concerning the indoor temperature of green roofs, especially for the attic [7, p. 9], [69, p. 80] instead were reproduced by the simulations

presented here beginning at noon. The green roofs of the buildings with the heights of 10 m and 20 m used in this study also were found to have an effect in the pedestrian area air temperature and UTCI with the strongest effect in areas with a high proportion of roof surfaces in all surfaces. Further aspects were mentioned in [7, pp. 15, 16] but are not investigated in this work: Increasing building height leads to a decreasing effect on the air temperature at pedestrian level and in case of extensive greening on slanting-roofs, the orientation of the building is important. Furthermore, green roofs can be used for precipitation retention and runoff delay [7, p. 17]. Also not investigated in this study were the influencing factors of greening type, substrate parameters, water availability, climate and weather, with studies showing that the cooling effect of building greening increases with dryness and temperature. Here, too, further studies are needed [7, pp. 13, 14]. However, it can be concluded that a proper combination of green roofs and facades, green surfaces and trees have the largest cooling effect [7, p. 16] and that the implementation of the adaption measure should correspond to the input data for the model as precisely as possible to estimate the effect of a climate change adaptation method correctly.

Part VI

Concluding remarks

18 Summary

Within the scope of this work, a sensitivity analysis method for input parameters of numerical models was developed and applied to the PALM model system. The PALM model system inter alia is capable of simulating the physical processes within urban environments. For an application of PALM in urban areas, input data concerning land use, surfaces, soil type, buildings and vegetation are required. They can be obtained from various sources like municipal data, Open Street Map, satellite data or aerial imagery to name a few. However, quality and availability of input data are very heterogeneous, which results in uncertainties in the input parameters, which are transferred to the model results. In the presented study, the quality of the input parameters is investigated with respect to the required accuracy of the model results. For the latter, required accuracies were defined based on a VDI guideline, that formulates requirements for numerical models to guarantee quality assurance. Furthermore, a systematical sensitivity analysis was carried out for the input parameters required for PALM simulations of the urban environment. The aim was to gain improved knowledge of the accuracy required for the data acquisition, since thorough measurement campaigns and data preparation of location data might be associated with effort and costs. With an adequate precision in the input data, PALM can deliver more reliable information on urban atmospheric processes for urban planning and in order to design actions for climate change mitigation and adaptation. In addition, conclusions were drawn on possible methods for the adaptation of urban areas to climate change based on the results of the sensitivity analysis. Therefore, quantities with a large impact on the 2 m air temperature and the UTCI were discussed concerning utilization in climate change adaptation. Furthermore, it was noted that the large effect of the considered input parameters on the 2 m air temperature and the UTCI can lead to the fact that the effect of a climate change adaptation method was incorrectly estimated if the implementation of the measure does not correspond to the input data for the model, which can lead to deviations between the actually obtained and the simulated 2 m air temperature and UTCI. Hence, it was mentioned which input parameters need to be paid particular attention to when planning the adaptation measures in order to be able to correctly assess the effect of the measures. It was found that a proper combination of green roofs and facades, green surfaces and trees have the largest cooling effect. While shadowed areas lead to a reduction of temperature during day time, a larger outgoing radiation reduces the night time temperature. To reduce the heat stress which especially develops during day time, it should be focused on the shading effect of trees. In order to perform the analysis, the input parameters had to be varied. Therefore, global sensitivity studies were combined with a OAT sensitivity study. In a first step, the Morris method and an uncertainty analysis based on Latin hypercube samples were applied to idealized areas with horizontally homogeneous properties or single obstacles described by one group of related parameters. The relevant parameters within this group were determined. Using the mean of the absolute values of the elementary effects, the input parameters can be ranked in order of their influence on the considered output using the Morris method. This ranking allows for further studies with a reduced number of input parameters to be investigated. With the input parameters found to have an increased influence on the considered model results, an uncertainty analysis can be performed in order to further study their effects and estimate the required accuracy of the input parameters for the

considered PALM model setup using the LHS sampling strategy. Since large computing resources and a large input parameter space are required for the considered more complex urban setting and the application of the Morris method would exceed the computational time capacities, in a second step, for the urban area, an OAT method is applied. For this, one parameter group or one parameter is varied for each model run while the remaining input parameters are kept constant and the model results from the three scenario packages, where land-surface parameters, parameters regarding the 3D vegetation and building parameters were varied, are compared to those of a reference simulation. The preliminary studies could be used to infer the parameters responsible for the detected relevances of parameter groups. For the urban domain, a building resolving simulation was performed applying an energy-balance model to natural and building surfaces taking into account shading, reflections and evapotranspiration. The area contains a park, an open place, street canyons with different aspect ratios and tree arrangements, a court yard and areas with single houses with gardens. It is located in a latitude of 55° and a summer day was simulated. The findings are valid for the selected domain and the autochthonous weather conditions, the study is focusing on. The results of the analysis were explained and evaluated concerning the influence of the building type, the LSM parameters and the tree characteristics on the model results. Furthermore, reference was made to the required accuracy of the model results which were compared to the simulated deviations and associated with the quality of the input parameters. The simulated variations of the model results resulted from modifications of the energy balance on the surfaces and thus the available energy due to variations in the input parameters. The effect of a variation of a considered input quantity was found to be dependent on the fraction of the quantity in the considered averaging domain and a dependency of the analysis results on the local position and the time was visible. It was found that the use of a wrong predefined building type leads to an exceeding of the permissible deviations for surface, indoor and air temperature and wind due to changes in the insulation. A classification of the building type via age and use is not sufficient due to the lack of information on renovation and the energetic properties should be available more precisely. The variation in the fraction of the facade greening resulted in exceedings of the allowed deviation for the air and surface temperature and wind speed in various sub-areas, which was explained by a varied long-wave albedo in the early morning and evaporative cooling during day time. This led to the conclusion that the green fraction of a building wall should be known more accurate than the used variation in this study, which can be obtained from field studies. The lack of information on roof greening also lead to the air temperature and the wind speed at heights above ground of 2 m and 10 m, respectively, in the densely build area due to the higher albedo, the evapotranspiration and the higher roughness length. This led to the recommendation that for dense development and low building heights, information on green roofs is required for an accurate determination of the 2 m maximum temperature and the wind speed at building height. These information can be obtained from municipal ortho near-infrared images, or further field surveys. Furthermore, the albedo of walls which influences the radiation budget that are strongly exposed to sunlight should be known more precisely than the bandwidth of the variation performed in this study using remote sensing to accurately model the maximum air and surface temperature. For the accurate modeling of the indoor temperature, the window fraction should be available more accurately than the given bandwidth, which can be obtained from field surveys. To guarantee the desired accuracy of the air and surface temperature and the wind speed at a height of 1.5 m, the input parameters concerning the vegetation type, especially LAI, as a higher value for LAI increases the latent heat flux and decreases the sensible heat flux, which leads to a lower surface temperature during day, albedo and roughness length,

must be more accurate than in the used bandwidth. The information can be obtained from ATKIS/ALKIS data, OSM or current aerial images. In case of a paved surface, this was found to be valid for the surface temperature and the albedo. The effects of the tree parameters were found to be especially focused on the tree positions. Uncertainties in tree height and crown diameter resulted in the largest amount of exceedings of the permissible deviations for the surface temperature, wind speed and UTCI due to shading effects during day time and modifications of the flow, which led to the recommendation to focus on these parameters in data acquisition. If the simulation results have to be accurate at tree positions or if an area with a lot of trees is investigated, the tree shape should be acquired and patch data should be used carefully for the surface temperature and especially near the ground levels concerning the wind speed. Concerning an accurate modeling of the wind speed, the drag coefficient was found to be required with a higher accuracy than 0.094 used in the investigation. The investigation was able to give recommendations for which input parameters a more intense data acquisition is required, e.g. for the thermal quantities of buildings, and for which parameters, e.g. soil parameters, the use of coarser, but more automatable, area-wide available data is sufficient. With the investigation, it was determined that the desired accuracies of the model results can mostly be achieved with the given quality of the input data (see Tables 1 and 2), whereby partly intense data acquisition is required and a recording of information on renovation and modernization of buildings is strongly recommended. The desired accuracy of the results can thus be achieved using field studies. For large areas, the data acquisition would be expensive.

19 Outlook

The findings of the presented analysis are valid for the selected domains and the autochthonous weather conditions, the study is focusing on. Since season and latitude influence the radiation budget, they have an influence on the available energy and might also influence the results, which should be further investigated. Hence, studies for different seasons, latitudes, and weather conditions including wind and cloud cover values are required. In case of an investigations of autumn, a larger bandwidth should be chosen for LAD in order to account for leaves fall. Concerning the domain not only the latitude influences the results, but also its properties. For more general conclusions, the representative uniform sub-areas were additionally investigated. This allowed for a better transferability of the findings to other locations with the same climatic conditions. Furthermore, it was tried to create a quite diverse urban area, but still a simplified urban setup was used. Since the sensitivities may differ between locations, for different areas further sensitivity studies might be necessary. To verify this, the study should be conducted for additional areas to check the uniformity of the results. Another point is, that only horizontal roof surfaces with constant height were used. Other shapes should be used for the roofs in order to investigate their influence on the results which might be visible in case of the effect of green roofs. Furthermore, only small water surfaces of $8\text{ m} \cdot 8\text{ m}$ were considered. For the impact of the properties of larger water surfaces on the urban areas further studies would be required, too.

Part VII

Appendix

20 The Universal Thermal Climate Index (UTCI)

The Universal Thermal Climate Index (UTCI) is a thermal assessment index which is calculated from the air temperature, the air humidity, the wind speed and the mean radiation temperature [38, p. 26], [66, p. 41]. The UTCI describes the human physiological response to the thermal environment. For a given combination of wind speed, radiation, humidity and air temperature, UTCI is defined as the air temperature of the reference environment, which produces an equivalent physiological response as the current environment. The reference environment is defined as following: It has 50 % RH, with the vapor pressure capped at 20 hPa, and a wind speed of 0.5 ms^{-1} at a height of 10 m. The mean radiant temperature is equal to the air temperature [6, p. 481], [66, pp. 27-29]. Furthermore, the reference person is an adult with a weight of 73.4 kg, a skin surface area of 1.85 m^2 , a body fat content of 14 % [13], and a metabolic heat production that corresponds to walking in the plane at 4 km h^{-1} [66, pp. 27-29]. A decrease of the wind speed coincides with an increase of the UTCI, since wind speed has a direct influence on the heat balance of the human body. Increased wind speed leads to increased cooling in the skin area when the skin temperature is higher than the air temperature, which is called wind chill [14]. The effect is depended on the the air temperature. The higher the air temperature is, the less efficient is the wind speed. For an air temperature above $35 \text{ }^\circ\text{C}$ and wind speeds above 7 ms^{-1} , the UTCI increases. An increase of the air temperature and the mean radiant temperature leads to an increase of the UTCI. The relative humidity does not have a large effect on the UTCI, except for air temperatures of more than about $30 \text{ }^\circ\text{C}$, where the UTCI increases for increasing RH [36].

Table 23 is taken from [6, p. 489] and categorizes the UTCI ranges in terms of thermal stress. The comfort range is defined to lie between $18 \text{ }^\circ\text{C}$ and $26 \text{ }^\circ\text{C}$ [66, pp. 27-29].

Table 23: UTCI equivalent temperatures categorised in terms of thermal stress (from [6, p. 489]), [66, p. 30].

UTCI range ($^\circ\text{C}$)	Stress category
$\text{UTCI} > +46$	Extreme heat stress
$+38 < \text{UTCI} \leq +46$	Very strong heat stress
$+32 < \text{UTCI} \leq +38$	Strong heat stress
$+26 < \text{UTCI} \leq +32$	Moderate heat stress
$+9 \leq \text{UTCI} \leq +26$	No thermal stress
$+9 > \text{UTCI} \geq 0$	Slight cold stress
$0 > \text{UTCI} \geq -13$	Moderate cold stress
$-13 > \text{UTCI} \geq -27$	Strong cold stress
$-27 > \text{UTCI} \geq -40$	Very strong cold stress
$\text{UTCI} < -40$	Extreme cold stress

21 Figures

21.1 Grassland - further results of the Morris method

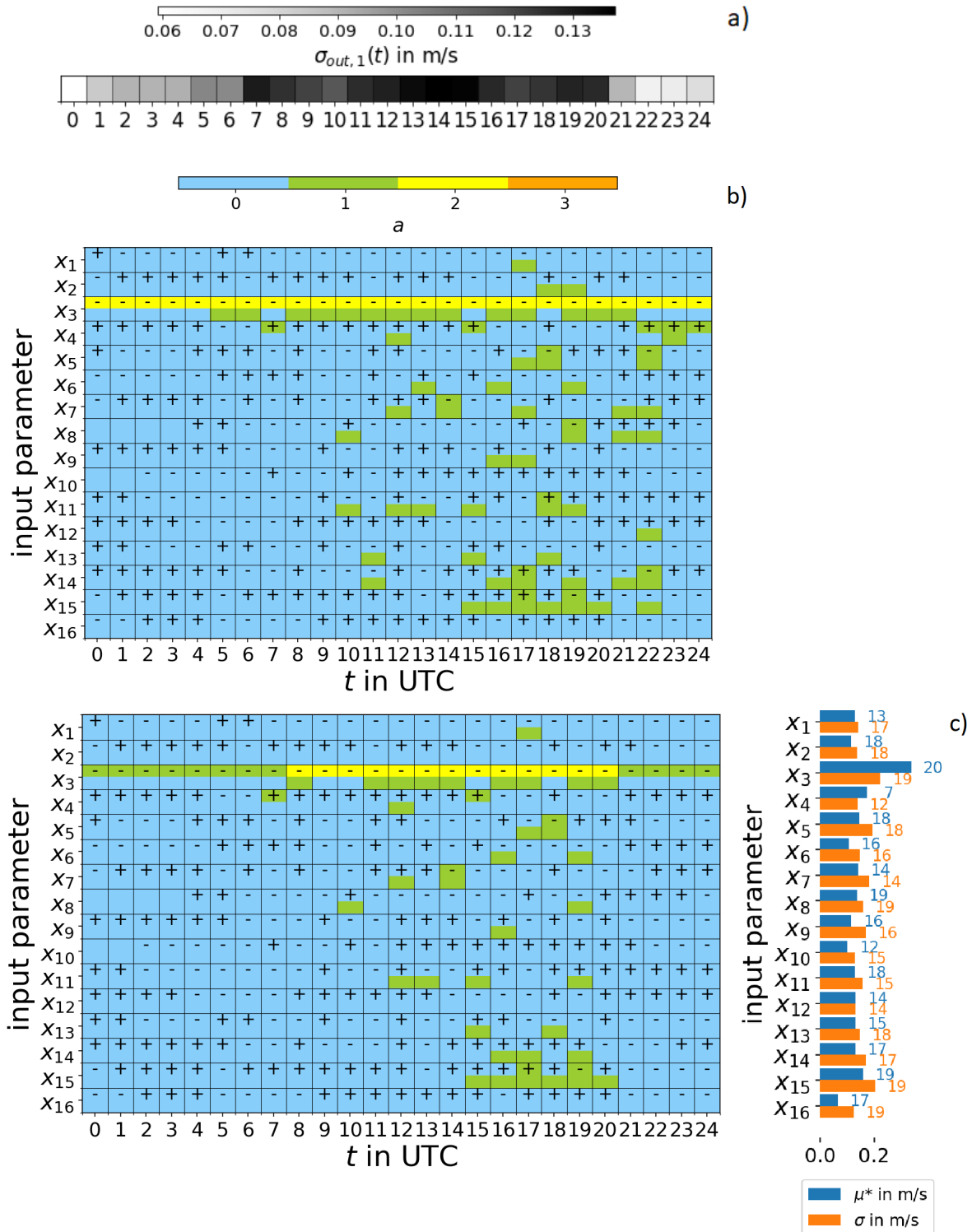


Figure 59: Grassland case: Visualization of the Morris sensitivity measures for the horizontally averaged 10 m wind speed $y_{k=1}(t)$.

a) $\sigma_{out,k=1}(t)$, b) Sensitivity measures colored according to $\mu_{i,k=1}^*(t)$ or $\sigma_{i,k=1}(t) \geq a \cdot \sigma_{out,k=1}(t)$, c) Sensitivity measures colored according to $\mu_{i,k=1}^*(t)$ or $\sigma_{i,k=1}(t) \geq a \cdot \max_t(\sigma_{out,k=1}(t))$ (left), $\max_t(\mu_{i,k=1}^*(t))$, $\max_t(\sigma_{i,k=1}(t))$ and corresponding t [UTC] (right).

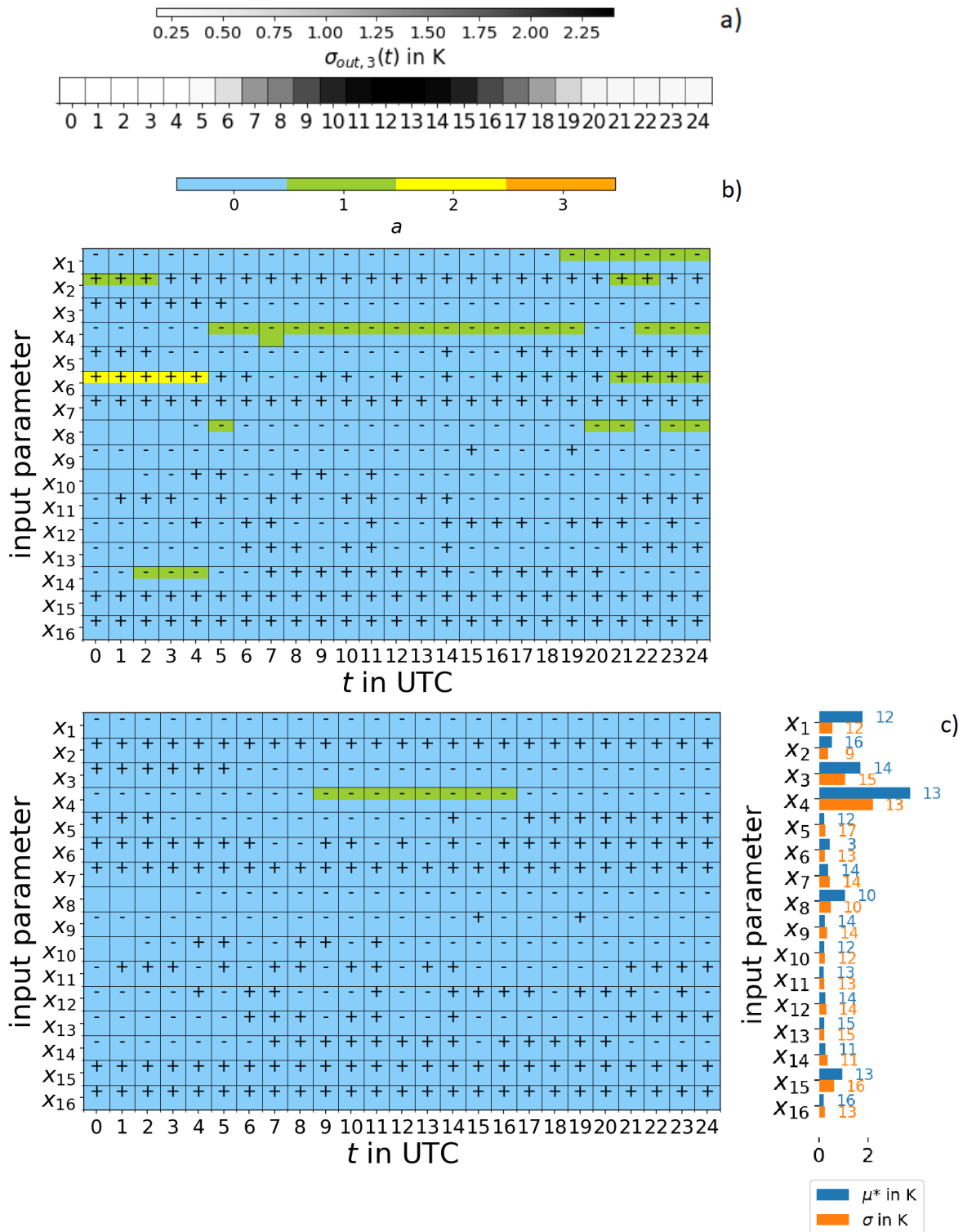


Figure 60: Grassland case: Visualization of the Morris sensitivity measures for the horizontally averaged surface temperature $y_{k=3}(t)$.
a) $\sigma_{out,k=3}(t)$., b) Sensitivity measures colored according to $\mu_{i,k=3}^*(t)$ or $\sigma_{i,k=3}(t) \geq a \cdot \sigma_{out,k=3}(t)$, c) Sensitivity measures colored according to $\mu_{i,k=3}^*(t)$ or $\sigma_{i,k=3}(t) \geq a \cdot \max_t(\sigma_{out,k=3}(t))$ (left), $\max_t(\mu_{i,k=3}^*(t))$, $\max_t(\sigma_{i,k=3}(t))$ and corresponding t [UTC] (right).

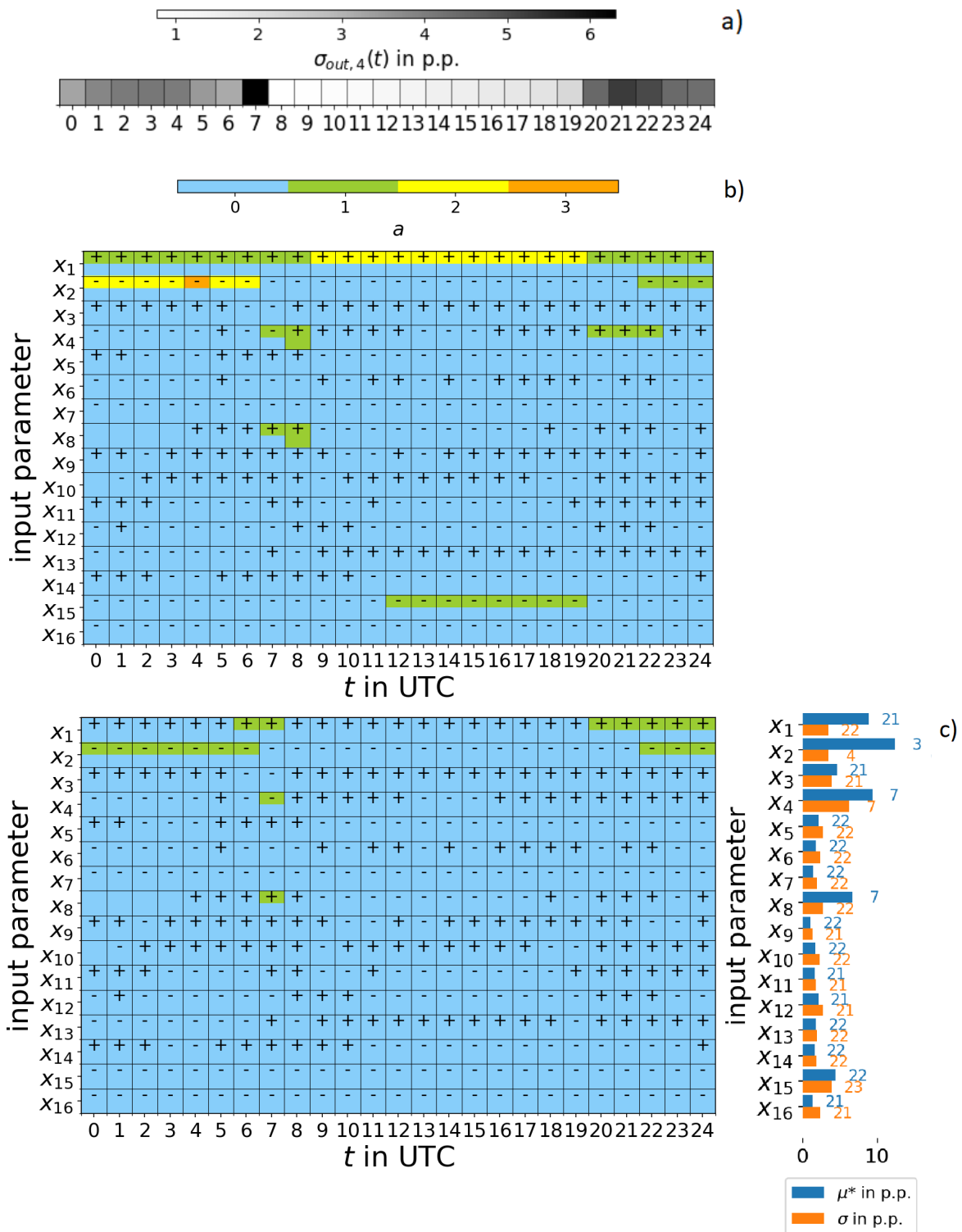


Figure 61: Grassland case: Visualization of the Morris sensitivity measures for the horizontally averaged RH $y_{k=4}(t)$.

a) $\sigma_{out,k=4}(t)$., b) Sensitivity measures colored according to $\mu_{i,k=4}^*(t)$ or $\sigma_{i,k=4}(t) \geq a \cdot \sigma_{out,k=4}(t)$, c) Sensitivity measures colored according to $\mu_{i,k=4}^*(t)$ or $\sigma_{i,k=4}(t) \geq a \cdot \max_t(\sigma_{out,k=4}(t))$ (left), $\max_t(\mu_{i,k=4}^*(t))$, $\max_t(\sigma_{i,k=4}(t))$ and corresponding t [UTC] (right).

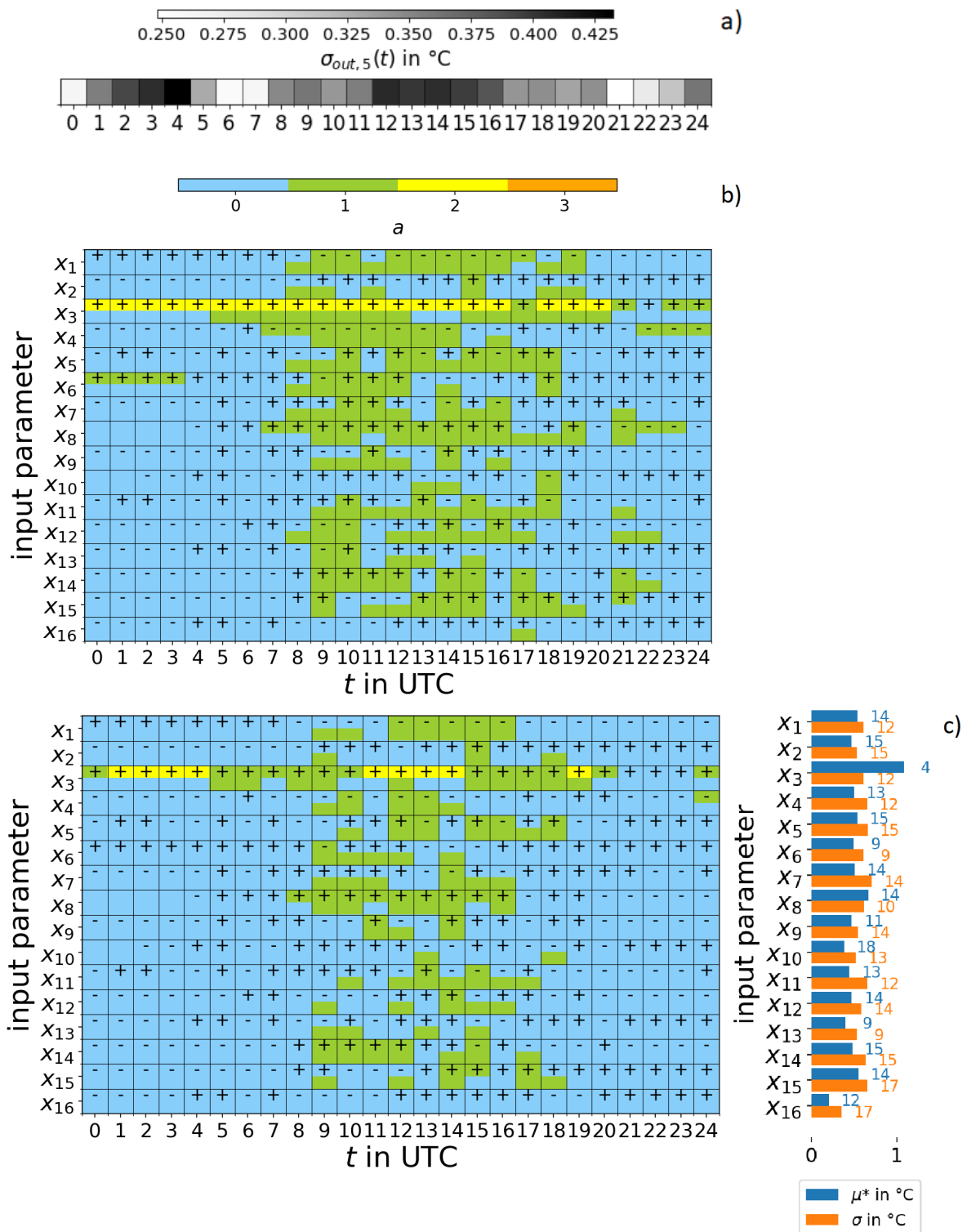


Figure 62: Grassland case: Visualization of the Morris sensitivity measures for the horizontally averaged UTCI $y_{k=5}(t)$.

a) $\sigma_{out,k=5}(t)$, b) Sensitivity measures colored according to $\mu_{i,k=5}^*(t)$ or $\sigma_{i,k=5}(t) \geq a \cdot \sigma_{out,k=5}(t)$, c) Sensitivity measures colored according to $\mu_{i,k=5}^*(t)$ or $\sigma_{i,k=5}(t) \geq a \cdot \max_t(\sigma_{out,k=5}(t))$ (left), $\max_t(\mu_{i,k=5}^*(t))$, $\max_t(\sigma_{i,k=5}(t))$ and corresponding t [UTC] (right).

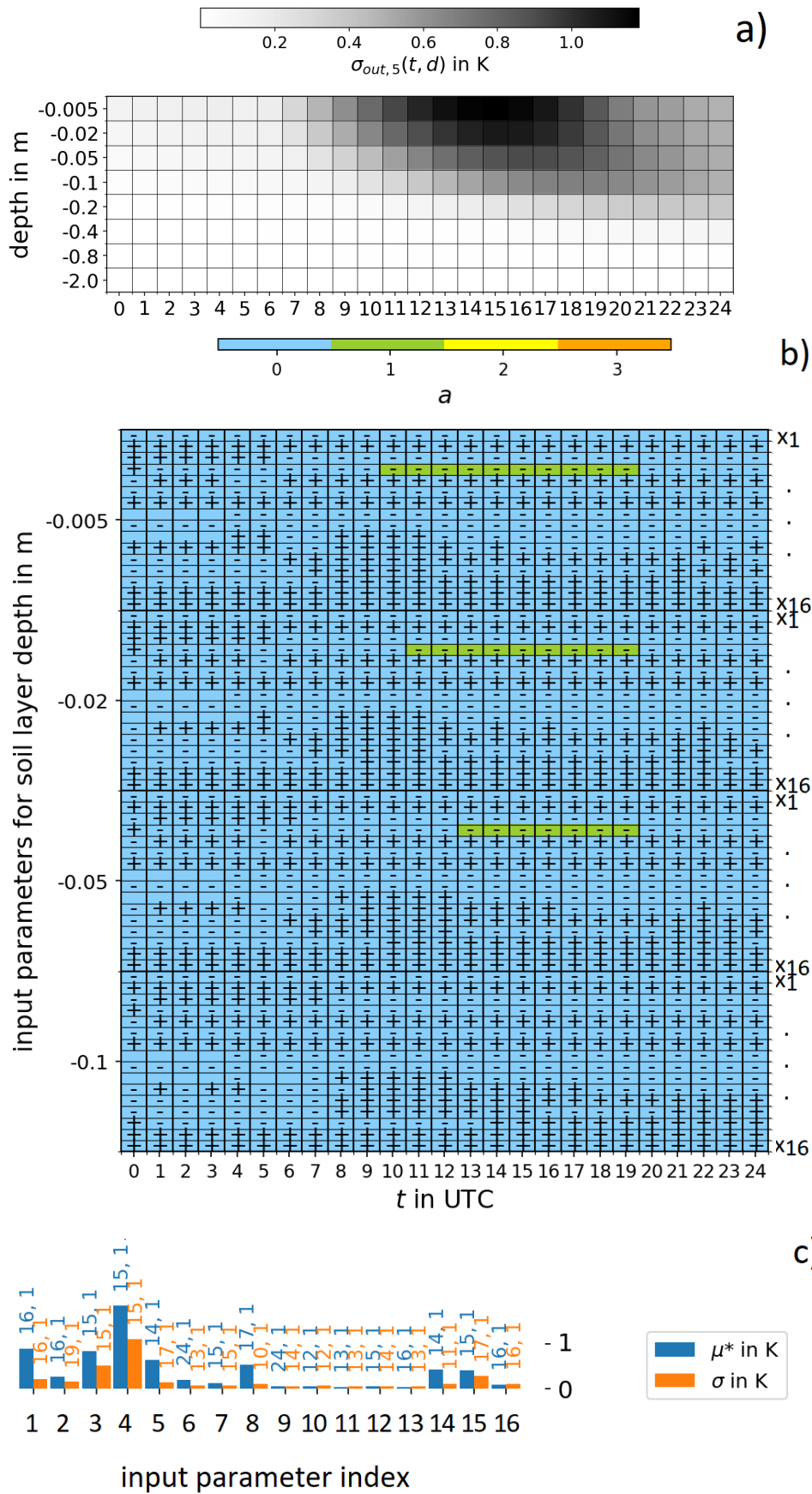


Figure 63: Grassland case: Visualization of the Morris sensitivity measures for the horizontally averaged soil temperature $y_{k=6}(t, d)$.

a) $\sigma_{out,k=6}(t, d)$, b) Sensitivity measures colored according to $\mu_{i,k=6}^*(t, d)$ or $\sigma_{i,k=6}(t, d) \geq a \cdot \max_{t,d}(\sigma_{out,k=6}(t, d))$, c) $\max_{t,d}(\mu_{i,k=6}^*(t, d))$, $\max_{t,d}(\sigma_{i,k=6}(t, d))$ and t [UTC], soil layer.

21.2 Paved surface - further results of the Morris method

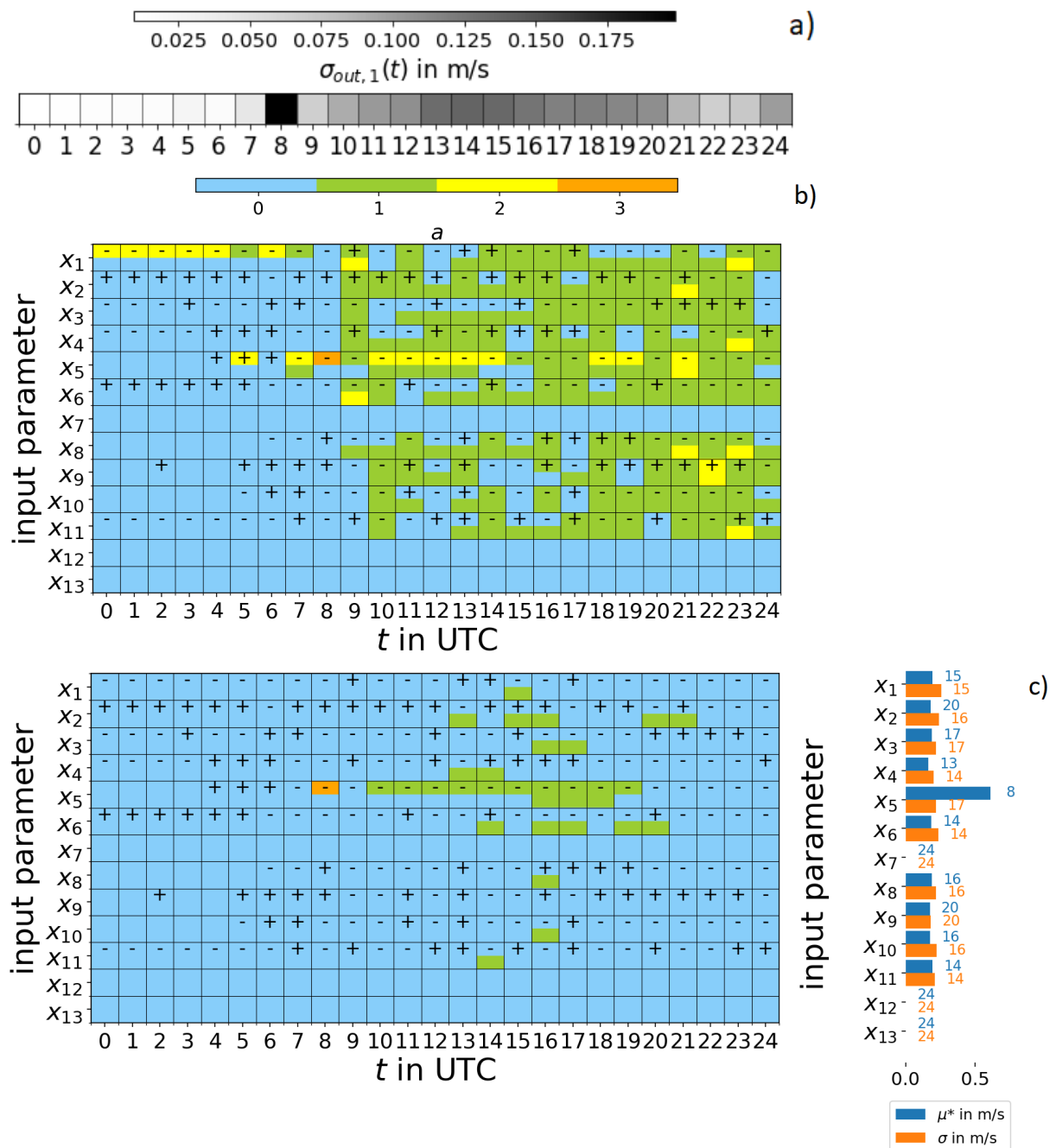


Figure 64: Pavement case: Visualization of the Morris sensitivity measures for the horizontally averaged 10 m wind speed $y_{k=1}(t)$.

a) $\sigma_{out,k=1}(t)$, b) Sensitivity measures colored according to $\mu_{i,k=1}^*(t)$ or $\sigma_{i,k=1}(t) \geq a \cdot \sigma_{out,k=1}(t)$, c) Sensitivity measures colored according to $\mu_{i,k=1}^*(t)$ or $\sigma_{i,k=1}(t) \geq a \cdot \max_t(\sigma_{out,k=1}(t))$ (left), $\max_t(\mu_{i,k=1}^*(t))$, $\max_t(\sigma_{i,k=1}(t))$ and corresponding t [UTC] (right).

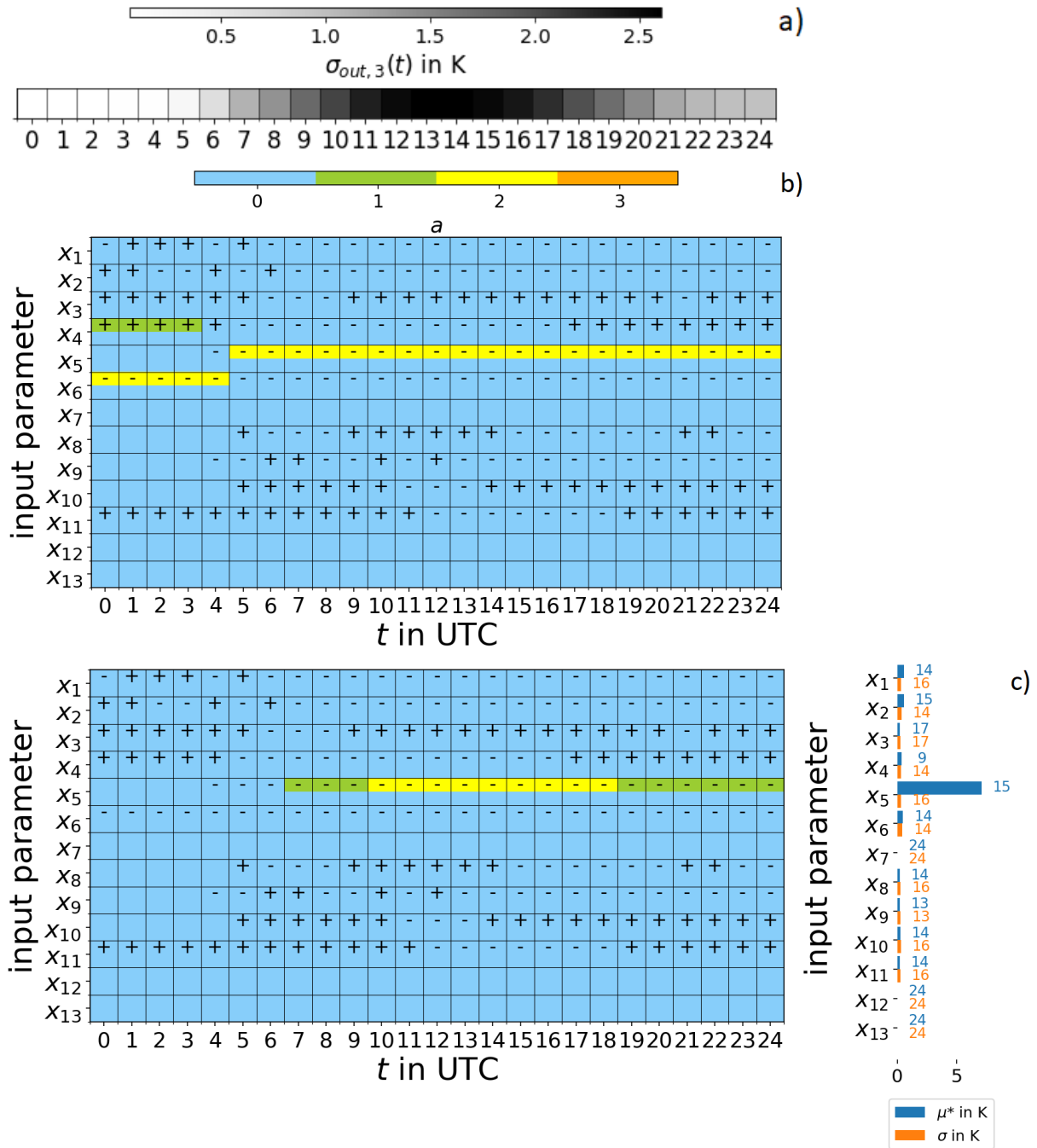


Figure 65: Pavement case: Visualization of the Morris sensitivity measures for the horizontally averaged surface temperature $y_{k=3}(t)$.

a) $\sigma_{out,k=3}(t)$, b) Sensitivity measures colored according to $\mu_{i,k=3}^*(t)$ or $\sigma_{i,k=3}(t) \geq a \cdot \sigma_{out,k=3}(t)$, c) Sensitivity measures colored according to $\mu_{i,k=3}^*(t)$ or $\sigma_{i,k=3}(t) \geq a \cdot \max_t(\sigma_{out,k=3}(t))$ (left), $\max_t(\mu_{i,k=3}^*(t))$, $\max_t(\sigma_{i,k=3}(t))$ and corresponding t [UTC] (right).

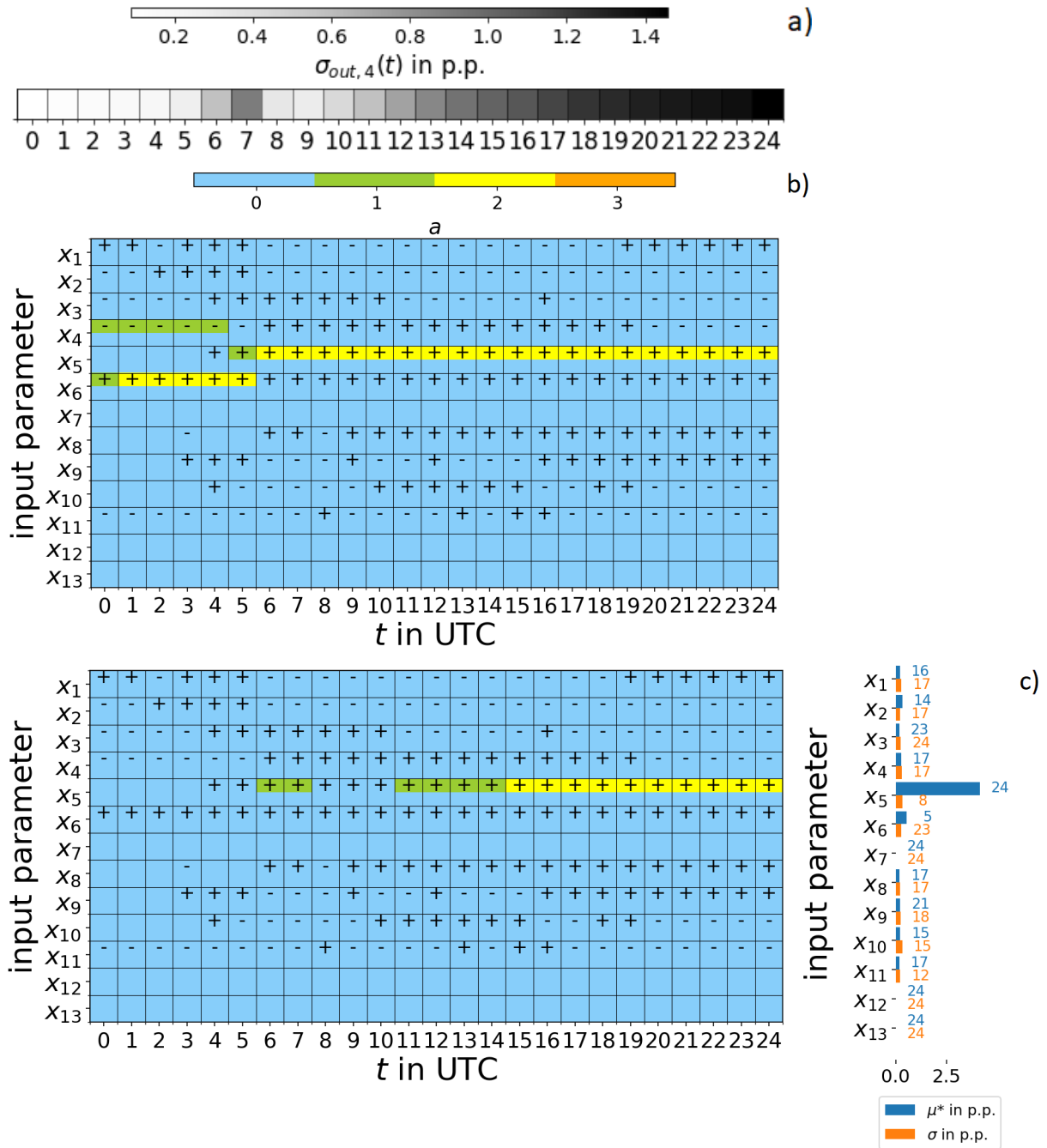


Figure 66: Pavement case: Visualization of the Morris sensitivity measures for the horizontally averaged RH $y_{k=4}(t)$.

a) $\sigma_{out,k=4}(t)$, b) Sensitivity measures colored according to $\mu_{i,k=4}^*(t)$ or $\sigma_{i,k=4}(t) \geq a \cdot \sigma_{out,k=4}(t)$, c) Sensitivity measures colored according to $\mu_{i,k=4}^*(t)$ or $\sigma_{i,k=4}(t) \geq a \cdot \max_t(\sigma_{out,k=4}(t))$ (left), $\max_t(\mu_{i,k=4}^*(t))$, $\max_t(\sigma_{i,k=4}(t))$ and corresponding t [UTC] (right).

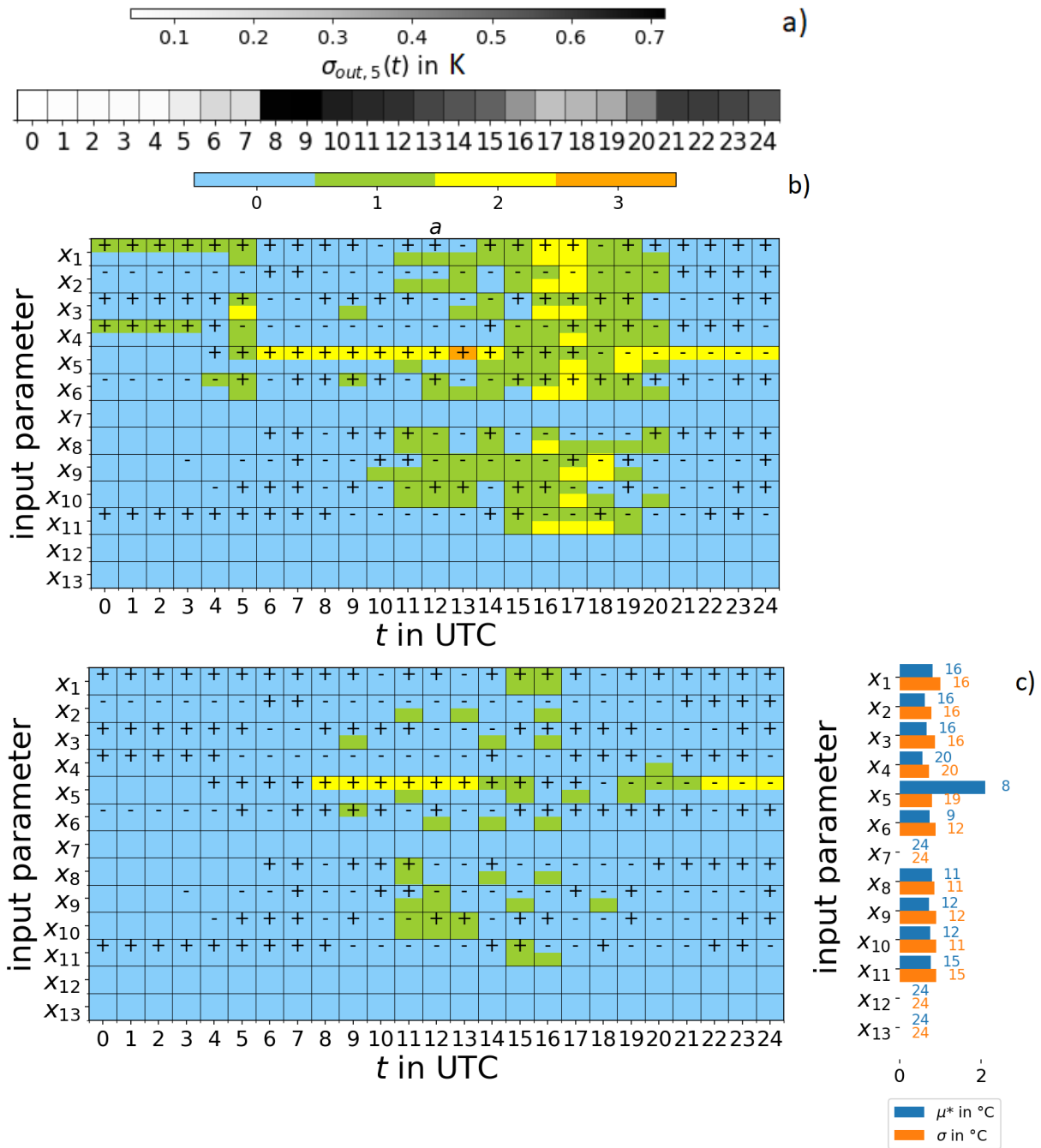


Figure 67: Pavement case: Visualization of the Morris sensitivity measures for the horizontally averaged UTCI $y_{k=5}(t)$.

a) $\sigma_{out,k=5}(t)$, b) Sensitivity measures colored according to $\mu_{i,k=5}^*(t)$ or $\sigma_{i,k=5}(t) \geq a \cdot \sigma_{out,k=5}(t)$, c) Sensitivity measures colored according to $\mu_{i,k=5}^*(t)$ or $\sigma_{i,k=5}(t) \geq a \cdot \max_t(\sigma_{out,k=5}(t))$ (left), $\max_t(\mu_{i,k=5}^*(t))$, $\max_t(\sigma_{i,k=5}(t))$ and corresponding t [UTC] (right).

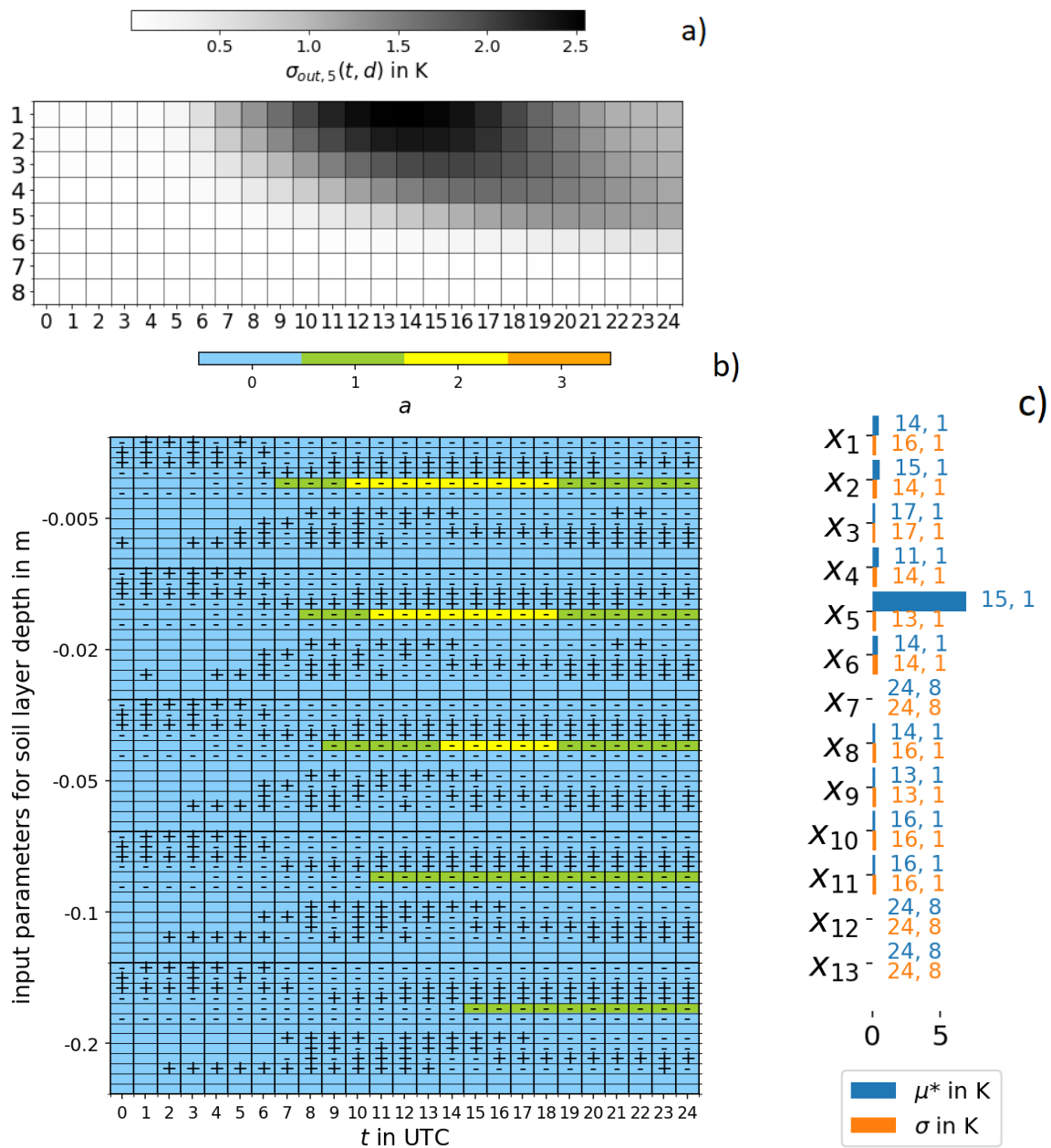


Figure 68: Pavement case: Visualization of the Morris sensitivity measures for the horizontally averaged soil temperature $y_{k=6}(t, d)$.

a) $\sigma_{out,k=6}(t, d)$, b) Sensitivity measures colored according to $\mu_{i,k=6}^*(t, d)$ or $\sigma_{i,k=6}(t) \geq a \cdot \max_t(\sigma_{out,k=6}(t))$, c) $\max_{t,d}(\mu_{i,k=6}^*(t, d))$, $\max_{t,d}(\sigma_{i,k=6}(t, d))$ and corresponding t, d [UTC], [soil layer].

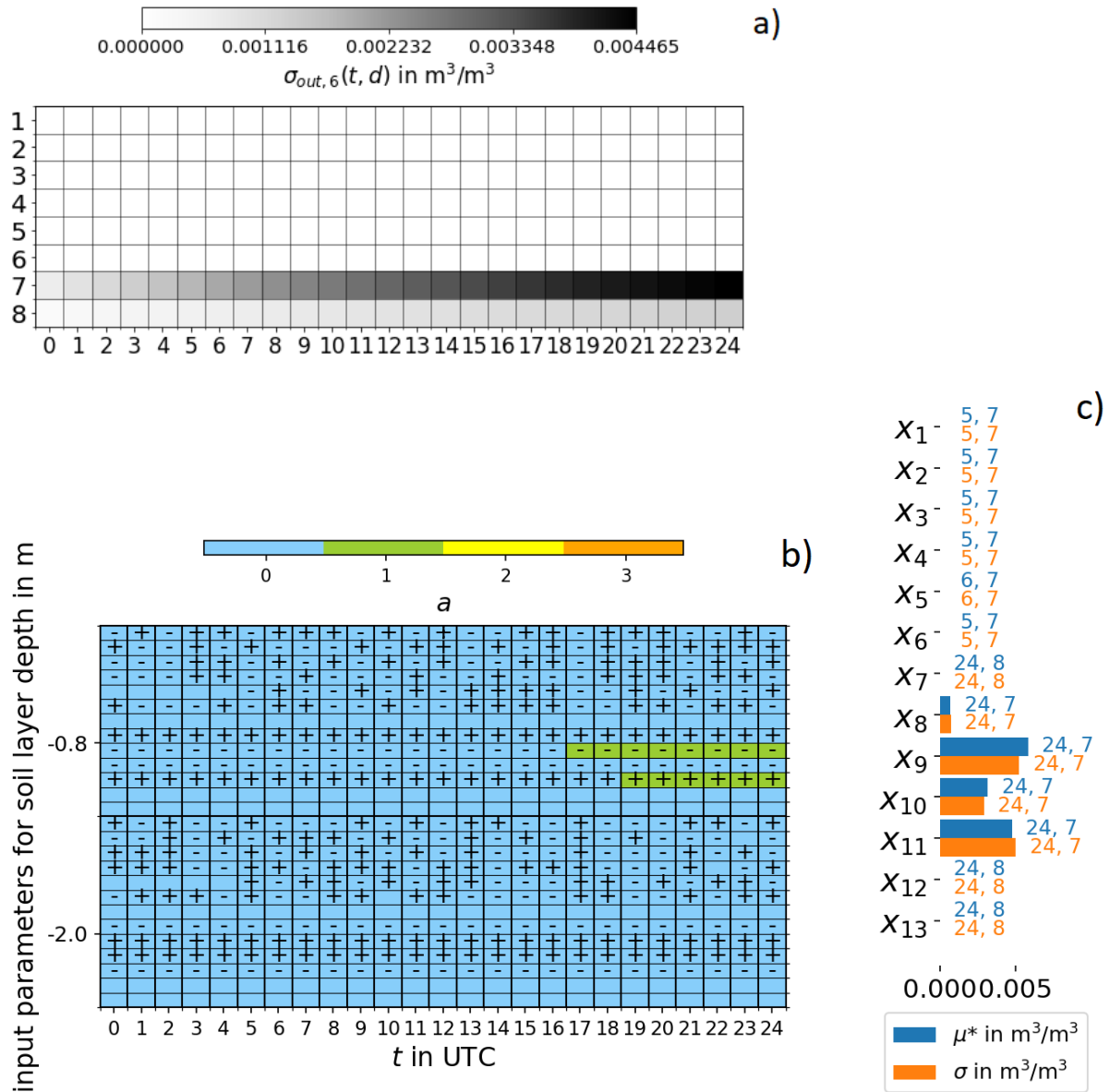


Figure 69: Pavement case: Visualization of the Morris sensitivity measures for the horizontally averaged soil moisture $y_{k=7}(t, d)$.

a) $\sigma_{out,k=7}(t, d)$, b) Sensitivity measures colored according to $\mu_{i,k=7}^*(t, d)$ or $\sigma_{i,k=7}(t) \geq a \cdot \max_t(\sigma_{out,k=7}(t))$, c) $\max_{t,d}(\mu_{i,k=7}^*(t, d))$, $\max_{t,d}(\sigma_{i,k=7}(t, d))$ and corresponding t, d [UTC], [soil layer].

21.3 Urban area - further results of the OAT analysis

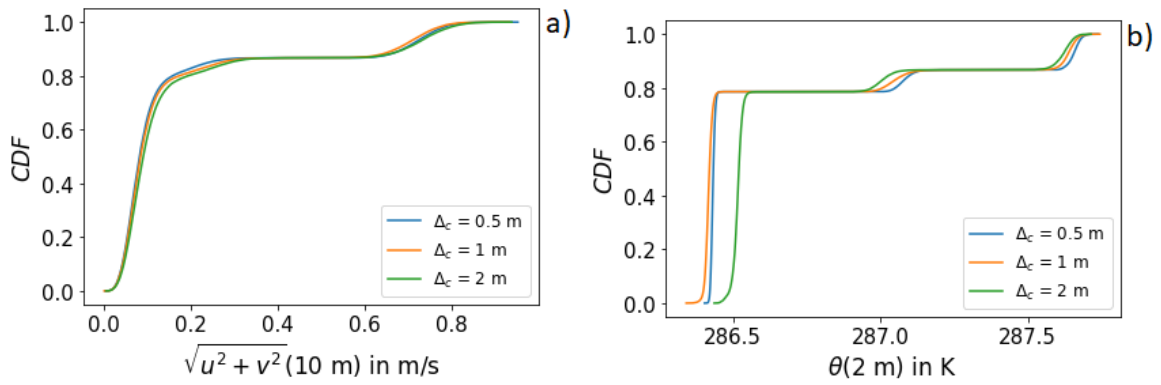


Figure 70: Grid sensitivity study for the urban child domain with stable stratification. CDF of a) the horizontal 10 m wind speed, b) the 2 m potential temperature.

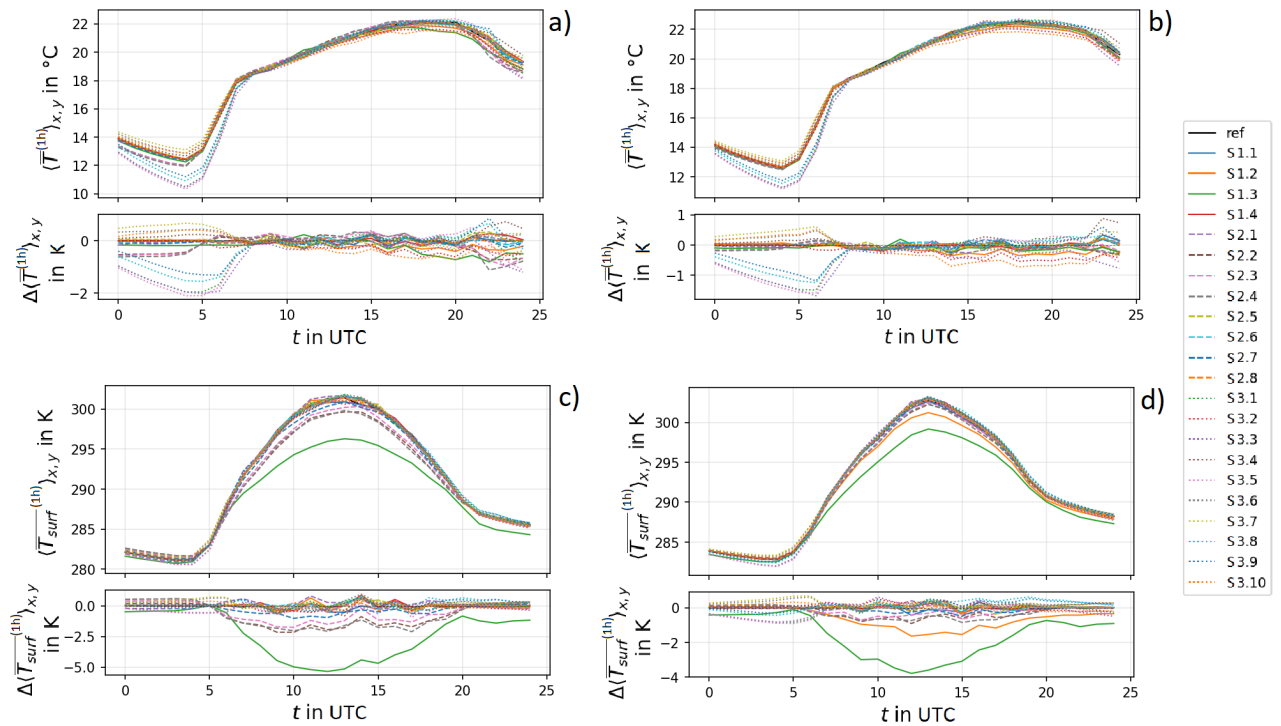


Figure 71: Further hourly and domain averaged output quantities and differences to the reference run for different averaging domains. a) park, b) open place c) park, d) single houses.

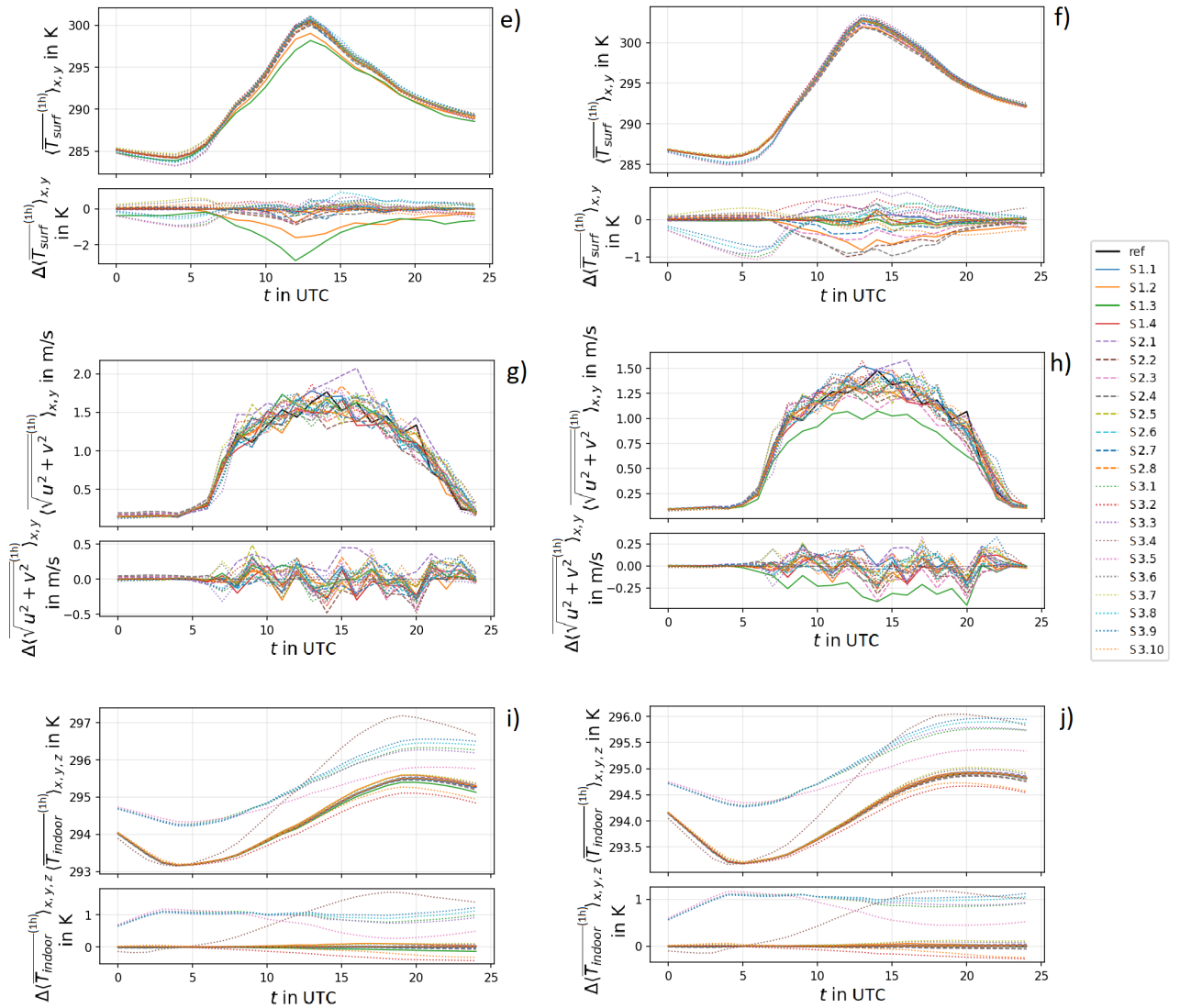


Figure 71: Continued: Further hourly and domain averaged output quantities and differences to the reference run for different averaging domains. e) street canyons, f) court yard, g) park, 10 m height h) park, 1.5 m height i) single houses j) court yard.

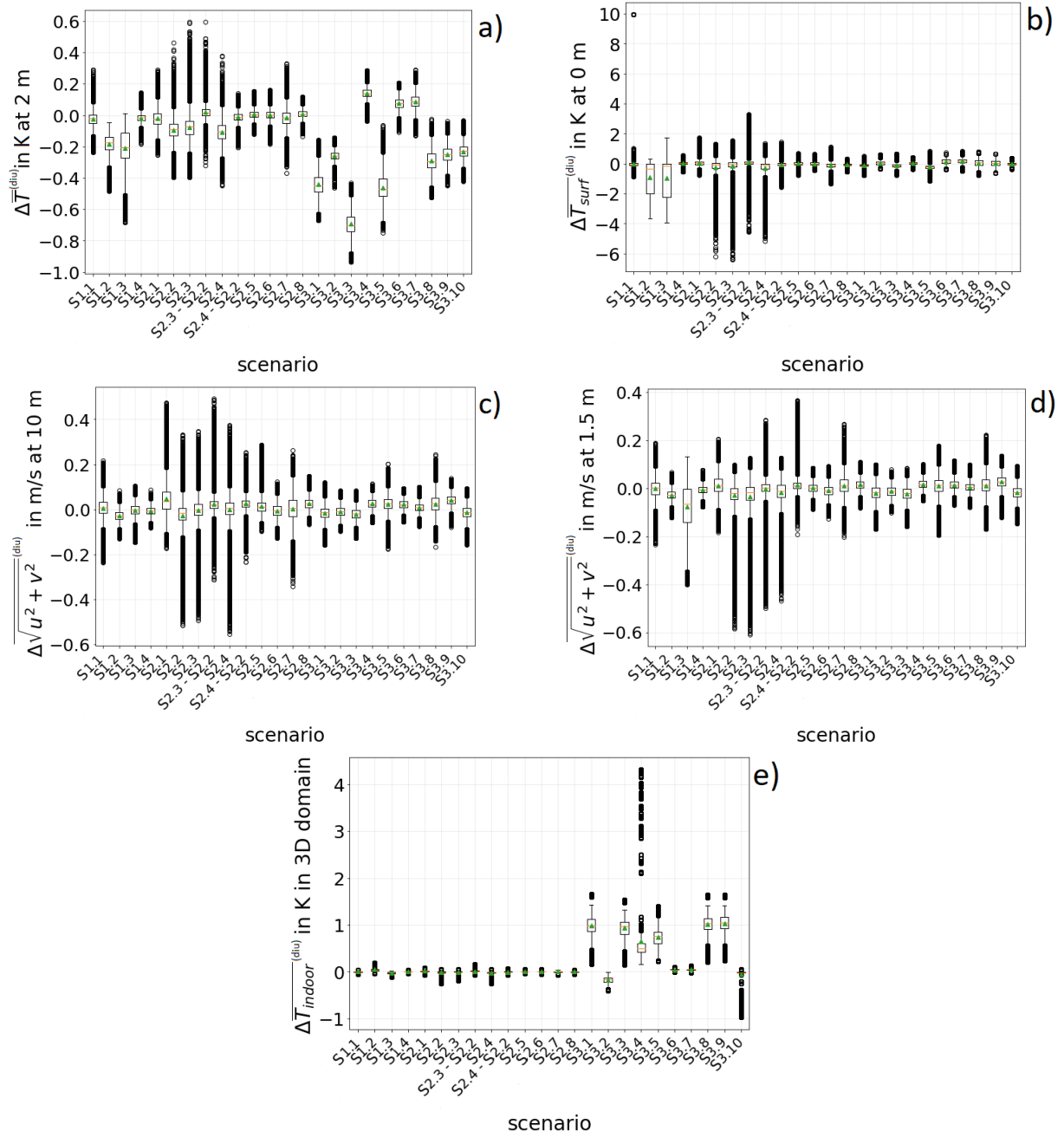


Figure 72: Bandwidth of local differences between diurnal averaged scenario and reference data in the total domain.

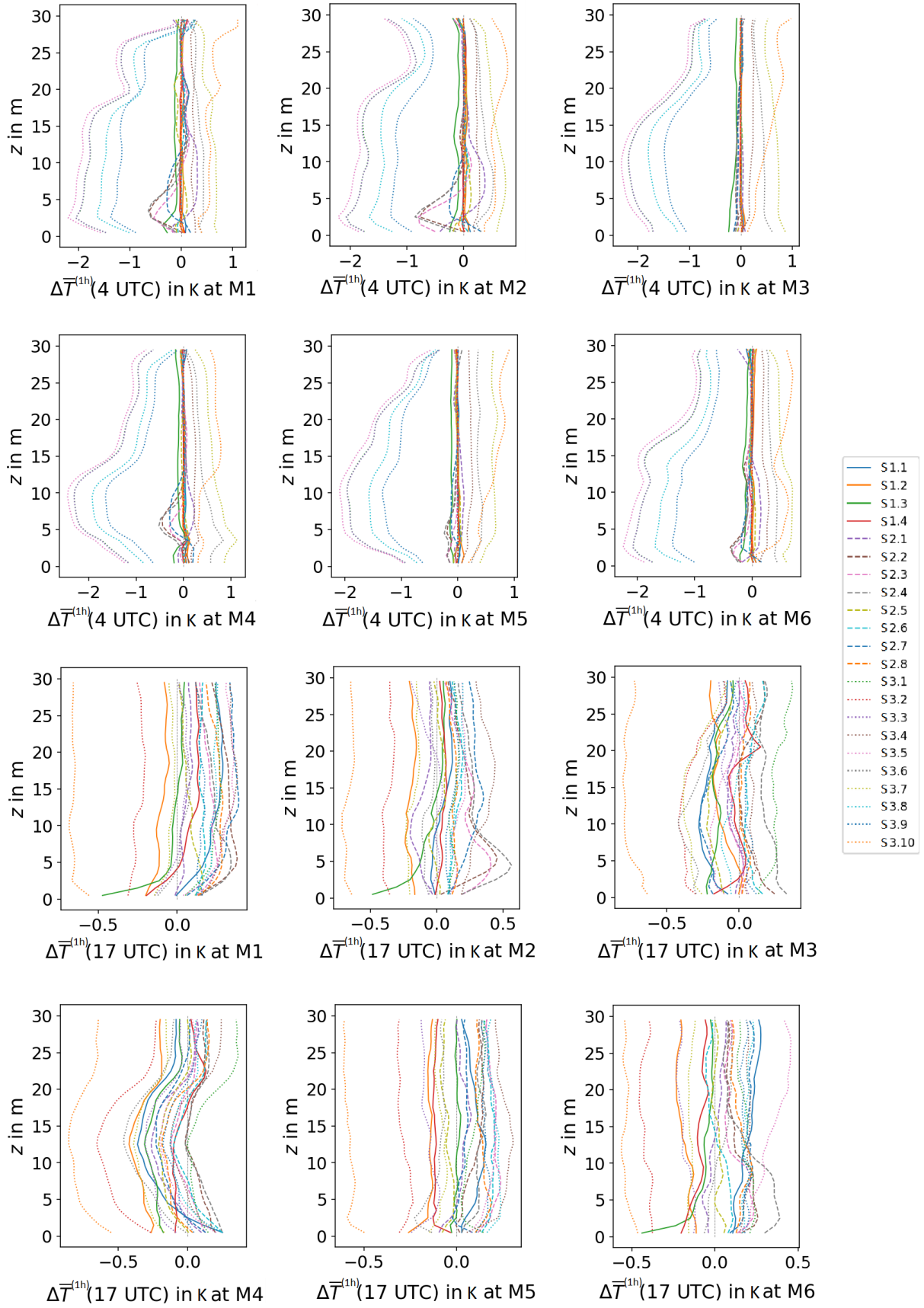


Figure 73: Local vertical profiles of differences between hourly averaged scenario and reference temperature extracted at the representative locations M_i , $i \in \{1, \dots, 6\}$ at 4 and 17 UTC.

References

- [1] Adams, B. M., Ebeida, M. S., Eldred, M. S., Geraci, G., Jakeman, J. D., Maupin, K. A., Monschke, J. A., Stephens, J. A., Swiler, L. P., Vigil, D. M., Wildey, T. M., Bohnhoff, W. J., Dalbey, K. R., Eddy, J. P., Frye, J. R., Hooper, R. W., Hu, K. T., Hough, P. D., Khalil, M., Ridgway, E. M., Rushdi, A.: Dakota, A Multilevel Parallel Object-Oriented Framework for Design Optimization, Parameter Estimation, Uncertainty Quantification, and Sensitivity Analysis: Version 6.7 User's Manual, University of California, 2017.
- [2] Andersen, H.-E., Reutebuch, S. E., McGaughey, R. J.: A rigorous assessment of tree height measurements obtained using airborne lidar and conventional field methods, *Canadian Journal of Remote Sensing*, Vol. 32, No. 5, 355-366, 2006.
- [3] Auvinen, M., Boi, S., Hellsten, A., Tanhuanpää, T., Järvi, L.: Study of Realistic Urban Boundary Layer Turbulence with High-Resolution Large-Eddy Simulation, *Atmosphere*, Vol. 11, 201, 2020.
- [4] Belda, M., Resler, J., Geletič, J., Krč, P., Maronga, B., Sührling, M., Kurppa, M., Kanani-Sührling, F., Fukal, V., Eben, K., Benešová, N., Auvinen, M.: Sensitivity analysis of the PALM model system 6.0 in the urban environment, *Geoscientific Model Development*, Vol. 14, No. 7, 4443–4464, 2021.
- [5] BMBF-Fördermaßnahme Stadtklima im Wandel, <http://uc2-program.org/>, Stand: 29.07.2020.
- [6] Bröde, P., Fiala, D., Błażejczyk, K., Holmér, I., Jendritzky, G., Kampmann, B., Tinz, B., Havenith, Ge.: Deriving the operational procedure for the Universal Thermal Climate Index (UTCI), *Int J Biometeorol*, Vol. 56, 481–494, 2012.
- [7] Brune, M., Bender, S., Groth, M.: Gebäudebegrünung und Klimawandel. Anpassung an die Folgen des Klimawandels durch klimawandeltaugliche Begrünung. Report 30. Climate Service Center Germany, Hamburg, 2017.
- [8] Die Bundesanstalt für Geowissenschaften und Rohstoffe: Bodenübersichtskarte 1:1.000.000 (BÜK1000), https://www.bgr.bund.de/DE/Themen/Boden/Informationsgrundlagen/Bodenkundliche_Karten_Datenbanken/BUEK1000/buek1000_node.html, last access: 05.02.2023.
- [9] Burkart, K., Meier, F., Schneider, A., Breitner, S., Canário, P., Alcoforado, M. J., Scherer, D., Endlicher, W.: Modification of Heat-Related Mortality in an Elderly Urban Population by Vegetation (Urban Green) and Proximity to Water (Urban Blue): Evidence from Lisbon, Portugal. *Environmental Health Perspect*, Vol. 24, 927–934, 2016.
- [10] Campbell, G. S., The researcher's complete guide to Leaf Area Index (LAI), <https://www.metergroup.com/en/meter-environment/education-guides/researchers-complete-guide-leaf-area-index-lai>, metergroup, last access: 31.07.2023.
- [11] Campolongo, F., Cariboni, J., Saltelli, A.: An effective screening design for sensitivity analysis of large models, *Environmental Modelling & Software*, Vol. 22, 1509-1518, 2007.

- [12] Copernicus: CORINE Land Cover, <https://land.copernicus.eu/pan-european/corine-land-cover/#>, last access: 05.02.2023.
- [13] Deardorff, J. W.: Stratocumulus-capped mixed layers derived from a three-dimensional model. *Boundary-Layer Meteorology*, Vol. 18, 495–527, 1980.
- [14] Deutscher Wetterdienst: Wetter- und Klimalexikon. Wind Chill-Effekt, <https://www.dwd.de/DE/service/lexikon/Functions/glossar.html?lv2=102936&lv3=103172>, last access: 27.03.2023.
- [15] Etling, Dieter: *Theoretische Meteorologie. Eine Einführung*, 3. erweiterte und aktualisierte Auflage, Springer, 2008.
- [16] El Guernaoui, O., Reuder, J., Esau, I., Wolf, T., Maronga, B.: Scaling the Decay of Turbulence Kinetic Energy in the Free-Convective Boundary Layer, *Boundary-Layer Meteorology*, Vol. 173, 79–97, 2019.
- [17] European Soil Data Centre (ESDAC): European Soil Database & soil properties, <https://esdac.jrc.ec.europa.eu/resource-type/european-soil-database-soil-properties>, last access: 05.02.2023.
- [18] Fang, H., Baret, F., Plummer, S., Schaepman-Strub, G.: An overview of global leaf area index (LAI). Methods, products, validation, and applications, *Reviews of Geophysics*, Vol. 57, 739-799, 2019.
- [19] Federer, C. A.: Trees modify the urban microclimate, *Journal of arboriculture*, Vol. 2, No. 7, 121–127, 1976.
- [20] Feng, K., Lu1, Z., Yang, C.: Enhanced Morris method for global sensitivity analysis: good proxy of Sobol’index, *Structural and Multidisciplinary Optimization*, Vol. 59, 373–387, 2019.
- [21] Fenniak, Mathieu: Latin Hypercube Sampling, <https://mathieu.fenniak.net/latin-hypercube-sampling/>, last access: 30.06.2022.
- [22] Garcia Sanchez, D., Lacarrière, B., Musy, M., Bourges, B.: Application of sensitivity analysis in building energy simulations: combining first- and second-order elementary effects methods, arXiv:1203.3055v2, 2012.
- [23] GDI-NI: Baumkataster der Stadt Springe, <https://geoportal.geodaten.niedersachsen.de/harvest/srv/api/records/588d9f4c-40d9-414b-9a61-e297b9036fdb>, last access: 05.02.2023.
- [24] Gehrke, K.F., Sühling, M., Maronga, B.: Modeling of land–surface interactions in the PALM model system 6.0: land surface model description, first evaluation, and sensitivity to model parameters, *Geoscientific Model Development*, Vol. 14, 5307–5329, 2021.
- [25] Gronemeier, Tobias: *Advances in Urban Ventilation Assessments using Large-Eddy Simulation*, Dissertation, Gottfried Wilhelm Leibniz Universität Hannover, 2021.
- [26] Gronemeier, T., Raasch, S., Ng, E.: Effects of Unstable Stratification on Ventilation in Hong Kong, *Atmosphere*, Vol. 8, No. 9, 168, 2017.
- [27] Groß, G.: A windthrow model for urban trees with application to storm „Xavier“, *Meteorologische Zeitschrift*, Vol. 27, No. 4, 299-308, 2018.

- [28] Groß, G.: Numerical simulation of canopy flows, Springer Verlag Heidelberg, 1993.
- [29] Groß, G.: On the range of boundary layer model results depending on inaccurate input data, *Meteorologische Zeitschrift*, Vol. 28, No. 3, 225–234, 2019.
- [30] Groß, G.: Some effects of water bodies on the environment – numerical experiments, *Journal of Heat Island Institute International*, Vol. 12-2, 1-11, 2017.
- [31] Groß, G., Raasch, S., Maronga, B.: Abschlussbericht für den Verbund MOSAIK Modellbasierte Stadtplanung und Anwendung im Klimawandel, Leibniz Universität Hannover, 2020.
- [32] Heldens, W., Burmeister, C., Kanani-Sühring, F., Maronga, B., Pavlik, D., Sühring, M., Zeidler, J., Esch, T.: Geospatial input data for the PALM model system 6.0: model requirements, data sources, and processing, *Geoscientific Model Development*, Vol. 13, 5833–5873, 2020.
- [33] Hellsten, A., Ketelsen, K., Sühring, M., Auvinen, M., Maronga, B., Knigge, C., Barmpas, F., Tsegas, G., Moussiopoulos, N., Raasch, S.: A nested multi-scale system implemented in the large-eddy simulation model PALM model system 6.0, *Geoscientific Model Development*, Vol. 14, 3185–3214, 2021.
- [34] Hughes, M., Palmer, J., Cheng, V., Shipworth, D.: Global sensitivity analysis of England’s housingenergy model, *Journal of Building Performance Simulation*, Vol. 8, No. 5, 283-294, 2015.
- [35] Iman, R.: Latin Hypercube Sampling, isbn: 9781118445112, 1999.
- [36] Kongsgaard, C., UTCI Parameter Sensitivity, <https://compute.procedural.build/docs/comfort/utci.sensitivity>, 12.07.2021, last access: 24.07.2023.
- [37] Kraetzig, N. M., up42: Aerial Imagery Explained: Top Sources and What You Need to Know, <https://up42.com/blog/tech/aerial-imagery-explained-top-sources-and-what-you-need-to-know>, last acces: 05.02.2023.
- [38] Kuttler, W., Weber S.: Characteristics and phenomena of the urban climate, *Meteorologische Zeitschrift*, Early Access Article, 2023.
- [39] Lindauer, M.: Dynamische Sensitivitätsanalysemethoden energetischer Wohngebäudequartierssimulationen, Dissertation, Technische Universität München, Fraunhofer Verlag, München 2017.
- [40] Markkanen, T., Rannik, Ü., Marcolla, B., Cescatti, A., Vesala, T.: Footprints and Fetches for Fluxes over Forest Canopies with Varying Structure and Density, *Boundary-Layer Meteorology*, Vol. 106, 437-459, 2003.
- [41] Maronga, B., Gryschka, M., Heinze, R., Hoffmann, F., Kanani-Sühring, F., Keck, M., Ketelsen, K., Letzel, M. O., Sühring, M., Raasch, S.: The Parallelized Large-Eddy Simulation Model (PALM) version 4.0 for atmospheric and oceanic flows: model formulation, recent developments, and future perspectives, *Geoscientific Model Development*, Vol. 8, 1539-1637, 2015.
- [42] Maronga, B, Groß, G., Raasch, S., Banzhaf, S., Forkel, R., Heldens, W., Kanani-Sühring, F., Matzarakis, A., Mauder, M., Pavlik, D., Pfafferott, J., Schubert, S., Seckmeyer, G., Sieker, H., Winderlich, K.: Development of a new urban climate model

based on the model PALM – Project overview, planned work, and first achievements, *Meteorologische Zeitschrift*, Vol. 28, No. 2, 105–119, 2019.

- [43] Maronga, B., Banzhaf, S., Burmeister, C., Esch, T., Forkel, R., Fröhlich, D., Fuka, V., Gehrke, K.F., Geletič, J., Giersch, S., Gronemeier, T., Groß, G., Heldens, W., Hellsten, A., Hoffmann, F., Inagaki, A., Kadasch, E., Kanani-Sühring, F., Ketelsen, K., Khan, B.A., Knigge, C., Knoop, H., Krč, P., Kurppa, M., Maamari, H., Matzarakis, A., Mauder, M., Pallasch, M., Pavlik, D., Pfafferott, J., Resler, Ja., Rissmann, S., Russo, E., Salim, M., Schrempf, M., Schwenkel, J., Seckmeyer, G., Schubert, S., Sühring, M., von Tils, R., Vollmer, L., Ward, S., Witha, B., Wurps, H., Zeidler, J., Raasch, S.: Overview of the PALM model system 6.0, *Geoscientific Model Development*, Vol. 13, 1335–1372, 2020.
- [44] Misara, S., Henze, N., Sidelev A., : Thermal Characteristica of BIPV (U-value and g-value), Fraunhofer Institute for Wind Energy and Energy System Technology IWES, Kassel, 2011.
- [45] Miyashita, A., Suzuki, S.: A method for measuring the forces acting on a tree trunk using strain gauges, *PLoS ONE*, Vol. 16, 2021.
- [46] Morris, Max D.: Factorial Sampling Plans for Preliminary Computational Experiments, *Technometrics*, Vol. 33, No. 2., 161-174, 1991.
- [47] NASA, Earthdata, open access for open science: What is Remote Sensing? Tutorial on remotely-sensed data, from sensor characteristics, to different types of resolution, to data processing and analysis, <https://www.earthdata.nasa.gov/learn/backgrounders/remote-sensing>, last access: 16.10.2023.
- [48] palm: Land Surface Parameters, https://palm.muk.uni-hannover.de/trac/wiki/doc/app/land_surface_parameters, last access: 03.03.2023.
- [49] palm: Plant Canopy Parameters, https://palm.muk.uni-hannover.de/trac/wiki/doc/app/plant_canopy_parameters, last access: 13.10.2020.
- [50] PALM webinar: E1: Convective boundary layer, Institute of Meteorology and Climatology, Leibniz Universität Hannover, 2022.
- [51] Pfafferott, J., Rißmann, S., Sühring, M., Kanani-Sühring, F., Maronga, B.: Building indoor model in PALM-4U: indoor climate, energy demand, and the interaction between buildings and the urban microclimate, *Geoscientific Model Development*, Vol. 14, 3511–3519, 2021.
- [52] Raasch, S., Schröter, M.: PALM - A large-eddy simulation model performing on massively parallel computers, *Meteorologische Zeitschrift*, Vol. 10, No. 5, 363 - 372, 2001.
- [53] Raasch, S., Maronga, B.: Stadtklima im Wandel. Stadtplanung mit hochauflösenden Simulationsmodellen, *Mission 2031. Zukunft denken - nachhaltig handeln*, *Unimagazin Ausgabe 01|02 • 2021*, p. 22, 2021.

- [54] Rosenzweig, C., Solecki, W. D., Slosberg, R. B.: Mitigating New York City’s Heat Island With Urban Forestry, Living Roofs, and Light Surfaces, New York City Regional Heat Island Initiative. Final Report, 2006.
- [55] Ruuska, T., Vinha, J., Kivioja, H.: Measuring thermal conductivity and specific heat capacity values of inhomogeneous materials with a heat flow meter apparatus, *Journal of Building Engineering*, Vol. 9, 135–141, 2017.
- [56] Ryan, J. C., Hubbard, A., Box, J. E., Brough, S., Cameron, K., Cook, J. M., Cooper, M., Doyle, S. H., Edwards, A., Holt, T., Irvine-Fynn, T., Jones, C., Pitcher, L. H., Rennermalm, A. K., Smith, L. C., Stibal, M., Snooke, N.: Derivation of High Spatial Resolution Albedo from UAV Digital Imagery: Application over the Greenland Ice Sheet, *Frontiers in Earth Science*, Vol. 5, Article 40, 2017.
- [57] Saltelli, A., Tarantola, S., Campolongo, F., Ratto, M.: *Sensitivity Analysis in Practice. A Guide to Assessing Scientific Models*, John Wiley & Sons Ltd, Chichester 2004.
- [58] Saltelli, A., Annoni, P., Azzini, I., Campolongo, F., Ratto, M., Tarantola, S.: Variance based sensitivity analysis of model output. Design and estimator for the total sensitivity index, *Computer Physics Communications*, Vol. 181, 259–270, 2010.
- [59] Scherer, D., Antretter, F., Bender, S., Cortekar, J., Emeis, S., Fehrenbach, U., Groß, G., Halbig, G., Hasse, J., Maronga, B., Raasch, S., Scherber, K.: Urban Climate Under Change [UC]2– A National Research Programme for Developing a Building-Resolving Atmospheric Model for Entire City Regions, *Meteorologische Zeitschrift*, Vol.28, No. 2, 95–104, 2019.
- [60] Shields, M. D., Zhang, J.: *Sensitivity Analysis in Practice. The generalization of Latin hypercube sampling*, arXiv:1507.06716v1, 2015.
- [61] Smith, K. R., Roebber, P. J.: Green Roof Mitigation Potential for a Proxy Future Climate Scenario in Chicago, Illinois, *Journal of Applied Meteorology and Climatology*, 50, 507–522, 2011.
- [62] Smith, R. C.: *Uncertainty Quantification. Theory, Implementation, and Applications*, North Carolina State University, *siam Computational Science & Engineering*, Philadelphia, USA, 2014.
- [63] Urrego-Blanco, J. R., Hunke, E. C., Urban, N.: Emergent Relationships Among Sea Ice, Longwave Radiation, and the Beaufort High Circulation Exposed Through Parameter Uncertainty Analysis, *Journal of Geophysical Research: Oceans*, 124, 9572–9589, 2019.
- [64] van Genuchten, M.: A closed form equation for predicting the hydraulic conductivity of unsaturated soils, *Soil Science Society of America Journal*, Vol.44, 892–898, 1980.
- [65] Verein deutscher Ingenieure: VDI-Richtlinie 3787, Umweltmeteorologie. Berücksichtigung von Klima und Lufthygiene in räumlichen Planungen, Blatt 9, 2004.
- [66] Verein deutscher Ingenieure: VDI-Richtlinie 3787, Umweltmeteorologie. Methoden zur human-biometeorologischen Bewertung der thermischen Komponente des Klimas, Blatt 2, 2022.

- [67] Verein deutscher Ingenieure: VDI-Richtlinie 3783, Umweltmeteorologie. Prognostische mesoskalige Windfeldmodelle Evaluierung für dynamisch und thermisch bedingte Strömungsfelder, Blatt 7, 2017.
- [68] Verein deutscher Ingenieure: VDI-Richtlinie 3787, Umweltmeteorologie. Stadtentwicklung im Klimawandel, Blatt 8, 2020.
- [69] von Tils, Robert: Einfluss von Gebäudebegrünung auf das Innenraumklima - Simulationen mit einem mikroskaligen Modell, Dissertation, Gottfried Wilhelm Leibniz Universität Hannover, 2020.
- [70] Weihs, P., Staiger, H., Tinz, B., Batchvarova, E., Rieder, H., Vuilleumier, L., Maturilli, M., Jendritzky, G.: The uncertainty of UTCI due to uncertainties in the determination of radiation fluxes derived from measured and observed meteorological data, *International Journal of Biometeorology*, Vol. 56, 537–555, 2012.
- [71] Wicker, L. J., Skamarock, W. C.: Time-Splitting Methods for Elastic Models Using Forward Time Schemes, *Monthly Weather Review*, Vol. 130, No. 8, 2088-2097, 2002.
- [72] Williamson, J. H.: Low-storage Runge-Kutta schemes, *Journal of Computational Physics*, Vol. 35, Issue 1, 48-56, 1980.
- [73] Westermann, J. R., Bolsius, J., Kunze, S., Schünemann, C., Sinning, H., Ziemann, A., Baldin, M.-L., Brüggemann, K., Brzoska, P., Ehnert, F., Goldberg, V., Großmann, L., Grunewald, K., Naumann, T., Reinfried, F., Richter, B., Spohr, G., Ortlepp, R.: Hitzeanpassung von Stadtquartieren. Akteursperspektiven und Umsetzungsansätze, *GAIA - Ecological Perspectives for Science and Society*, Vol. 30, No. 4, 257–267, 2021.

Acknowledgements

The current study was performed as part of MOSAIK, the Module A of the research programme ‘[UC]² - Urban climate under change’, which is funded by the Federal Ministry of Education and Research (BMBF) under grant 01LP1601 within the framework of the Strategy ‘Research for Sustainability’. The simulations were carried out on the computer clusters of the North-German Supercomputing Alliance (HLRN).

This dissertation was supervised by Prof. Dr. Günter Groß, to whom I would like to express my sincere thanks. Through his professional guidance and scientific advice, he has supported me in both the master’s thesis and the doctoral dissertation. Likewise, I would like to thank Prof. Dr. Björn Maronga and Prof. Dr. Dieter Scherer who agreed to act as co-examiners, and Prof. Dr. Gunnar Friege who agreed to hold the chair of the Doctoral Commission. Furthermore, I would like to express my sincere thanks to Henning Teickner and my family for proofreading. A special thanks goes to my entire family, who always support me.

Curriculum Vitae

Personal Details

Name Simone Pfau
Date of Birth 14 July 1995 in Hannover
Address Am Ortfelde 4, 30916 Isernhagen
Phone 015151496361
E-Mail simone.pfau@t-online.de
Nationality German

Education

Aug 2001 – Jun 2005 Grundschule Gartenheimstraße
Aug 2005 – Jun 2013 Gymnasium: Käthe-Kollwitz-Schule, Degree: Abitur, Grade: 1.8
Oct 2013 – Sep 2017 Leibniz University Hannover
Physics studies with the degree Bachelor of Science
Grade: 1.2
Oct 2017 – Oct 2019 Leibniz University Hannover
Physics studies with the degree Master of Science
Grade: 1.3
Since Nov 2019 Leibniz University Hannover
PhD program (Meteorology)

Career

Dec 2016 – Mar 2018 Tutoring at Studienkreis Altwarmbüchen
Mai 2018 – Apr 2019 Student assistant at the Institute for Gravitational Physics
Nov 2019 – Aug 2022 Research associate at the Institute of Meteorology and Climatology
Since Jun 2022 Research associate at the GEO-NET Umweltconsulting GmbH

Publications

Theses

Pfau, S.: Das de Finetti'sche Theorem. Bachelor thesis, Leibniz University Hannover, Hannover, Germany, 2017.

Pfau, S.: Emissionsratenbestimmung für städtischen Verkehr zur Einhaltung von Schadstoffgrenzwerten mit Hilfe Inverser Modellierung. Master thesis, Leibniz University Hannover, Hannover, Germany, 2019.

Poster

Pfau, S., Groß, G.: Sensitivity analysis of the PALM model system input parameters, Leibniz University Hannover, Hannover, Germany, 2023.

Conference contributions

Pfau, S., GEO-NET Umweltconsulting GmbH: Berücksichtigung des Einflusses des Klimawandels in Energieertragsprognosen, 31. Windenergietage 08. – 10. November 2023, Potsdam, Germany, 2023.

Abstracts

Pfau, S., GEO-NET Umweltconsulting GmbH: PO164: Energy yield assessments considering climate change, <https://windeurope.org/annual2024/conference/posters/PO164/>, last access: 02.01.2024.